

Lars Hoff
Acoustic characterization of
contrast agents for medical
ultrasound imaging

NTNU Trondheim
Norges teknisk-naturvitenskapelige
universitet

Doktor ingeniøravhandling 2000:27
Fakultet for elektroteknikk og
telekommunikasjon
Institutt for teleteknikk

420002



**Acoustic Characterization
of
Contrast Agents
for
Medical Ultrasound Imaging**

Lars Hoff

Submitted to
the Norwegian University of Science and Technology
in partial fulfillment of the requirements
for the degree of
Doktor ingeniør

Norwegian University of Science and Technology
Department of Telecommunications
N-7491 Trondheim, Norway

April, 2000

Abstract

The acoustic properties of contrast agent have been studied *in vitro*.

Various theories for bubbles in acoustic fields have been reviewed, both linear and nonlinear. A theoretical model for the oscillation of a gas bubble in a shell has been developed. The shell was modeled using the linear viscoelastic parameters shear modulus G and shear viscosity η . The shell was included into the theory for linear bubble oscillations, giving expressions for the resonance frequency, damping, scattering, attenuation and speed of sound. The nonlinear models were formulated as ordinary differential equations for the motion of the bubble wall. The shell was included into these models as a boundary condition at the bubble wall.

A system for measuring the acoustic attenuation as function of frequency was constructed. This system can be closed and set under pressure, to investigate how the agents respond to hydrostatic pressure. Another system to measure acoustic scatter from the agents was developed. This system can transmit a sequence of pulses with defined shape into a sample of contrast agent. The scattered echoes are recorded as digitized RF-traces.

Measurements of acoustic attenuation spectra were used to investigate and compare three different contrast agents made by Nycomed Amersham. The resonance frequency of the microbubbles was found to be between 2 and 5 times higher than predicted from the theory for gas bubbles of the same size. This increased resonance frequency is explained by the shell, which increases the stiffness of the bubbles. The measured acoustic attenuation spectra were compared with theoretical measurements, and were used to estimate the unknown material parameters of the shell. Differences were found between the three investigated substances. These differences could not be explained by the size of the bubbles alone, but must be caused by the different shell materials. The stiffness of the microbubbles was estimated, measured as bulk modulus. The bulk modulus was estimated to around 3 MPa for *Albunex*, 2.5 MPa for the polymer shelled bubbles and around 0.7 kPa for *Sonazoid*. For comparison, the bulk modulus of a gas under isothermal compression is 0.10 MPa. The shell increases microbubble stiffness between 5 and 40 times, depending on the shell type and bubble size.

Measurements of sound speed showed small, but measurable dispersion. For concentrations relevant for diagnostic imaging, the change in phase velocity is less than 1%. The measured dispersion curves fit well to theoretical calculations for shell encapsulated bubbles. The measured dispersion was less than predicted for free gas bubbles of the same size.

Exposed to 120 mmHg increased hydrostatic pressure, the polymeric microbubbles showed a decrease in resonance frequency. This shift under pressure

was reversible. Such a downshift in resonance frequency is contrary to what is expected, and was explained by the polymer shell being curled and made more flexible by the increased pressure. *Sonazoid* gave a reversible increase in resonance frequency when exposed to the same pressure. This is as expected from the reduction in bubble size under pressure.

The scatter from *Sonazoid* at higher harmonics was investigated. When exposed to driving pulses of center frequency 1 MHz, peaks up to the 9th harmonic were measured. The measured harmonics agreed with predictions from the nonlinear theory.

The nonlinear models were implemented into computer programs, simulating the response of a contrast agent bubble to a driving ultrasound pulse. These programs were used to simulate effects reported in the literature. Pulse inversion was modeled, describing how the responses from two inverted pulses change from two inverted to two phase-shifted echoes. The subharmonic response was modeled, showing how a subharmonic mode emerges at a certain driving pressure, and that the contrast agent bubbles can respond chaotic under some conditions.

Preface

This dissertation is submitted to the Norwegian University of Science and Technology, NTNU, in partial fulfillment of the requirements for the degree of Doktor ingeniør.

The work has been performed at the Acoustic group at the Department of Telecommunications at the Faculty for Electrical and Electronics Engineering, NTNU, in the years from 1995 to 2000. My supervisor has been professor Jens M. Hovem. The first year, 1995, was financed by Nycomed Imaging AS, which was my employer at the time. The work was interrupted for one and a half years during 1996 and 1997, due to problems with financial funding. During the last years of the work, from 1997 to 1999, I have been employed at the Department of Telecommunications at NTNU, financed by a grant from the Norwegian Research Council.

Acknowledgements

I wish to especially thank my supervisor, Jens Hovem, for being of great help, support and encouragement during this work. Thanks also to all my colleagues at the Acoustics group for creating an interesting and stimulating work environment, especially mentioned are Svein Arne Frivik and Bjarte Berntsen and our helpful secretary Åse Vikdal. I also thank Bjørn Angelsen, Tonni Johansen and Gunnar Taraldsen at Department of Physiology and Biomedical Engineering, NTNU, for a fruitful collaboration and many stimulating discussions about nonlinear bubble oscillations.

I also wish to thank Jonny Østensen and Kjell Øygarden at Nycomed. Jonny supported me during the start of this project, and initially made it very clear for me that I ought to complete a Doctoral Thesis. Kjell kept me in contact with the research work going on in contrast agent imaging, and has brought me in contact with many interesting persons and places. Also many thanks to all my former colleagues in the Research and Development division of Nycomed Imaging, for fruitful discussions, and for accepting me as a part of

them even after I left to complete this thesis. Special thanks to Audun Tørnes, Andrew Healey and Morten Eriksen for interesting discussions concerning the clinical use and state of the art in ultrasound contrast agent research, and to Per Christian Sontum, for good collaboration in the characterization of various particles. Also many thanks to Tore Skotland and Nico de Jong, who introduced me to the field of ultrasound contrast agents, and to Andrew Baker at CMR for many helpful discussions about nonlinear acoustics.

Finally, great thanks to my mother, Sigrunn Hoff, for letting me live in her house during my stays in Trondheim, and for taking excellent care of me during these stays. I also wish to thank my father, Rolv Hoff, who sadly could not see this work finished. At last, many thanks to Aasne Aasmundtveit Hoff, the girl who became my wife midway in this work, for her support and understanding during the time I worked with this thesis.

Contents

Preface	v
List of Figures	xiii
List of Tables	xv
Symbols and Abbreviations	xvii
1 Introduction	1
1.1 Medical Ultrasound Imaging and Contrast Agents	1
1.2 Underwater Acoustics and Bubbles	3
1.3 Definition of the Problem	4
1.4 Medical Applications	5
1.5 Overview of the Thesis	6
2 The Bubble as a Linear Oscillator	9
2.1 Some Comments Regarding Scale and Dimensions	10
2.2 Rayleigh-scatter	10
2.3 The Bubble as an Oscillator	14
2.3.1 Equation of Motion for the Bubble	23
2.3.2 Scatter and Absorption	26
2.3.3 Attenuation	31
2.3.4 Speed of Sound in a Bubbly Liquid	34
2.4 Gas Bubble in a Shell	41
3 Nonlinear Bubble Theory	49
3.1 Nonlinear Acoustics in Diagnostic Ultrasound	49
3.1.1 Nonlinearity in Liquids with and without Bubbles . . .	50
3.1.2 Linear and Nonlinear Systems	51
3.1.3 Bubble Detection Based on Nonlinear Acoustics	53

3.2	Equations of Motion for the Liquid	56
3.2.1	Incompressible Liquid: The Rayleigh-Plesset Equation	62
3.2.2	Linear Propagation I: Trilling Model	66
3.2.3	Linear Propagation II: Keller-Miksis Model	71
3.2.4	Comparison between the Liquid Models	75
3.3	Viscous Damping in the Liquid	77
3.3.1	Incompressible Liquid	78
3.3.2	Compressible Liquid: Acoustic Approximation	79
3.4	Pressure Difference across a Spherical Shell	79
3.4.1	Shell Elasticity	80
3.4.2	Comments and Alternative Shell Models	85
3.4.3	Shell Viscosity	86
3.4.4	Summary: Tension across the Shell	89
3.5	Pressure in the Gas	89
3.6	Boundary Condition: Pressure at the Bubble Surface	91
3.7	Equations in Dimensionless Variables	92
3.7.1	Pressure at the Bubble Surface	93
3.7.2	Rayleigh-Plesset Model	95
3.7.3	Trilling Model	95
3.7.4	Keller-Miksis Model	97
3.7.5	Modified Rayleigh-Plesset Model	97
3.7.6	Reconstitution of Dimensional Variables	98
4	Measurement Systems	99
4.1	Acoustic Attenuation	99
4.1.1	Measurement of Attenuation Spectra	100
4.1.2	Sensitivity to Hydrostatic Pressure	105
4.2	Acoustic Backscatter	109
5	Estimation of Shell Material Properties	117
5.1	Composition of the Microbubbles	117
5.2	Theory	118
5.2.1	Church's Model for <i>Albunex</i> : Comparison with the Models of Chapter 3	119
5.2.2	Linearization	121
5.2.3	Acoustic Attenuation and Scatter	122
5.2.4	Thermal and Acoustic Damping	123
5.3	Results	123
5.3.1	Size Distribution	123
5.3.2	Acoustic Attenuation Spectra	124
5.3.3	Estimation of Shell Parameters	125

5.4	Some Calculations Based on the Results	127
5.4.1	Damping Constants	127
5.4.2	Microbubble Stiffness	129
5.4.3	Resonance Frequency and Scattering Cross Section . . .	129
5.5	Discussion	132
5.5.1	Shell Thickness	132
5.6	Summary	133
6	Comparison Between Contrast Agents	135
6.1	Properties of the Three Agents	135
6.1.1	Size Distributions	136
6.1.2	Acoustic Attenuation Spectra	139
6.2	Estimates for Shell Material Properties	140
6.2.1	Albunex	140
6.2.2	<i>Sonazoid</i>	142
6.3	Sensitivity to Hydrostatic Pressure	143
6.3.1	Polymeric Microbubbles	143
6.3.2	<i>Sonazoid</i>	146
6.4	Velocity Dispersion	146
6.4.1	Calculation of Phase Velocity	146
6.4.2	Measured Dispersion	147
6.5	Theoretical Calculations Based on the Results	150
6.5.1	Resonance Frequency and Bulk Modulus	150
6.5.2	Scattering Cross Section	152
6.5.3	Damping Constants	152
6.6	Summary: Comparison between the Agents	154
7	Scatter at Higher Harmonics	159
7.1	Experimental Setup	159
7.1.1	Transmit Pulses	161
7.1.2	Receiver Characteristics	163
7.2	Results	163
7.2.1	Received Spectra	163
7.2.2	Simulated Spectra	166
7.3	Simulated Bubble Radius and Bubble Destruction	169
7.4	Discussion	171
7.5	Conclusion	171

8	Simulations of Nonlinear Bubble Response	173
8.1	Implementation of Nonlinear Bubble Models	173
8.1.1	Simulation Parameters	176
8.2	Pulse Inversion	176
8.2.1	Results of Simulations	178
8.2.2	Summary and Comments	190
8.3	Subharmonic Oscillations	191
8.3.1	Simulations of Subharmonic Response	191
8.3.2	Comments and Relation to Earlier Results	199
8.3.3	Pulse Responses	203
8.3.4	Difference between Pulse and CW Responses	205
9	Summary and Conclusions	215
	References	218

List of Figures

2.1	Mono- and dipole scatter	12
2.2	Rayleigh-scatter	13
2.3	Analogy between bubble and oscillator	14
2.4	Definition of pressures and force on a bubble.	16
2.5	Thermal damping parameters	22
2.6	Dimensionless damping constants	24
2.7	Radial displacement transfer function	25
2.8	Scattering cross section	27
2.9	Extinction cross section	27
2.10	Ratio between scattering and extinction cross section	31
2.11	Illustration of attenuation	32
2.12	Speed of sound and attenuation. Single-sized bubbles	38
2.13	Speed of sound and attenuation. Distribution of bubble sizes	38
2.14	Speed of sound at low frequency	40
3.1	Linear system	52
3.2	Illustration of bubble in liquid	63
3.3	Radial stress and pressures on the bubble shell	80
3.4	Pressure across a shell	85
3.5	Contribution to shell viscosity	88
3.6	Pressure inside a bubble	90
3.7	Tensions at the bubble wall	91
4.1	Attenuation measurement setup	100
4.2	Pulses measured with the 3.5 MHz transducer	102
4.3	Acquisition of attenuation results	103
4.4	Processing of attenuation results	104
4.5	Relationship between <i>mmHg</i> and <i>Pa</i>	107
4.6	Pressure sensitivity system	108
4.7	Report from pressure test system	110
4.8	Setup for sampling RF-traces	111

4.9	Acquisition of RF	113
4.10	Acquisition of RF-traces: GUI menu	114
5.1	Drawing of polymeric microbubble	118
5.2	Size distribution of polymeric microbubbles	124
5.3	Acoustic attenuation spectra of the polymeric microbubbles	125
5.4	Damping constants for polymeric microbubbles. $d=4.0 \mu\text{m}$	128
5.5	Damping constants for polymeric microbubbles. $d=8.0 \mu\text{m}$	128
5.6	Resonance frequency for polymeric microbubbles	130
5.7	Scattering cross section for polymeric microbubbles. Diameter variation	131
5.8	Scattering cross section for polymeric microbubbles. Frequency variation	131
6.1	Size distributions of three agents	137
6.2	Acoustic attenuation spectra of three agents	138
6.3	Measured and calculated spectra for <i>Albunex</i>	141
6.4	Measured and calculated spectra for <i>Sonazoid</i>	142
6.5	Pressure stability, polymeric microbubbles	144
6.6	Pressure stability, <i>Sonazoid</i>	145
6.7	Velocity dispersion, polymeric microbubbles	148
6.8	Velocity dispersion, <i>Sonazoid</i>	149
6.9	Calculated dispersion and attenuation for <i>Sonazoid</i>	150
6.10	Bulk modulus of three agents	151
6.11	Resonance frequency of three agents	151
6.12	Scattering cross section for three agents. Diameter variation	153
6.13	Scattering cross section for three agents. Frequency variation	153
6.14	Damping constants of three agents. $3 \mu\text{m}$	155
6.15	Damping constants of three agents. $5 \mu\text{m}$	156
7.1	Scatter at harmonics: Measurement setup	160
7.2	Transmitted pulses	162
7.3	Receiver response	164
7.4	Measured spectra with harmonics, 20 cycle pulses	165
7.5	Size distribution of <i>Sonazoid</i>	167
7.6	Simulated radial amplitude, 5 cycle pulses	168
7.7	Ratio between maximum and minimum bubble radius	170
8.1	<i>Bubblesim</i> . GUI menu	174
8.2	Pulse inversion. Driving pulses, 2.25 MHz	179
8.3	Pulse inversion. Time responses, 2.25 MHz	180

8.4	Pulse inversion. Cross-correlations, 2.25 MHz	181
8.5	Pulse inversion. Power spectra, 2.25 MHz	182
8.6	Pulse inversion. Simulated radius, 2.25 MHz	184
8.7	Pulse inversion. Driving pulses, 6.0 MHz	185
8.8	Pulse inversion. Time responses, 6.0 MHz	186
8.9	Pulse inversion. Cross-correlations, 6.0 MHz	187
8.10	Pulse inversion. Power spectra, 6.0 MHz	188
8.11	Pulse inversion. Simulated radius, 6.0 MHz	189
8.12	Subharmonics. CW, $d=2.0 \mu\text{m}$	195
8.13	Subharmonics. CW, $d=3.0 \mu\text{m}$	196
8.14	Subharmonics. CW, $d=4.0 \mu\text{m}$	197
8.15	Subharmonics. CW, $d=6.0 \mu\text{m}$	198
8.16	Subharmonic level. Pressure amplitude 500 kPa	200
8.17	Subharmonic level. Pressure amplitude 1000 kPa	200
8.18	Subharmonics. Driving pulses	204
8.19	Subharmonics. Hanning pulse, $d=2.0 \mu\text{m}$	206
8.20	Subharmonics. Hanning pulse, $d=3.0 \mu\text{m}$	207
8.21	Subharmonics. Hanning pulse, $d=4.0 \mu\text{m}$	208
8.22	Subharmonics. Hanning pulse, $d=6.0 \mu\text{m}$	209
8.23	Subharmonic: Cosine-tapered pulse, $d=2.0 \mu\text{m}$	210
8.24	Subharmonics. Cosine-tapered pulse, $d=3.0 \mu\text{m}$	211
8.25	Subharmonics. Cosine-tapered pulse, $d=4.0 \mu\text{m}$	212
8.26	Subharmonics. Cosine-tapered pulse, $d=6.0 \mu\text{m}$	213

List of Tables

2.1	Rayleigh-scatter	11
4.1	Attenuation measurements: Transducer data	101
4.2	Solubility of gases in water	106
4.3	RF sampling parameters	112
4.4	Results of backscatter measurement	115
5.1	Shell properties estimated for polymeric microbubbles	127
5.2	Bulk modulus of polymeric microbubbles and other substances	130
6.1	Comparison between three ultrasound contrast agents	140
7.1	Scatter at harmonics. Transducer parameters	160
7.2	Scatter at harmonics. Transmit pulse parameters	161
7.3	Scatter at harmonics. Sampling parameters	166
8.1	Simulation of bubble response. Input parameters	175
8.2	Pulse inversion. Simulation parameters	178
8.3	Subharmonics. Simulation parameters	192
8.4	Subharmonics. List of result figures	193
8.5	Subharmonics. Summary of results	199

Symbols and Abbreviations

Symbols

a	Bubble radius
\dot{a}	Bubble wall velocity
c	Speed of sound
c_w	Speed of sound in water
d	Bubble diameter
d_S	Shell thickness
$e \approx 2.718$	Base of natural logarithms
f	Frequency
f_i	Frequency of the driving sound field
f_0	Resonance frequency
h	Enthalpy per unit volume
$i = \sqrt{-1}$	Imaginary unit
$k = 2\pi/\lambda$	Acoustic wavenumber
k_c	Complex acoustic wavenumber
$k_r = \text{Re}(k_c)$	Real part of acoustic wavenumber
$k_i = \text{Im}(k_c)$	Imaginary part of acoustic wavenumber
$m = 4\pi\rho a^3$	Dynamic mass of bubble
p	Pressure
p_i	Driving acoustic pressure
p_s	Scattered acoustic pressure
p_∞	Pressure far from the bubble surface
p_0	Atmospheric pressure
(r, θ, ϕ)	Spherical coordinates
t	Time
u	Particle velocity
x	Radial strain, $a(t) = a_e(1 + x(t))$
(x, y, z)	Cartesian coordinates

\mathbf{D}, D_{ij}	Rate-of-strain tensor
G	Shear modulus
H	Transfer function: Acoustic pressure to bubble radius
I	Intensity of sound
K	Bulk modulus
P	Acoustic power
R	Mechanical resistance
\mathbf{T}, T_{ij}	Stress tensor
V	Volume
Z	Mechanical impedance
$\delta = \frac{R}{\omega_0 m}$	Dimensionless damping constant
δ_c	Damping constant from acoustic radiation
δ_{th}	Damping constant from thermal conduction
δ_L	Damping constant from liquid viscosity
δ_S	Damping constant from shell viscosity
$\delta_{tot} = \sum_k \delta_k$	Total damping constant, sum of all contributions
δ_{ij}	$\delta_{ij} = 0$ for $i \neq j$, $\delta_{ii} = 1$ Kronecker delta
ϵ, ϵ_{ij}	Strain tensor
η	Shear viscosity
κ	Polytropic exponent of a gas
λ	Acoustic wavelength
λ, μ	Lamé coefficients of an elastic solid
ϕ	Volume fraction of bubbles
ϕ	Phase of acoustic pulse
ρ	Density
τ	Surface tension
σ_s	Scattering cross section
σ_a	Absorption cross section
σ_e	Extinction cross section
ξ	Change in bubble radius, $a(t) = a_e + \xi(t)$
ξ	Strain vector
$\omega = 2\pi f$	Angular frequency
$\omega_0 = 2\pi f_0$	Angular resonance frequency
Φ	Velocity potential, defined by $\mathbf{u} = \nabla\Phi$
$\Omega = \omega/\omega_0$	Normalized frequency
$\frac{dx}{dt} = \frac{\partial x}{\partial t} + (\mathbf{u}\nabla)x$	Material derivative
$\dot{x} = \frac{dx}{dt}$	Differentiation of x with time

$Tr\mathbf{T} = \sum_k T_{kk}$	Trace of tensor \mathbf{T}
$Im(x)$	Imaginary part of quantity x
$Re(x)$	Real part of quantity x
$\ln x$	Natural logarithm of x
$\lg x$	Base 10 logarithm of x
$\hat{x}(\omega)$	Fourier transform of $x(t)$
x_e	Value of x when the bubble is at equilibrium
x_i	Value of x in the driving sound field
x_s	Value of x in the scattered sound field
x_∞	Value of x in the liquid far from the bubble
X_w	Value of physical parameter X for water
X_L	Value of physical parameter X for the liquid surrounding the bubble
X_S	Value of physical parameter X for the shell encapsulating the bubble

Abbreviations

ADC	Analog to digital converter
CW	Continuous wave
DE	Differential equation
FT	Fourier Transform
FFT	Fast Fourier Transform
HSA	Human serum albumin
ODE	Ordinary differential equation
PDE	Partial differential equation
PRF	Pulse repetition frequency
RF	Radio frequency signals, received before demodulation or amplitude detection
SNR	Signal to noise ratio

Chapter 1

Introduction

1.1 Medical Ultrasound Imaging and Contrast Agents

Ultrasound imaging has been commonly in use in medical diagnosis since the 1970s. The technique is today widely used, for a variety of medical investigations. It is especially the low cost and easy use that makes ultrasound imaging so attractive.

Contrast agents for medical ultrasound imaging were proposed in 1968 [51], a more systematic search for good ultrasound contrast agents started around 1980. The first agent was approved by the health care authorities in 1991, this was *Echovist* from the German company Schering AG. Two years later came the agent *Albunex*, from the company Molecular Biosystems Inc. in San Diego, California, USA. This agent was co-developed by several pharmaceutical companies, one of these was Nycomed Imaging AS in Norway. After 1990, the research efforts towards better contrast agents for ultrasound imaging have been intensified. There are now several contrast agents in clinical trials, and a few are already on the market.

Medical ultrasound imaging is based on echoes, i.e. the scatter and reflection of sound from inhomogeneities in the tissue. These echoes are interpreted in the Ultrasound scanner, and are used to compose an image of the interior of the body. Ultrasound scatter from blood is much weaker than scatter from other tissue, typically 30 to 60 dB weaker. But the Doppler effect causes a frequency shift in the echoes from moving blood, and these weak signals can be separated from tissue echoes. This is used to estimate the velocity and direction of the blood flow in various diagnostic ultrasound Doppler techniques.

The aim of introducing contrast agents is to increase the scatter of sound from the blood. This will be used to increase the information contents in ultra-

sound images and obtain diagnostic information that is not available without contrast agent. Examples are:

- Volume, shape and movement of blood filled cavities, notably the ventricles of the heart.
- Studies of blood flow in small vessels that are difficult to investigate without contrast agents.
- Measurements of blood perfusion, that is, blood flow through the tissue. This is especially interesting in the heart muscle, myocardium.

To achieve these goals, the scatter of sound from blood should be increased by approximately 30 dB. Various new detection techniques are now in use or being tested to enhance the signals from the contrast agent above the signals from the tissue. The most well known are *2nd harmonic imaging* and *pulse inversion imaging*. Such techniques reduce the required increase in scattered power from the contrast agents.

Ultrasound is a macroscopic phenomenon: Contrary to x-rays, sound is scattered and reflected from macroscopic structures, not on single atoms or molecules. A contrast agent for ultrasound must therefore be based on particles, not on water soluble molecules. Frequencies used in medical ultrasound imaging range from 2 to 10 MHz, giving wavelengths between 150 and 800 μm . The contrast agent particles have to pass through capillaries with diameters of about 7 μm [63], giving an upper limit for the particle diameter that is much smaller than the wavelength of the sound. About 40% of the blood volume consists of particles of this size, mainly red blood cells [30]. Particles used as an ultrasound contrast agent must therefore be very powerful ultrasound scatterers. Theory [117] and experiments show that such strong sound scatter can be achieved by using extremely compressible particles. As a consequence of this, most of the research on ultrasound contrast agents is concentrated on microbubbles, where the gas is stabilized by a shell.

There are some interesting alternatives to the use of shell encapsulated bubbles as ultrasound contrast agents. The substances *Echovist* and *Levovist* (Schering AG, Berlin, Germany) consist of sugar crystals that liberate air while being slowly dissolved in the blood. The agent *Echogen* (Sonus, Bothell, Wash., USA) contains perfluoropentane, which is a liquid at room temperature, but boils and generates gas when the temperature is raised to body temperature. Another approach being tested is to make a particle with an irregular hydrophobic surface, which traps gas in small cavities. This is the concept behind the *Bubbicles* [132]. Hwang et al. [66] have described a device that generates bubbles in the urinary bladder by emitting long ultrasound bursts at frequency 1.8 MHz.

A rather new approach is to make “targeted” contrast agents. These contrast agents contain particles that specifically bind to pathological tissue, enhancing the ultrasound echoes from such tissue [87, 86].

The agents studied in this thesis all consist of gas bubbles stabilized by various types of shells. For the reasons mentioned above, this is by far the most common approach to creating an ultrasound contrast agent.

1.2 Underwater Acoustics and Bubbles

From underwater acoustics, it is well known that bubbles in water are powerful ultrasound scatterers. Studies of underwater bubble acoustics date back to Lord Rayleigh [143], who in 1917 looked at cavitation and collapse phenomena. Later, in 1933, Minnaert published a model where the bubble was viewed as a harmonic oscillator [113], explaining the characteristic resonance frequency of oscillating bubbles. This model, with some improvements, is still the basic description of bubbles oscillating at small amplitudes, i.e. under linear conditions. From 1950 until today, a large amount of studies on bubble acoustics were published, both theoretical and experimental, describing effects like the stability of bubbles towards gas diffusion [41], the effect of encapsulating the gas in a membrane [47], and damping mechanisms of the oscillating bubble [34]. A nice summary of linear bubble acoustics is given by Medwin [110], nonlinear bubble acoustics is summarized by Prosperetti [141, 142]. A more complete description of oscillating bubbles can be found in the book by Leighton [96]. The acoustics of bubbles shows nonlinear behavior at lower acoustic pressures than in a homogeneous liquid [142]. One result of these nonlinear oscillations is the creation of higher harmonics. This effect has been used to selectively detect bubbles in a flowing liquid [111], and is now being used to detect medical contrast agents. Nonlinear frequency mixing, creating sum- and difference frequencies, has been used to measure the size of bubbles [123]. The use of nonlinear properties to detect contrast agents *in vivo* is described in a patent by Schering AG [165].

The understanding of contrast agents for medical imaging has gained great benefit from decades of bubble research in underwater acoustics, as several theoretical and experimental models can be directly transferred. However, there are differences between medical ultrasound and underwater acoustics, and medical ultrasound introduces new phenomena not previously studied. Compared to bubbles in underwater acoustics, contrast agents in medical ultrasound differ mainly in the following ways:

- The scale is different, involving higher frequencies, shorter distances and smaller bubbles

- Bubbles used in medical ultrasound imaging are encapsulated in a shell, which alters the acoustic properties compared to free bubbles
- Blood is a highly inhomogeneous liquid, about 40% of its volume is particles. Blood has also higher viscosity and lower surface tension than water, and higher solubility for oxygen.
- The different size and time scales introduce different absorption mechanisms. These mechanisms alter the transfer of sound energy into heat.

Studies of the scatter and transmission of sound from a contrast agent were published by de Jong et al. in the early 1990s [29, 28]. The theoretical models here were based on bubble models by Fox and Herzfeld [47] and Medwin [110]. These studies could explain why and how the acoustic properties of the ultrasound contrast agent *Albunex* differed from free bubbles. This theory was extended by Holm et al. in 1994 [64], to give a more complete model for the attenuation and scatter from contrast agents in tissue.

1.3 Definition of the Problem

Although there exists a vast amount of studies in bubble acoustics, medical contrast agents introduce phenomena that are yet not fully understood. The aim of this thesis is to increase the understanding of the acoustics of ultrasound contrast agents. Specifically, the scatter and absorption of ultrasound from microbubbles is studied. The bubbles' acoustic properties are described in terms of:

- Physical properties, including the encapsulating shell.
- Include nonlinear oscillations into the models.

Ethical Aspects

All medical research involves ethical considerations. This work is in essence basic technology, but aims towards medical applications. All experiments are purely technical, and were performed *in vitro* in laboratories.

It is a goal that ideas and results from the thesis shall be implemented into medical diagnostic ultrasound equipment, and that the results may be helpful in the diagnosis of diseases. New technology must be tested in biological trials involving animals or humans. This implementation and testing lies outside this thesis. Any biological testing, whether in animals or in humans, must be performed by persons who are qualified to do so, and who are qualified to do

the necessary ethical considerations. Likewise, any evaluation of the clinical diagnostic value of the methods must be done by qualified persons, with the necessary medical training and expertise.

The anticipated medical applications of this work are to increase the ability to detect the presence and measure the flow of blood. This shall improve the diagnosis of the patients. Any final evaluation and decision concerning the use of these methods must be done by qualified medical personnel.

1.4 Medical Applications

A goal of this work is to obtain a better understanding of the signals from the contrast agents. This may increase the diagnostic information in ultrasound images, and help improving medical diagnosis in some patients.

Specifically, the sound scattered from contrast agents can have signatures that distinguish it from sound scattered from tissue. Better understanding of these effects will help optimizing diagnostic ultrasound equipment towards detecting such signatures. It will also help the manufacturers of contrast agents to design the agents to give as much information as possible.

The information gained may be used in a variety of clinical applications, the most attractive seem to be:

- Visualization of presence of contrast agent in the tissue, e.g. by color coding. This is interesting for studying the liver function, by looking at uptake of particles by the liver.
- Measurement of blood supply to an organ, e.g. the heart muscle. Visualization of regions with normal, reduced or increased blood supply.

Measuring the blood supply to the heart muscle is of very high interest, as reduced blood supply to the heart caused by occluded vessels is a cause of serious heart diseases. A reliable method to detect reduced blood supply to regions of the heart at an early stage might help diagnosis and treatment of these diseases.

Detection of contrast agent in the liver is another area of great interest. The particles will be taken up by a functioning liver, hence, detecting particles in the liver will tell if parts of the liver do not function. This may provide a simple and reliable method to diagnose spread of cancer to the liver, and might help to improve the treatment of some cancer patients.

1.5 Overview of the Thesis

This thesis describes work done to characterize and better understand the acoustic properties of contrast agents used in medical ultrasound imaging.

The thesis contains rather extensive chapters on linear and nonlinear bubble acoustics, Chapters 2 and 3. These were included partly as a background for the experimental and theoretical descriptions later in the thesis. But it has also been my ambition to collect and give a unified presentation of the acoustic theory behind the bubbles used in medical contrast agents, including the shell enclosing them. Hence, I hope that these chapters will be of general interest for persons working with the acoustics of ultrasound contrast agents, not only as a background for the rest of this thesis.

The experimental part of the thesis consists of Chapters 4 to 7. It describes the development of two different systems used to characterize the agents, and results of these characterizations. The results are linked to the theory described in the earlier chapters.

The last chapter, Chapter 8, describes the implementation of the nonlinear bubble models, and gives the results of simulations based on these models. It is shown how some effects reported in the literature can be explained by the bubble models.

The contents of the thesis is summarized as:

Chapter 2. Linear Bubble Theory Overview of the interaction between sound and small gas bubbles. Emphasis is on the effects, bubble sizes and sound frequencies that are important in diagnostic ultrasound imaging.

Chapter 3. Nonlinear Bubble Models A review of nonlinear bubble models. A theoretical model of the effect of enclosing the bubble in a solid shell.

Chapter 4. Measurement Systems Description of two *in vitro* systems used to characterize ultrasound contrast agents:

- Acoustic attenuation spectra, with hydrostatic over-pressure
- Acoustic backscatter, sampled as RF traces.

Chapter 5. Estimation of Shell Material Properties An experimental method to estimate the unknown material parameters of the shell.

Chapter 6. Comparison between Three Contrast Agents Results from acoustic *in vitro* characterization of Albunex, polymer shelled air-bubbles and *Sonazoid*. The three agents are characterized and compared acoustically, with emphasis on the effect of the different shell materials.

Chapter 7. Scatter at Higher Harmonics Measurements of acoustic scatter at higher harmonics. Comparison with numerical simulations.

Chapter 8. Simulations of Nonlinear Oscillations Implementation of nonlinear bubble models as simulation programs. The bubble response to a driving ultrasound pulse is simulated. The following effects are simulated:

- Scatter at higher harmonics
- Pulse inversion
- Subharmonic oscillation

Chapter 2

The Bubble as a Linear Oscillator

Gas bubbles in liquids are known to be highly efficient scatterers of sound, even if the bubble diameter is much smaller than the wavelength of the sound. This makes bubbles unique compared to other particles of equal size. The strong acoustic scatter makes bubbles important in several applications of acoustics, as sources of noise, absorption and scatter. Some examples of applications are:

Fish Sonar The target strength of fish can be strongly enhanced by the swim bladder. Fish without swim bladder give lower target strength than fish with swim bladder.

Attenuation Attenuation of sound in water is increased in presence of even very low concentrations of bubbles.

Contrast agents for medical ultrasound imaging A tiny concentration of small gas bubbles is injected into the blood vessels. This increases the power of the ultrasound echoes from blood by several orders of magnitude, and opens new possibilities for studying blood flow by ultrasound.

This chapter gives an overview of the basic linear theory for the scattering of sound on small gas bubbles. In this context, *small* means that the bubble diameter is much smaller than the wavelength of the driving sound field. The theoretical description models the bubble with its surrounding liquid as a linear oscillator.

2.1 Some Comments Regarding Scale and Dimensions

Diagnostic medical imaging uses ultrasound frequencies typically between 2 and 8 MHz. Some special applications uses higher frequencies, 15 or even up to 30 MHz. An example of this is intracardiac imaging with the transducer placed on a catheter inside the blood vessel. When using contrast agents, non-linear techniques have gained popularity, such as imaging at the 2nd harmonic frequency and pulse inversion imaging. These techniques tend to use lower frequencies, 1.5 to 2.5 MHz. Pulses for imaging are mostly short, typically a few oscillations, with bandwidth around 50% of the center frequency. Pulses used in Doppler techniques are longer, with narrower bandwidth. 2nd harmonic imaging tend to use longer pulses than in conventional imaging, to reduce the transmitted sideband level at the 2nd harmonic frequency. Coded pulses, with a high time-bandwidth product, are also used in medical imaging. For these long pulses, the radial resolution is regained by correlating the received signal with the transmit pulse.

The wavelength λ of the ultrasound is determined by the frequency f by

$$\lambda = \frac{c}{f}, \quad (2.1)$$

where c is the speed of sound in the tissue. Typical sound velocities in soft tissue are $c \approx 1540$ m/s. This means that the frequencies used in medical ultrasound imaging cause wavelengths between $200 \mu\text{m}$ and 1 mm. Frequencies used in intracardiac imaging give much shorter wavelengths, between $10 \mu\text{m}$ and $30 \mu\text{m}$.

The diameter of particles injected into the blood stream is limited by the diameters of the capillaries. The capillary diameter varies between 2 and $10 \mu\text{m}$, with a mean around $7 \mu\text{m}$ [63].

This means that the particle diameters must be much smaller than the acoustic wavelength.

A contrast agent for diagnostic ultrasound imaging must consist of particles that are much smaller than the acoustic wavelength, but nevertheless are extremely powerful sound scatterers. The only known solution to this is using microbubbles.

2.2 Rayleigh-scatter

The simplest model for scatter of sound from small particles is due to Rayleigh. *Small* means that the particle diameter is much smaller than the wavelength

Table 2.1. Rayleigh-scatter: Contributions from compressibility and from density for various materials. Data from Kinsler et al. [73].

Material	Bulk modulus (adiabatic)	Density	Contribution to scatter	
	K [MPa]	ρ [kg/m ³]	$\left(\frac{K-K_0}{3K}\right)^2$	$\frac{1}{3}\left(\frac{\rho-\rho_0}{2\rho+\rho_0}\right)^2$
Air (37°C)	0.14	1.14	2.9×10^7	0.33
Rubber (soft)	1000	950	0.17	0.00001
Water (37°C)	2250	1000	0	0
Glass (Pyrex)	39000	2300	0.10	0.018
Aluminum	75000	2700	0.10	0.024
Steel	170000	7700	0.11	0.056
Tungsten	310000	19300	0.11	0.071

of the sound,

$$d \ll \lambda \quad \text{or} \quad ka \ll 1, \quad (2.2)$$

where d is the particle diameter, λ is the wavelength of the incoming sound, $k = 2\pi/\lambda$ is the acoustic wavenumber and $a = \frac{1}{2}d$ is the particle radius.

Rayleigh-scatter is not a model suited for describing the scatter of sound from bubbles. It ignores both resonance phenomena and sound absorption by the bubble. But the Rayleigh model gives a first impression of the mechanisms and properties causing the scatter of sound, and it illustrates why bubbles are so extremely powerful sound scatterers.

A model for the scatter of sound from small objects is given in Lord Rayleigh's book "The theory of sound", published in 1896 [144]. When this model is formulated as a scattering cross section σ_s , it gives the expression [118]

$$\sigma_s = 4\pi a^2 (ka)^4 \left[\left(\frac{K - K_0}{3K} \right)^2 + \frac{1}{3} \left(\frac{\rho - \rho_0}{2\rho + \rho_0} \right)^2 \right], \quad (2.3)$$

where ρ and ρ_0 are the densities of the particle and of the embedding fluid, and K and K_0 are the bulk moduli of the particle and of the embedding fluid.

The factors outside the brackets give the dependence on particle size and sound frequency:

- πa^2 is the geometric cross section of the particle.
- $(ka)^4$ gives dependence on frequency.

According to Rayleigh's model, the scattering cross section increases by k^4 , that is, by frequency to the 4th power, and by a^6 , by particle diameter to the 6th power.

The terms inside the brackets give dependence on the material parameters of the particle, *bulk modulus* K and *density* ρ . The bulk modulus is a measure of the volume stiffness of a material, it is the inverse of compressibility. The bulk modulus is defined by

$$K = -V \frac{\Delta p}{\Delta V}, \quad (2.4)$$

where Δp is the change in pressure and ΔV is the change in volume. If a particle with bulk modulus different from the embedding fluid is exposed to a sound pulse, the particle will oscillate in volume. This causes the particle to radiate sound in a spherically symmetric pattern, giving *monopole scatter*. If the density of the particle differs from that of the liquid, the particle will undergo a translatory motion. It will oscillate back and forth in the sound field. The particle will radiate sound in a dipole pattern, with directionality as the cosine to the angle with the incoming sound wave. These two radiation patterns are illustrated in Figure 2.1.

The expression (2.3) for the scattering cross section predicts that the density term cannot exceed $\frac{1}{3}$, regardless of the value of the density ρ . There is no limit to the magnitude of the compressibility term. The monopole scattering increases towards infinity as K is reduced towards zero.

The most compressible materials are the gases. Under isothermal compression, the ideal gas law predicts that $pV = \text{constant}$. This gives a bulk modulus of the gas equal to the ambient pressure p_0 . Adiabatic compression is more common in acoustics. The relation for adiabatic compression, $pV^\gamma = \text{constant}$, predicts that the adiabatic compressibility of a gas is

$$K = \gamma p_0, \quad (2.5)$$



Figure 2.1. Scattering diagrams for monopole and dipole scatter. Scattered intensity as function of angle for a plane sound wave.

where γ is the adiabatic constant of the gas. The value of γ for diatomic gases, such as air, is $\gamma=1.40$. Noble gases, being mono-atomic, have $\gamma=1.67$, while multi-atomic gases have γ between 1.0 and 1.3.

Liquids and solids have much larger bulk moduli than gases, ranging from 10^4 to 10^6 times the atmospheric pressure p_0 . Examples of K and ρ for selected substances are listed in Table 2.1. The same table lists values of the density and compressibility terms, calculated from (2.3). The contributions from compressibility and density to scattering cross section are plotted in Figure 2.2. The compressibility term for air is several orders of magnitude larger than all the other terms, illustrating the extreme ability of air bubbles to scatter sound.

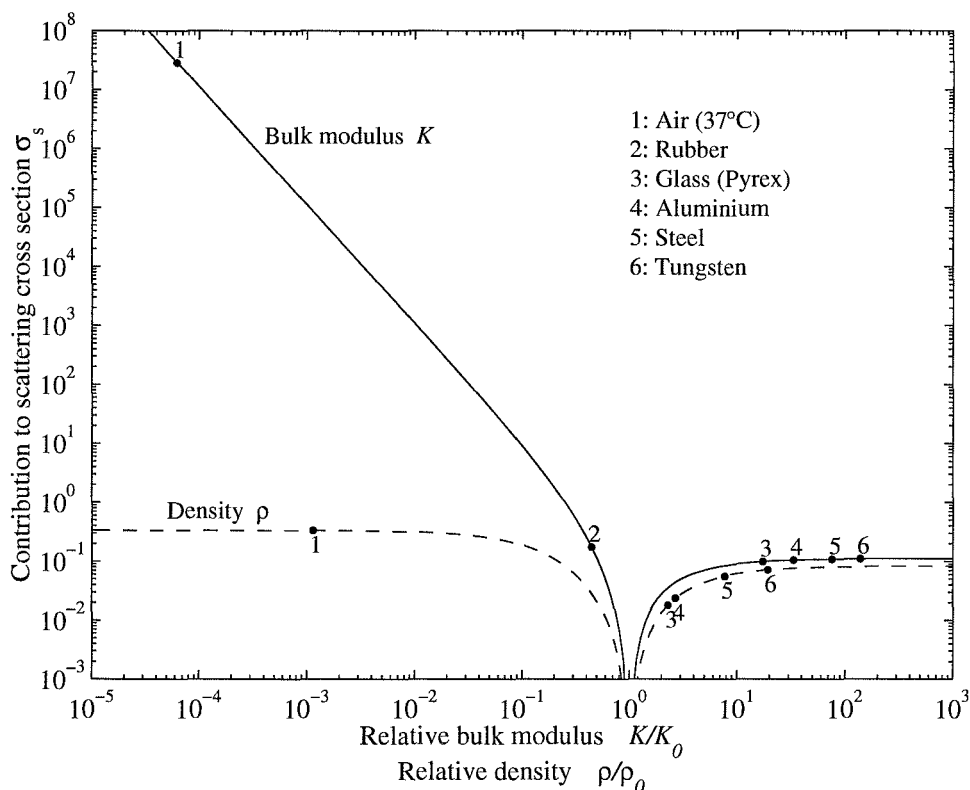


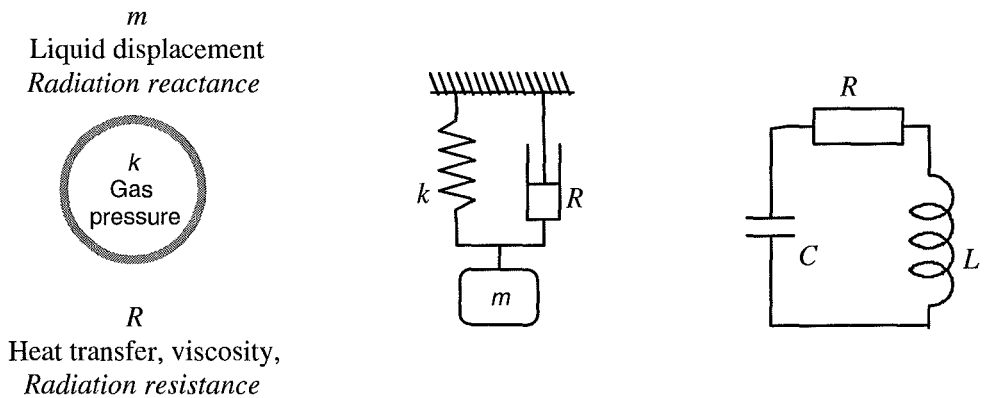
Figure 2.2. Rayleigh-scatter: Contributions from compressibility and density.

2.3 The Bubble as an Oscillator

Rayleigh's model ignores resonance, and is not suited for calculating the scatter of sound from a bubble. A better model is to consider the bubble as a linear oscillator. This requires that the oscillation amplitude is small relative to the equilibrium radius.

Table 2.1 shows that the difference in compressibility is the dominating source of scatter for gas bubbles. The density term is several orders of magnitude smaller and can be neglected. It is convenient to compare the oscillating bubble with electrical and mechanical oscillators.

Mass Oscillation of the bubble surface requires the surrounding liquid to be displaced. This adds inertia to the system. The liquid mass corresponds to the mass of a mechanical oscillator, or to the inductor of an electrical oscillator.



Bubble	Mechanical oscillator	Electrical oscillator
Gas pressure	Spring, stiffness	Capacitor, capacitance
Liquid mass	Mass, inertia	Coil, inductance
Radiation resistance viscosity, heat transfer	Dash-pot, friction	Electrical resistance

Figure 2.3. Analogy between a gas bubble and mechanical and electrical oscillators.

Spring Compression or expansion of the gas gives a spring force acting against the change in volume. The gas pressure corresponds to the spring of a mechanical oscillator, or to the capacitor of an electrical oscillator.

Damping Viscosity, radiation of sound, and heat exchange between gas and liquid introduce damping. They correspond to the dash-pot of a mechanical oscillator, or to electrical resistance.

The bubble will have an eigenfrequency, giving a resonance peak in the scattering cross section. The first oscillator-description for the bubble is due to Minnaert. In 1933, he studied the sound emitted from air bubbles in water, listening to the emitted sound and comparing it to a tune-fork. The results were published in a paper titled *On Musical Air-Bubbles and the Sounds of Running Water* [113]. Minnaert derived equation for resonance frequency from energy equations. In this chapter, equations of force balance are used, as this makes it easier to include damping from frictional forces. It also makes easier to include the response to an external pressure field. Parts of the following derivation are based on the paper *Counting Bubbles Acoustically* by Medwin [110] and on the book *The Acoustic Bubble* by Leighton [96].

It is assumed that the bubble retains its spherical shape during the oscillations. Nonspherical bubbles were studied theoretically and experimentally by Strasberg in 1953 [159]. He concluded that deviations from the spherical shape change the resonance frequency by less than 5% for spheroids, when the ratio between the long and short axes is less than 3. The treatment is also limited to bubbles embedded in a liquid of infinite extent, wall effects are ignored. Strasberg [159] also studied bubbles close to a rigid wall or a free surface. He concluded that when the boundary is more than 5 bubble diameters away, it alters the resonance frequency by less than 5%.

Stiffness: Gas Pressure

In acoustics, compression is mostly regarded as adiabatic, there is no heat transport. This is not true for all bubble diameters and frequencies. For micrometer-size bubbles driven at Megahertz-frequencies, the oscillation is closer to isothermal. A more convenient model is to describe the bubble compression and expansion with the polytropic gas model. The relation between pressure p and volume V is modeled as

$$pV^\kappa = \text{constant}, \quad (2.6)$$

where κ is the polytropic exponent of the gas. For adiabatic oscillations, κ equals the adiabatic constant γ of the gas, while for isothermal oscillations,

κ is equal to one. In general, κ is a function of bubble radius and sound frequency. Expressions for κ can be found in the literature, this is discussed in the section about thermal damping later in this chapter.

On differential form, the polytropic relation between changes in volume and pressure takes the form

$$\frac{dp}{p} = -\kappa \frac{dV}{V}. \quad (2.7)$$

The bulk modulus K of the bubble is, from (2.4),

$$K = \kappa p_e, \quad (2.8)$$

where p_e is the equilibrium pressure inside the bubble.

The topic of this chapter is linear oscillations. Small volume changes ΔV around the equilibrium volume V_0 are studied. The situation is illustrated in Figure 2.4. The instantaneous radius $a(t)$ of the bubble is expressed as

$$a(t) = a_e + \xi(t), \quad |\xi| \ll a_e. \quad (2.9)$$

where a_e is the equilibrium bubble radius and ξ is the radial displacement. The radial displacement ξ is much smaller than the bubble radius, To the first order in ξ , the change in bubble volume ΔV is

$$\Delta V = 4\pi a^2 \xi, \quad \text{with} \quad V = \frac{4}{3}\pi a^3. \quad (2.10)$$

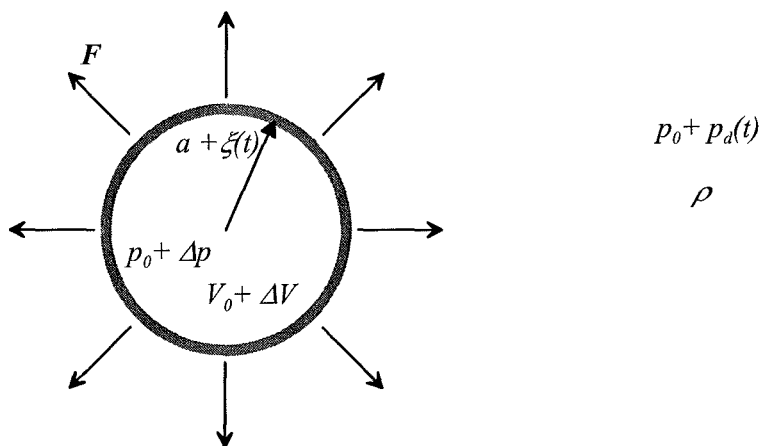


Figure 2.4. Definition of pressures and force on a bubble.

The change in volume causes a change in pressure $\Delta p = p - p_e$ inside the bubble. The polytropic model (2.7) gives this pressure change as

$$\Delta p = -\frac{3\kappa p_e}{a}\xi. \quad (2.11)$$

The force F_s on the bubble surface is the integral of the pressure over the bubble surface

$$F_s = \iint_S p_s dS = 4\pi a^2 p_s = -12\pi a \kappa p_e \xi = -s\xi, \quad (2.12)$$

where s is a "spring constant" of the bubble. The bubble compression and expansion follows Hooke's law, with spring constant s given by

$$s = 12\pi a \kappa p_e. \quad (2.13)$$

This derivation has not included the effect of a shell encapsulating the bubble, neither was surface tension considered. Both shell and surface tension will increase the stiffness compared to the free bubble. The effect of a shell is described in Chapter 2.4. A surface tension τ at the gas-liquid interface increases the pressure by $2\tau/a$. This increases the equilibrium pressure p_e inside the bubble to

$$p_e = p_0 + \frac{2\tau}{a}, \quad (2.14)$$

where p_0 is the hydrostatic pressure in the fluid. For an air-water interface, the surface tension is $\tau_w = 0.07 \text{ N/m}$ [100]. For bubbles with radii in the μm -range, this causes an increase in gas pressure in the order of one atmosphere. This is not negligible. But if the water is polluted or contains surface active ingredients, its surface tension will be substantially reduced. Blood contains surface active protein molecules, causing the surface tension of blood to be much lower than of water.

Inertia: Mass of the Moving Liquid

When the bubble oscillates, it sets the surrounding liquid in motion, introducing inertia to the system. The mass of the gas will also add some inertia. But as the density of a gas is approximately 1000 times less than the density of a liquid, the inertia of the gas can safely be neglected. Inertia is calculated from the pressure field p_s radiated from the oscillating bubble. This is a diverging spherical wave, with radial variation as

$$p_s(r) = p_s(a) \frac{a}{r} e^{i(\omega t - kr)}, \quad (2.15)$$

where $p_s(a)$ is the pressure at the bubble surface $r = a$. The relation between pressure p and velocity u is found from the Euler equation [82], neglecting the nonlinear term

$$\rho \frac{\partial u}{\partial t} = -\nabla p. \quad (2.16)$$

At the bubble surface, where the liquid velocity $u = \dot{\xi}$ and $r = a$, this gives

$$\rho \ddot{\xi} = -\frac{\partial p_s}{\partial r} = \frac{p_s(a)}{a} (1 + ika). \quad (2.17)$$

Dots denote differentiation with time. The pressure p_s radiated from the bubble is

$$p_s(a) = \rho a \frac{1 - ika}{1 + (ka)^2} i\omega \dot{\xi} \approx \omega \rho a (ka + i) \dot{\xi}, \quad (2.18)$$

where the approximation is valid for $ka \ll 1$. The integral of p_s over the bubble surface gives the force F_m on the bubble surface from the liquid motion

$$F_m = -4\pi a^2 p_s = -4\pi a^3 \rho \omega (ka + i) \dot{\xi}. \quad (2.19)$$

The mechanical impedance Z_m at the bubble surface is defined by

$$F_m = -Z_m \dot{\xi} = -(R\dot{\xi} + m\ddot{\xi}) = -(R + i\omega m)\dot{\xi}, \quad (2.20)$$

where R is the radiation resistance and ωm is the radiation reactance. The effective mass m of the oscillating bubble is identified from (2.19) and (2.20) as

$$m = 4\pi a^3 \rho. \quad (2.21)$$

The effective mass of the oscillating bubble is equal to the mass of a liquid volume three times larger than the bubble. ωm is the reactive source impedance of a simple acoustic source [118].

Damping

Various frictional mechanisms will damp out the oscillations of the bubble. The three main sources of damping are:

- Radiation resistance. Energy is lost as the bubble radiates sound energy.
- Viscosity in the surrounding liquid.

- Heat transport between the gas and the liquid. This causes energy absorption if the oscillation is neither perfectly isothermal nor adiabatic, but somewhere in between.

The frictional force is defined as a force F_R of the form

$$F_R = -R\dot{\xi}, \quad (2.22)$$

where R is the mechanical resistance of the oscillating bubble. R is modeled as a sum contributions from the three mechanisms above, $R = R_c + R_\eta + R_{Th}$. R_c is the radiation resistance, R_η is the resistance from liquid viscosity, and R_{Th} is the resistance from heat transport inside the gas.

Radiation resistance The radiation resistance R_c is the real part of the radiation impedance Z_m from (2.19) and (2.20)

$$R_c = Re(Z_m) = 4\pi a^2 \rho c (ka)^2. \quad (2.23)$$

$4\pi a^2$ is surface area of the bubble and ρc is the specific acoustic impedance of the liquid.

$4\pi a^2 c$ would be the radiation resistance of a source that is large compared to the wavelength [118]. The factor $(ka)^2 \ll 1$ makes the radiation resistance of the bubble much smaller than this. It is caused by the bubble radius being much smaller than the wavelength of the sound.

Viscous damping Damping from viscosity in the embedding liquid is important for bubbles diameters in the μm -range. Mechanical resistance from the viscosity of the liquid was calculated from the viscous stress-tensor of a Newtonian liquid in Chapter 3.3, (3.103) on page 79. This gives the radial stress T_L at the bubble surface as

$$T_L = -p_L - 4\eta \frac{\dot{a}}{a}. \quad (2.24)$$

This corresponds to a viscous resistance force F_η on the bubble surface equal to

$$F_\eta = -4\pi a^2 \times 4\eta \frac{\dot{\xi}}{a} = -16\pi a \eta \dot{\xi}. \quad (2.25)$$

The viscous resistance R_η is, by the definition (2.22)

$$R_\eta = 16\pi a \eta. \quad (2.26)$$

Thermal damping The thermal damping is found by analyzing the heat transport inside the gas during the oscillations. The liquid is treated as a reservoir of constant temperature.

These calculations were done by Devin in 1959 [34], who found expressions for viscous, acoustic and thermal damping calculated at the resonance frequency of the bubbles. Devin's results were extended in 1970 by Eller [37], to give values also off-resonance. An outline of these calculations can also be found in the book by Leighton [90].

Prosperetti extended Eller's results in 1977 [140], allowing the pressure inside the gas to vary with radius. Prosperetti found differences from Eller's calculated polytropic exponent for large bubbles at high frequencies. In almost all situations of practical interest, the results of Devin-Eller and Prosperetti are identical, as was shown by Crum in 1983 [24]. Crum also compared the theoretically calculated values of the polytropic exponent κ with experimental measurements, finding a good agreement between the theoretical and experimental results.

The thermal damping is a relaxation process. At low frequencies, the heat transport in the gas goes fast enough to keep the temperature constant in the bubble. This gives isothermal oscillation with no thermal damping. At high frequencies, the heat transport is too slow to be considered. This gives adiabatic oscillations and no damping. However, in an intermediate frequency range, the oscillation is neither isothermal nor adiabatic. In this range, the temperature oscillates inside the gas so that the pressure caused by the temperature variations is out of phase with the driving acoustic pressure. Oscillatory energy is converted to heat, causing a damping of the oscillations. Across this intermediate frequency range, the exponent κ changes from its low frequency isothermal value $\kappa = 1$ to its high frequency adiabatic value $\kappa = \gamma$.

The results for thermal damping parameter summarized here are based on the works by Devin [34] and Eller [37], assuming that the pressure in the gas does not vary with position. Devin derived an expression for the relation between applied pressure $\hat{p}_i(\omega)$ and volume change $\hat{v}(\omega)$ in the gas bubble, calculated in the frequency domain. This is formulated in Devin's Equations (49) and (50) as

$$\frac{\hat{v}(\omega)}{\hat{p}_i(\omega)} = \frac{V}{p_e} \Phi(a, \omega), \quad (2.27)$$

with

$$\Phi(a, \omega) = \frac{1}{\gamma} \left(1 + \frac{3(\gamma - 1)}{\Psi^2} (\Psi \coth \Psi - 1) \right), \quad (2.28a)$$

$$\Psi(a, l_D(\omega)) = \frac{1}{2}(1 + i) \frac{a}{l_D}, \quad (2.28b)$$

$$l_D(\omega) = \sqrt{\frac{K_g}{2\omega\rho_g C_p}}, \quad (2.28c)$$

The quantity l_D is the thermal diffusion length, which is a function of the thermodynamic properties of the gas: ρ_g is the density, C_p is the heat capacity at constant pressure, K_g is the thermal conductivity and γ is the adiabatic constant of the gas.

The thermal diffusion length l_D expresses the typical thermal diffusion distance during one oscillation cycle. When the bubble is much smaller than the thermal diffusion length, the heat transport is fast enough to keep the temperature constant during the oscillation cycle. Contrary, when the bubble is much larger than the thermal diffusion length, the heat transport is negligible over the bubble radius.

From the definitions of bubble stiffness and damping constant, the polytropic exponent κ and the resistance from thermal conduction R_{Th} are identified as

$$\kappa = Re\left(\frac{1}{\Phi(a, \omega)}\right), \quad (2.29a)$$

$$R_{Th} = \frac{12\pi a p_e}{\omega} Im\left(\frac{1}{\Phi(a, \omega)}\right). \quad (2.29b)$$

The thermal diffusion length $l_D(\omega)$ for air bubbles and the real and imaginary parts of the function $1/\Phi$ are plotted in Figure 2.5. The real part of $1/\Phi$ is the polytropic exponent κ , while the imaginary part is a measure of the thermal resistance R_{Th} . The graph of $Re(1/\Phi)$ shows how κ changes from its isothermal value $\kappa=1.0$ to its adiabatic value $\kappa=1.4$ as the bubble radius increases relative to the thermal diffusion length. The graph of the imaginary part of $1/\Phi$ shows how thermal damping is important only in the intermediate region where κ is between its isothermal and its adiabatic value.

For bubble sizes and frequencies used in ultrasound contrast agents, the bubble oscillation is mainly in the transition region between isothermal and adiabatic oscillations. Hence, for typical contrast agent bubbles used in medical ultrasound imaging, the damping from thermal conduction must be considered.

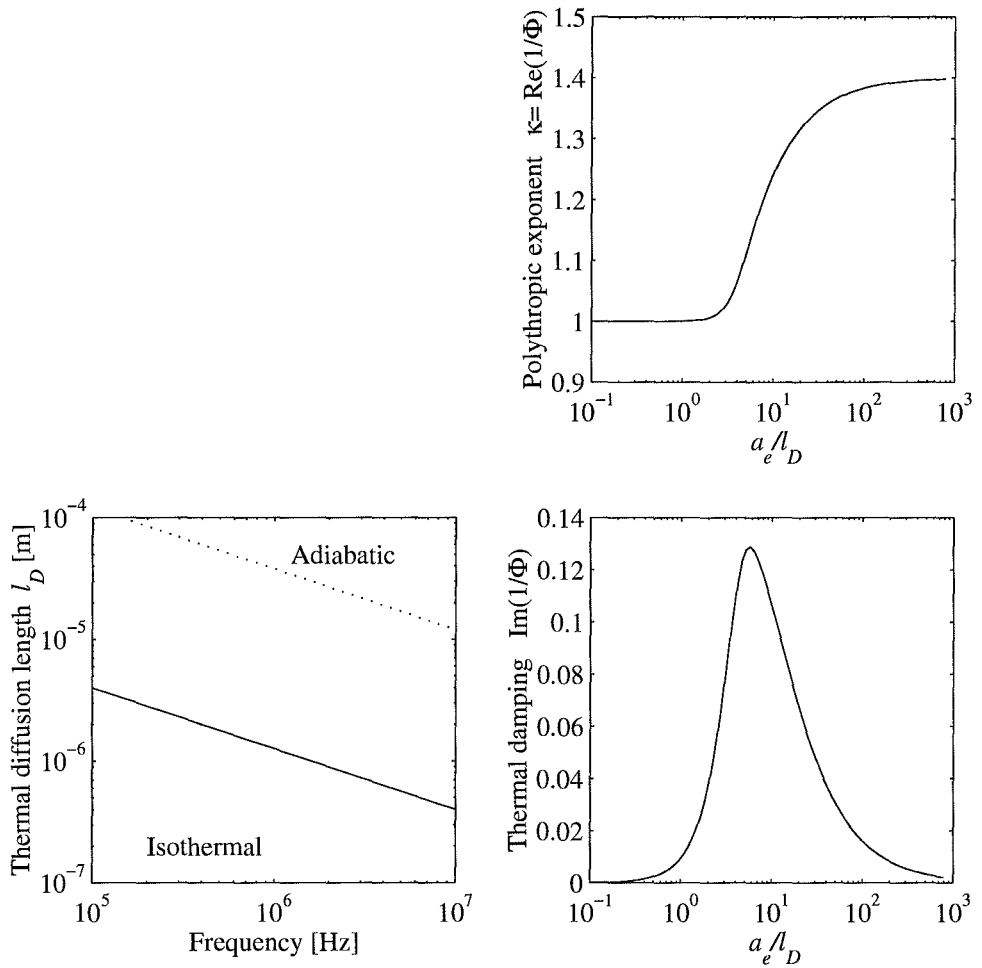


Figure 2.5. Thermal diffusion length l_D as function of frequency. The thermodynamic gas properties are for air. Polytropic exponent κ and thermal damping constant d_{Th} as function of bubble radius a , relative to thermal diffusion length l_D .

2.3.1 Equation of Motion for the Bubble

An equation of motion is found from the forces at the bubble surface. These forces consist of restoring stiffness from the gas, inertia from the liquid, damping from mechanical resistance, and the driving acoustic pressure $p_i(t)$. The resulting equation is

$$F_m + F_R + F_s = \iint_S p_i(t) dS. \quad (2.30)$$

The expressions for F_s , F_R and F_m , (2.12) and (2.20), are inserted into this equation, giving a differential equation for the radial displacement ξ

$$m\ddot{\xi} + R\dot{\xi} + s\xi = -4\pi a^2 p_i. \quad (2.31)$$

This is recognized as the equation of motion for a linear mechanical oscillator. The equation is best handled in the frequency domain. Fourier-transformation yields

$$(-\omega^2 + i\omega\omega_0\delta + \omega_0^2)\hat{\xi}(\omega) = -\frac{1}{\rho a}\hat{p}_i(\omega). \quad (2.32)$$

The angular resonance frequency ω_0 and the damping constant δ are

$$\omega_0^2 = \frac{s}{m} = \frac{3\kappa p_e}{a^2\rho}, \quad (2.33a)$$

$$\delta = \frac{R}{\omega_0 m}. \quad (2.33b)$$

The linear resonance frequency $f_0 = \omega_0/2\pi$ is

$$f_0 = \frac{1}{2\pi a} \sqrt{\frac{3\kappa p_e}{\rho}}, \quad (2.34)$$

f_0 is called the Minnaert-frequency [113].

The mechanical resistance R is a sum of three terms, $R_m = R_c + R_\eta + R_{Th}$. This gives the damping constant δ as a sum of three corresponding terms

$$\delta = \delta_c + \delta_\eta + \delta_{Th}. \quad (2.35)$$

The damping constants from radiation resistance and viscosity are identified from the expressions (2.23), (2.26) and (2.29b) as

$$\delta_c = \frac{\omega^2 a}{\omega_0 c}, \quad (2.36a)$$

$$\delta_\eta = \frac{4\eta}{\omega_0 \rho a^2}, \quad (2.36b)$$

$$\delta_{Th} = \frac{3p_e}{\omega\omega_0\rho a^2} \text{Im}\left(\frac{1}{\Phi}\right). \quad (2.36c)$$

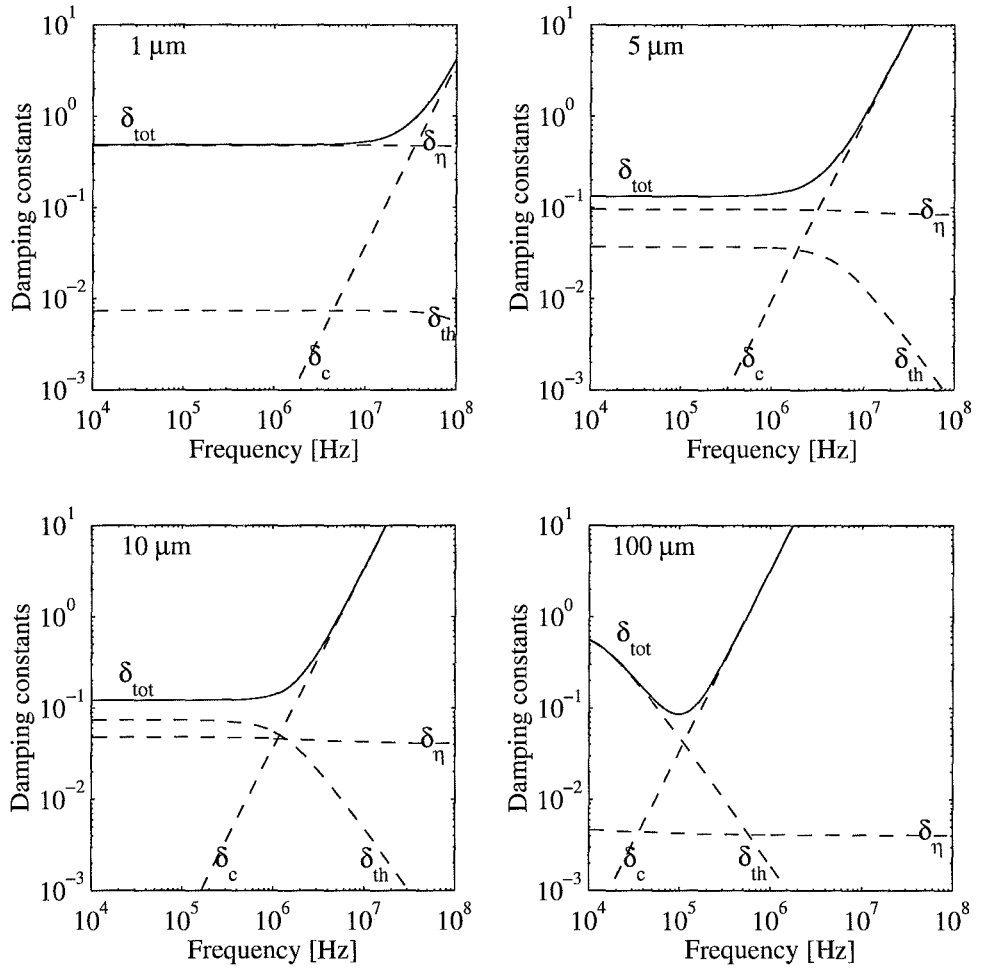


Figure 2.6. Dimensionless damping constants for free bubbles with diameter 1 μm , 5 μm , 10 μm and 100 μm , plotted as function of frequency. The total damping constant is $\delta_{tot} = \delta_\eta + \delta_c + \delta_{th}$.

The damping constants for three different bubble sizes are plotted in Figure 2.6. At low frequencies, the damping from liquid viscosity dominates for the smallest bubbles, while thermal damping dominates for the larger bubbles. At high frequencies, the radiation damping takes over and becomes the dominating damping mechanism for all bubble sizes.

Several slightly different definitions of the damping constant δ are found in the literature. The definition used here is the same as that used by Church [22], but differs by a factor ω/ω_0 from those used by Medwin [110] and Leighton [90].

The radial displacement $\hat{\xi}$ as function frequency and driving pressure $\hat{p}_i(\omega)$ is found from the equation of motion (2.32) to

$$\hat{\xi}(\omega) = \frac{1}{\rho a \omega_0^2} \frac{\hat{p}_i(\omega)}{(\omega/\omega_0)^2 - 1 - i\omega/\omega_0 \delta}. \quad (2.37)$$

This can be expressed by a transfer function for radial displacement $H(\Omega)$, defined by

$$H(\Omega) = \rho a \omega_0^2 \frac{\hat{\xi}(\omega)}{\hat{p}_i(\omega)} = \frac{1}{\Omega^2 - 1 - i\Omega \delta}, \quad \Omega = \frac{\omega}{\omega_0}. \quad (2.38)$$

Ω is the normalized frequency.

The transfer function $H(\Omega)$ is plotted in Figure 2.7. The radial displacement amplitude has its maximum at the resonance frequency ω_0 . Below res-

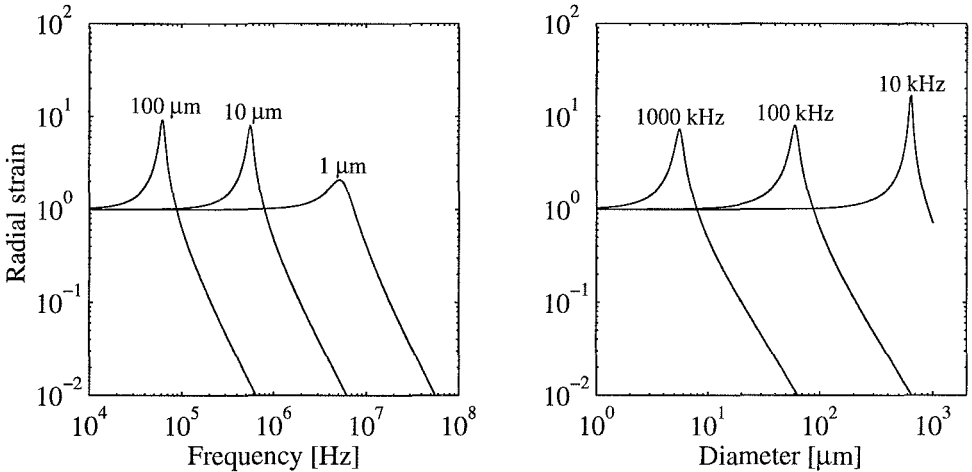


Figure 2.7. Normalized radial displacement as function of frequency and bubble diameter. The transfer function is defined as $\frac{\hat{\xi}(\omega)}{p_i/(\rho a \omega_0^2)}$.

onance, the transfer function is constant. Above resonance, it decays rapidly with increasing frequency.

The radial displacement transfer function gives a hint to where the linear model is most likely to be valid. The linear model requires the radial displacement to be small. For a given driving pressure, the radial amplitude is larger below resonance than above resonance. From this it can be expected that the bubble is more easily driven into nonlinear oscillations for driving frequencies below resonance than above. Maximum radial displacement is found at resonance. This is where the bubble is expected to be most easily driven into nonlinear oscillations.

2.3.2 Scatter and Absorption

Scattering Cross Section

The radiated sound pressure $p_s(a, t)$ at the surface of the bubble was found in equation (2.18) to

$$\hat{p}_s(a, \omega) = a\rho\ddot{\xi} \frac{1}{1 + ika} \approx -\omega^2 a\rho\hat{\xi}(\omega) \quad (2.39)$$

The radial oscillation $\hat{\xi}$ is expressed as function of the driving pressure \hat{p}_i from (2.37). This gives a relation between the driving pressure field \hat{p}_i and the radiated pressure $\hat{p}_s(a)$ at the bubble surface as

$$\hat{p}_s(a, \omega) = \frac{\Omega^2}{1 - \Omega^2 + i\Omega\delta} p_i(\omega). \quad (2.40)$$

The scattering cross section $\sigma_s(a, \omega)$ is defined as the ratio between the scattered power $P_s(a, \omega)$ and the incoming sound intensity $I_i(\omega)$

$$\sigma_s(a, \omega) = \frac{P_s(a, \omega)}{I_i(\omega)}. \quad (2.41)$$

σ_s has dimension area. Expressed by the pressure amplitudes of the incoming and scattered field, the scattering cross section becomes

$$\sigma_s(a, \omega) = 4\pi a^2 \left| \frac{\hat{p}_s(a, \omega)}{\hat{p}_i(\omega)} \right|^2. \quad (2.42)$$

The relation (2.40) between $\hat{p}_s(a, \omega)$ and $\hat{p}_i(\omega)$ gives the scattering cross section as

$$\sigma_s(a, \omega) = 4\pi a^2 \frac{\Omega^4}{(1 - \Omega^2)^2 + (\Omega\delta)^2}, \quad \Omega = \frac{\omega}{\omega_0}. \quad (2.43)$$

Examples of scattering cross sections for selected bubble sizes and frequencies are plotted in Figure 2.8.

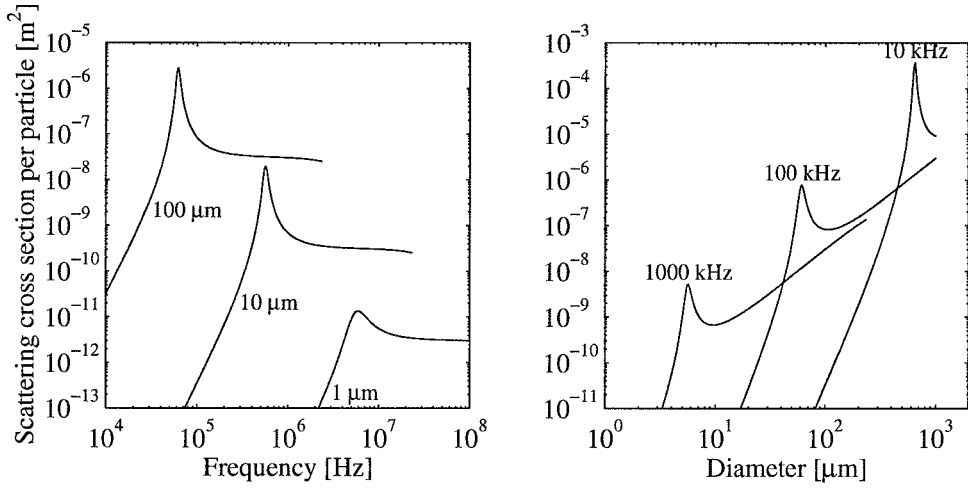


Figure 2.8. Scattering cross section as function of frequency and bubble diameter.

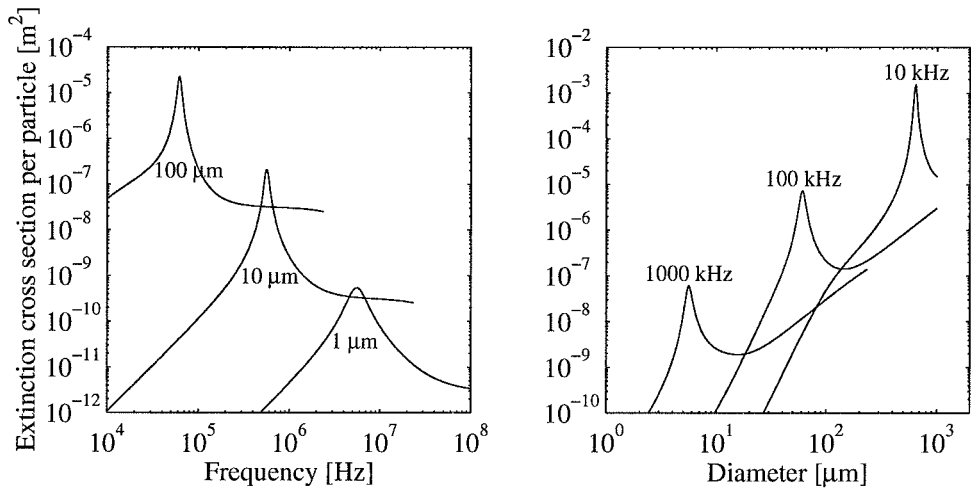


Figure 2.9. Extinction cross section as function of frequency and bubble diameter.

Variation with frequency The left diagram in Figure 2.8 displays how the scattering cross section varies with frequency. For frequencies well below resonance, σ_s increases by f^4 . In this region, the expression (2.43) for σ_s equals the compressibility term in the Rayleigh scattering model, (2.3). For frequencies above resonance σ_s is independent of the frequency. The scatter from a bubble deviates strongly from Rayleigh scatter around and above the resonance frequency.

Variation with diameter The right diagram in Figure 2.8 displays how the scattering cross section varies with bubble diameter. For diameters smaller than the resonance diameter, the scattering cross section increases with the sixth power of the diameter, $\sigma_s \propto d^6$. In this region, the oscillator-model (2.43) gives the same result as the compressibility term in Rayleigh's model, (2.3). For diameters larger than resonance diameter, the scattering cross section increases as the geometric cross section of the bubble, $\sigma_s \propto d^2$.

Comparison between Rayleigh's Model and the Oscillator Model

Rayleigh scatter gave the expression (2.3) for the scattering cross section of small particles. The oscillator model gave the expression (2.43) for the scattering cross section of the bubble. For frequencies below resonance, these two models should give equal results.

For frequencies well below resonance, the oscillator model (2.43) gives

$$\Omega \ll 1, \quad \sigma_s \approx 4\pi a^2 \frac{\Omega^4}{1 + (\Omega\delta)^2} \approx 4\pi a^2 \Omega^4. \quad (2.44)$$

The angular resonance frequency was found in (2.33a) to

$$\omega_0^2 = \frac{3\kappa p_e}{\rho a^2}. \quad (2.45)$$

The angular frequency is expressed by the wave number as $\omega = ck$. This is inserted into the expression (2.44), giving

$$\sigma_s = 4\pi a^2 (ka)^4 \left(\frac{\rho c^2}{3\kappa p_e} \right)^2. \quad (2.46)$$

The speed of sound in a fluid is $c = \sqrt{K/\rho}$, and the bulk modulus K_0 in the Rayleigh model is expressed by the speed of sound in the liquid as

$$K_0 = \rho c^2. \quad (2.47)$$

The bulk modulus of the gas is $K = \kappa p_e$. This is inserted into the equation (2.3) for Rayleigh scatter, giving

$$\sigma_s = 4\pi a^2 (ka)^4 \left[\left(\frac{\kappa p_e - \rho c^2}{3\kappa p_e} \right)^2 + \frac{1}{3} \left(\frac{\rho - \rho_0}{2\rho + \rho_0} \right)^2 \right]. \quad (2.48)$$

The bulk modulus in the liquid is much larger than in the gas, $\rho c^2 \gg \kappa p_e$. This allows the first term inside the brackets to be simplified. The second term can be neglected compared to the first term. This makes (2.48) equal to the low-frequency expression for the bubble, (2.46). The scattering cross section from Rayleigh scatter is equal to that from the oscillator model, provided that the driving frequency is well below the resonance.

Absorption- and Extinction Cross Sections

Viscosity and heat transfer cause absorption of sound. Some of the energy in the sound is converted from wave energy into heat in the bubble and the liquid. This conversion is described by an *absorption cross section* σ_a . The total loss of energy from the sound beam, including both absorption and scatter, is described by the *extinction cross section*, σ_e .

The absorption cross section for one absorption mechanism is defined as

$$\sigma_{ak} = \frac{P_{ak}}{I_i}, \quad (2.49)$$

where P_{ak} is the power absorbed by the absorption mechanism k . k denotes the source of absorption, viscosity or heat conduction.

The extinction cross section σ_e is defined by

$$\sigma_e = \frac{P_e}{I_i}, \quad (2.50)$$

where P_e is the sum of scattered and absorbed power. This is the total loss of power from the incoming sound field.

The relation between the various cross sections is found by expressing the power P_{ak} absorbed by absorption mechanism k as function of the mechanical resistance R_k from damping mechanism k . This is

$$P_{ak} = -F_{Rk}\dot{\xi} = R_k\dot{\xi}^2. \quad (2.51)$$

The ratio between power absorbed by damping mechanism k and the scattered power can now be expressed by the damping constants δ as

$$\frac{P_{ak}}{P_s} = \frac{R_k}{R_c} = \frac{\delta_k}{\delta_c}. \quad (2.52)$$

The absorption cross section is the sum of viscous and thermal damping. The absorbed power is expressed by the scattered power P_s as

$$P_a = \sum_k P_{ak} = \frac{\sum_k \delta_k}{\delta_c} P_s. \quad (2.53)$$

The absorption cross section can then be expressed by the scattering cross section σ_s as

$$\sigma_a = \frac{\sum_k \delta_k}{\delta_c} \sigma_s. \quad (2.54)$$

The total power removed from the acoustic beam is

$$P_e = P_a + P_s. \quad (2.55)$$

This gives the extinction cross section expressed by the scattering cross section σ_s as

$$\sigma_e = \sigma_a + \sigma_s = \frac{\delta}{\delta_c} \sigma_s, \quad (2.56)$$

where δ is the sum of all damping constants, including radiation. Inserting the expression (2.43) for the scattering cross section gives the extinction cross section as

$$\sigma_e = \sigma_s \frac{\delta}{\delta_c} = 4\pi a^2 \frac{\Omega^4}{(1 - \Omega^2)^2 + (\Omega\delta)^2} \frac{\delta}{\delta_c}. \quad (2.57)$$

The efficiency η of the bubble as a sound scatterer is defined as the ratio between scattered and consumed power as

$$\eta = \frac{P_s}{P_e} = \frac{\delta_c}{\delta} = \frac{\delta_c}{\delta_\eta + \delta_{Th} + \delta_c}. \quad (2.58)$$

The scattering efficiency for selected bubbles and frequencies is plotted in Figure 2.10.

For large bubbles, with diameters in the mm-range, radiation is the major source of damping for frequencies above about 10 kHz, $\delta_c \gg \delta_\eta, \delta_{Th}$. For these bubbles, almost all the absorbed power is reradiated, giving a scattering efficiency $\eta \approx 1$.

For micrometer-sized bubbles and frequencies in the Megahertz-range, viscous and thermal damping dominate over radiation, $\delta_c < \delta_\eta, \delta_{Th}$. Most of the consumed power is absorbed, giving low scattering efficiency. Typically η is of the order 10^{-1} for these bubbles.

2.3.3 Attenuation

Attenuation measures how much the incoming sound is reduced when passing through the medium. Attenuation is commonly measured in dB per unit length. In medical ultrasound imaging, dB/cm is most commonly used.

The bubble concentrations studied are low, typical volume fractions are 10^{-5} to 10^{-6} . At these low concentrations, the the bubble oscillations do not interact. The bubbles oscillate, absorb and scatter sound independently of one another. The reduction in power from in the sound field is the sum of power absorbed and scattered for all bubbles treated individually.

A justification for this approach is given at the end of this section, giving a condition for when the bubbles can be treated individually.

Consider sound absorbed and scattered within a small volume $dV = dAdz$, as illustrated in Figure 2.11. Each bubble n in dV removes the power P_n from the sound field. The total power removed from the sound field dP_i is the sum of power absorbed by all bubbles. This is expressed by the extinction cross section as

$$dP_i = \sum_{n=1}^N P_n = I_i \left(\int_0^\infty \sigma_e(a)n(a)da \right) dV, \quad (2.59)$$

where the sum is taken over all N bubbles in the small volume element dV . I_i is the intensity of the incoming sound and $n(a)da$ is the number of bubbles

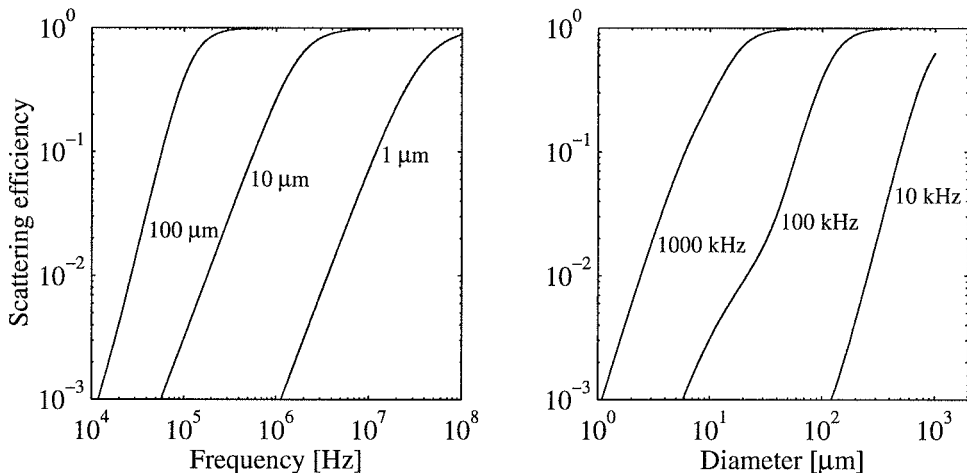


Figure 2.10. Ratio between scattering and extinction cross section. This is the ratio between the power scattered and the power absorbed by the bubble.

per unit volume with radius in the interval $(a, a + da)$.

The change dI_i in sound intensity associated with this consumption of power is

$$dI_i = -\frac{dP_i}{dA} = -I_i \left(\int_0^\infty \sigma_e(a)n(a)da \right) dz. \quad (2.60)$$

This gives the intensity $I_i(z)$ as function of distance z through the bubble suspension as

$$I(z) = I(0)e^{-n\langle\sigma_e\rangle z}, \quad (2.61)$$

where the $\langle\sigma_e\rangle$ is the average extinction cross section per bubble,

$$\langle\sigma_e\rangle = \frac{1}{n} \int_0^\infty \sigma_e(a)n(a)da, \quad n = \int_0^\infty n(a)da. \quad (2.62)$$

n is the number of bubbles per unit volume. The attenuation coefficient α , in dB per unit length, becomes

$$\alpha = -\frac{1}{z} 10 \lg \left(\frac{I_i(z)}{I_i(0)} \right) = 10(\lg e) n \langle\sigma_e\rangle \quad [dB], \quad (2.63)$$

where the factor $10 \lg e \approx 4.34$ comes from the definition of the dB -scale.

Treating the Bubbles as Individual Scatterers: The Waterman and Truell Condition

A classic description of the multiple scattering of waves is due to Waterman and Truell from 1961 [167]. They give a condition for treating the bubbles as

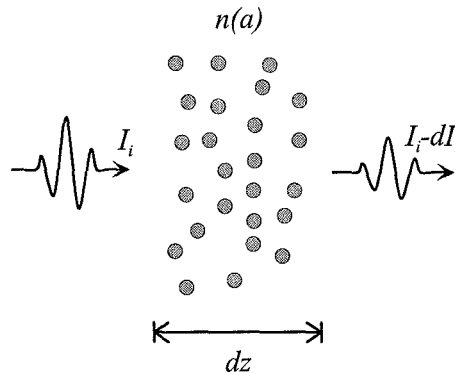


Figure 2.11. Attenuation from a population of bubbles.

individual scatterers, later formulated by Commander and Prosperetti as [23] “the multiple scattering field caused by insertion of a bubble is much smaller than the field exciting that bubble”.

The criterion for this to be valid is found from [167] to

$$\frac{n\sigma_s}{k_r} \ll 1, \quad (2.64)$$

where n is the number of scatterers per unit volume, σ_s is the scattering cross section of each scatterer, and $k_r = 2\pi/\lambda$ is the real part of the acoustic wavenumber.

The propagation of a plane harmonic wave is described by a complex wavenumber $k_c = k_r + ik_i$, so that the pressure $p(z, t)$ varies as

$$p(z, t) = p_0 e^{i(\omega t - k_c z)} = p_0 e^{k_i z} e^{i(\omega t - k_r z)} \quad (2.65)$$

This expression is compared with the expression (2.61) for the attenuation of acoustic intensity. This gives the relation between the imaginary wavenumber k_i and the extinction cross section $\sigma_e(a, \omega)$

$$k_i = -\frac{1}{2} n \sigma_e. \quad (2.66)$$

For simplicity, it is assumed that all bubbles are of equal size in these calculations. The extinction cross section σ_e is expressed by the scattering cross section σ_s by (2.56)

$$\sigma_e = \sigma_s \frac{\delta}{\delta_c}, \quad (2.67)$$

The Waterman and Truell condition (2.64) can now be reformulated to a ratio between the real and imaginary parts of the complex wavenumber

$$\left| \frac{k_i}{k_r} \right| \ll \frac{1}{2} \frac{\delta}{\delta_c}. \quad (2.68)$$

The ratio δ/δ_c is always greater than one. Hence, the condition above will always be fulfilled when the attenuation per wavelength is small. The condition can be expressed by the wavelength λ and the attenuation per distance α by using $\alpha = -20(\lg e)k_i$

$$\alpha \ll 10(\lg e)2\pi \frac{\delta}{\delta_c} \frac{1}{\lambda}. \quad (2.69)$$

Insertion of the worst case values, $(\delta/\delta_c)_{min}=1$ and $\lambda_{max}=1.5$ mm gives $\alpha \ll 180$ dB/cm.

The condition above is always true in the experimental systems used to study the contrast agents. Hence, the Waterman and Truell condition is always fulfilled, and the bubbles can be treated as individual scatterers.

Commander and Prosperetti [23] observed a discrepancy around the resonance frequency between their theoretical calculations and experimental results. They explained this discrepancy by the Waterman and Truell condition (2.64) being violated around resonance. The contrast agent studies described in this thesis and the studies by Commander and Prosperetti were done at comparable attenuation per distance. But the frequencies used by Commander and Prosperetti were much lower, giving a larger attenuation per wavelength. The attenuation per wavelength is always low in the contrast agent studies, and the Waterman and Truell condition is always fulfilled.

2.3.4 Speed of Sound in a Bubbly Liquid

A small volume fraction of bubbles can alter the speed of sound in the liquid. Bubbles can also make the sound speed frequency dependent, that is, introduce velocity dispersion. The radial displacement and volume change of the bubble is in general not in phase with the driving acoustic pressure. In the frequency domain, this corresponds to a complex and frequency dependent compressibility for the bubbly liquid. From this, a complex and frequency dependent speed of sound $c_c(\omega)$ and wavenumber $k_c(\omega) = k_r(\omega) + ik_i(\omega)$ can be calculated.

The phase velocity of the sound is calculated from the real part k_r of the complex wavenumber k_c . The imaginary part k_i gives the attenuation. The attenuation calculated from k_i by this method should give the same result as the attenuation calculated from the extinction cross section, Equation (2.63).

A calculation of the speed of sound in bubbly liquids is given by Leighton [91]. Experimental measurements of velocity dispersion in bubbly liquids were done by Silberman in 1957 [154]. Reviews of experimental and theoretical data are given by Anderson and Hampton [1] and by Commander and Prosperetti [23]. More rigorous mathematical treatments are given by Caffisch et al. [12] and Lu et al. [105].

The sound velocity calculations presented here are done assuming the bubble oscillations to be linear. This means that the relative changes in bubble radii due to the applied acoustic pressure must be small. In general, sound propagations through bubbly liquids may display strong nonlinearities, reducing the validity of this model. But as long as the nonlinear effects are small, the following calculations should give a fairly good model for the phase velocity in the bubbly liquid.

The complex wave number $k_c(\omega)$ for the sound propagating through the

bubbly liquid is calculated from the linear model for bubble oscillations presented in the previous sections. The speed of sound in a medium depends on its compressibility, expressed by the bulk modulus K , and on its density ρ , according to

$$c = \sqrt{\frac{K}{\rho}}. \quad (2.70)$$

For an inhomogeneous medium, the simplest model for effective bulk modulus and density describes the effective medium parameters K and ρ as the average of its components [91, 161]

$$\frac{1}{K} = \frac{1 - \phi}{K_L} + \sum_k \frac{\phi_k}{K_k} \quad (2.71a)$$

$$\rho = (1 - \phi)\rho_L + \sum_k \phi_k \rho_k, \quad (2.71b)$$

$$\phi = \sum_k \phi_k$$

where ϕ_k is the volume fraction of component k , ϕ is the total volume fraction of particles, K_k is the bulk modulus of component k , K_L is the bulk modulus of the liquid, ρ_k is the density of component k and ρ_L is the density of the liquid.

The bulk modulus K_b of the bubble is found from the radial oscillation of the bubble, (2.37) and (2.38). K_b is calculated in the frequency domain as a complex, frequency dependent quantity. It includes static stiffness of the bubble, inertia caused by the displacement of liquid as the bubble oscillates and damping from various frictional mechanisms.

The relation between radial displacement $\hat{\xi}(\omega)$ and applied sound pressure $\hat{p}_i(\omega)$ is expressed from (2.38) as

$$\hat{\xi}(\omega) = H(\Omega) \frac{1}{\rho a \omega_0^2} \hat{p}_i(\omega), \quad (2.72a)$$

$$H(\Omega) = \frac{1}{\Omega^2 - 1 - i\Omega\delta}, \quad \Omega = \frac{\omega}{\omega_0}. \quad (2.72b)$$

The volume change $\hat{V}(\omega)$, associated with the radial motion $\hat{\xi}$ is

$$\hat{V}(\omega) = 4\pi a^2 \hat{\xi}(\omega) = \frac{4\pi a}{\rho \omega_0^2} H(\Omega) \hat{p}_i(\omega). \quad (2.73)$$

This gives the complex bulk modulus modulus of the single bubble as function of its radius a

$$K_b(a, \omega) = -\frac{4}{3}\frac{\pi a^3}{\hat{V}(\omega)}\hat{p}_i(\omega) = -\frac{1}{3}\rho a^2 \omega_0^2 H^{-1}(\Omega). \quad (2.74a)$$

The bulk modulus K_w of water is

$$K_w = \rho c_w^2, \quad (2.74b)$$

where c_w is the speed of sound in water. The compressibility of a bubbly liquid is calculated from (2.71a) as the sum over all bubbles within a volume

$$\frac{1}{K} = \frac{1 - \phi}{\rho_w c_w^2} - \frac{4\pi}{\rho} \sum_k n_k \frac{a_k}{\omega_0^2} H_k(\Omega), \quad (2.75)$$

where n_k is the number of bubbles per unit volume with radius a_k . The volume fraction ϕ_k of bubbles with radius a_k is

$$\phi_k = \frac{4}{3}\pi a_k^3 n_k \quad (2.76)$$

The fraction $\phi = \sum_k \phi_k$ of bubbles in the liquid will always be very small compared to unity. This allows the expressions for K and ρ to be simplified to

$$\phi \ll 1, \quad \rho_g \ll \rho_w \quad \frac{1}{K} \approx \frac{1}{\rho_w c_w^2} - \frac{4\pi}{\rho} \sum_k n_k \frac{a_k}{\omega_0^2} H_k(\Omega) \quad (2.77a)$$

$$\rho = (1 - \phi)\rho_w + \phi\rho_g \approx \rho_w. \quad (2.77b)$$

The complex, frequency dependent speed of sound c_w in the bubbly liquid is found from the expressions for K and ρ above as

$$\frac{1}{c_c^2} = \frac{\rho}{K} = \frac{1}{c_w^2} - 4\pi \int_0^\infty \frac{a}{\omega_0^2} H(\Omega) n(a) da, \quad (2.78)$$

where the sum over the bubbles have been replaced by an integral. $n(a)da$ is the number of bubbles with radius in $(a, a + da)$ per unit volume.

The result above is identical to the expression found by Commander and Prosperetti after a more rigorous mathematical treatment, see Equation (36) in Reference [23].

Equation (2.78) is a closed expression for the complex speed of sound $c_c(\omega)$, assuming linear oscillations and low volume fractions of bubbles. The complex wavenumber k_c is found from c_c , giving the phase velocity and the attenuation in the bubbly liquid.

Phase velocity and attenuation A plane wave propagating in the positive z direction is expressed by its complex wavenumber k_c as

$$\begin{aligned} p(z, t) &= p_0 e^{i(\omega t - k_c z)} = p_0 e^{k_i z} e^{i(\omega t - k_r z)}, \\ k_c(\omega) &= k_r + ik_i. \end{aligned} \quad (2.79)$$

The complex wavenumber k_c and speed of sound $c(\omega)$ are related as

$$\frac{1}{c_c} = \frac{1}{c_w} (u + iv), \quad (2.80a)$$

$$k_c = \frac{\omega}{c_c} = k_w (u + iv), \quad k_w = \omega / c_w, \quad (2.80b)$$

$$p(z, t) = p_0 e^{vk_w z} e^{i(\omega t - uk_w z)}, \quad (2.80c)$$

where the quantities u and v are found from (2.78) as

$$(u + iv)^2 = 1 - 4\pi c_w^2 \int_0^\infty \frac{a}{\omega_0^2} H(\Omega) n(a) da, \quad (2.81a)$$

$$u^2 - v^2 = 1 - 4\pi c_w^2 \int_0^\infty \frac{a}{\omega_0^2} H_R(\Omega) n(a) da, \quad (2.81b)$$

$$2uv = -4\pi c_w^2 \int_0^\infty \frac{a}{\omega_0^2} H_I(\Omega) n(a) da, \quad (2.81c)$$

$$H_R(\Omega) = \text{Re}(H(\Omega)) = \frac{\Omega^2 - 1}{(\Omega^2 - 1)^2 + (\Omega\delta)^2}, \quad (2.81d)$$

$$H_I(\Omega) = \text{Im}(H(\Omega)) = \frac{\Omega\delta}{(\Omega^2 - 1)^2 + (\Omega\delta)^2}. \quad (2.81e)$$

The phase velocity c and the attenuation α in decibels are found from the real and imaginary parts of k_c as

$$c = \frac{\omega}{\text{Re}(k_c)} = \frac{c_w}{u}, \quad (2.82a)$$

$$\alpha = -20(\lg e) \text{Im}(k_c) = -20(\lg e) \frac{\omega v}{c_w} \quad [dB], \quad (2.82b)$$

where the factor $20 \lg e \approx 8.69$ comes from the definition of the decibel-scale.

The velocity and attenuation as function of frequency for suspensions of single-sized bubbles with diameter $3 \mu\text{m}$ are plotted in Figure 2.12. The volume fractions of bubbles were selected to 10^{-6} , 10^{-5} and 10^{-4} . The somewhat more realistic situation of a distribution of bubble sizes is plotted in Figure 2.13. This figure shows a Gaussian distribution of sizes, with mean diameter $3 \mu\text{m}$ and standard deviation $1 \mu\text{m}$.

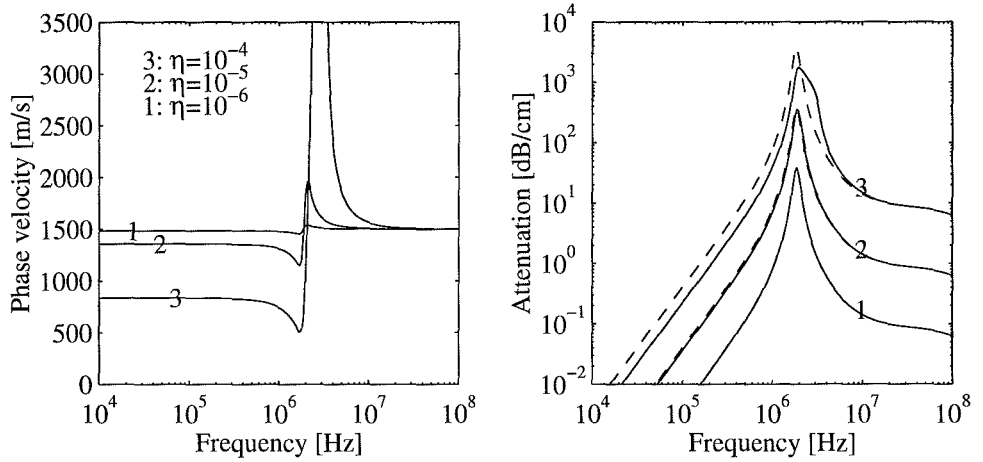


Figure 2.12. Speed of sound and attenuation in a bubbly liquid for single sized bubbles with diameter $3 \mu\text{m}$. Volume fractions of bubbles are 10^{-6} , 10^{-5} and 10^{-4} . Results are calculated from the complex wavenumber model in this section (solid lines) and from the extinction cross section, (2.63) (dashed lines).

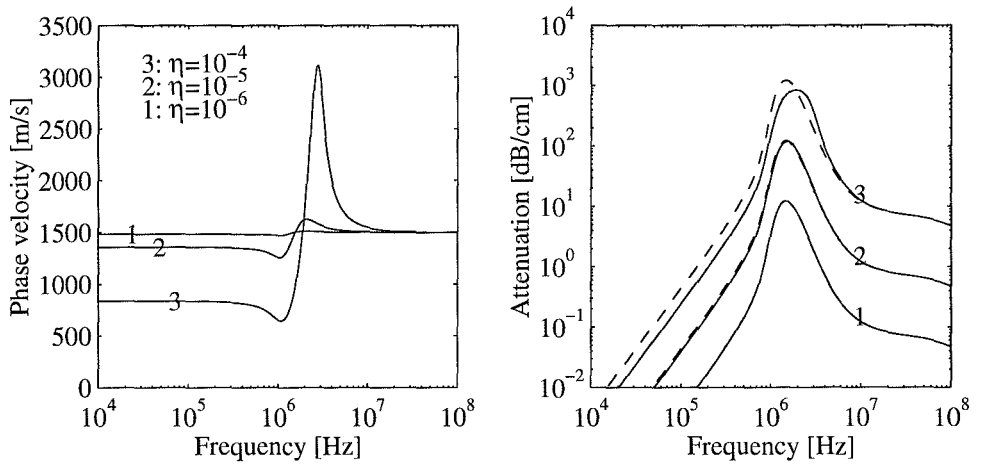


Figure 2.13. Speed of sound and attenuation in a bubbly liquid for a Gaussian size distribution of bubbles. The mean diameter is $3 \mu\text{m}$ and the standard deviation is $1 \mu\text{m}$. Volume fractions of bubbles are 10^{-6} , 10^{-5} and 10^{-4} . Results are calculated from the complex wavenumber model in this section (solid lines) and from the extinction cross section, (2.63) (dashed lines).

For a bubble volume fraction of 10^{-6} , the speed of sound is hardly affected. The attenuation shows a very steep peak at resonance, going up to 30 dB/cm. As the volume fraction of bubble increases, velocity dispersion becomes apparent. However, for these concentrations, the attenuation is extremely large.

Approximation: Low attenuation For almost all situations of practical interest, the attenuation will be low, in the sense that the reduction in amplitude per wavelength is small. This means that the imaginary part k_i of the wavenumber k_c is much smaller than the real part k_r . Under these conditions, (2.81a) can be simplified to give separate analytic expressions for u and v as

$$\begin{aligned} |k_i| \ll |k_r|, \quad |v| \ll |u| \quad u &= \sqrt{1 - 4\pi c_w^2 \int_0^\infty \frac{a}{\omega_0^2} H_R(\Omega) n(a) da}, \\ v &= \frac{-2\pi c_w^2}{u} \int_0^\infty \frac{a}{\omega_0^2} H_I(\Omega) n(a) da. \end{aligned} \quad (2.83)$$

Approximation: Small changes in velocity The quantity u is a measure of the phase velocity in the bubbly mixture relative to the speed of sound in the pure liquid. When the changes in phase velocity due to bubbles are small, the expressions can be simplified further by setting $u \approx 1$ in the calculation of v . This gives

$$\begin{aligned} u = 1 + \epsilon, \quad |\epsilon| \ll 1 \quad u &= 1 - 2\pi c_w^2 \int_0^\infty \frac{a}{\omega_0^2} H_R(\Omega) n(a) da, \\ v &= -2\pi c_w^2 \int_0^\infty \frac{a}{\omega_0^2} H_I(\Omega) n(a) da. \end{aligned} \quad (2.84)$$

This gives the phase velocity c and the attenuation α as

$$c = c_w \left(1 + 2\pi c_w^2 \int_0^\infty \frac{a}{\omega_0^2} \frac{\Omega^2 - 1}{(\Omega^2 - 1)^2 + (\Omega\delta)^2} n(a) da \right), \quad (2.85a)$$

$$\alpha = 20(\lg e) \times 2\pi \int_0^\infty \frac{a c_w}{\omega_0} \frac{\Omega^2 \delta}{(\Omega^2 - 1)^2 + (\Omega\delta)^2} n(a) da. \quad (2.85b)$$

The expression (2.36a) gives the radiation damping constant as $\delta_c = \Omega^2 \omega_0 a / c$. If this is inserted into the expression for α above, it gives the same result as equation (2.63) derived from the extinction cross section (2.57).

Hence, the two methods of calculation give the same result when the attenuation per wavelength is low and the velocity dispersion is small.

Low Frequency Limit

The bubbles have the largest effect on the phase velocity for frequencies around the resonance frequency of the bubbles. For frequencies above resonance, the speed of sound rapidly approaches the sound speed c_w in the pure liquid. Below the resonance frequency, the sound speed of the bubbly mixture can be significantly lower than the speed of sound in the liquid. In this frequency range, the acoustic attenuation can be quite low, even at high bubble concentrations. Hence, it is interesting to study how the speed of sound varies with bubble concentration for frequencies well below resonance.

The compressibility and density are calculated from (2.71a). Well below resonance, the dynamics of the bubble is determined by the stiffness alone. The dynamic compressibility $K_c(\omega)$ used in the previous section can be replaced by the static value for the bulk modulus of a gas under isothermal compression

$$K_b = p_e \quad (2.86)$$

The effective bulk modulus K and density ρ of the bubbly mixture is now

$$\frac{1}{K} = \frac{1 - \phi}{\rho_w c_w^2} + \frac{\phi}{p_e} = \frac{1}{\rho_w c_w^2} \left(1 - \phi + \phi \frac{\rho_w c_w^2}{p_e} \right) \quad (2.87a)$$

$$\rho = (1 - \phi)\rho_w + \phi\rho_g = \rho_w(1 - \phi + \phi \frac{\rho_g}{\rho_w}) \quad (2.87b)$$

Note that in this situation, the size of the bubbles does not influence the compressibility. Only the total volume fraction of gas matters. This is valid

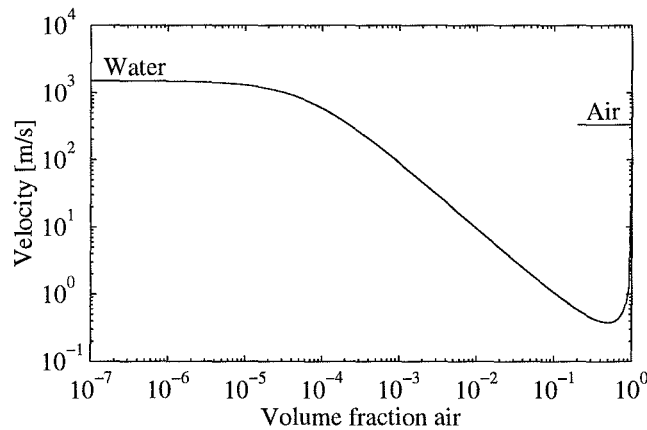


Figure 2.14. Speed of sound at frequencies well below resonance, as function of bubble volume concentration.

when the bubbles are small enough, so that the resonance frequency of the individual bubble is much higher than the frequency used. The speed of sound at low frequencies becomes

$$c = \sqrt{\frac{K}{\rho}} = c_w \left[\left(1 - \phi \left(1 - \frac{\rho_g}{\rho_w} \right) \right) \left(1 - \phi \left(1 - \frac{\rho_w c_w^2}{\kappa p_e} \right) \right) \right]^{-1/2}. \quad (2.88)$$

The result here differs slightly from the simpler expression given by Leighton [91], as the latter does not consider the change in density associated with the bubbles. However, for all realistic bubble concentration the expressions yield identical results. Differences appear at high bubble concentrations, where the attenuation is very large, and the bubbly liquid is better described as a foam.

A plot of the low frequency limit for the speed of sound is shown in Figure 2.14. Small volume fractions of bubbles can reduce the speed of sound considerably. The speed of sound in the mixture can even be lower than the speed of sound in air. This somewhat surprising result appears because the bubbles reduce the bulk modulus K of the mixture much more than they reduce the density ρ . Hence, a bubbly liquid may end up as a medium that is very compressible due to the bubbles. But the density of the bubbly liquid is still rather high, due to the density of the liquid.

2.4 Gas Bubble in a Shell

Most ultrasound contrast agents consist of gas bubbles encapsulated in a shell. The gas gives the bubbles a high compressibility, ensuring that they are powerful acoustic scatterers. The shell stabilizes the microbubbles, preventing the gas from dissolving into the liquid.

The shell will reduce the compressibility of the bubble. This alters its acoustic properties, by increasing its resonance frequency and adding extra viscous damping to the oscillation.

Shell Stiffness

The difference in radial stress across an elastic shell was found in Chapter 3.4 to be

$$T_2 - T_1 = 12G_S \frac{dS_e}{a_e} \left(\frac{a_e}{a} \right)^4 \left(\frac{a}{a_e} - 1 \right), \quad (2.89)$$

where T_2 and T_1 are the radial components of the stress tensor at the outer and inner shell surfaces. This is linearized by setting

$$a(t) = a_e + \xi(t), \quad |\xi| \ll 1. \quad (2.90)$$

The stress difference across the shell is expanded to the first order in $\xi(t)$, yielding

$$T_2 - T_1 = 12G_S \frac{d_{Se}}{a_e^2} \xi. \quad (2.91)$$

The boundary conditions at the inner and outer shell surfaces are

$$T_2 = T_L(a) \quad T_1 = -p_g \quad (2.92)$$

where $T_L(a)$ is the radial stress in the liquid and p_g is the pressure in the gas.

The pressure from the gas is taken from (2.11). This is combined with (2.91), giving the radial stress at the outer shell surface

$$T_L = (T_2 - T_1) - p_g = \left(\frac{3\kappa p_e}{a} + 12G_S \frac{d_{Se}}{a^2} \right) \xi, \quad (2.93)$$

where the equilibrium bubble radius a_e is replaced by a , consistent with the linear approximation. The force F_S acting on the liquid from the shell encapsulated bubble is now

$$F_S = - \iint_S T_L dS = -4\pi a^2 T_L = -(12\pi a \kappa p_e + 48\pi G_S d_{Se}) \xi. \quad (2.94)$$

The spring constant for the shelled bubble is identified from the definition $F_S = -s\xi$ to

$$s = 12\pi a \kappa p_e + 48\pi G_S d_{Se}. \quad (2.95)$$

The shell is assumed to be thin: The shell thickness is small compared to the bubble radius, $d_{Se} \ll a$. The inertia of the shell is neglected compared to the inertia of the liquid being displaced as the bubble oscillates. This means that the dynamic mass of the shell encapsulated bubble is set equal to the dynamic mass of the free bubble. This was calculated in (2.21) to

$$m = 4\pi a^3 \rho, \quad (2.96)$$

where ρ is the density of the liquid.

Damping

For the free bubble, the damping of the oscillations was caused by three mechanisms: Radiation, liquid viscosity and thermal conduction in the gas. When a shell is added, viscous forces in the shell may introduce a new damping mechanism.

Radiation resistance The radiation resistance depends only on the liquid and on the motion of the bubble surface. Hence, the expression for radiation damping does not change with the introduction of a shell. The radiation resistance R_c is, from (2.23),

$$R_c = 4\pi a^2 \rho c (ka)^2. \quad (2.97)$$

Liquid viscosity The mechanical resistance from viscous forces in the liquid depends only on the bubble diameter and on the viscosity of the surrounding fluid. This does not change with the introduction of a shell, and the viscous resistance is, from (2.26),

$$R_{\eta L} = 16\pi a \eta. \quad (2.98)$$

Thermal conduction in the gas The thermal damping depends on the motion of the bubble surface and on properties of the gas. The model for the thermal damping was taken from Devin [34] and Eller [37]. They studied temperature variations in the gas, modeling the liquid as a heat reservoir of constant temperature. Using this model for a shelled bubble means assuming the shell to have the same constant temperature as the surrounding liquid. Heat generation in the shell during the oscillations is neglected. This seems as a reasonable assumption, as the heat capacity of the shell material is of the same order of magnitude as the heat capacity of water, which is three orders of magnitude greater than the heat capacity of air [129]. Hence, it is assumed that the results by Devin and Eller for the free bubble can also be applied when a shell is present.

Under these assumptions, the polytropic exponent κ and the mechanical resistance from thermal conduction R_{Th} for the shelled bubble are, from (2.29a) and (2.29b),

$$\kappa = Re \left(\frac{1}{\Phi} \right), \quad R_{Th} = \frac{12\pi a p_e}{\omega} Im \left(\frac{1}{\Phi} \right), \quad (2.99)$$

where Φ is a function of the thermal properties of the gas, defined in (2.28a).

Shell viscosity The stress difference across the shell due to shell viscosity was derived in Chapter 3.4 to

$$T_2 - T_1 = 12\eta_S \frac{dS_e}{a_e} \left(\frac{a_e}{a} \right)^4 \frac{\dot{a}}{a_e}. \quad (2.100)$$

This is linearized for small radial displacements $\xi = a - a_e$, giving

$$T_2 - T_1 = 12\eta_S \frac{dS_e}{a^2} \dot{\xi}. \quad (2.101)$$

The viscous force $F_{\eta S}$ from the shell viscosity is

$$F_{\eta S} = - \iint_S (T_2 - T_1) dS = -4\pi a^2 (T_2 - T_1) = -48\pi\eta_S dS_e \dot{\xi}. \quad (2.102)$$

The mechanical resistance $R_{\eta S}$ from shell viscosity is identified from the definition $F_R = -R\dot{\xi}$ as

$$R_{\eta S} = 48\pi\eta dS_e. \quad (2.103)$$

Damping Constants

The dimensionless damping constants are calculated from the mechanical resistance by the definition $\delta = R/(\omega_0 m)$. This gives

$$\delta_c = \frac{\omega^2 a}{\omega_0 c}, \quad (2.104a)$$

$$\delta_\eta = \frac{4\eta L}{\omega_0 \rho a^2}, \quad (2.104b)$$

$$\delta_{Th} = \frac{3p_e}{\omega \omega_0 \rho a^2} \text{Im} \left(\frac{1}{\Phi} \right), \quad (2.104c)$$

$$\delta_S = \frac{12\eta_S dS_e}{\omega_0 \rho a^3}. \quad (2.104d)$$

The expressions for the three first damping constants δ_c , δ_η , and δ_{Th} are equal to the expressions for the free bubble. But the the resonance frequency ω_0 is changed by the shell, and this will change the values of the damping constants.

Resonance Frequency

The angular resonance frequency of the shelled bubbles is calculated from the bubble stiffness s and dynamic mass m , using (2.95) and (2.96), to

$$\omega_0^2 = \frac{1}{\rho a^2} \left(3\kappa p_e + 12G_S \frac{dS_e}{a} \right). \quad (2.105)$$

The linear resonance frequency is

$$f_0 = \frac{\omega_0}{2\pi} = \frac{1}{2\pi a} \sqrt{\frac{3\kappa p_e + 12G_S dS_e/a}{\rho}}. \quad (2.106)$$

Scattering and Extinction Cross Section

An equation of motion for the encapsulated bubble is set up based on the expressions for the spring constant, mechanical resistance, damping constants, and resonance frequency. This equation of motion is equal to the equation of motion for the free bubble, (2.31) and (2.32). But the parameters ω_0 and δ have different values.

The equation of motion in the time domain is

$$m\ddot{\xi} + R\dot{\xi} + s\xi = -4\pi a^2 p_i, \quad (2.107)$$

where the parameters R and s are for the encapsulated bubble. In the frequency domain, this equation of motion is transformed to

$$(-\omega^2 + i\omega\omega_0\delta + \omega_0^2)\hat{\xi} = -\frac{1}{\rho a}\hat{p}_i, \quad (2.108)$$

where the expressions for the resonance frequency ω_0 and the damping constant δ are for the shell encapsulated bubble.

Various expressions for the interaction between the bubble and the ultrasound field were derived for the free bubble, based on the equation of motion. These include expressions for radial oscillation amplitude, scattered pressure field, scattering and extinction cross sections and scatterer efficiency. Since the equations of motion for the encapsulated and free bubbles take the same form, these expressions are equal for the shelled and unshelled bubbles. The differences between the two bubble types is handled by the different values of the parameters, ω_0 and δ , and of the normalized frequency $\Omega = \omega/\omega_0$.

The expressions for the shelled bubble are

Normalized frequency

$$\Omega = \frac{\omega}{\omega_0} \quad (2.109a)$$

Radial displacement $\hat{\xi}$ as function of applied pressure field p_i

$$\hat{\xi}(\omega) = \frac{1}{\rho a \omega_0^2} \frac{\hat{p}_i(\omega)}{\Omega^2 - 1 - i\Omega\delta} \quad (2.109b)$$

Transfer function for radial strain

$$H(\Omega) = \frac{1}{\Omega^2 - 1 - i\Omega\delta} \quad (2.109c)$$

Radiated pressure

$$\hat{p}_s(a, \omega) = \frac{\Omega^2}{1 - \Omega^2 + i\Omega\delta} \hat{p}_i(\omega) \quad (2.109d)$$

Scattering cross section

$$\sigma_s = 4\pi a^2 \frac{\Omega^4}{(1 - \Omega^2)^2 + (\Omega\delta)^2} \quad (2.109e)$$

Extinction cross section

$$\sigma_e = \sigma_s \frac{\delta}{\delta_c} = 4\pi a^2 \frac{\Omega^4}{(1 - \Omega^2)^2 + (\Omega\delta)^2} \frac{\delta}{\delta_c} \quad (2.109f)$$

The efficiency of the bubble as a sound scatterer

$$\eta = \frac{\delta_c}{\delta_\eta + \delta_{Th} + \delta_c + \delta_S} \quad (2.109g)$$

The attenuation coefficient α , in dB per unit length

$$\alpha = 10(\lg e) \int_0^\infty \sigma_e(a) n(a) da \quad [dB] \quad (2.109h)$$

Complex, frequency dependent speed of sound

$$\frac{1}{c_c^2} = \frac{1}{c_w^2} - 4\pi \int_0^\infty \frac{a}{\omega_0^2} H(\Omega) n(a) da \quad (2.109i)$$

$$\frac{1}{c_c} = \frac{1}{c_w} (u + iv) \quad (2.109j)$$

$$(u + iv)^2 = 1 - 4\pi c_w^2 \int_0^\infty \frac{a}{\omega_0^2} H(\Omega) n(a) da \quad (2.109k)$$

$$H_R(\Omega) = \text{Re}(H(\Omega)) = \frac{\Omega^2 - 1}{(\Omega^2 - 1)^2 + (\Omega\delta)^2}, \quad (2.109l)$$

$$H_I(\Omega) = \text{Im}(H(\Omega)) = \frac{\Omega\delta}{(\Omega^2 - 1)^2 + (\Omega\delta)^2}. \quad (2.109m)$$

Phase velocity and attenuation

$$c = \frac{c_w}{u} \quad (2.109n)$$

$$\alpha = -20(\lg e) \frac{\omega v}{c_w} \quad [dB] \quad (2.109o)$$

Low attenuation, $|v| \ll |u|$

$$u = \sqrt{1 - 4\pi c_w^2 \int_0^\infty \frac{a}{\omega_0^2} H_R(\Omega) n(a) da} \quad (2.109p)$$

$$v = -\frac{1}{u} 2\pi c_w^2 \int_0^\infty \frac{a}{\omega_0^2} H_I(\Omega) n(a) da \quad (2.109q)$$

Low dispersion, $u = 1 + \epsilon$, with $|\epsilon| \ll 1$

$$u = 1 - 2\pi c_w^2 \int_0^\infty \frac{a}{\omega_0^2} H_R(\Omega) n(a) da \quad (2.109r)$$

$$v = -2\pi c_w^2 \int_0^\infty \frac{a}{\omega_0^2} H_I(\Omega) n(a) da \quad (2.109s)$$

Chapter 3

Nonlinear Bubble Theory

The previous chapter modeled the bubbles as linear oscillators. This enabled the theoretical descriptions to be made in the frequency domain. The concepts resonance frequency, damping constant and scattering and absorption cross section were defined. These concepts are useful in linear theory, where time-domain response can be calculated from a transfer function or an impulse response of the system.

In many practical situations, the bubble response is nonlinear, and the description in Chapter 2 is insufficient. For a nonlinear response, the use of impulse response and Fourier synthesis loses its value. The time domain responses are no longer the sum of responses to the individual Fourier components.

A classic paper modeling nonlinear bubble responses is due to Lauterborn from 1976 [88]. He modeled the bubbles with the Rayleigh-Plesset equation, driving the bubbles with a CW ultrasonic field. Lauterborn's simulations show a strongly nonlinear response, giving harmonics, sub- and ultraharmonics of the driving ultrasound frequency.

3.1 Nonlinear Acoustics in Diagnostic Ultrasound

Acoustic propagation is basically nonlinear [52, 119]. This nonlinearity is caused partly by the particle movement associated with the acoustic wave, and partly by a nonlinear compressibility of the medium. For sound propagation in water, these two mechanisms are of comparable magnitude [9].

In most applications of acoustics, the nonlinear effects are small and can be neglected. A linear treatment is sufficient, and this is what is found in standard textbooks on acoustics [74, 120]. However, the interest in nonlinear propagation for diagnostic ultrasound imaging has increased dramatically since

about 1996, because of so-called *Native harmonic imaging*, where ultrasound images are formed based on the second harmonic of the transmit frequency [5]. A theoretical description [20] and experimental measurements [21] of nonlinear sound propagation in pulse-echo imaging systems was given by Christopher in 1997 and 1998, including phase aberrations.

3.1.1 Nonlinearity in Liquids with and without Bubbles

In most fluids, including water, the local nonlinearity is very small, but nonlinear effects add up as the wave propagates. This allows nonlinear sound propagation to be treated as perturbations to the linear case. Classic models for nonlinear propagation, the Westervelt, Burgers and the KZK (Khokhlov-Zabolotskaya-Kuznetsov) equations, include local nonlinearity to the second order [52], and effects are added up as the wave propagates.

In contrast to the weak *local* nonlinearity in liquids, a bubble may create a large local nonlinearity, making a perturbation approach difficult. A measure of local nonlinearity in a fluid is the relative volume compression. For small compression, this is equal to the acoustic Mach-number $M = u/c$, and is given by the ratio between the acoustic pressure and the bulk modulus of the fluid. This can be expressed as [83]

$$-\frac{\Delta V}{V} = \frac{u}{c} = \frac{p_a}{K}, \quad (3.1)$$

where $-\Delta V/V$ is the relative volume compression, u is the particle velocity, c is the speed of sound in the fluid, p_a is the acoustic pressure and $K = \rho c^2$ is the bulk modulus of the fluid.

The condition for local linearity is that the relative volume compression is small, which is equivalent to saying that the acoustic Mach-number is small

$$\left| \frac{\Delta V}{V} \right| = \left| \frac{u}{c} \right| \ll 1 \quad \text{Requirement for local linearity} \quad (3.2)$$

The values of the bulk modulus of water K_w and of air K_{air} differ by four orders of magnitude

$$\begin{array}{ll} \text{Water} & K_w = \rho c^2 = 2200 \text{MPa} \\ \text{Air (adiabatic)} & K_{air} = \gamma p_0 = 0.14 \text{MPa} \end{array} \quad (3.3)$$

The acoustic pressure amplitude in diagnostic ultrasound equipment can at maximum reach a few MPa [169]. For sound propagation in water p_a/K_w is always small, giving low local nonlinearity. The nonlinear effects accumulate as the wave propagates, but the propagation is adequately described by including

local nonlinearity terms to the second order in p_a/K . For the bubble, the situation is different. The local nonlinearity term p_a/K_{gas} need not be small, it may very well exceed unity, and an expansion in the parameter p_a/K_{gas} is not meaningful. This simplified picture is complicated by the inertia of the moving liquid, which will influence the bubble oscillation, especially for frequencies above resonance. In addition, a shell around the bubble may increase its bulk modulus.

These arguments illustrate why an expansion in acoustic Mach-number $M = u/c = p_a/K$ to the second order, which is sufficient for sound propagation in liquids, is of limited value when studying bubbles exposed to diagnostic ultrasound. Instead, the bubble's response is calculated from time domain simulations of a nonlinear differential equation.

Second order, and also higher order, perturbation solutions for the oscillation of bubbles have been published. Typically, specific nonlinear components are studied using Taylor-expansion of the governing nonlinear equations of motion. This was done for the response at the second harmonic frequency for free bubbles by Miller [111] and for shell encapsulated bubbles by de Jong et al. [26], by Church [22] and by Miller [112]. These studies describe second-order frequency domain calculations, giving the response to a CW acoustic driving field. Such calculations are of limited value for diagnostic ultrasound pulses, which are normally very short and broadband. A second-order model for the response of these broadband pulses must include the response to all sum- and difference frequencies of the driving ultrasound pulses, analogous to what is done in the *Bergen-code* solution of the KZK-equation. The response of the bubble becomes strongly nonlinear even for moderate driving pressure amplitudes, and a second order solution gets inaccurate. However, one important reason for finding these approximate analytical solutions, is the insight these solutions give in the underlying physics. The analytical results provided by Miller for the second harmonic response [112] and by Prosperetti for the subharmonic response [138, 139] give valuable insight into mechanisms for the phenomena, such as frequency dependence and amplitude thresholds.

In the following, the second order solutions are not considered, only time domain solutions are used. With today's fast computers and efficient numerical software, these time domain simulations are rapidly and easily obtained.

3.1.2 Linear and Nonlinear Systems

For a linear system, the response to two input signals is the sum of the responses to the individual inputs. More general, if the system response $y(t)$ to

an input $x(t)$ is described by the operator linear L as

$$y(t) = L\{x(t)\} \quad L: \text{Linear operator}, \quad (3.4)$$

then, the response to a linear combination of input signals $\alpha_1 x_1(t) + \alpha_2 x_2(t)$ is

$$\begin{aligned} x(t) &= \alpha_1 x_1(t) + \alpha_2 x_2(t) \\ y(t) &= L\{\alpha_1 x_1 + \alpha_2 x_2\} = \alpha_1 L\{x_1\} + \alpha_2 L\{x_2\} \\ &= \alpha_1 y_1(t) + \alpha_2 y_2(t). \end{aligned} \quad (3.5)$$

The response $y(t)$ of the linear system is completely described by its impulse response $h(t)$, or in frequency domain, by its frequency response $H(\omega)$. The response can be expressed as

$$\begin{aligned} y(t) &= h(t) * x(t) = \int_{-\infty}^{\infty} x(\tau)h(t - \tau)d\tau, \\ \hat{y}(\omega) &= H(\omega)\hat{x}(\omega), \end{aligned} \quad (3.6)$$

where the symbol $*$ denotes temporal convolution and $\hat{x}(\omega)$ is the Fourier transform of $x(t)$.

Some characteristics of a linear system are

1. The system is completely described by its frequency response $H(\omega)$. The input signal $x(t)$ can be decomposed into its frequency components, and the system response is the sum of the responses for the individual frequency components.
2. The response $\hat{y}(\omega)$ contains only frequency components that are already present in the input signal $\hat{x}(\omega)$. The response at one frequency is independent of the input on other frequencies.

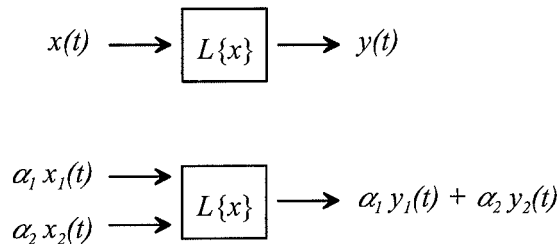


Figure 3.1. The response of a linear system $L\{x\}$ to an input signal $x(t)$ and to a linear combination of input signals $\alpha_1 x_1(t) + \alpha_2 x_2(t)$.

3. A scaling of the input signal causes a scaling of the response,

$$x_2(t) = \alpha x_1(t) \Rightarrow y_2(t) = \alpha y_1(t). \quad (3.7)$$

A special case is the response to input signals with inverted polarity, $\alpha = -1$. This causes responses that are inverted copies of one another.

For a nonlinear systems, the relations in (3.5) and (3.6) are not valid. The list of characteristics above is changed to

1. The nonlinear system response is *not* described by an impulse or frequency response. The system response *cannot* be calculated from Fourier synthesis.
2. The response contains new frequency components, not present in the input signal. The response at one frequency depends not only on the input on this frequency, but also on the input on other frequencies.
3. The response to a scaled version of the input is *not* a scaling of the response. The responses to pulses with inverted polarity are *not* inverted versions of one another.

3.1.3 Bubble Detection Based on Nonlinear Acoustics

The nonlinear response introduces qualitatively new effects, effects that are not known from linear acoustics. These effects can be used to enhance echoes from bubbles over echoes from tissue, because the bubbles typically respond more nonlinearly than tissue. In ultrasound contrast imaging, several different nonlinear effects are in use or have been proposed to enhance the contrast agent signal compared to the tissue signals.

So called “shadowing” is a major limitation with linear imaging methods [164]. This occurs because the attenuation from the contrast agent reduces the sound intensity behind the contrast filled region. More sensitive detection techniques allow use of lower contrast agent concentrations, and reduce the attenuation introduced by the contrast agent. What we see today is probably only the start of nonlinear acoustics used in diagnostic ultrasound imaging.

Detection methods based on nonlinear acoustics that are either in use or have been proposed include:

Second harmonic The received signals are filtered at twice the transmit frequency. The image is formed based on the power received at this second harmonic. This technique requires the bandwidth of the transducer to cover both the transmit frequency and its second harmonic frequency.

To achieve this, the transducer is normally driven at a frequency near the lower end of its frequency response.

The use of the 2nd harmonic to detect bubbles in blood was proposed in 1968 by Tucker and Welsby [163]. It was demonstrated experimentally by Miller in 1981 [111] and described theoretically in detail by Vacher and Gimnez in 1984 [166]. Second harmonic echoes from ultrasound contrast agents have been studied by a number of authors [26, 27, 13]. Krishnan and O'Donnel [77] proposed to suppress the second harmonic generated by the tissue propagation. They suggested transmitting a second harmonic signal with a phase that cancels the propagation generated second harmonic. This might increase the specificity of the technique.

Higher harmonics The same principle as in 2nd harmonic imaging may be applied to higher harmonics of the transmit frequency. Images can be formed based on the received power at $3f_i$, $4f_i$, etc. where f_i is the transmit frequency.

The third harmonic, $3f_i$, is of particular interest, as thickness mode transducers have natural resonances at odd harmonics. But the third harmonic is also sensitive to distortion, as saturation in the transmit and receiver stages typically create odd harmonics. 4th and higher harmonics can hardly be detected using the transmit transducer. This would require a new transducer arrangement, probably using separate transducer elements for transmit and receive.

Higher harmonics are presently of low importance. But contrast agents have been shown to emit sound at these frequencies, and the higher harmonics may have a potential to detect contrast agents with high specificity.

Nonlinear frequency mixing Two frequencies are transmitted. The nonlinear response creates frequency components at the sum- and differences of the transmit frequencies. A typical arrangement will be to transmit one high "imaging" frequency f_i and one lower "pumping" frequency f_p . The image will be formed based on the difference frequency $f_i - f_p$, or on the sum frequency $f_i + f_p$.

Nonlinear frequency mixing has not yet been applied to detection of contrast agents *in vivo*. But the method has been tested experimentally in various other situations. During the last half of the 1980s, Newhouse, Chapelon, Shankar and co-workers demonstrated the use of nonlinear frequency mixing for various types of bubble detection, sizing and pressure measurements [123, 15, 151, 14]. Boyle and Chotiros [11] presented

in 1998 a model for using the difference frequency to detect bubbles trapped in the seabed. Ostrovsky et al. [130] have given theoretical and experimental results for generation of a difference frequency signal using the resonance of the whole bubble layer instead of the of individual bubbles, applied to parametric acoustic arrays. Kripfgans et al. [76] in 1998 reported *in vitro* results measuring the sum- and difference frequency echoes from the contrast agent MRX-115 (ImaRx, Tucson, Arizona, USA). A very interesting technique related to this, although not involving bubbles, was presented recently by Fatemi and Greenleaf [43, 44]. They used nonlinear frequency mixing to detect solid objects, where the nonlinear mixing was created by the radiation force.

Pulse inversion Two pulses are emitted. The second pulse is a copy of the first with inverted polarity. The echoes from the two pulses are summed, and an image is formed from the summed signal.

The technique requires two transmit pulses. Motion during the interval between the pulses will be misinterpreted as nonlinearities. The energy in the summed signal is mainly at twice the transmit frequency. Hence, it is important that the receiver is sensitive at twice the transmit frequency. As for second harmonic imaging, the transmit transducer is normally driven at the lower part of its sensitivity spectrum. Pulse inversion can be viewed as an alternative way of doing second harmonic imaging, reducing the problem of sideband leakage from the transmitter to the receiver.

The use of such pulse-inversion imaging combined with Doppler processing has been demonstrated *in vitro* and *in vivo* by Simpson [156, 155].

Sub- and ultra harmonics Subharmonics are frequency components below the driving frequency. Oscillating bubbles have the potential to create subharmonic peaks at integer fractions of the driving frequency. Most important is the peak at $\frac{1}{2}f_i$, where f_i is the driving frequency. Subharmonic peaks at $\frac{1}{3}f_i$ and *ultraharmonics* at $\frac{3}{2}f_i$ and $\frac{5}{2}f_i$ are also reported. Subharmonics require long pulses to develop, the driving pulse must contain several cycles. This may give degraded axial resolution.

The subharmonic response from *Albunex* was measured by Lotsberg et al. in 1996 [104]. Results from subharmonic imaging implemented on a clinical scanner were reported by Shi et al. in 1999 [153].

Acoustic destruction of bubbles Bubbles can be destroyed by the acoustic pulses used in diagnostic imaging. Two different mechanisms for bubble destruction have been reported.

1. The shell or membrane encapsulating the bubble membrane can be damaged, causing the gas inside the bubble to dissolve. The dissolution times of bubbles were calculated in 1950 by Epstein and Plesset [41]. From their models, the dissolution of a μm -sized bubble will typically takes from a few hundred microseconds to a few seconds, depending on the type of gas inside the bubble.
2. The violent collapse of the bubble can cause it to fragment, and these fragments are then dissolved in the liquid. The fragmentation takes place within one ultrasound cycle. This instability of the bubble has been explained by oscillations set up on the bubble surface. Under some conditions, at large amplitude oscillations, small surface oscillations on the bubble will grow, causing the bubble to become unstable. The phenomenon was studied theoretically in 1961 by Hsieh and Plesset [65] and later extended by Eller and Crum in 1970 [38]. These studies provide criteria for regions of stability and instability of bubbles exposed to ultrasound pulses.

Both these destruction mechanisms have been observed experimentally on microbubbles exposed to ultrasonic pulses [25]. An overview of various modes of bubble oscillation and destruction mechanisms was written by Leighton [95].

Combination of techniques The specificity of bubble detection can be increased further by combining two or more of the techniques above. An example of such a combination is given by Leighton et al. [97], who studied the detection of bubbles in seawater. The bubbles were insonified by one imaging and one pumping frequency. The most specific bubble detection was found by receiving at the sum or difference between the imaging frequency and the order $\frac{1}{2}$ subharmonic of the pumping frequency.

Coded excitation may also provide new opportunities combined with a nonlinear detection technique. Coded excitation improves signal to noise ratio by increasing the pulse length, while preserving the axial resolution. Theoretical simulations of coded excitation combined with 2nd harmonic imaging was described by Li in 1999 [99].

3.2 Equations of Motion for the Liquid

Equations of motion for the liquid are derived from the conservation equations for mass and momentum and from the equations of state for the liquid. These equations give relations between changes in pressure, density and enthalpy in

the liquid. The basic equations are combined, making some approximations, to obtain an equation of motion for the liquid surrounding the bubble. The basic idea of the following derivations is to reduce the partial differential equations describing the motion of the liquid to an ordinary differential equation for the bubble radius as function of time.

Contrast agent bubbles have diameters much smaller than the wavelength of the ultrasound field. Hence, only such small bubbles are considered, with

$$ka \ll 1, \quad (3.8)$$

where k is the acoustic wavenumber and a is the bubble radius.

The sound radiated from bubbles oscillating at higher shape modes, for low values of ka , was studied by Strasberg in 1956 [160]. He found that the sound radiated from the bubble is dominated by the zeroth order oscillation mode, that is, the spherically symmetric volume pulsation. The contribution to the radiated field from the higher order shape modes is negligible compared to the contribution from the zeroth mode.

Bubbles with size comparable to the wavelength of the sound was studied by Nishi in 1975 [124], decomposing the incident and scattered waves in spherical Bessel and Hankel functions. Later, Ye [170] used this approach to investigate theoretically the contribution from higher order modes to the scattering of sound from *Albunex*. Ye's results (e.g. Figure 5 in Reference [170]) show that for low values of ka , the scattering is dominated by the spherically symmetric, zeroth order oscillation mode, in accordance with the earlier results of Strasberg. A summary of nonspherical bubble oscillations has been given by Prosperetti [142].

The treatment in this chapter is limited to bubbles surrounded by a liquid of infinite extent. Wall effects are not included. Bubbles in a tube were studied by Chen and Prosperetti [16]. Their approach might be useful when studying contrast agent bubbles in capillaries with diameter close to that of the bubble. Such studies are not included in this thesis.

Equations of State

The equations of state establish a link between changes in pressure p , density ρ and enthalpy h per unit mass of the liquid. The equations are formulated as partial derivatives under constant entropy, following the common assumption in acoustics that the processes are adiabatic. This adiabatic approximation is used consistently for the acoustic wave in the *liquid* surrounding the bubble. For the dynamics of the *gas* inside the bubble, the adiabatic model is not adequate. A model for the dynamics of the gas was given in Chapter 2, for linear

oscillations. In most situations involving μm -sized bubbles and MHz-frequency ultrasound, the gas behaves closer to isothermally than adiabatically.

The first part of this derivation follows a review by Prosperetti from 1984 [141]. For the liquid, the two basic equations of state for sound speed c and enthalpy h are [82, 83]

$$\left(\frac{\partial\rho}{\partial p}\right)_S = \frac{1}{c^2}, \quad \left(\frac{\partial h}{\partial p}\right)_S = \frac{1}{\rho}. \quad (3.9)$$

The index S means that the partial derivatives are to be evaluated at constant entropy. p is the pressure in the liquid and ρ is the density.

The two basic conservation equations for the liquid are the continuity equation, giving conservation of mass, and the Navier-Stokes equation, giving conservation of momentum.

The continuity equation for the liquid is [82]

$$\frac{\partial\rho}{\partial t} + \mathbf{u}\nabla\rho + \rho\nabla\mathbf{u} = 0, \quad (3.10)$$

where \mathbf{u} is the velocity vector and t is time.

Conservation of momentum is given by the Navier-Stokes equation for the liquid. The flow is purely radial and irrotational, $\nabla \times \mathbf{u} = 0$. Bulk viscosity is ignored. Under these conditions, the Navier-Stokes equation is [84]

$$\rho\left(\frac{\partial\mathbf{u}}{\partial t} + (\mathbf{u}\nabla)\mathbf{u}\right) = -\nabla p + \frac{4}{3}\eta\nabla^2\mathbf{u}, \quad (3.11)$$

where η is the viscosity of the liquid. The volume dilation $\nabla\mathbf{u}$ can be reformulated by using the continuity equation (3.10) and the equations of state (3.9) to

$$\nabla\mathbf{u} = -\frac{1}{\rho}\frac{d\rho}{dt} = -\frac{1}{\rho c^2}\frac{dp}{dt}. \quad (3.12)$$

For irrotational flow, $\nabla \times \mathbf{u} = 0$ and $\nabla^2\mathbf{u} = \nabla(\nabla\mathbf{u})$, giving

$$\nabla^2\mathbf{u} = -\nabla\left(\frac{1}{\rho c^2}\frac{dp}{dt}\right) \approx -\frac{1}{\rho c^2}\frac{d\nabla p}{dt}. \quad (3.13)$$

This reformulates the Navier-Stokes equation to

$$\rho\frac{d\mathbf{u}}{dt} + \nabla p = -\frac{4}{3}\frac{\eta}{\rho c^2}\frac{d\nabla p}{dt}. \quad (3.14)$$

Here $\frac{d}{dt}$ denotes the total, or material, derivative, defined as

$$\frac{d}{dt} = \frac{\partial}{\partial t} + (\mathbf{u}\nabla). \quad (3.15)$$

For liquids of interest, $\omega\eta \ll \rho c^2$, where ω is the highest frequency involved. The viscosity term on the right side is small to the second order in $1/c$, compared to the ∇p term on the left side. This implies that the contribution from viscosity can be neglected in the bulk of the liquid, and the Navier-Stokes equation (3.11) is replaced by the Euler equation [82]

$$\rho \left(\frac{\partial \mathbf{u}}{\partial t} + (\mathbf{u}\nabla)\mathbf{u} \right) + \nabla p = 0 \quad (3.16)$$

Although the viscosity term was shown to be negligible in the bulk of the liquid, viscosity gives a contribution at the surface of the bubble. Viscosity will be included into the boundary conditions at the bubble surface.

Spherical Symmetry and Velocity Potential

The liquid motion is spherically symmetric. The flow is purely radial and irrotational, and the velocity field $\mathbf{u}(\mathbf{r}, t)$ can be derived from a potential $\Phi(\mathbf{r}, t)$ [82], defined by

$$\mathbf{u} = \nabla\Phi. \quad (3.17)$$

Under spherical symmetry, where $\mathbf{u} = u\mathbf{e}_r$, the equations (3.10), (3.16) and (3.17) take the form

$$\frac{1}{\rho} \left(\frac{\partial \rho}{\partial t} + u \frac{\partial \rho}{\partial r} \right) + \frac{1}{r^2} \frac{\partial}{\partial r} (ur^2) = 0, \quad (3.18a)$$

$$\frac{\partial u}{\partial t} + u \frac{\partial u}{\partial r} + \frac{1}{\rho} \frac{\partial p}{\partial r} = 0, \quad (3.18b)$$

$$u = \frac{\partial \Phi}{\partial r}. \quad (3.18c)$$

Conservation of mass, (3.18a), is reformulated to an equation in velocity potential and enthalpy. Inserting (3.18c) and (3.9) into (3.18a) gives

$$\nabla^2 \Phi + \frac{1}{c^2} \left(\frac{\partial h}{\partial t} + \nabla\Phi \frac{\partial h}{\partial r} \right) = 0. \quad (3.19)$$

The Euler equation (3.18b), is integrated from an arbitrary position r in the liquid to infinity

$$\int_r^\infty \left(\frac{\partial u}{\partial t} + u \frac{\partial u}{\partial r} \right) dr = -\frac{\partial \Phi}{\partial t} - \frac{1}{2}(\nabla \Phi)^2, \quad (3.20a)$$

$$\int_r^\infty \frac{1}{\rho} \frac{\partial p}{\partial r} dr = \int_r^\infty \frac{1}{\rho} dp = -h(r). \quad (3.20b)$$

These integrals were evaluated utilizing that the velocity potential $\Phi(r, t)$ vanishes at $r = \infty$. The enthalpy $h(r, t)$ is defined relative to its value at $r = \infty$, so that $h(r = \infty) = 0$.

This converts (3.18b) to a Bernoulli-equation for the flow of the liquid [82]

$$\frac{\partial \Phi}{\partial t} + \frac{1}{2}(\nabla \Phi)^2 + h(r) = 0 \quad (3.21)$$

Equation of Motion for the Liquid

The continuity equation (3.18a), alternatively (3.19), and the Bernoulli equation (3.21), together with the equations of state (3.9), form a set of equations of motion for the liquid. The only approximation used so far, is neglecting the viscosity in the bulk of the liquid.

These equations are used to formulate equations of motion for the bubble surface. The set of equations is summed up for completeness as

Equations of state

$$\left(\frac{\partial \rho}{\partial p} \right)_S = \frac{1}{c^2}, \quad \left(\frac{\partial h}{\partial p} \right)_S = \frac{1}{\rho}. \quad (3.22a)$$

Continuity equation

$$\frac{1}{\rho} \left(\frac{\partial \rho}{\partial t} + u \frac{\partial \rho}{\partial r} \right) + \frac{1}{r^2} \frac{\partial}{\partial r} (ur^2) = 0, \quad (3.22b)$$

$$\nabla^2 \Phi + \frac{1}{c^2} \left(\frac{\partial h}{\partial t} + \nabla \Phi \frac{\partial h}{\partial r} \right) = 0. \quad (3.22c)$$

Conservation of momentum, Bernoulli equation

$$\frac{\partial \Phi}{\partial t} + \frac{1}{2}(\nabla \Phi)^2 + h(r) = 0 \quad (3.22d)$$

Small Variations in ρ and c : Taylor Expansion

The enthalpy h , density ρ and speed of sound c are functions of the pressure p . The variations are given by the equations of state, (3.9). The variations in c and ρ are small compared to their equilibrium values at infinity, c_∞ and ρ_∞ . The enthalpy $h(p)$ and speed of sound $c(p)$ is expressed as a Taylor expansion around the equilibrium, $p = p_\infty$.

Following a formulation by Prosperetti [141], the enthalpy is expressed as

$$\begin{aligned} h(r) &= \int_{p_\infty}^{p(r)} \frac{1}{\rho(p)} dp \\ &= \int_{p_\infty}^{p(r)} \left(\frac{1}{\rho_\infty} + (q - q_\infty) \left(-\frac{1}{\rho_\infty^2} \right) \frac{\partial \rho}{\partial q} \Big|_{r=\infty} + \dots \right) dq \\ &= \frac{p - p_\infty}{\rho_\infty} - \frac{(p - p_\infty)^2}{2\rho_\infty^2 c_\infty^2} + O(c_\infty^{-4}). \end{aligned} \quad (3.23a)$$

Likewise, the speed of sound $c(p)$ is expanded around its equilibrium value c_∞

$$\begin{aligned} \frac{1}{c^2} &= \frac{1}{c_\infty^2} + (p - p_\infty) \frac{\partial(c^{-2})}{\partial p} \Big|_{r=\infty} + \dots \\ &= \frac{1}{c_\infty^2} - \frac{p - p_\infty}{c_\infty^4} \frac{\partial c^2}{\partial p} \Big|_{r=\infty} + \dots \\ &= \frac{1}{c_\infty^2} + O(c_\infty^{-4}). \end{aligned} \quad (3.23b)$$

This results in expressions for enthalpy h and speed of sound c correct to the second order in $1/c$

$$h = \frac{p - p_\infty}{\rho_\infty} - \frac{(p - p_\infty)^2}{2\rho_\infty^2 c_\infty^2} + O(c_\infty^{-4}), \quad (3.24a)$$

$$\frac{1}{c^2} = \frac{1}{c_\infty^2} + O(c_\infty^{-4}), \quad (3.24b)$$

$$\frac{1}{c^2} \frac{\partial h}{\partial t} = \frac{1}{c_\infty^2 \rho_\infty} \frac{\partial p}{\partial t} + O(c_\infty^{-4}). \quad (3.24c)$$

Equations of Motion for the Liquid

The expressions for enthalpy, (3.24a), and speed of sound, (3.24b), are inserted into the continuity equation (3.22c) and the Bernoulli-equation (3.22d). This results in equations correct to the second order in $1/c$

Continuity equation

$$\nabla^2 \Phi + \frac{1}{c_\infty^2 \rho_\infty} \left(\frac{\partial p}{\partial t} + \frac{\partial \Phi}{\partial r} \frac{\partial p}{\partial r} \right) = 0, \quad (3.25a)$$

Bernoulli-equation

$$\frac{\partial \Phi}{\partial t} + \frac{1}{2} (\nabla \Phi)^2 + \frac{p - p_\infty}{\rho_\infty} \left(1 - \frac{p - p_\infty}{2 \rho_\infty c_\infty^2} \right) = 0. \quad (3.25b)$$

Linear Wave Equation

If the pressure and velocity amplitudes are small, only the lowest order terms from the equations above need to be considered. This means that the liquid is treated as compressible and linear, and the equations of motion are approximated as

$$\nabla^2 \Phi + \frac{1}{c_\infty^2 \rho_\infty} \frac{\partial p}{\partial t} = 0, \quad (3.26a)$$

$$\frac{\partial \Phi}{\partial t} + \frac{p - p_\infty}{\rho_\infty} = 0. \quad (3.26b)$$

These equations can be combined to yield the linear wave equation in the velocity potential $\Phi(r, t)$

$$\nabla^2 \Phi - \frac{1}{c_\infty^2} \frac{\partial^2 \Phi}{\partial t^2} = 0. \quad (3.26c)$$

3.2.1 Incompressible Liquid: The Rayleigh-Plesset Equation

The first studies of bubble oscillations are due to Lord Rayleigh [143]. The resulting nonlinear differential equation for the bubble surface is commonly called the Rayleigh-Plesset equation. This is the simplest, most basic nonlinear equation of motion for a gas bubble in a liquid.

Treating the liquid as incompressible is equivalent to keeping terms to the zeroth order in the acoustic Mach-number $M = \dot{a}/c$ for the bubble surface. This requires the bubble wall velocity $\dot{a}(t)$ to be small compared to the speed of sound c in the liquid. For moderate oscillation amplitudes, this assumption is fulfilled.

The Rayleigh-Plesset model does not include energy loss caused by the radiation of sound. There is no propagation of sound energy in an incompressible liquid. This may seem as a rather strong limitation. However, according to the results of the linear theory in Chapter 2, acoustic radiation is not the main

source of energy loss from the bubble. Damping from viscosity in the liquid is included, and this is normally larger than the radiation damping. Radiation damping is small for small bubbles at low frequencies. Acoustic radiation starts to become an important source of damping for $ka \gtrsim 0.1$. For frequency 5 MHz, this means that acoustic radiation damping becomes important for bubble diameters above about $10 \mu\text{m}$.

Basic Equations

The equation of state (3.9) for an incompressible liquid is

$$\rho = \text{constant}, \quad \left(\frac{\partial \rho}{\partial p} \right)_S = 0. \quad (3.27)$$

When the density ρ is constant, the other basic equations are simplified to

Continuity equation, (3.22b) or (3.22c)

$$\frac{\partial}{\partial r}(ur^2) = 0 \quad \text{or} \quad \frac{\partial^2 \Phi}{\partial r^2} + \frac{2}{r} \frac{\partial \Phi}{\partial r} = 0. \quad (3.28a)$$

Enthalpy, from (3.23a) by setting $\rho = \text{constant}$

$$h(r) = \frac{p(r) - p_\infty}{\rho}. \quad (3.28b)$$

Bernoulli-equation, from (3.22d)

$$\frac{\partial \Phi}{\partial t} + \frac{1}{2}(\nabla \Phi)^2 + \frac{p(r) - p_\infty}{\rho} = 0. \quad (3.28c)$$

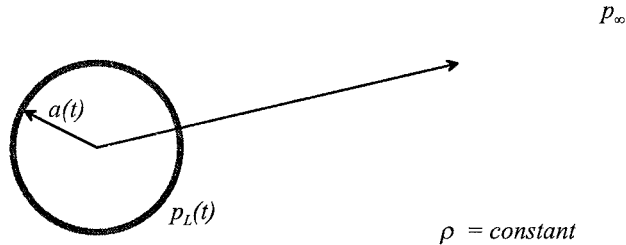


Figure 3.2. Illustration of a bubble in liquid. $a(t)$ is the bubble radius, $p_L(t)$ is the pressure in the liquid at the bubble surface, p_∞ is the pressure in the liquid far from the bubble, and ρ is the density of the liquid.

Solution at the Bubble Surface

The continuity equation (3.28a) and the Bernoulli equation (3.28c) are solved to obtain an equation of motion for the bubble radius $a = a(t)$. The boundary conditions at the bubble surface are

$$\begin{aligned} u(r = a) &= \left. \frac{\partial \Phi}{\partial r} \right|_{r=a} = \dot{a}, \\ p(r = a) &= p_L. \end{aligned} \quad (3.29)$$

The continuity equation (3.28a) requires the velocity $u(r, t)$ and the velocity potential $\Phi(r, t)$ to be of the form

$$u(r, t) = \frac{f(t)}{r^2}, \quad \Phi(r, t) = -\frac{f(t)}{r}, \quad (3.30)$$

where $f(t)$ is an arbitrary function of time. The partial derivative of $\Phi(r, t)$ with time is

$$\frac{\partial \Phi(r, t)}{\partial t} = -\frac{f'(t)}{r}. \quad (3.31)$$

The boundary conditions at the bubble surface, (3.29), together with (3.30) give the velocity $\dot{a}(t)$ and acceleration $\ddot{a}(t)$ of the bubble surface

$$\dot{a} = \frac{f(t)}{a^2}, \quad (3.32a)$$

$$\ddot{a} = \frac{d}{dt} \left(\frac{f(t)}{a^2} \right) = \frac{f'(t)}{a^2} - 2f(t) \frac{\dot{a}}{a^3}. \quad (3.32b)$$

By its definition, (3.30), $f(t) = ur^2$, and $f'(t)$ can be expressed by the position, velocity and acceleration of the bubble surface as

$$f'(t) = a^2 \ddot{a} + 2a \dot{a}^2. \quad (3.33)$$

Inserting this expression for $f'(t)$ into the Bernoulli equation (3.28c) gives the velocity $u(r, t)$ and pressure $p(r, t)$ at an arbitrary radius r in the liquid as

$$\frac{a^2 \ddot{a} + 2a \dot{a}^2}{r} - \frac{1}{2} u^2 + \frac{p_\infty - p(r)}{\rho} = 0. \quad (3.34)$$

The equation of motion for the bubble surface is obtained by setting $r = a(t)$. This relates the radius $a(t)$, velocity $\dot{a}(t)$ and acceleration $\ddot{a}(t)$ of the bubble surface to the difference between the pressure $p_L(t)$ at the bubble surface and the pressure $p_\infty(t)$ in the liquid far from the bubble

$$\ddot{a}a + \frac{3}{2} \dot{a}^2 + \frac{p_\infty - p_L}{\rho} = 0. \quad (3.35)$$

This is commonly called the *Rayleigh-Plesset* equation for the oscillating bubble. It is based on the work by Lord Rayleigh from 1917 [143], who studied the collapse of vapor-filled cavities around ship propellers.

A driving acoustic field was included in 1949 by Plesset [133], by letting the background pressure p_∞ vary with time as $p_\infty = p_0 + p_i(t)$. Here, p_0 is the static background pressure and $p_i(t)$ is the driving sound field. This results in

$$\ddot{a}a + \frac{3}{2}\dot{a}^2 + \frac{p_0 + p_i(t) - p_L}{\rho} = 0. \quad (3.36)$$

Extensions by Noltingk and Neppiras [125, 122] and by Poritsky [137] have added the effect of a gas inside the bubble, a constant vapor pressure, a surface tension, and liquid viscosity. These effects are not included in (3.35), as this describes the motion of the liquid only, with the pressure $p_L(t)$ at the bubble surface as a boundary condition. The contributions from the gas and from the viscosity will be included into the expression for the pressure $p_L(t)$. This expression will also contain the effect of a shell surrounding the bubble.

This approach makes it easier to separate various models for the motion of the liquid, and to replace the gas-liquid interface with a shell.

Scattered Sound Field

The Bernoulli equation (3.28c) gives the pressure as function of velocity potential as

$$p(r) - p_\infty = -\rho \left(\frac{\partial \Phi}{\partial t} + \frac{1}{2}(\nabla \Phi)^2 \right). \quad (3.37)$$

Inserting the expressions (3.30) and (3.31) for $f(t)$ and $f'(t)$ gives the velocity and the pressure in the liquid, expressed by $f(t)$, as

$$p(r) - p_\infty = \rho \left(\frac{f'(t)}{r} - \frac{f^2(t)}{2r^4} \right). \quad (3.38)$$

The expressions (3.32a) and (3.33) for $f(t)$ and $f'(t)$ are inserted to obtain the the pressure field as function of the radius $a(t)$, velocity $\dot{a}(t)$ and acceleration \ddot{a} of the bubble surface

$$p(r) - p_\infty = \rho \left(\frac{a^2\ddot{a} + 2a\dot{a}^2}{r} - \frac{a^2\dot{a}^4}{2r^4} \right). \quad (3.39)$$

Only the far-field part of the pressure field is of interest when receiving scattered energy from the bubble

$$p_s(r, t) = (p(r) - p_\infty) \Big|_{Far-field} = \rho \frac{a^2\ddot{a} + 2a\dot{a}^2}{r}. \quad (3.40)$$

This expression requires the bubble wall acceleration \ddot{a} to be calculated. Numerical differentiation can easily become inaccurate and unstable. To overcome this, (3.40) is reformulated using the equation of motion (3.35), to

$$p_s(t) \Big|_{Far-field} = \frac{a}{r} \left(\frac{1}{2} \rho \dot{a}^2 + p_L(t) - p_\infty(t) \right). \quad (3.41)$$

3.2.2 Linear Propagation I: Trilling Model

Several different formulations exist for the equation of motion of an oscillating bubble, derived from a ‘‘Synthesis of incompressible and acoustic approximations’’ [141]. In addition to the Rayleigh-Plesset equation, commonly used models are those due to Trilling [162] and to Keller et al. [68, 69].

This section derives the *Trilling model*. The derivation is based on a paper by Trilling from 1952 [162]. Trilling in turn refers to work by Herring [54] and by Kirkwood and Bethe [75], studying gas bubbles from underwater explosions. The Trilling model was used by Chin to model contrast agent bubbles in 1997 [18, 17].

Basic Equations

The Trilling model is based on the acoustic approximation. The speed of sound in the liquid surrounding the bubble is assumed constant, that is, independent of acoustic pressure. The linear wave equation is valid. In this approximation, the equation of state (3.9) takes the form

$$\left(\frac{\partial \rho}{\partial p} \right)_s = \frac{1}{c^2} = \frac{1}{c_\infty^2} = constant. \quad (3.42)$$

The oscillating bubble radiates a wave that follows the linear wave equation, (3.26c). With only a diverging spherical wave, the linear wave equation can be written

$$\left(\frac{\partial}{\partial t} + c \frac{\partial}{\partial r} \right) (r\Phi) = 0, \quad (3.43)$$

with the general solution

$$\Phi(r, t) = \frac{1}{r} f(t - r/c), \quad (3.44)$$

where $f(x)$ is an arbitrary function.

The Bernoulli-equation (3.22d) is differentiated with time to give

$$\frac{\partial \Phi}{\partial t} = -\frac{1}{2}u^2 - h, \quad (3.45a)$$

$$\frac{\partial^2 \Phi}{\partial t^2} = -u \frac{\partial u}{\partial t} - \frac{\partial h}{\partial t}. \quad (3.45b)$$

Likewise, the wave equation for diverging spherical waves, (3.43), is differentiated with time to give

$$\frac{r}{c} \frac{\partial^2 \Phi}{\partial t^2} + \frac{\partial \Phi}{\partial t} + r \frac{\partial u}{\partial t} = 0. \quad (3.46)$$

The differentiated Bernoulli and wave equations, (3.45b) and (3.46), are combined to give

$$r \left(1 - \frac{u}{c}\right) \frac{\partial u}{\partial t} - \frac{1}{2}u^2 - h - \frac{r}{c} \frac{\partial h}{\partial t} = 0. \quad (3.47)$$

The density ρ as function of pressure p is found from the equation of state (3.42) to

$$\rho = \rho_\infty + \frac{p - p_\infty}{c^2}, \quad (3.48)$$

where the speed of sound c is a constant. This expression for the density $\rho(p)$ is inserted into the enthalpy integral (3.23a), which can now be evaluated exactly

$$\begin{aligned} h(r) &= \int_{p_\infty}^{p(r)} \frac{1}{\rho(p)} dp \\ &= c^2 \int_{p_\infty}^{p(r)} \frac{1}{c^2 \rho_\infty + p - p_\infty} dp = c^2 \ln \left(1 + \frac{p - p_\infty}{\rho_\infty c^2}\right). \end{aligned} \quad (3.49)$$

For liquids such as water, $\rho c^2 \approx 10^9 Pa$. This is much greater than the acoustic pressures involved, and (3.49) can be simplified to

$$h(r) = \frac{p(r) - p_\infty}{\rho_\infty}, \quad (3.50)$$

This result is correct to the first order in $1/c$. It is equal to the result in (3.24a), which was derived from an expansion in powers of $1/c$.

The enthalpy, (3.50), is differentiated with time to give

$$\frac{\partial h}{\partial t} = \frac{\partial p}{\partial t} \frac{d}{dp} \int_{p_\infty}^p \frac{1}{\rho} dp = \frac{\partial p}{\partial t} \frac{1}{\rho(r)} \approx \frac{\partial p}{\partial t} \frac{1}{\rho_\infty}, \quad (3.51)$$

which is equal to the result of the series expansion, (3.24c).

This expression for the enthalpy $h(r)$ is inserted into the Bernoulli equation (3.47), and an equation of motion for the liquid is achieved

$$r \left(1 - \frac{u}{c} \right) \frac{\partial u}{\partial t} - \frac{1}{2} u^2 + \frac{p_\infty - p}{\rho_\infty} - \frac{r}{\rho c} \frac{\partial p}{\partial t} = 0. \quad (3.52)$$

This equation of motion is for a fixed coordinate r . What is sought, is an equation of motion for the bubble surface. To achieve this, (3.52) is converted to an equation of motion at the bubble radius $r = a(t)$, which varies with time. This requires the partial derivatives of u and p with respect to space and time to be expressed by the motion of the bubble wall, $a(t)$, $\dot{a}(t)$ and $\ddot{a}(t)$.

The conservation equations for mass, (3.18a), and momentum, (3.18b), and the definitions of the total time derivatives of pressure and velocity constitute four equations. These four equations combined give the partial derivatives of p and u with respect to t and r .

The continuity equation (3.18a) is reformulated, using the relations

$$\frac{\partial \rho}{\partial t} = \frac{d\rho}{dp} \frac{\partial p}{\partial t} = \frac{1}{c^2} \frac{\partial p}{\partial t} \quad \frac{\partial \rho}{\partial r} = \frac{1}{c^2} \frac{\partial p}{\partial r}. \quad (3.53)$$

The resulting four equations for the four partial derivatives are

$$\begin{aligned} \frac{1}{\rho c^2} \frac{\partial p}{\partial t} + \frac{u}{\rho c^2} \frac{\partial p}{\partial r} + \frac{\partial u}{\partial r} + \frac{2u}{r} &= 0, \\ \frac{\partial u}{\partial t} + u \frac{\partial u}{\partial r} + \frac{1}{\rho} \frac{\partial p}{\partial r} &= 0, \\ \frac{\partial p}{\partial t} + \dot{a} \frac{\partial p}{\partial r} &= \frac{dp_L}{dt} = \dot{p}_L, \\ \frac{\partial u}{\partial t} + \dot{a} \frac{\partial u}{\partial r} &= \frac{da}{dt} = \dot{a}. \end{aligned} \quad (3.54)$$

They have solution

$$\begin{aligned} \frac{\partial p}{\partial t} &= \dot{p}_L + \rho \dot{a} \ddot{a}, & \frac{\partial p}{\partial r} &= -\rho \ddot{a}, \\ \frac{\partial u}{\partial t} &= \ddot{a} + \frac{2\dot{a}^2}{a} + \frac{\dot{a}}{\rho c^2} \dot{p}_L, & \frac{\partial u}{\partial r} &= -2 \frac{\dot{a}}{a} - \frac{1}{\rho c^2} \dot{p}_L. \end{aligned} \quad (3.55)$$

Equation of Motion for the Bubble Surface

The expressions for $\frac{\partial p}{\partial t}$ and $\frac{\partial u}{\partial t}$ from (3.55) are inserted into the equation of motion (3.52). This gives an ODE for the bubble surface $a(t)$

$$\ddot{a} a \left(1 - 2 \frac{\dot{a}}{c} \right) + \frac{3}{2} \dot{a}^2 \left(1 - \frac{4}{3} \frac{\dot{a}}{c} \right) - \frac{a}{\rho c} \left(1 - \frac{\dot{a}}{c} + \left(\frac{\dot{a}}{c} \right)^2 \right) \dot{p}_L + \frac{p_\infty - p_L}{\rho} = 0, \quad (3.56)$$

where ρ_∞ is rewritten as ρ , which now denotes the equilibrium density of the liquid. The Trilling model is derived from the acoustic approximation, the speed of sound is modeled as constant. It is only meaningful to the first order in the acoustic Mach-number $M = \dot{a}/c$. Terms of order $1/c^2$ are removed from (3.56), reducing it to

$$\ddot{a}a \left(1 - 2\frac{\dot{a}}{c}\right) + \frac{3}{2}\dot{a}^2 \left(1 - \frac{4}{3}\frac{\dot{a}}{c}\right) - \frac{a}{\rho c} \dot{p}_L + \frac{p_\infty - p_L}{\rho} = 0. \quad (3.57)$$

This equation of motion for a gas bubble was published by Trilling in 1952 [162]. For an incompressible liquid, $c = \infty$, and (3.57) is converted to the Rayleigh-Plesset equation (3.35).

There are two differences between the Trilling model (3.57) and the Rayleigh-Plesset model (3.35). The factors $(1 - 2\dot{a}/c)$ and $(1 - \frac{4}{3}\dot{a}/c)$ change the inertia of the liquid for high velocities, when the bubble wall velocity \dot{a} becomes comparable to the speed of sound c in the liquid. If the bubble wall velocity \dot{a} exceeds $c/2$ the factor $(1 - 2\frac{\dot{a}}{c})$ over-compensates, giving an unphysical negative inertia, which can cause the solution to become unstable. This unphysical result is caused by the approximation of constant speed of sound, or constant compressibility. It predicts negative volume for Mach numbers larger than $\frac{1}{2}$. Hence, the Trilling model is only meaningful for acoustic Mach-numbers much smaller than $\frac{1}{2}$.

A more important improvement of the Trilling model is the term containing \dot{p}_L . This term predicts acoustic damping, the oscillations are damped because the bubble radiates acoustic energy as it oscillates.

Driving Sound Field

Trilling's original work [162] considered only the sound radiated from the oscillating bubble. A driving sound field was not included. A driving sound field is included by letting the background pressure p_∞ vary with time as

$$p_\infty = p_0 + p_i(t), \quad (3.58)$$

where p_0 is the static background pressure and $p_i(t)$ is the driving sound field. A varying background pressure p_∞ changes the expression (3.51) for the time derivative of the enthalpy to

$$\frac{\partial h}{\partial t} = \frac{1}{\rho_\infty} \left(\frac{\partial p}{\partial t} - \frac{dp_i}{dt} \right), \quad (3.59)$$

This causes an additional term $\frac{r}{\rho c} \dot{p}_i$ in the equation of motion for the liquid, (3.52), and in the resulting ODE for the bubble surface. Hence, with a driving

pressure $p_i(t)$, the Trilling equation is modified to

$$\ddot{a}a \left(1 - 2\frac{\dot{a}}{c}\right) + \frac{3}{2}\dot{a}^2 \left(1 - \frac{4}{3}\frac{\dot{a}}{c}\right) - \frac{a}{\rho c}\dot{p}_L + \frac{a}{\rho c}\dot{p}_i(t) + \frac{p_0 + p_i(t) - p_L}{\rho} = 0. \quad (3.60)$$

This equation is equal to the model proposed by Chin (Equation (6) in Reference [18]), if the terms of second and higher order in $1/c$ are removed from Chin's equation.

Scattered Sound Field

The velocity potential $\Phi(r, t)$ represents a diverging spherical wave. It obeys the wave equation (3.43), and has solution (3.44)

$$\Phi(r, t) = \frac{f(t - r/c)}{r}. \quad (3.61)$$

The velocity potential $\Phi(r, t)$ and the enthalpy $h(r, t)$ are given by (3.22d) and (3.50) as

$$\frac{\partial\Phi(r, t)}{\partial t} = -h - \frac{1}{2}u^2, \quad h(r, t) = \frac{p(r, t) - p_\infty}{\rho}. \quad (3.62)$$

These equations are approximately satisfied by a potential $\Phi(r, t)$ of the form

$$\Phi(r, t) = \frac{1}{r} \int_0^{t-(r-a_e)/c} \left(\frac{p_\infty - p_L(\tau)}{\rho} + \frac{1}{2}\dot{a}^2(\tau) \right) a(\tau) d\tau. \quad (3.63)$$

The scattered velocity field $u(r, t)$ and pressure field $p(r, t)$ are found from the velocity potential (3.61) and (3.62) to

$$u = \frac{\partial\Phi}{\partial r} = -\frac{f(t - (r - a_e)/c)}{r^2} - \frac{f'(t - (r - a_e)/c)}{rc}, \quad (3.64a)$$

$$p(r) - p_\infty = -\rho \frac{\partial\Phi}{\partial t} + \frac{1}{2}u^2. \quad (3.64b)$$

The term $\frac{1}{2}u^2$ decays as $1/r^2$, and is a near field effect. Only the far field terms are of interest when receiving sound scattered from the bubble. The scattered sound pressure in the far field is

$$p_s(r) = p(r) - p_\infty \Big|_{Far-field} = -\rho \frac{\partial\Phi}{\partial t}. \quad (3.65)$$

The expression (3.63) for the velocity potential $\Phi(r, t)$ gives the scattered pressure $p_s(r, t)$ in the far field of the bubble as

$$p_s(t) = \frac{a(\tau)}{r} \left(p_L(\tau) - p_\infty + \frac{1}{2} \rho \dot{a}^2(\tau) \right), \quad \tau = t - \frac{r - a_e}{c}. \quad (3.66)$$

This is equal to the expression for the scattered field in the Rayleigh-Plesset equation, (3.41), except that the time is replaced by the retarded time $\tau = t - (r - a_e)/c$. For the incompressible Rayleigh-Plesset model, the speed of sound is infinite, and there is no difference between the time t and the retarded time τ .

3.2.3 Linear Propagation II: Keller-Miksis Model

Another approach based on essentially the same assumptions as the Trilling model, is due to Keller and Kolodner [68]. This was later extended by Epstein and Keller [40] and modified by Keller and Miksis [69] to include a driving sound field.

This approach combines the Bernoulli equation (3.22d) with the linear wave equation (3.26c), under the assumption of a constant speed of sound in the liquid. The basic equations are

$$\frac{\partial \Phi}{\partial t} + \frac{1}{2} \left(\frac{\partial \Phi}{\partial r} \right)^2 + h = 0 \quad \text{Bernoulli equation.} \quad (3.67a)$$

$$\frac{\partial^2 \Phi}{\partial r^2} - \frac{1}{c^2} \frac{\partial^2 \Phi}{\partial t^2} = 0 \quad \text{Linear wave equation.} \quad (3.67b)$$

The speed of sound c and the enthalpy h are taken from (3.22a) and (3.23a), setting the speed of sound c independent of the pressure

$$\left(\frac{\partial \rho}{\partial p} \right)_S = \frac{1}{c^2} = \text{constant} \quad \text{Speed of sound.} \quad (3.67c)$$

$$h = \frac{p(r) - p_\infty}{\rho_\infty} \quad \text{Enthalpy.} \quad (3.67d)$$

The expression (3.67d) for the enthalpy h is correct to the first order in $1/c$. The boundary conditions at the bubble surface $r = a(t)$ are

$$\begin{aligned} p(a, t) &= p_L(t), \\ \frac{\partial \Phi(a, t)}{\partial r} &= u(a, t) = \dot{a}(t). \end{aligned} \quad (3.68)$$

The equations above are combined to give a set of equations for the velocity potential $\Phi(a, t)$ at the bubble surface

$$\frac{\partial \Phi}{\partial t} + \frac{1}{2} \dot{a}^2 + h = 0, \quad (3.69a)$$

$$\frac{\partial^2 \Phi}{\partial r^2} - \frac{1}{c^2} \frac{\partial^2 \Phi}{\partial t^2} = 0, \quad (3.69b)$$

$$\frac{\partial \Phi}{\partial r} = \dot{a}. \quad (3.69c)$$

The general solution to the wave equation (3.69b) is

$$\Phi(r, t) = \frac{f_1(t - r/c)}{r} + \frac{f_2(t + r/c)}{r}, \quad (3.70a)$$

where $f_1(x)$ and $f_2(x)$ are arbitrary functions. The partial derivatives with time and radius are

$$\frac{\partial \Phi}{\partial t} = \frac{f'_1}{r} + \frac{f'_2}{r}, \quad (3.70b)$$

$$\frac{\partial \Phi}{\partial r} = -\frac{f'_1}{rc} - \frac{f_1}{r^2} + \frac{f'_2}{rc} - \frac{f_2}{r^2}. \quad (3.70c)$$

These expressions are inserted into the Bernoulli equation (3.69a), using (3.69c) to replace the potential. The results are combined and f'_1 is eliminated, giving

$$c(f_1 + f_2) = a^2(\frac{1}{2}\dot{a}^2 - ca + h) + 2af'_2. \quad (3.71)$$

Differentiation with time gives

$$\begin{aligned} & c\left(1 - \frac{\dot{a}}{c}\right)(f'_1 + f'_2) \\ &= ca\left(-2\dot{a}^2\left(1 - \frac{1}{2}\frac{\dot{a}}{c}\right) - a\ddot{a}\left(1 - \frac{\dot{a}}{c}\right) + 2\frac{\dot{a}}{c}h + \frac{a}{c}\dot{h}\right) + 2a\left(1 + \frac{\dot{a}}{c}\right)f''_2. \end{aligned} \quad (3.72)$$

The time derivatives of f_1 and f_2 are eliminated by (3.69a), formulated as

$$\frac{f'_1 + f'_2}{a} + \frac{1}{2}\dot{a}^2 + h = 0. \quad (3.73)$$

This is inserted, the terms are sorted, and an equation of motion for the bubble surface $a(t)$ is obtained

$$\begin{aligned} & a\ddot{a}\left(1 - \frac{\dot{a}}{c}\right) + \frac{3}{2}\dot{a}^2\left(1 - \frac{1}{3}\frac{\dot{a}}{c}\right) - h\left(1 + \frac{\dot{a}}{c}\right) - \frac{a}{c}\dot{h} \\ & \quad - \frac{2}{c}\left(1 + \frac{\dot{a}}{c}\right)f''_2(t + a/c) = 0. \end{aligned} \quad (3.74)$$

The equation above is as formulated by Prosperetti [141]. It is equivalent to the equation derived by Keller and Miksis [69], but viscosity terms from the bulk of the liquid are neglected. The omission of the viscosity in the bulk of the liquid was justified in (3.11) to (3.16). A driving acoustic pressure is included by the term containing $f_2''(t + a/c)$, as $f_2(t + r/c)$ represents a converging spherical wave.

Driving Acoustic Pressure

The driving acoustic field is described by a velocity potential $\Phi_i(\mathbf{r}, t)$. The driving field is decomposed into spherical harmonics and spherical Bessel functions, as described e.g. in Morse and Ingard [117]. The bubble oscillation is purely radial, and zeroth term in the decomposition is the only term interacting with this radial oscillation mode. The zeroth term is expressed as

$$\Phi_{i0}(r, t) = \frac{f_2(t + r/c) + f_3(t - r/c)}{r}. \quad (3.75)$$

The potential of the driving field $\Phi_i(\mathbf{r}, t)$ must exist in the bubble center, $r = 0$. This implies that $f_3 = -f_2$, and the driving acoustic field $\Phi_{i0}(r, t)$ is

$$\Phi_{i0}(r, t) = \frac{f_2(t + r/c) - f_2(t - r/c)}{r}. \quad (3.76)$$

The bubble diameter is small compared to the wavelength of the driving pressure field. This allows only small variations in the function f_2 over a distance equal to the bubble diameter $2a$. The variation in f_2 over the bubble diameter can therefore be approximated as

$$\frac{f_2(t + a/c) - f_2(t - a/c)}{a} \approx \frac{2}{c} f_2'(t). \quad (3.77)$$

The driving acoustic field is treated linearly. The driving pressure $p_i(a, t)$ at the bubble surface is calculated from the velocity potential $\Phi_i(a, t)$ to

$$p_i(a, t) = -\rho \frac{\partial \Phi_{i0}}{\partial t} \Big|_{r=a} = -\frac{2\rho}{c} f_2''(t). \quad (3.78)$$

This expression is inserted into (3.74) to include the driving acoustic pressure explicitly. The enthalpy h is expressed by (3.67d), correct to the first order in $1/c$. The driving acoustic field Φ_{i0} vanishes at $r = \infty$, giving $p_\infty = p_0$, the hydrostatic background pressure.

$$a\ddot{a} \left(1 - \frac{\dot{a}}{c}\right) + \frac{3}{2}\dot{a}^2 \left(1 - \frac{1}{3}\frac{\dot{a}}{c}\right) - \left(1 + \frac{\dot{a}}{c}\right) \frac{p_L - p_0 - p_i(t + a/c)}{\rho} - \frac{a}{\rho c} \dot{p}_L = 0. \quad (3.79)$$

This is an equation of motion for the bubble, including a driving acoustic field p_i . This model is commonly referred to as the *Keller-Miksis* model [69].

The Keller-Miksis model possess the same basic features as the Trilling model, and the comments given to the Trilling model apply also here: The factors of type $(1 \pm \frac{\dot{a}}{c})$ change the inertia due to the compressibility of the liquid, but can cause the solution to become unstable for high Mach-numbers. The term containing \dot{p}_L introduces damping from acoustic radiation.

Scattered Sound Field

The scattered sound field $\Phi_s(r, t)$ is defined as the difference between the total field $\Phi(r, t)$ and the incoming field $\Phi_i(r, t)$ as

$$\Phi_s(r, t) = \Phi(r, t) - \Phi_i(r, t). \quad (3.80)$$

This is expressed by (3.70a) and (3.76) as

$$\Phi_s(r, t) = \frac{1}{r} \left(f_1(t - r/c) + f_2(t - r/c) \right). \quad (3.81)$$

The scattered pressure $p_s(r, t)$ is given by the velocity potential $\Phi_s(r, t)$ as

$$p_s(r, t) = -\rho \left(\frac{\partial \Phi_s}{\partial t} + \frac{1}{2} \left(\frac{\partial \Phi_s}{\partial r} \right)^2 \right). \quad (3.82)$$

The last term, $\frac{\partial \Phi_s}{\partial r}$, give rise to terms decaying as $1/r^2$ and faster. These near field effects do not contribute to the scattered energy from the bubble. The scattered pressure in the far-field is

$$p_s(r, t)|_{far-field} = -\rho \frac{\partial \Phi_s}{\partial t} = -\frac{\rho}{r} (f_1'(t - r/c) + f_2'(t - r/c)). \quad (3.83)$$

The difference between the derivatives of f_2 is found from (3.77) to

$$f_2'(t + a/c) - f_2'(t - a/c) = \frac{2a}{c} f_2''(t), \quad (3.84)$$

which is combined with the Bernoulli equation (3.73) to yield

$$f_1'(t - a/c) + f_2'(t - a/c) = -a \left(\frac{1}{2} \dot{a}^2 + h(a, t) + \frac{2}{c} f_2''(t) \right). \quad (3.85)$$

Note that in (3.73), $f_1' = f_1'(t - r/c)$ and $f_2' = f_2'(t + r/c)$. $f_2''(t)$ is expressed by the driving acoustic pressure $p_i(t)$ from (3.78). This gives

$$f_1'(t - a/c) + f_2'(t - a/c) = -\frac{a}{\rho} \left(\frac{1}{2} \rho \dot{a}^2 + p_L(t) - p_0 - p_i(t) \right), \quad (3.86)$$

where the enthalpy at the bubble surface $h(a, t)$ is taken from (3.67d).

The time origin is changed by letting $t \rightarrow t + (r - a)/c$. The expression (3.86) for $f'_1 + f'_2$ is inserted into (3.83). This gives the scattered pressure in the far-field as

$$p_s(r, t + \frac{1}{c}(r - a)) = \frac{a}{r} \left(\frac{1}{2} \rho \dot{a}^2 + p_L(t) - p_0 - p_i(t) \right). \quad (3.87)$$

This result for the scattered field is equal to the results of the incompressible Rayleigh-Plesset model, (3.41), and of the Trilling model, (3.66), except for the shift in time scale. The difference between the three models is in the equations of motion. These are slightly different, and may give different solutions for $a(t)$ and $p_L(t)$.

3.2.4 Comparison between the Liquid Models

Three models for the liquid around the bubble have been presented

- **Rayleigh-Plesset** Incompressible liquid
- **Trilling** Linear compressibility, finite and constant speed of sound
- **Keller-Miksis** Linear compressibility, finite and constant speed of sound

Other models for the oscillation of the liquid exist. The model by Gilmore [50] goes one step further than the presented models, taking into account a pressure-dependent speed of sound in the liquid. The Gilmore equation does not require the bubble wall velocity to be small compared to the speed of sound in the liquid, and is better at handling large acoustic Mach-numbers. It is especially useful when studying the extreme velocities associated with single bubble sonoluminescence. The Gilmore model has not been tested or implemented here. Another approach to the nonlinearly oscillating bubble was given by Flynn [45, 46]. Flynn's approach includes thermal processes in the gas, resulting in a more complex mathematical formulation, and has not been tested.

The Rayleigh-Plesset model is frequently used in the literature. It assumes an incompressible liquid, and is only useful for small acoustic Mach-numbers, where

$$M = \left| \frac{\dot{a}}{c} \right| \ll 1, \quad (3.88)$$

where \dot{a} is the bubble wall velocity and c is the speed of sound in the liquid. In most situations involving ultrasound contrast agents, this requirement is

fulfilled. It can be violated in some extreme cases, during very short time-intervals near the end of the contraction cycle of the oscillation. The major weakness with the Rayleigh-Plesset model is that it does not include damping from acoustic radiation. This becomes important at larger bubble diameters, above about $10\ \mu\text{m}$, and at high frequencies, above about 10 MHz. For linear oscillations, the contribution from radiation damping is compared with other damping mechanisms in Chapter 6, see Figure 6.14 on page 155 and Figure 6.15 on page 156.

The Trilling and Keller-Miksis models go one step further than the Rayleigh-Plesset model, by including a finite but constant speed of sound in the liquid. The main advantage by going from the Rayleigh-Plesset to the Trilling or Keller-Miksis model, is including the term containing \dot{p}_L , which accounts for radiation damping. The terms of type $(1 - \dot{a}/c)$ give small improvements at lower Mach-numbers, but over-compensate and may cause numerical instability for Mach-numbers approaching unity.

For the Keller-Miksis model, the driving acoustic pressure $p_i(t)$ was included explicitly in the derivation. In the Rayleigh-Plesset and Trilling models, a driving acoustic pressure was included as an addition to the background pressure p_∞ .

The Trilling and Keller-Miksis models were derived from the same assumption; constant speed of sound in the liquid. Prosperetti [141] has shown that the differences between these two models are of second order in \dot{a}/c . It is therefore difficult to state which of the two models are “best” at describing the behavior of the liquid. One difference is that the unphysical negative inertia term occur for $\dot{a} = \frac{1}{2}c$ in the Trilling model, but at $\dot{a} = c$, in the Keller-Miksis model. This might be a reason for preferring the Keller-Miksis model.

An intermediate model that includes radiation damping, but avoids the numerical problems with the Trilling and Keller-Miksis models, is a *Modified Rayleigh-Plesset* equation. This has been used by Hilgenfeldt et al. [55]. The radiation damping term from the Trilling and Keller-Miksis equations is included, but the $(1 - \dot{a}/c)$ -terms are omitted. This modified Rayleigh-Plesset equation takes the form

$$a\ddot{a} + \frac{3}{2}\dot{a}^2 - \frac{p_L - p_0 - p_i(t)}{\rho} - \frac{a}{\rho c}\dot{p}_L = 0. \quad (3.89)$$

The various models have been tested for shell-encapsulated bubbles, for frequencies and diameters relevant in medical ultrasound imaging. The four different models yielded very similar results in all situations. Small differences were found for frequencies above 10 MHz, where the Rayleigh-Plesset model tends to predict a few decibels higher scattered power than the others do.

For high driving pressures and low frequencies, the velocity in the compression cycle can get very large. Velocities comparable to the speed of sound in the liquid were found during very small fractions of the oscillation cycle, for some extreme combinations of low driving frequency and high driving amplitude. In these situations, the Trilling and Keller-Miksis models could become numerically unstable. The Rayleigh-Plesset models handle this without numerical problems, as the Mach-number in these models is always zero. But as the surface velocity approaches and perhaps exceeds the speed of sound, the assumption behind the model is violated.

These large velocities occur in a very short fraction of the total oscillating cycle, and the results are assumed to be reliable outside this part of the cycle. But since high Mach-numbers have been found, an improved model should be considered, including a pressure-dependent speed of sound in the liquid. The Gilmore model should be a good choice for these high Mach-numbers, but has not been tested here.

3.3 Viscous Damping in the Liquid

For for spherically symmetric motion, it was shown in Chapter 3.1 that viscous damping vanishes in the bulk of an incompressible liquid. In a compressible liquid, the viscosity causes a damping term of second order in $1/c$. Terms of this order are neglected in the models considered. Hence, damping from liquid viscosity can be ignored in the bulk of the liquid. But viscous damping forces can give significant contributions at the surface of the bubble. This section introduces viscous damping from the liquid as a boundary condition to the equations of motion presented in the previous sections. The effect of the viscosity is on the pressure $p_L(t)$ at the bubble wall.

The liquid flow around the oscillating bubble is spherically symmetric and purely radial. The angular components and the angular derivatives of the velocity vector \mathbf{u} disappear, giving

$$u_r = u(r), \quad u_\theta = u_\phi = 0, \quad \frac{\partial u}{\partial \theta} = \frac{\partial u}{\partial \phi} = 0. \quad (3.90)$$

The components of the rate-of-strain tensor D_{ij} are [79]

$$D_{rr} = \frac{\partial u_r}{\partial r}, \quad D_{\theta\theta} = D_{\phi\phi} = \frac{u_r}{r}, \quad D_{ij} = 0, \quad i \neq j. \quad (3.91a)$$

The trace of the rate of strain velocity tensor is the rate of volume dilation [147]

$$\text{Tr } \mathbf{D} = \sum_{i=r,\theta,\phi} D_{ii} = \nabla \mathbf{u}. \quad (3.92)$$

The liquid is modeled as Newtonian. Only shear viscosity is considered, bulk viscosity is neglected. The components of the stress tensor T_{ij} are expressed by the rate of strain tensor D_{ij} as [147]

$$\begin{aligned} T_{ii} &= -p + 2\eta_L \left(D_{ii} - \frac{1}{3} \text{Tr} \mathbf{D} \right), \\ T_{ij} &= 2\eta_L D_{ij} = 0, \quad i \neq j, \end{aligned} \quad (3.93)$$

where η_L is the shear viscosity in the liquid. This gives the radial and angular components of the stress tensor

$$T_{rr} = -p + 2\eta_L \left(\frac{\partial u}{\partial r} - \frac{1}{3} \nabla \mathbf{u} \right), \quad (3.94a)$$

$$T_{\theta\theta} = T_{\phi\phi} = -p + 2\eta_L \left(\frac{u}{r} - \frac{1}{3} \nabla \mathbf{u} \right), \quad (3.94b)$$

From (3.93), it is seen that the trace of the stress tensor T_{ij} is -3 times the hydrostatic pressure p

$$\text{Tr} \mathbf{T} = \sum_{i=r,\theta,\phi} T_{ii} = -3p. \quad (3.95)$$

3.3.1 Incompressible Liquid

For an incompressible liquid, there is no volume dilation, $\nabla \mathbf{u} = 0$, and (3.92) simplifies to

$$\text{Tr} \mathbf{D} = \nabla \mathbf{u} = 0. \quad (3.96)$$

The components of the stress tensor \mathbf{T} from (3.94a) and (3.94b) are

$$T_{rr} = -p + 2\eta_L \frac{\partial u_r}{\partial r}, \quad (3.97a)$$

$$T_{\theta\theta} = T_{\phi\phi} = -p + 2\eta_L \frac{u_r}{r}, \quad (3.97b)$$

The relation (3.95) between the trace of T_{ij} and the hydrostatic pressure p gives the radial component T_{rr} of the viscous stress tensor as

$$T_{rr} = -p - 4\eta_L \frac{u}{r}. \quad (3.98)$$

A similar derivation of the viscous stress can be found in the book by Leighton [92], using the pressure tensor instead of the stress tensor.

3.3.2 Compressible Liquid: Acoustic Approximation

For a compressible liquid, pressure variations will cause volume dilation. In this situation, $\nabla \mathbf{u} \neq 0$, but is given by (3.12) as

$$\nabla \mathbf{u} = -\frac{1}{\rho} \frac{d\rho}{dt} = -\frac{1}{\rho c^2} \frac{dp}{dt}. \quad (3.99)$$

The components of the stress tensor at the bubble surface are given by (3.94a) and (3.94b). These are combined with (3.95) to obtain the radial component T_{rr}

$$T_{rr} = -p - 4\eta_L \frac{u}{r} + \frac{4}{3}\eta_L \nabla \mathbf{u}. \quad (3.100)$$

The volume dilation $\nabla \mathbf{u}$ is replaced by (3.99), giving

$$T_{rr} = -p - 4\eta_L \frac{u}{r} - \frac{4}{3}\eta_L \frac{1}{\rho c^2} \frac{dp}{dt}. \quad (3.101)$$

The last term in this expression is small to second order in $1/c$, and is neglected. The resulting expression for the stress tensor of the compressible liquid is equal that for the incompressible liquid,

$$T_{rr} = -p - 4\eta_L \frac{u}{r}. \quad (3.102)$$

This gives the radial component of the stress tensor at the bubble surface, where $r = a(t)$ and $u = \dot{a}(t)$

$$T_{rr}(a) = -p_L - 4\eta_L \frac{\dot{a}}{a}, \quad (3.103)$$

where $p_L(t)$ is the pressure at the bubble surface. The result above is valid to the first order in $1/c$.

The expression (3.103) for T_{rr} is used to obtain a boundary condition for the motion of the liquid at the bubble surface. T_{rr} is required to be continuous at the liquid-bubble interface.

3.4 Pressure Difference across a Spherical Shell

The gas bubbles used in ultrasound contrast agents are normally stabilized by a thin shell. The shell can influence the mechanical properties of the bubble by increasing its stiffness and by introducing added viscous damping.

The purpose of this section is to develop a theoretical model for the influence of a shell. The shell is described as a visco-elastic solid, using the Lamé-coefficients λ and μ and shear viscosity η_S .

Models for the tension in an elastic spherical shell can be found in textbooks in continuum mechanics, such as the book by Lai et al. [81]. Fox and Herzfield [47] postulated in 1954 that gas bubbles in the ocean were stabilized by an organic skin, and presented a theoretical model for the effect of this skin on the resonance frequency of the bubbles. The hypothesis was later withdrawn. But the model for the increased resonance frequency due to a shell is still useful for other types of encapsulated bubbles. The effect of the shell on the contrast agent *Albunex* was studied in 1992 and 1993 by de Jong and Hoff [29, 28], using a linear model. Church [22] in 1995 published a nonlinear model for the effect of a shell on contrast agent bubbles. He used a slightly different approach than what is done in this section, modeling an incompressible shell of arbitrary thickness. In 1998 and 1999, Frinking et al. [48, 49] presented a different nonlinear model for the contrast agent Quantison. They modeled the shell-encapsulated bubbles as particles with a constant bulk modulus, based on the linear model by Hoff et al. [61].

3.4.1 Shell Elasticity

The motion of an elastic solid is described by the Navier equation [148]. In absence of body forces, this is

$$\rho \frac{d\mathbf{u}}{dt} = \mu \nabla^2 \xi + (\lambda + \mu) \nabla(\nabla \xi), \quad (3.104)$$

where λ and μ are the Lamé-coefficients, ξ is the strain vector, \mathbf{u} is the velocity field and ρ is the density of the solid. The shells studied here are thin. The mass of the shell is negligible compared to the dynamic mass $m = 4\pi\rho a^3$ of

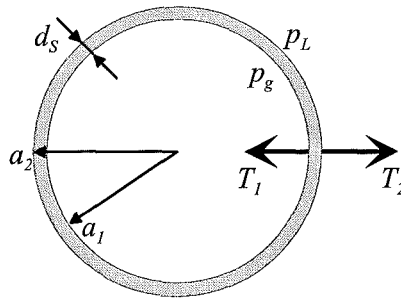


Figure 3.3. Definition of the radial stress and pressures on the bubble shell.

the moving liquid, (2.21) on page 18. The inertia of the shell is neglected by letting $\rho \rightarrow 0$.

The bubble oscillation is purely radial, giving a strain ξ that is spherically symmetric and radial. The angular derivatives and the tangential components of ξ vanish, giving

$$\xi_r = \xi(r), \quad \xi_\theta = \xi_\phi = 0, \quad \frac{\partial \xi}{\partial \theta} = \frac{\partial \xi}{\partial \phi} = 0. \quad (3.105)$$

The Navier equation (3.104) is transformed to spherical coordinates and the inertia of the shell is neglected. The resulting differential equation for the radial strain $\xi(r, t)$ is

$$(\lambda + 2\mu) \frac{\partial}{\partial r} \left(\frac{2\xi}{r} + \frac{\partial \xi}{\partial r} \right) = 0. \quad (3.106)$$

The pressure difference across the shell is found from the radial components of the stress tensor $T_{ij}(r)$ in the shell. The components of T_{ij} are expressed by the Lamé coefficients λ and μ and by the spatial strain tensor ϵ_{ij} , using the generalized Hooke's law [148]

$$T_{ij} = 2\mu\epsilon_{ij} + \lambda(\text{Tr } \epsilon)\delta_{ij}, \quad (3.107)$$

where the Kronecker delta δ_{ij} is

$$\delta_{ij} = \begin{cases} 1 & i = j \\ 0 & i \neq j \end{cases} \quad (3.108)$$

Under spherical symmetry the components of the strain tensor ϵ_{ij} are [79]

$$\epsilon_{rr} = \frac{\partial \xi}{\partial r}, \quad \epsilon_{\theta\theta} = \epsilon_{\phi\phi} = \frac{\xi}{r}, \quad \epsilon_{ij} = 0, \quad i \neq j. \quad (3.109)$$

These are inserted into the expression (3.107) for T_{ij} , giving

$$T_{rr} = \lambda \left(\frac{\partial \xi}{\partial r} + 2\frac{\xi}{r} \right) + 2\mu \frac{\partial \xi}{\partial r}, \quad (3.110a)$$

$$T_{\theta\theta} = T_{\phi\phi} = \lambda \left(\frac{\partial \xi}{\partial r} + 2\frac{\xi}{r} \right) + 2\mu \frac{\xi}{r}, \quad (3.110b)$$

$$T_{ij} = 0, \quad i \neq j. \quad (3.110c)$$

The components of the stress tensor are expressed by the stresses T_1 and T_2 at the inner and outer surfaces of the shell, see Figure 3.3

$$T_1 = T_{rr}(r = a_1), \quad T_2 = T_{rr}(r = a_2) \quad (3.111)$$

The difference in radial stress between the inner and outer shell surfaces gives the pressure difference across the shell. This difference is calculated from (3.110a). Equation (3.106) gives

$$\left(\frac{\partial \xi}{\partial r} + 2\frac{\xi}{r}\right) = C(t) = \text{spatial constant}, \quad (3.112)$$

which is inserted into (3.110a) to give

$$T_{rr}(r) = (\lambda + 2\mu)C - 4\mu\frac{\xi}{r}. \quad (3.113)$$

The difference in radial stress between the outer and inner shell surface is now found as

$$T_2 - T_1 = -4\mu\left(\frac{\xi_2}{a_2} - \frac{\xi_1}{a_1}\right), \quad (3.114)$$

where ξ_1 and ξ_2 are the displacements of the inner and outer shell surfaces.

This expresses the difference in radial stress across the shell as a function of the displacements of the two shell surfaces. The relation between ξ_1 and ξ_2 depends on the elastic properties of the shell material, λ and μ .

The oscillation of contrast agent bubbles is governed by the stress difference found in (3.114). The value of the stresses themselves are of less importance. Solutions for these stresses $T_{rr}(r)$ and $T_{\theta\theta}(r)$ inside the shell can be found from (3.106), using an approach similar to that in the book by Lai et al. [80]. The general solution of (3.106) for $\xi = \xi(r, t)$ is

$$\xi = Ar + \frac{B}{r^2}, \quad (3.115)$$

where A and B are arbitrary constants in space. This expression for $\xi(r)$ is inserted into (3.110a) and (3.110b) and adapted to the boundary conditions (3.111). The resulting solutions for the constants A and B are

$$(3\lambda + 2\mu)A = \frac{T_2 a_2^3 - T_1 a_1^3}{a_2^3 - a_1^3}, \quad (3.116a)$$

$$2\mu B = \frac{1}{2} \frac{a_1^3 a_2^3 (T_2 - T_1)}{a_2^3 - a_1^3}. \quad (3.116b)$$

Insertion into (3.110a) and (3.110b) gives the radial T_{rr} and tangential components $T_{\theta\theta}, T_{\phi\phi}$ of the stress tensor as

$$T_{rr} = \frac{1}{a_2^3 - a_1^3} \left(T_2 a_2^3 - T_1 a_1^3 - \frac{a_1^3 a_2^3}{r^3} (T_2 - T_1) \right), \quad (3.117a)$$

$$T_{\theta\theta} = T_{\phi\phi} = \frac{1}{a_2^3 - a_1^3} \left(T_2 a_2^3 - T_1 a_1^3 + \frac{a_1^3 a_2^3}{2r^3} (T_2 - T_1) \right). \quad (3.117b)$$

Two assumptions will be made about the shell: The shell is thin compared to the bubble radius, and the shell is incompressible during the oscillations.

Thin Shell

The shell is thin compared to the bubble radius,

$$d_S \ll a, \quad (3.118)$$

where $d_S = d_S(t)$ is the instantaneous shell thickness. The shell thickness may vary as the bubble radius $a = a(t)$ oscillates. The outer shell radius is $a = a_2(t)$, see Figure 3.3. The inner shell radius a_1 is expressed as

$$a_1 = a - d_S = a(1 - \beta), \quad \text{with } \beta = \frac{d_S}{a} \ll 1. \quad (3.119)$$

The expressions (3.117a) and (3.117b) for T_{rr} and $T_{\theta\theta}$ are expanded in the small quantity β , keeping terms to the first order. This yields simplified expressions for the components of the stress tensor, valid for a thin shell

$$T_{rr} \approx T_1 + (T_2 - T_1) \left(\frac{1}{3\beta} + \left(\frac{a}{r} \right)^3 \left(1 - \frac{1}{3\beta} \right) \right), \quad (3.120a)$$

$$T_{\theta\theta} = T_{\phi\phi} \approx \frac{1}{2\beta} (T_2 - T_1). \quad (3.120b)$$

These expressions allow the radial stress difference across the thin shell T_{rr} to be expressed by the tangential stress $T_{\theta\theta}$ in the shell as

$$T_2 - T_1 = -\frac{2d_S T_{\theta\theta}}{a}. \quad (3.121)$$

This well-known result for the pressure difference across a thin shell can be derived from geometric arguments of pressure balance, and is found in text books of mechanical engineering.

A model for the tension $T_{\theta\theta}$ in the shell as a function of its radial strain can be postulated. This model can be used to obtain an expression for the stress difference $T_2 - T_1$ across the shell by (3.121).

Incompressible Shell

For an incompressible material, the volume dilation is zero, and the trace of the strain tensor ϵ disappears

$$\text{Tr } \epsilon = \nabla \xi = 0. \quad (3.122)$$

This reduces (3.106) to

$$\frac{\partial \xi}{\partial r} + 2\frac{\xi}{r} = 0. \quad (3.123)$$

(3.123) is the continuity equation for an incompressible material. It gives the relation between radius r and radial strain ξ as

$$\xi r^2 = \text{spatial constant} = \xi_1 a_1^2 = \xi_2 a_2^2, \quad (3.124)$$

where a_1 and a_2 are the inner and outer bubble radii, and ξ_1 and ξ_2 are the radial strains at the inner and outer bubble shell surfaces.

The difference in radial stress T_{rr} between the inner and outer shell surfaces, (3.114), can now be expressed by the strain ξ_2 at the outer shell surface alone

$$T_2 - T_1 = -4\mu \left(\frac{\xi_2}{a_2} - \frac{\xi_1}{a_1} \right) = -4\mu \frac{\xi_2}{a_2} \left(1 - \left(\frac{a_2}{a_1} \right)^3 \right). \quad (3.125)$$

A thin shell allows simplification of this expression, by use of (3.119)

$$\left(\frac{a_2}{a_1} \right)^3 \approx 1 + \frac{3d_S}{a}, \quad T_2 - T_1 \approx 12\mu \frac{d_S}{a} \frac{\xi_2}{a}. \quad (3.126)$$

The incompressible shell model implies that the shell thickness varies to keep its volume constant, so that,

$$a_2^3 - a_1^3 = a_{2e}^3 - a_{1e}^3 = \text{constant in time} \quad (3.127a)$$

which for a thin shell is approximated by

$$d_S a^2 = d_{Se} a_e^2 = \text{constant}, \quad (3.127b)$$

where the subscript e denotes values at equilibrium. By these approximations, the radial stress difference across a thin, incompressible shell can be expressed as

$$T_2 - T_1 = 12\mu \frac{d_{Se}}{a_e} \left(\frac{a_e}{a} \right)^4 \frac{\xi_2}{a_e}. \quad (3.128)$$

The radial strain ξ_2 is the value at the outer bubble surface

$$\xi_2 = \xi_2(t) = a(t) - a_e. \quad (3.129)$$

This gives the pressure difference across the shell as function of radius $a(t)$

$$T_2 - T_1 = 12\mu \frac{d_{Se}}{a_e} \left(\frac{a_e}{a} \right)^4 \left(\frac{a}{a_e} - 1 \right) \quad (3.130)$$

This result, for the incompressible shell, can also be derived from the result found by Church [22], by letting the shell thickness in his model become much smaller than the bubble radius.

3.4.2 Comments and Alternative Shell Models

The shell model was derived from the theory for a linear elastic material. The tension in the shell material was modeled by the Lamé coefficients, using the linear relation (3.107). The derivation that followed ended up with the nonlinear relation (3.130). The nonlinearity in this equation comes from the geometry of the system, assuming that the material properties stay linear. The validity of this combination of linear material and nonlinear geometry is questionable.

An alternative approach would be to postulate a relation between the radial strain and the pressure difference, and test this postulate against experiments.

In addition to the model (3.130), three other models for the stress-strain relation in the shell are suggested

Linear relation The pressure difference is proportional to the radial strain, giving

$$T_2 - T_1 = 12\mu \frac{ds_e}{a_e} \left(\frac{a}{a_e} - 1 \right). \quad (3.131)$$

This linear relation is appealing as a first order model. It predicts that the shell is equally stiff no matter how much it is expanded or con-

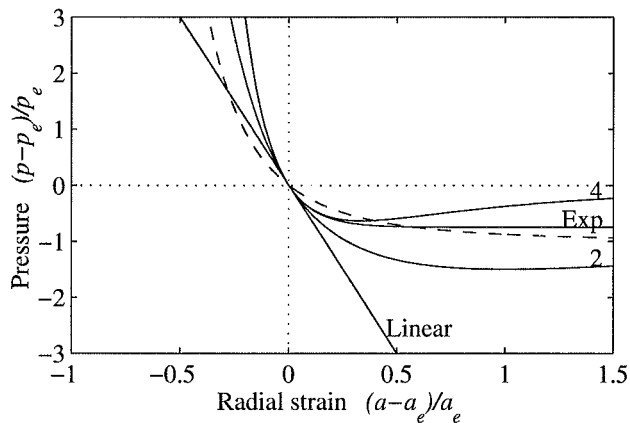


Figure 3.4. Pressure difference across the shell as function of radial strain. The curve marked '4' is the “linear material-nonlinear geometry” model, (3.130), '2' is the “intermediate” model, (3.132), 'Exp' is the exponential model, (3.133), with $x_0 = \frac{1}{8}$, and 'Linear' is the linear model (3.131). The dashed line is the pressure-strain relation for the gas, for comparison.

tracted. This models gives no softening of the shell as it expands, and it is suspected to overestimate the shell stiffness in expansion.

Intermediate model An intermediate between the “linear material-nonlinear geometry” model (3.130) and the linear model (3.131) is

$$T_2 - T_1 = 12\mu \frac{dS_e}{a_e} \left(\frac{a_e}{a}\right)^2 \left(\frac{a}{a_e} - 1\right) \quad (3.132)$$

This is a compromise between the two assumptions. The factor $(a_e/a)^2$ adds some softening to the shell as it expands, but not so much as in (3.130).

Exponential model An exponential relation between pressure and radial strain. This has been found successful in describing the elasticity of blood vessel walls. It was suggested used on the shell of contrast agents by Angelsen et al. [4]. This model is appealing as it gives softening in shell expansion. In addition, it gives a monotonic decrease in pressure as the shell is expanded. The exponential relation is formulated as

$$T_2 - T_1 = 12\mu \frac{dS_e}{a_e} x_0 (1 - e^{-x/x_0}), \quad x = \frac{a}{a_e} - 1. \quad (3.133)$$

The value of the parameter x_0 should be estimated from the stress-strain relationship for the shell at large expansions. Another estimate for x_0 can be found by comparing the exponential shell model with the model derived from linear material and nonlinear geometry, (3.130). x_0 can be selected so that the second derivatives at no strain, $x = 0$, are equal for the two models. This gives

$$x_0 = \frac{1}{8}. \quad (3.134)$$

It is difficult to assess which is the best of the proposed models without good experimental data at large amplitude oscillations. Experimental data from measurements at low radial amplitudes give estimates for the values around $x = 0$, hence, for the shear modulus μ .

The pressure-radius curves for these polynomial and exponential shell models are shown in Figure 3.4.

3.4.3 Shell Viscosity

In addition to elasticity, the shell material can also possess viscosity. Viscous forces in the shell cause energy to be absorbed as the bubble oscillates, and increases the damping of the oscillations.

The shell is modeled with a shear viscosity η_S . The radial component of the stress tensor in a newtonian liquid under spherically symmetric oscillations was found in (3.103) to

$$T_{rr} = -p - 4\eta_S \frac{u}{r}, \quad (3.135)$$

where T_{rr} is the radial component of the stress tensor, p is the hydrostatic pressure, η_S is the shear viscosity of the shell material, $u = u_r(r, t)$ is the radial velocity, and r is the radial coordinate.

The shell is modeled as incompressible, and the volume dilation is zero,

$$\nabla \mathbf{u} = 0, \quad (3.136)$$

which under spherical symmetry gives

$$\frac{\partial}{\partial r}(r^2 u) = 0, \quad \text{or} \quad ur^2 = \text{constant}. \quad (3.137)$$

This gives the relation between the instantaneous radii and velocities of the shell surfaces as

$$\dot{a}_1 a_1^2 = \dot{a}_2 a_2^2, \quad (3.138)$$

where a_1 is the radius of the inner and a_2 the radius of the outer shell surface. The stress difference across the shell due to viscosity is found from (3.135) to

$$T_2 - T_1 = -4\eta_S \left(\frac{\dot{a}_2}{a_2} - \frac{\dot{a}_1}{a_1} \right) = -4\eta_S \frac{\dot{a}}{a} \left(1 - \left(\frac{a}{a_1} \right)^3 \right), \quad (3.139)$$

where $a = a_2$. The shell is thin, with thickness $d_S \ll a$. This allows simplifications

$$\left(\frac{a}{a_1} \right)^3 = (1 - \beta)^{-3} \approx 1 + 3\beta, \quad \beta = \frac{d_S}{a} \ll 1. \quad (3.140)$$

This is inserted into (3.139), giving the pressure difference across the shell from shell viscosity as

$$T_2 - T_1 = 12\eta_S \frac{d_S}{a} \frac{\dot{a}}{a}. \quad (3.141)$$

The shell thickness and surface velocity are expressed relative to the equilibrium bubble radius a_e , and the instantaneous shell thickness d_S is replaced by its equilibrium value d_{Se} by (3.127b). The result is

$$T_2 - T_1 = 12\eta_S \frac{d_{Se}}{a_e} \left(\frac{a_e}{a} \right)^4 \frac{\dot{a}}{a_e}. \quad (3.142)$$

As for the shell stiffness models, (3.142) was derived assuming a constant, linear material property η_S . The nonlinear factor $(a_e/a)^4$ is a result of the geometry of the system. As for the shell elasticity, the validity of this approach is questionable. It may be argued that the nonlinear factor $(a_e/a)^4$ should best be removed, leaving only the first-order term. However, it is physically appealing to keep a factor that reduces the influence of the shell as the bubble expands.

An alternative is to postulate how the viscosity contribution from the shell changes with bubble radius, and eventually test and verify these postulates with experimental results.

As for the shell stiffness term, an exponential relation for the relation is postulated. This takes the form

$$T_2 - T_1 = 12\eta_S \frac{d_{Se}}{a_e} e^{-x/x_1} \frac{\dot{a}}{a_e}, \quad x = \frac{a}{a_e} - 1. \quad (3.143)$$

An estimate for the constant x_1 is proposed by setting it so that the first derivative of the exponential model equals the result from the “linear material-nonlinear geometry”, (3.142), for $x = 0$. This results in

$$x_1 = \frac{1}{4}. \quad (3.144)$$

The contributions to viscous shell damping for these models are compared in Figure 3.5.

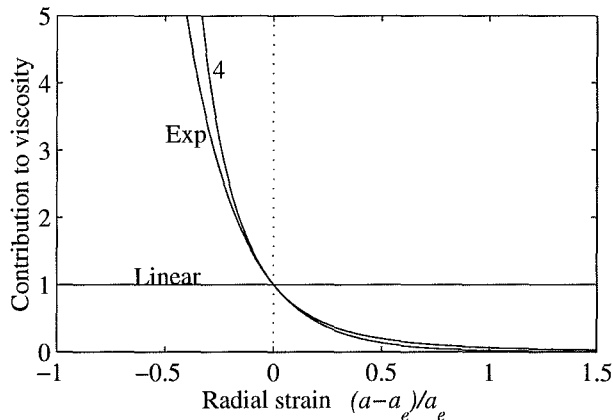


Figure 3.5. Relative contribution to shell viscosity as function of bubble radius. The curve marked '4' is the “linear material-nonlinear geometry” model, (3.142), 'Exp' is the exponential model, (3.143), with $x_1 = \frac{1}{4}$, and 'Linear' is a linear model.

3.4.4 Summary: Tension across the Shell

The models for tension across the shell due to elasticity and viscosity are summarized in the following four different models. The second Lamé coefficient μ_S of the shell, the shear modulus, is rewritten as G_S to avoid confusion with other quantities denoted by μ .

Linear material - nonlinear geometry

$$T_2 - T_1 = 12 \frac{d_{Se}}{a_e} \left(\frac{1}{1+x} \right)^4 (G_S x + \eta_S \dot{x}). \quad (3.145a)$$

Fully linearized model

$$T_2 - T_1 = 12 \frac{d_{Se}}{a_e} (G_S x + \eta_S \dot{x}). \quad (3.145b)$$

Intermediate model

$$T_2 - T_1 = 12 \frac{d_{Se}}{a_e} \left(\frac{1}{1+x} \right)^2 (G_S x + \eta_S \dot{x}). \quad (3.145c)$$

Exponential shell

$$T_2 - T_1 = 12 \frac{d_{Se}}{a_e} \left(G_S x_0 (1 - e^{-x/x_0}) + \eta_S e^{-x/x_0} \dot{x} \right), \quad (3.145d)$$

where

$$x = \frac{a - a_e}{a_e}, \quad \dot{x} = \frac{\dot{a}}{a_e}. \quad (3.145e)$$

3.5 Pressure in the Gas

The pressure p_g in the gas is calculated from a polytropic gas model. The oscillations of interest occur at Megahertz-frequencies, giving typical time scales less than a microsecond. It is assumed that no condensation or evaporation takes place during the oscillation cycle, and the effect of a constant vapor pressure is not included. The vapor pressure of water at body temperature is 6 kPa or 0.06 atmospheres [101]. This is in any case a small correction to the total gas pressure in the bubble.

The polytropic gas model assumes a relation between gas pressure and volume as

$$pV^\kappa = \text{constant} \quad (3.146)$$

where κ is the polytropic gas constant. For adiabatic oscillations, $\kappa = \gamma$, the adiabatic constant of the gas. For isothermal oscillations $\kappa = 1$. The validity of the polytropic assumption, the value of κ and the transition between adiabatic and isothermal oscillations has been studied by several authors for linear oscillations. A review of this was given in Chapter 2.

The polytropic law assumes the gas pressure to be uniform within the bubble. This is equivalent to saying that the velocity of the bubble surface is smaller than the speed of sound in the gas. At large radial oscillation amplitudes, the surface velocity can reach very high velocities during the compressional phase of the oscillation, violating this assumption. These high velocities will occur in a very small fraction of the oscillation cycle. In the following, the gas is always assumed to follow the polytropic law.

The value for κ is estimated from linear theory for the bubble diameter and driving frequency used. For the bubble diameters and frequencies most common in ultrasound contrast agent imaging, this causes $\kappa \approx 1.0$, that is, isothermal oscillations.

For a sphere, the polytropic gas law gives the pressure inside the bubble

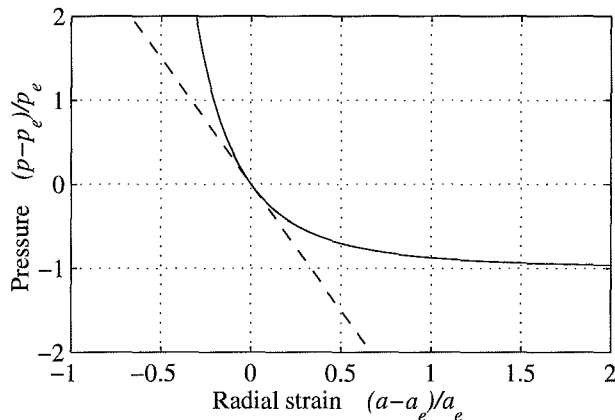


Figure 3.6. Pressure inside the bubble as function of radial strain. The curve is calculated from the polytropic gas law (3.148) with $\kappa = 1$. The pressure from a linear spring is plotted for comparison (dashed line).

as function of radius $a(t)$

$$p_g(a) = p_e \left(\frac{a_e}{a} \right)^{3\kappa}, \quad (3.147)$$

where p_e is the pressure in the gas at equilibrium. If there is no tension in the shell at equilibrium and no surface tension, p_e is equal to the hydrostatic pressure p_0 in the liquid

$$p_g(a) = p_0 \left(\frac{a_e}{a} \right)^{3\kappa}. \quad (3.148)$$

The gas acts a nonlinear spring. In compression, the bubble is stiffening, its pressure increases more than proportional with radial strain. In expansion, the gas is softening, the pressure decreases less than proportional with strain.

The pressure in the bubble is plotted in Figure 3.6, for $\kappa = 1$. For comparison, the pressure of a linear spring is plotted in the same figure.

3.6 Boundary Condition: Pressure at the Bubble Surface

The calculations in this chapter have resulted in

- An equation of motion for the liquid, selected from four alternative models. These equations contain the pressure $p_L(t)$ at the surface of the bubble.

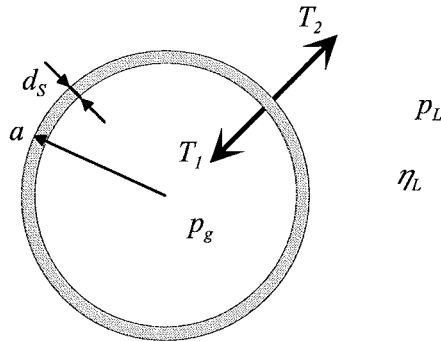


Figure 3.7. Boundary conditions at the inner and outer bubble shell surfaces. Illustration of the pressures and tensions acting at the shell.

- The added radial stress T_L at the bubble surface from viscous forces, (3.103).
- The difference in radial stress $T_2 - T_1$ across the shell, due to elastic and viscous forces in the shell, (3.145a) to (3.145d).
- The pressure p_g in the gas, calculated from a polytropic gas model (3.148).

The pressures and stresses are illustrated in Figure 3.7. The boundary conditions require continuity in radial stress at the shell-liquid and shell-gas interfaces. These boundary conditions are

$$\begin{aligned} T_L &= T_2 && \text{Continuity at outer shell surface.} \\ p_g &= -T_1 && \text{Continuity at inner shell surface.} \end{aligned} \quad (3.149)$$

The expressions for the stresses involved are

$$T_L = -p_L - 4\eta_L \frac{\dot{a}}{a} \quad \text{Stress at the bubble-liquid surface} \quad (3.150a)$$

$$T_2 - T_1 \quad \text{Stress difference across the shell} \quad (3.150b)$$

$$p_g = p_0 \left(\frac{a_e}{a} \right)^{3\kappa} \quad \text{Pressure in the gas} \quad (3.150c)$$

These equations are combined with the boundary conditions (3.149), giving an expression for the pressure $p_L(t)$ at the bubble surface

$$p_L = -4\eta_L \frac{\dot{a}}{a} - (T_2 - T_1) + p_0 \left(\frac{a_e}{a} \right)^{3\kappa}, \quad (3.151)$$

where the stress difference across the shell $T_2 - T_1$ is taken from one of the shell models in Chapter 3.4.4.

The effect of surface tension has not been included here. It is assumed that the shell reduces the surface tensions of both the gas-shell and the shell-liquid interfaces, so that these can be neglected. Typical dilution liquids used with ultrasound contrast agents, e.g. *Isoton II* and blood, have much lower surface tension than pure water.

3.7 Equations in Dimensionless Variables

The equation derived in the previous sections shall be applied to simulate the bubble response to a driving ultrasound pulse. The equations are rescaled to

dimensionless variables for numerical simulations on a computer. This rescaling reduces the number of parameters in the simulations and allows better control over the precision.

The rescaling is done by introducing the following new variables

Dimensionless time, radius and pressure

$$x = \frac{a - a_e}{a_e} \quad \text{Radial strain} \quad (3.152a)$$

$$\omega_0 = \sqrt{\frac{p_0}{\rho a_e^2}} \quad \text{Characteristic frequency} \quad (3.152b)$$

$$\tau = \omega_0 t \quad \text{Dimensionless time} \quad (3.152c)$$

$$x' = \frac{dx}{d\tau} = \frac{1}{\omega_0} \frac{dx}{dt} = \frac{\dot{x}}{\omega_0} \quad \text{Time differentiation} \quad (3.152d)$$

$$q = \frac{p}{p_0} \quad \text{Normalized pressure} \quad (3.152e)$$

Dimensionless liquid and shell parameters

$$\gamma = \frac{c}{a_e \omega_0} \quad \text{Normalized speed of sound} \quad (3.152f)$$

$$\nu_L = \eta_L \frac{\omega_0}{p_0} \quad \text{Shear viscosity of the liquid} \quad (3.152g)$$

$$\nu_S = \eta_S \frac{\omega_0 d_{Se}}{p_0 a_e} \quad \text{Shear viscosity of the shell} \quad (3.152h)$$

$$g_S = G_S \frac{d_{Se}}{p_0 a_e} \quad \text{Shear modulus of the shell} \quad (3.152i)$$

3.7.1 Pressure at the Bubble Surface

The pressure at the bubble wall is expressed by (3.151) as a sum of contributions from the gas, the pressure difference across the shell and the extra tension due to liquid viscosity.

Equation (3.151) for the pressure q_L at the bubble wall is reformulated to dimensionless variables as

$$q_L = -4\nu_L \frac{x'}{1+x} + q_S + q_g \quad \text{Pressure at the bubble surface,} \quad (3.153a)$$

$$q_S = -\frac{T_2 - T_1}{p_0} \quad \text{Pressure difference across the shell,} \quad (3.153b)$$

$$q_g = (1+x)^{-3\kappa} \quad \text{Pressure in the gas.} \quad (3.153c)$$

The derivatives of q_L are

$$q_1(x, x') = \frac{\partial q_L}{\partial x} = 4\nu_L \frac{x'}{(1+x)^2} + \frac{\partial q_S}{\partial x} - 3\kappa(1+x)^{-3\kappa-1} \quad (3.154a)$$

$$q_2(x, x') = \frac{\partial q_L}{\partial x'} = -4\nu_L \frac{1}{1+x} + \frac{\partial q_S}{\partial x'} \quad (3.154b)$$

Different models were postulated for the pressure difference q_S across the shell, see Chapter 3.4.2. These models are:

Linear shell

$$q_S = -12(g_S x + \nu_S x') . \quad (3.155a)$$

$$\frac{\partial q_S}{\partial x} = -12g_S \quad (3.155b)$$

$$\frac{\partial q_S}{\partial x'} = -12\nu_S \quad (3.155c)$$

Linear material - nonlinear geometry

$$q_S = -12 \frac{1}{(1+x)^4} (g_S x + \nu_S x') . \quad (3.155d)$$

$$\frac{\partial q_S}{\partial x} = -12 \left(g_S \left(\frac{1}{(1+x)^4} - \frac{4x}{(1+x)^5} \right) - \nu_S \frac{4x'}{(1+x)^5} \right) \quad (3.155e)$$

$$\frac{\partial q_S}{\partial x'} = -12\nu_S \frac{1}{(1+x)^4} \quad (3.155f)$$

Intermediate model

$$q_S = -12 \frac{1}{(1+x)^2} (g_S x + \nu_S x') . \quad (3.155g)$$

$$\frac{\partial q_S}{\partial x} = -12 \left(g_S \left(\frac{1}{(1+x)^2} - \frac{2x}{(1+x)^3} \right) - \nu_S \frac{2x'}{(1+x)^3} \right) \quad (3.155h)$$

$$\frac{\partial q_S}{\partial x'} = -12\nu_S \frac{1}{(1+x)^2} \quad (3.155i)$$

Exponential shell

$$q_S = -12 \left(g_S x_0 (1 - e^{-x/x_0}) + \nu_S e^{-x/x_1} x' \right) \quad (3.155j)$$

$$\frac{\partial q_S}{\partial x} = -12 \left(g_S e^{-x/x_0} - \nu_S \frac{1}{x_1} e^{-x/x_1} x' \right) \quad (3.155k)$$

$$\frac{\partial q_S}{\partial x'} = -12\nu_S e^{-x/x_1} . \quad (3.155l)$$

3.7.2 Rayleigh-Plesset Model

The Rayleigh-Plesset equation, (3.36) on page 65, is converted to dimensionless variables, giving

$$x''(1+x) + \frac{3}{2}x'^2 + 1 + q_i - q_L = 0. \quad (3.156)$$

This is solved for the highest order derivative of x ,

$$x'' = \frac{-1}{1+x} \left(\frac{3}{2}x'^2 + 1 + q_i - q_L \right). \quad (3.157)$$

Equation (3.156) is converted to a set of first order ordinary differential equations, suitable for numerical simulation on a computer. These are written on vector form as

$$\begin{aligned} \mathbf{x} &= \begin{bmatrix} x_1 \\ x_2 \end{bmatrix} = \begin{bmatrix} x(\tau) \\ x'(\tau) \end{bmatrix} \\ \mathbf{x}' &= \begin{bmatrix} x'_1 \\ x'_2 \end{bmatrix} = \begin{bmatrix} x' \\ x'' \end{bmatrix} = \begin{bmatrix} x_2 \\ f(x_1, x_2) \end{bmatrix} \end{aligned} \quad (3.158)$$

This gives the following set of first order equations

$$\begin{aligned} x'_1 &= x_2 \\ x'_2 &= \frac{-1}{1+x_1} \left(\frac{3}{2}x_2^2 + 1 + q_i - q_L \right). \end{aligned} \quad (3.159)$$

The scattered pressure in the far field of the bubble is taken from (3.41). Written in dimensionless variables, the far-field scattered pressure $q_S(\tau) = p_S(a_e, t)/p_0$ at distance equal to the equilibrium radius of the bubble, is

$$q_s = (1+x) \left(\frac{1}{2}x'^2 + q_L - 1 - q_i \right). \quad (3.160)$$

The numerical ODE solver returns x and x' . All the quantities needed to calculate q_S from (3.160) are calculated when simulating the differential equation.

3.7.3 Trilling Model

Trilling's model, including a driving acoustic field, (3.60) on page 70, is converted to

$$\begin{aligned} x''(1+x) \left(1 - 2\frac{x'}{\gamma} \right) + \frac{3}{2}x'^2 \left(1 - \frac{4}{3}\frac{x'}{\gamma} \right) - \frac{1}{\gamma}(1+x)q'_L \\ + \frac{1}{\gamma}(1+x)q'_i + 1 + q_i - q_L = 0. \end{aligned} \quad (3.161)$$

The pressure at the bubble wall q_L is selected from one of the models in Chapter 3.7.1.

Equation (3.161) is rewritten in terms of the derivatives of q_L with respect to x and x'

$$x''(1+x)\left(1-2\frac{x'}{\gamma}\right) + \frac{3}{2}x'^2\left(1-\frac{4}{3}\frac{x'}{\gamma}\right) - \frac{1}{\gamma}(1+x)\left(\frac{\partial q_L}{\partial x}x' + \frac{\partial q_L}{\partial x'}x''\right) + \frac{1}{\gamma}(1+x)q'_i + 1 + q_i - q_L = 0. \quad (3.162)$$

This equation is solved for the highest order derivative of x

$$x'' = -\frac{1}{q_3}\left(\frac{3}{2}x'^2\left(1-\frac{4}{3}\frac{x'}{\gamma}\right) - \frac{1}{\gamma}(1+x)q_1x' + \frac{1}{\gamma}(1+x)q'_i + 1 + q_i - q_L\right) \quad (3.163)$$

with

$$q_1(x, x') = \frac{\partial q_L}{\partial x} \quad (3.164a)$$

$$q_2(x, x') = \frac{\partial q_L}{\partial x'} \quad (3.164b)$$

$$q_3(x, x') = (1+x)\left(1-2\frac{x'}{\gamma}\right) - \frac{1}{\gamma}(1+x)q_2. \quad (3.164c)$$

For computer simulations, these equations are rewritten as a set of first order ODEs, giving

$$\begin{aligned} x'_1 &= x_2 \\ x'_2 &= \frac{-1}{q_3}\left(\frac{3}{2}x_2^2\left(1-\frac{4}{3}M\right) - \frac{1}{\gamma}(1+x_1)q_1x_2 + \frac{1}{\gamma}(1+x_1)q'_i + 1 + q_i - q_L\right), \end{aligned} \quad (3.165)$$

with

$$q_3 = (1+x_1)\left(1-2M\right) - \frac{1}{\gamma}(1+x_1)q_2 \quad (3.166a)$$

$$M = \frac{x_2}{\gamma} \quad (3.166b)$$

The pressure q_L at the bubble wall and its derivatives $q_1 = \frac{\partial q_L}{\partial x}$ and $q_2 = \frac{\partial q_L}{\partial x'}$ are taken from the expressions in Chapter 3.7.1.

The scattered pressure in the far field of the bubble is taken from (3.66). This is rewritten to dimensionless variables. The far-field scattered pressure $q_s(\tau)$ calculated at distance equal to the equilibrium radius of the bubble is

$$q_s = p_s(a_e, t)/p_0 = (1+x)(q_L - 1 - q_i + \frac{1}{2}x'^2). \quad (3.167)$$

This result is identical to that from the Rayleigh-Plesset model, (3.160).

3.7.4 Keller-Miksis Model

The Keller-Miksis equation, (3.79) on page 73, is in dimensionless variables

$$x''(1+x)(1-M) + \frac{3}{2}x'^2(1 - \frac{1}{3}M) - (1+M)(q_L - 1 - q_i) - \frac{1}{\gamma}(1+x)q'_L = 0. \quad (3.168)$$

The driving pressure q_i is to be taken at time $t + a/c$, or $\tau + (1+x)/\gamma$. The pressure q_L at the bubble surface is taken from one of the models in Chapter 3.7.1. The equation is solved for the highest order derivative of x expressed as function of the derivatives of q_L with respect to x and x'

$$x'' = -\frac{1}{q_3} \left(\frac{3}{2}x'^2(1 - \frac{1}{3}M) - (1+M)(q_L - 1 - q_i) - \frac{1}{\gamma}(1+x)q'_L \right), \quad (3.169)$$

with

$$q_1(x, x') = \frac{\partial q_L}{\partial x} \quad (3.170a)$$

$$q_2(x, x') = \frac{\partial q_L}{\partial x'} \quad (3.170b)$$

$$q_3(x, x') = (1+x)(1-M) - \frac{1}{\gamma}(1+x)q_2, \quad (3.170c)$$

$$M = \frac{x'}{\gamma}. \quad (3.170d)$$

The scattered pressure in the far field of the bubble is taken from (3.87). The far-field scattered pressure $q_s(\tau)$, calculated at distance equal to the equilibrium radius of the bubble, is

$$q_s = p_s(a_e, t)/p_0 = (1+x)(q_L - 1 - q_i + \frac{1}{2}x'^2). \quad (3.171)$$

The pressure q_s found from this expression is at normalized time $\tau - x/\gamma$.

3.7.5 Modified Rayleigh-Plesset Model

The Rayleigh-Plesset equation modified to include radiation damping, (3.89) on page 76, is converted to dimensionless variables, giving

$$x''(1+x) + \frac{3}{2}x'^2 + 1 + q_i - q_L - \frac{1}{\gamma}(1+x)q'_L = 0. \quad (3.172)$$

The pressure q_L at the bubble surface is taken from one of the models in Chapter 3.7.1. The equation is solved for the highest order derivative of x

$$x'' = -\frac{1}{q_3} \left(\frac{3}{2}x'^2 + 1 + q_i - q_L - \frac{1}{\gamma}(1+x)q_1x' \right), \quad (3.173)$$

with

$$q_1(x, x') = \frac{\partial q_L}{\partial x} \quad (3.174a)$$

$$q_2(x, x') = \frac{\partial q_L}{\partial x'} \quad (3.174b)$$

$$q_3(x, x') = (1+x) - \frac{1}{\gamma}(1+x)q_2. \quad (3.174c)$$

The scattered pressure in the far field of the bubble is identical to the results for the Rayleigh-Plesset model, (3.160). The far-field scattered pressure $q_s(\tau)$, calculated at distance equal to the equilibrium radius of the bubble, is

$$q_s = \frac{p_s(a_e, t)}{p_0} = (1+x)(q_L - 1 - q_i + \frac{1}{2}x'^2). \quad (3.175)$$

3.7.6 Reconstitution of Dimensional Variables

The radius $a(t)$ and velocity $\dot{a}(t)$ as function of time t are reconstituted from the dimensionless variables τ , $x(\tau)$ and $x'(\tau)$ by

$$t = \frac{\tau}{\omega_0}, \quad (3.176a)$$

$$a(t) = a_e(1 + x(t)), \quad (3.176b)$$

$$\dot{a}(t) = a_e\omega_0 \frac{dx}{d\tau} = a_e\omega_0 x'. \quad (3.176c)$$

The scattered pressure $p_s t$ in the far-field of the bubble is

$$p_s = \frac{a_e}{r} p_0 q_s, \quad (3.176d)$$

where r is the radial distance from the bubble center. The scattered pressure is normally calculated for a reference distance $r = r_0 = 1\text{m}$.

Chapter 4

Measurement Systems

4.1 Acoustic Attenuation

Acoustic attenuation measured as function of frequency is the basic method used to characterize the contrast agents. The attenuation spectra give information about the resonance frequency and damping, or Q-value, of the bubbles as oscillators.

The acoustic attenuation through a suspension of contrast agent shows a simple, monotonic variation with concentration and extinction cross section, provided the concentration of bubbles is not too high. This can be compared with the scatter from a region within the contrast agent suspension. The scattered echoes depend on the combined effect of the scatter from the bubbles and attenuation from bubbles in the sound path between the transducer and the region studied.

The attenuation introduced by the bubbles is measured by comparing measurements without and with contrast agent in the sound path. The measurement without contrast agent gives a reference which is used to compensate for the frequency response of the transducers and for characteristics of the sound path.

The attenuation measurements are for basic characterization of the agent properties. There is no simple relationship between attenuation level and performance as contrast agent. For more direct measurements of the efficiency of the agent, acoustic backscatter is measured, as described in the following section.

4.1.1 Measurement of Attenuation Spectra

System Setup

The measurement system for acoustic attenuation spectra is based on a method described by de Jong et al. [29]. The system illustrated in Figure 4.1. The equipment consist of a combined pulser and receiver (*Panametrics 5800PR*, Panametrics Inc., Waltham, Mass., USA), a coaxial cable relay for selecting transducers (*CX-600N*, Toyo Tsusho Electric Co. Ltd., Tsuchiura, Japan), two transducers (*Panametrics Videoscan*, exchangeable) and a digital oscilloscope (*LeCroy 9310A*, LeCroy Corporation, Chestnut Ridge, New York, USA).

The transducers can be exchanged to select the frequency range most appropriate for the contrast agent being investigated. Possible transducers are listed in Table 4.1. The mounting brackets were made to fit the *Standard Case Style Panametrics Immersion* transducers. All the transducers are unfocused. Most measurements are done using the *Panametrics Videoscan V382-SU* 3.5 MHz and *V326-SU* 5.0 MHz transducers.

The pulser/receiver and oscilloscope are connected to a PC-type computer via a GPIB-board (*AT-GPIB*, National Instruments Inc, Austin, Texas, USA). The coaxial relay is controlled by a digital in/out board (*PC-DIO24*, National Instruments Inc.). The measurement system is controlled and digitized results are acquired by programs written in the programming language *C*, using the software package *LabWindows* (National Instruments Inc.).

The two transducers are mounted in parallel in a water tank made of *Per-*

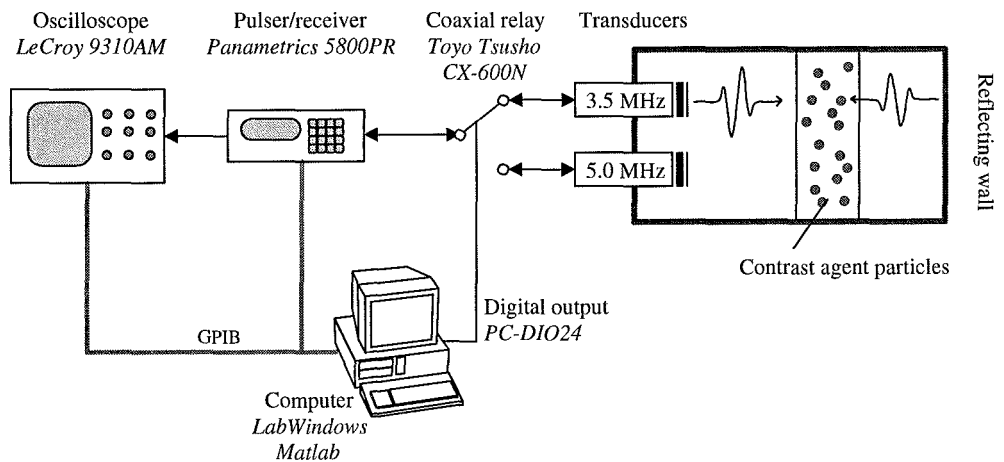


Figure 4.1. Measurement system for measuring acoustic attenuation spectra.

Table 4.1. Transducers used to measure acoustic attenuation spectra. All are of type *Panametrics Immersion Videoscan*, in *Standard Case Style*.

Center frequency [MHz]	Aperture diameter		Panametrics part no.
	[mm]	[inches]	
1.0	13	0.5	V-303-SU
2.25	13	0.5	V-306-SU
3.5	13	0.5	V-382-SU
3.5	10	0.375	V-383-SU
5.0	10	0.375	V-326-SU
5.0	6	0.25	V-310-SU

spec. The sample cell has thin *Teflon* membranes acting as acoustic windows. The cell is placed 10 cm from the transducer faces and is 3.15 cm long. The back wall of the water tank is used as an acoustic reflector. This was positioned 15 cm from the transducer faces.

Sample Preparation

The sample cell is filled with 55 ml *Isoton II* (Coulter Electronics Ltd., Luton, UK). *Isoton II* is a standardized dilution liquid, used in hospital laboratories. It is a 0.9% saline solution with a phosphate pH-buffer and a detergent to reduce surface tension.

The contrast agent is diluted in the *Isoton II* in the sample cell. The concentration of contrast agent is adapted to the size and concentration of the bubbles in the agent. Best results are obtained when the attenuation from the agent is between 15 and 20 dB, or around 3 dB/cm. This typically means that the contrast agent is diluted by a factor 10^3 to 10^4 . This concentration and attenuation level is common in clinical use of the agents.

The results of the measurements are calculated as dB/cm and are normalized to a standardized dilution of 1:1000, assuming linearity with the concentration.

Acquisition of Pulses

The transducers are excited by short pulses from the pulser/receiver, sending broadband ultrasound pulses through the sample cell. The repetition rate is 50 pulses per second. The transmitted pulses traverse through the water tank and sample cell, and are reflected at the back wall of the tank. The reflected

pulses are received by the transmitting transducer. On their path, the pulses pass through the sample cell twice, giving a total sound path length through the contrast agent equal to 6.3 cm.

The received signals are amplified in the receiver section of the pulser/-receiver and recorded by the oscilloscope. The oscilloscope is set to sample only the reflection from the back wall of the sample cell, using delayed trigger and time-gating. The received pulses are digitized in the oscilloscope at sample rate 25 Msa/s. Results are averaged over 50 successive pulses to improve signal to noise ratio. The digitized pulses are transferred via the GPIB interface to the computer and are stored on the computer disk for processing.

Figure 4.2 shows an example of received pulses and their power spectra, without and with contrast agent in the sample cell. The acquisition of the pulses is illustrated in the flowchart in Figure 4.3. The results acquired are displayed real time on the computer screen during the measurement sequence.

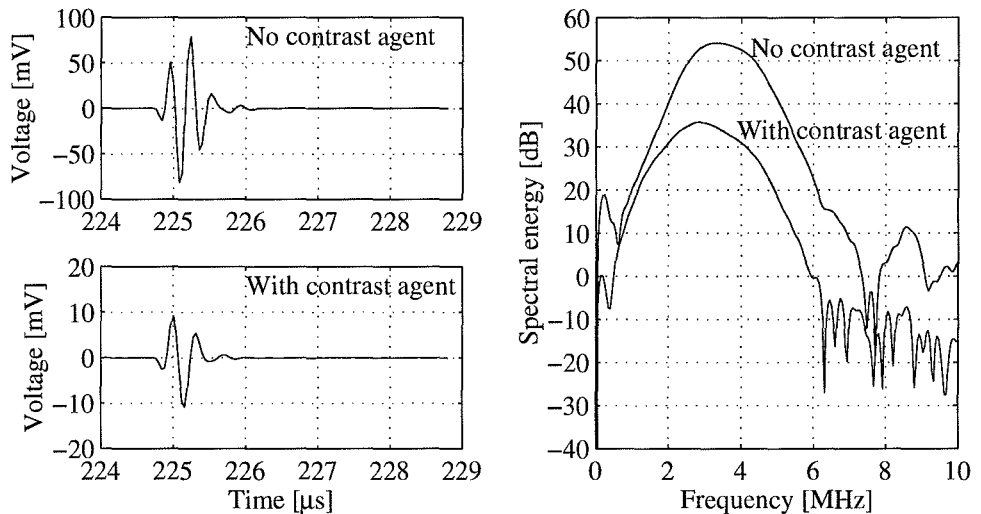


Figure 4.2. Example of pulses measured with the 3.5 MHz transducer. The left diagrams show pulses received after reflections from the back wall, traversing the sample cell twice. The upper pulse is from a reference measurement with no contrast agent in the sample cell, the lower pulse is received with contrast agent in the cell. The right diagram shows the power spectra of the two pulses. This 3.5 MHz transducer was used to evaluate spectra in the frequency range from 1.5 to 5.0 MHz.

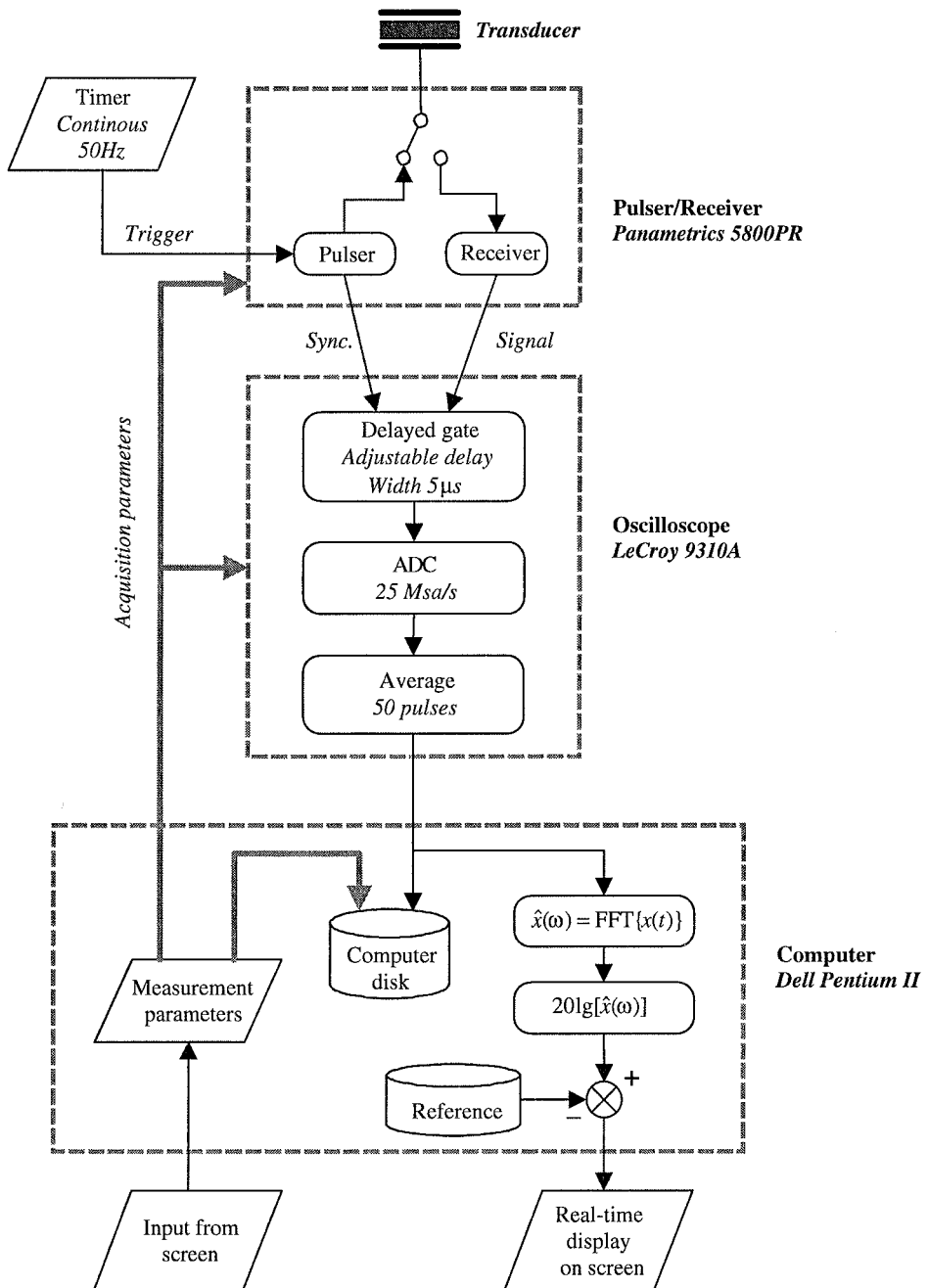


Figure 4.3. Attenuation measurements. Acquisition of ultrasound pulses reflected from back wall.

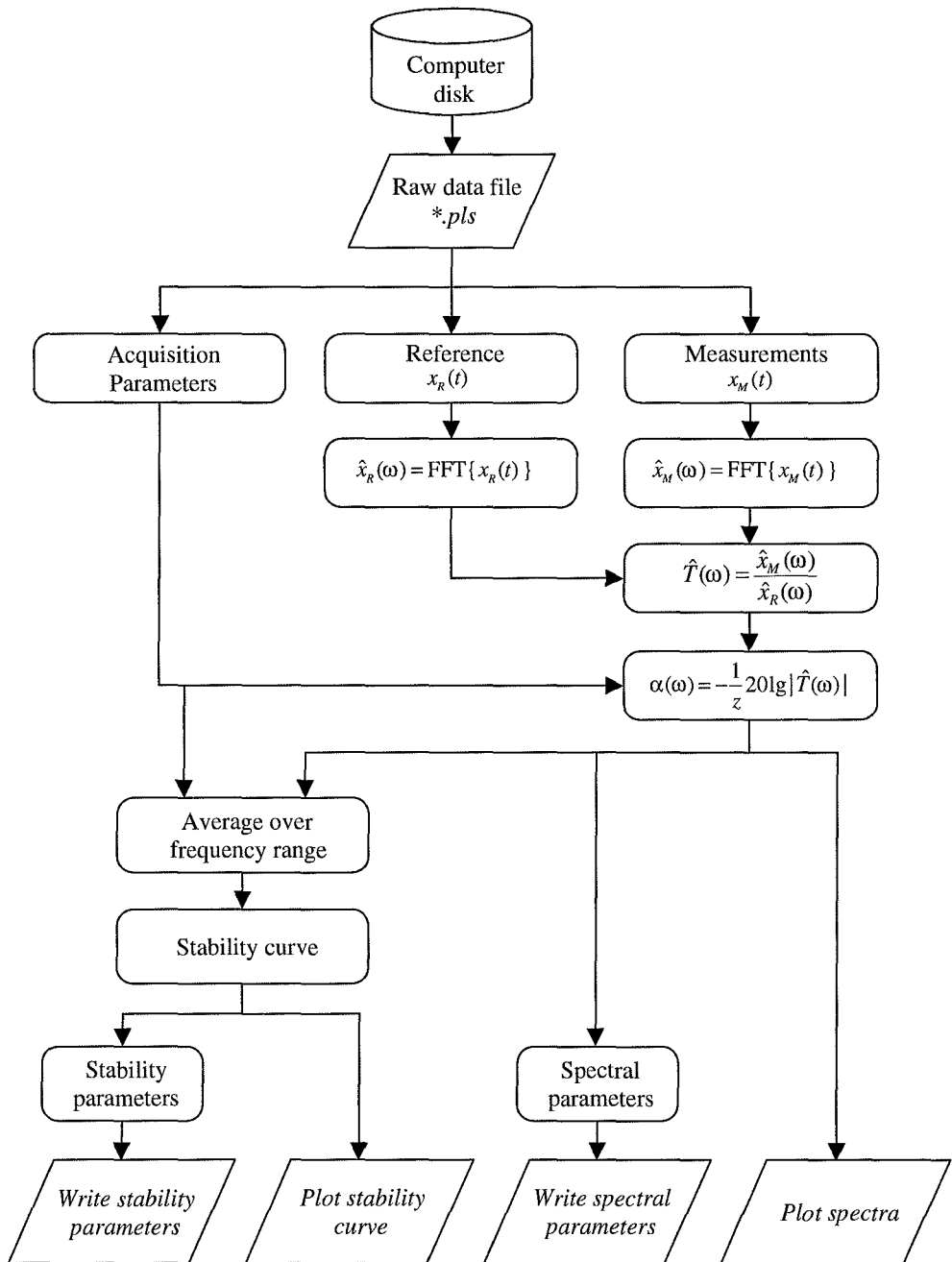


Figure 4.4. Attenuation measurements. Processing of results.

Calculation of Results

The attenuation spectra are calculated from the acquired pulses using the software package *Matlab* (The Math Works Inc., Natick, Mass., USA). The signal processing is illustrated in Figure 4.4.

Power spectra are calculated from FFT on the pulses. The part of the spectrum containing useful information for each transducer is singled out. The 3.5 MHz transducer displayed in Figure 4.2 is used between 1.5 and 5.0 MHz. Spectra are always measured with two transducers of different center frequency. The overlap region, where both transducers provide spectral information, gives a test of the validity of the results, as the different transducers should give equal results here.

The power spectra measured with contrast agent present are normalized by dividing them with spectra measured without contrast agent in the sound path. This corrects for the frequency responses of the transducers and for propagation path characteristics.

Several spectra are measured at fixed time intervals. The development with time is plotted in a “stability curve” showing how the contrast agent response changes with time.

4.1.2 Sensitivity to Hydrostatic Pressure

Stability under hydrostatic pressure is an important feature of a contrast agent.

Hydrostatic pressure can drive gas out of the bubbles, causing them to dissolve. The liquid in which the bubbles are suspended has a certain ability to dissolve gas. Normally, the partial pressures of dissolved gases in the liquid will be in equilibrium with the atmospheric pressure. In the blood, the contents of dissolved gases is regulated by the respiratory system [31].

Diffusion constants of gas molecules in water are around 2×10^{-9} m²/s for most common gases [102]. This makes gas diffusion through a liquid a slow process, diffusion over centimeters typically takes hours. Over distances corresponding to the dimensions of a bubble, a few μm , the diffusion takes only fractions of a second [41], and the gas inside the bubble can rapidly be dissolved in the liquid. Convection in the liquid will speed up the diffusion process considerably, especially over larger distances, that is, centimeters.

When the atmospheric pressure is increased, the hydrostatic pressure in the liquid and the pressure inside the bubbles increase rapidly. But the pressures of dissolved gases in the liquid will remain almost constant, due to the slow gas diffusion in the liquid. The gas in the interior of the bubble will no longer be in equilibrium with the dissolved gases in the liquid. This can drive gas out of the bubble into the liquid by diffusion, and cause the bubble to dissolve.

Table 4.2. Solubility of gases in water at 37°C, measured as volume gas per volume liquid. The partial pressure of the gas is 1 atmosphere minus the vapor pressure of water. The volume fraction ϕ_s is calculated from the mass solubility m_s by $\phi_s = \frac{m_s RT}{Mp}$, where R is the gas constant, $T=310$ K is the absolute temperature, M is the molar mass of the gas, and $p=95$ kPa is the pressure of the gas. Data from Aylward and Findlay [6].

Gas		Solubility Volume fraction ϕ_s [%]
Nitrogen	N ₂	1.6
Oxygen	O ₂	3.1
Carbon dioxide	CO ₂	83
Helium	He	0.95
Argon	Ar	3.4
Methane	CH ₄	3.3
Ethane	C ₂ H ₆	4.5
Perfluoromethane	CF ₄	0.52
Sulfur hexafluoride	SF ₆	0.69

The shell enclosing the gas in the bubble will slow down or stop this process.

In clinical use, the contrast agents will be exposed to hydrostatic overpressures in two different situations.

During injection In the syringe, before the agent has been diluted in blood, the volume fraction of gas is typically around 1%, which is very high. The pressure in the syringe can reach a few hundred mmHg. Under these conditions, the amount of gas in the bubbles is normally high enough to saturate the dilution liquid at this increased pressure. The agent's response to the pressure in the syringe has not been studied in this thesis.

In the blood After the agent is injected, it is rapidly diluted in the blood of the patient. The dilution factor may vary a great deal, both between different agents and depending on the method of use. Typically, the agent will be diluted a factor 10^3 to 10^4 when reaching the left ventricle of the heart. This gives gas volume fractions in the order of 10^{-5} to 10^{-6} . In the heart and arteries, the agents are exposed to the systolic blood pressure. This pressure is typically 120 mmHg, but may exceed 200 mmHg in some persons [32].

In this high dilution, the amount of gas in the contrast agent is low compared to the solubility of gases in the blood, see Table 4.2. Dissolution of the contrast agent bubbles and release of the gas inside them will have a small influence on the amount of dissolved gases in the blood.

Blood pressure is most commonly measured in *millimeters of mercury*, mmHg. Since the over-pressure test is intended to be compared with systolic blood pressures, the pressure applied in this test is also measured in *mmHg*. All other pressures in this thesis are measured in *Pascal*, Pa. The relationship between Pa and mmHg is

$$760 \text{ mmHg} = 101.3 \text{ kPa} , \quad 1 \text{ mmHg} = 133.3 \text{ Pa} . \quad (4.1)$$

This relation is plotted in Figure 4.5.

Measurement System

The response to hydrostatic pressure is tested by measuring acoustic attenuation spectra under pressure. Changes in overall attenuation level and in resonance frequency are registered when the agents are exposed to pressure.

The pressure test system is illustrated in Figure 4.6. It is based on the attenuation measurement system shown in Figure 4.1. The tank is now closed, making the tank with sample cell and transducers into an airtight pressure chamber. The interior of the tank is connected via a tube to a 3-way magnetic valve. This valve is connected so that the interior of the tank is either open to

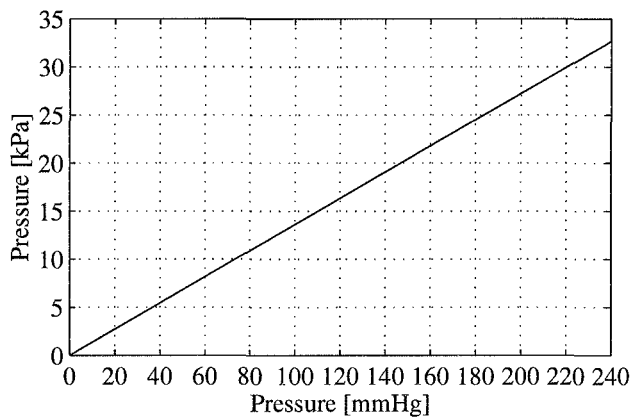


Figure 4.5. Relationship between the two pressure units *mmHg* and *Pa*. One atmosphere equals 760 mmHg or 101 kPa.

the atmosphere or to a pressure reservoir, made of a plastic bottle containing compressed air. The valve is opened and closed by the computer via the digital in/out board (*PC-DIO-24*, National Instruments Inc.).

The sample preparation, acquisition of pulses and calculation of results is identical to that described in the section about acoustic attenuation measurements, Chapter 4.1.1.

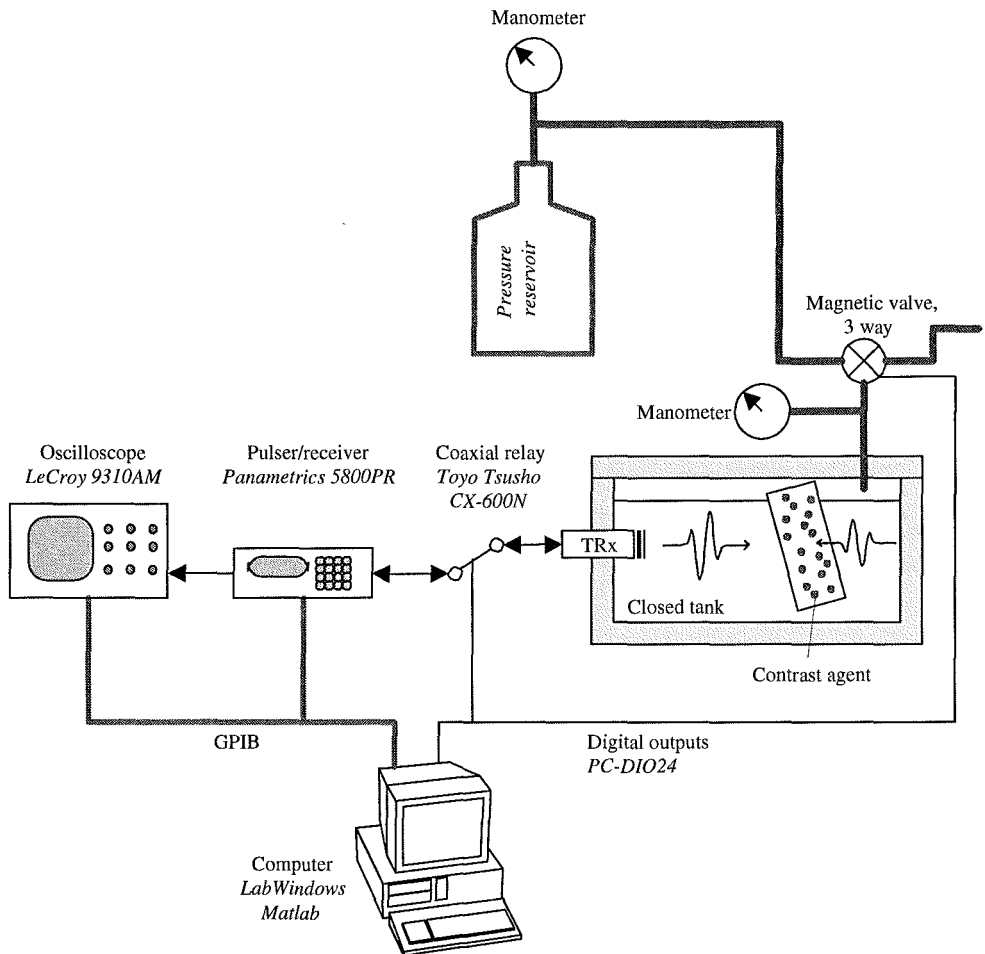


Figure 4.6. Pressure sensitivity test. System for measuring acoustic attenuation spectra under increased hydrostatic pressure.

Measurement Sequence

Pressure stability is measured according to the following sequence:

Before pressure The magnetic valve is in “position 1”, so that the tank is open to the atmosphere. 3 attenuation spectra are measured at 10 seconds intervals.

During pressure The magnetic valve is switched to “position 2”, where the tank is open to the the pressure reservoir. The pressure in the tank increases to the specified value, typically 120 mmHg over atmospheric pressure. 3 or more attenuation spectra are measured at 10 seconds intervals.

After pressure The magnetic valve is released to “position 1”. The tank is open to the atmosphere again, and 3 attenuation spectra are measured at 10 seconds intervals.

This procedure gives 3 attenuation spectra measured before the pressure is applied, 3 or more spectra during pressure, and 3 spectra measured after the pressure was released. The results of the pressure test are plotted in two graphs:

Attenuation vs. frequency The attenuation spectra measured before, during and after exposure to pressure are plotted in one diagram. Different line styles are used to mark the different situations.

Attenuation vs. time The attenuation at the center frequencies of the transducers are plotted as function of time. The time points where pressure was applied and released are marked in the diagram.

An example of results from the pressure test system is displayed in Figure 4.7.

4.2 Acoustic Backscatter

Diagnostic ultrasound imaging is based on acoustic backscatter. An ultrasound pulse is transmitted into the body, and the received echoes are used to form an image of the internal structures. Hence, measurement of backscattered power in some form is important for characterization of ultrasound contrast agents.

Several transmission schemes and signal processing algorithms are used to process the received echoes and form an image. The most common imaging modus is *B-mode*: One focused ultrasound pulse is transmitted for each scan-line, and the power of the received echoes is used to form an image. When

Acoustic Attenuation Measurement

10.03.2000 22:54

Measurement program version 4.40

Date	13.08.1996	Dilution vol.	55.0 ml
Operator	GEH	Contrast agent vol.	10.0 ul
Journal no.	FKA 014/16-1	Dilution factor	5500
Sample ID	FF 608902	Path length	6.3 cm
Comment	ASPK96358	Over-pressure	120.0 mmHg
Data file(s)	oh135001.pl1 oh135001.pl2		

Results normalized to dilution 1:1000

Transducer frequency		3.5 MHz	5.0 MHz
Frequency giving max. att.	[MHz]	4.1	4.3
Maximum attenuation	[dB/cm]	28.56	30.21
Attenuation at 2.0 MHz	[dB/cm]	7.66	NaN
Attenuation at 3.5 MHz	[dB/cm]	25.26	25.00
Attenuation at 5.0 MHz	[dB/cm]	26.64	27.68
Attenuation before pressure	[%]	100	100
Attenuation after pressure	[%]	97	100
Maximum att. during pressure	[%]	59	86
Minimum att. during pressure	[%]	53	86
Half life	[s]	Inf	Inf

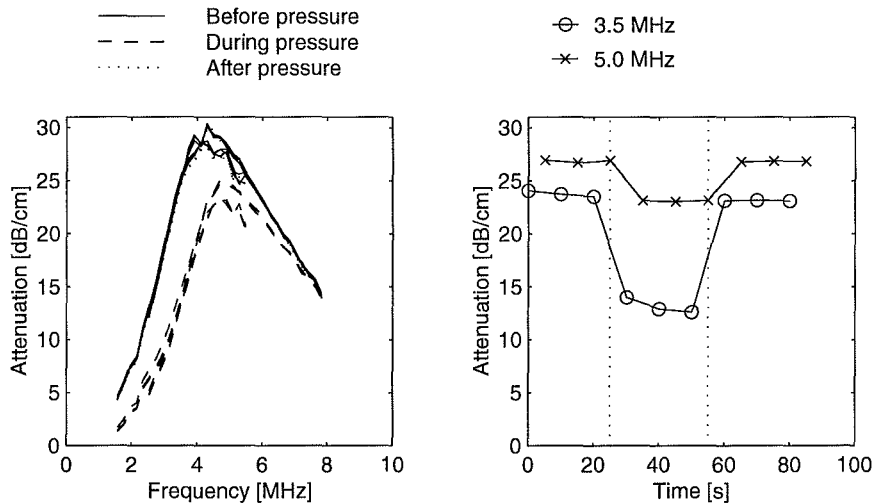


Figure 4.7. Example of a result report from the pressure test system. Acoustic attenuation spectra measured before, during and after exposure to hydrostatic pressure.

using contrast agents, *2nd harmonic imaging* in some situations seems to give better results than imaging at the transmit frequency. *Pulse inversion* is another imaging scheme that seems promising when using contrast agents. These and other nonlinear imaging methods are described in Chapter 3.

Hence, several different imaging methods may be used in conjunction with contrast agents. Several more probably exist, not yet invented. A characterization system to measure backscatter from the contrast agents has to be flexible, allowing testing of different known and potential new techniques.

To obtain this, a system has been constructed that transmits pulses of defined shape into a contrast agent sample, and then captures the RF signals scattered from them. This system consists of a programmable function generator to define the pulses (*Wavetek 395*, Wavetek Wandel Goltermann, Research Triangle Park, NC, USA), a power amplifier (*ENI 2100L*, ENI, Rochester, New York, USA), a variable gain receiver with high- and lowpass filters (*Panametrics 5800PR*, Panametrics Inc., Waltham, Mass., USA), and a digital storage oscilloscope to capture the RF traces (*LeCroy 9310AM*, LeCroy Corporation, Chestnut Ridge, New York, USA). Several different transducers can be used

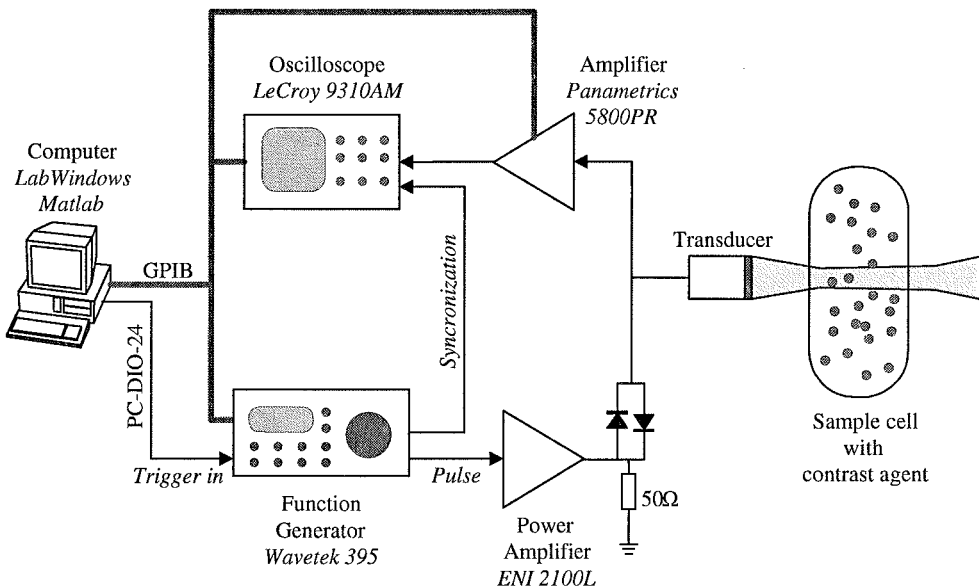


Figure 4.8. Setup for sampling RF traces backscattered from the contrast agent. Various different transducers may be used. The displayed setup shows use of one single element transducer for both transmit and receive, but separate transducers for transmit and receive may also be used.

Table 4.3. Sampling RF results. Oscilloscope sampling parameters.

Time/Div. [μs]	Trace length [μs]	No. of points per trace	Sample rate [Msa/s]
0.2	2	200	100
0.5	5	500	100
1.0	10	1000	100
2.0	20	2000	100
5.0	50	2500	50
10	100	2500	25
20	200	2000	10
50	500	2500	5

for transmit and receive.

The system transmits a predefined number of shaped ultrasound pulses into a sample of contrast agent, at a specified pulse repetition rate. The echoes received from the contrast agent are digitized and saved to the computer disk. Sample parameters and equipment settings are also stored with the results.

The typical setup used in these measurements is displayed in Figure 4.8. A flow scheme for the transmit and acquisition of pulses is illustrated in Figure 4.9. The system is controlled by a PC-type computer. This is connected to the external components via a GPIB interface (*AT-GPIB*, National Instruments Inc.) and a digital in/out board (*PC-DIO-24*, National Instruments Inc.). The software used to define transmit pulses and to acquire traces is written in the programming language *C* using the *LabWindows* development package (National Instruments Inc.). The operation of the system is controlled by a graphical user interface, shown in Figure 4.10.

Trigger pulses The trigger pulses are defined by the clock in the computer.

The accuracy of the timer is 1 kHz, limiting the maximum pulse repetition rate to about 200 pulses/s. The trigger pulses are transferred to the function generator using an output from the *PC-DIO-24* digital in/out board.

The accuracy and maximum rate of the trigger has been satisfactory for the experiments so far. The maximum trigger rate can be increased by installing a more sophisticated digital timer board into the computer. The *PC-DIO-24* board was used because this board was already installed into the computer for other purposes.

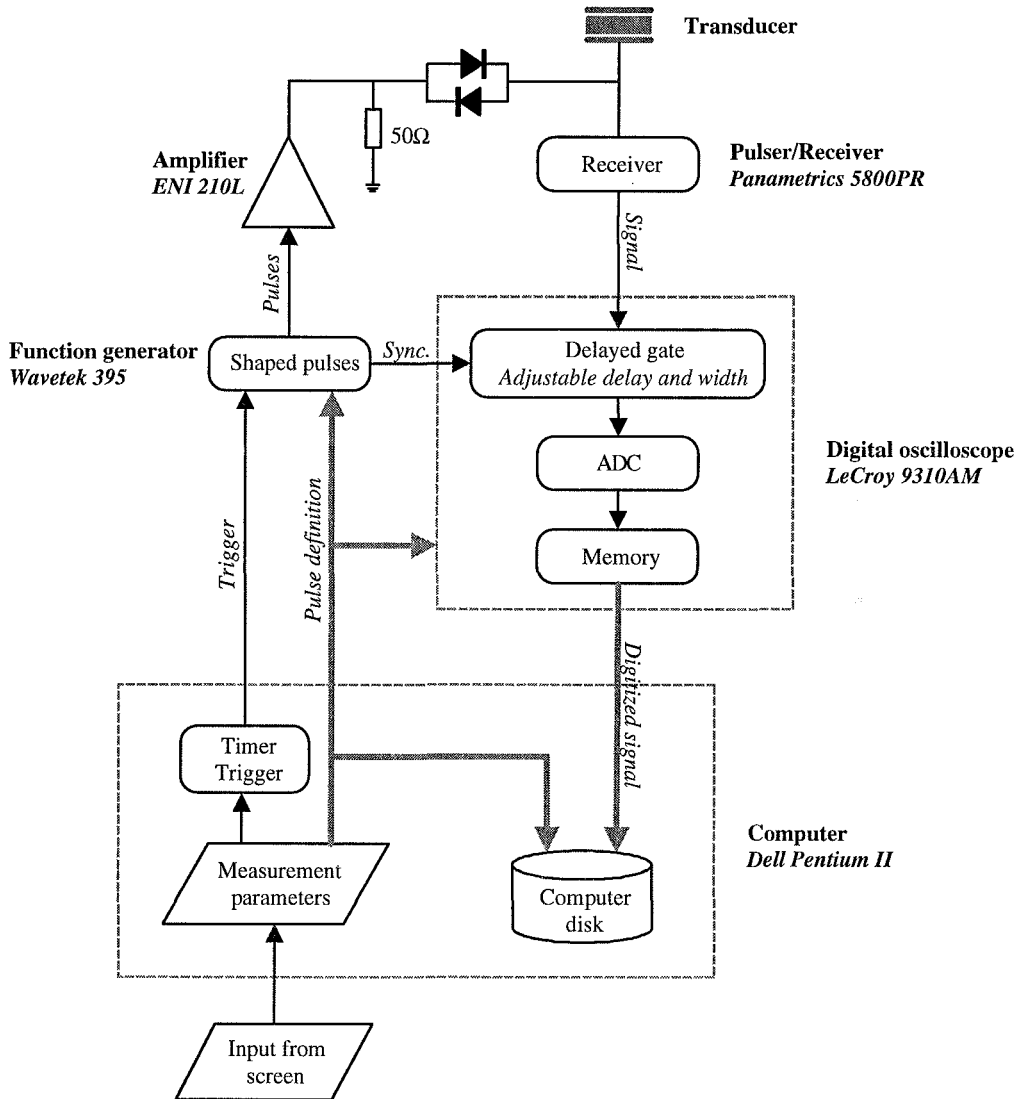


Figure 4.9. Acquisition of RF traces scattered from the contrast agent.

Transmit pulses The transmit pulses are produced by the programmable *Wavetek 395 Arbitrary Function Generator*. The pulse is defined in software in the computer, and the pulse shape is transferred as a sequence of points to the function generator, using the GPIB interface. Any pulse shape can be defined. Standard pulses are defined by their frequency, amplitude, number of cycles, and envelope.

Receiver The *Panametrics 5800PR pulser/receiver* is used as receiver. The values of the high- and lowpass receive filters, gain and attenuation are set in the computer.

Digitizer The *LeCroy 9310AM Digital Storage Oscilloscope* is used as digitizer. The resolution of the ADC is 8 bit, and the oscilloscope memory is 200 000 sample points. For these measurements, the memory is divided into segments of 2500 or 2000 sample points length.

Echoes from the different transmit pulses are stored in different segments

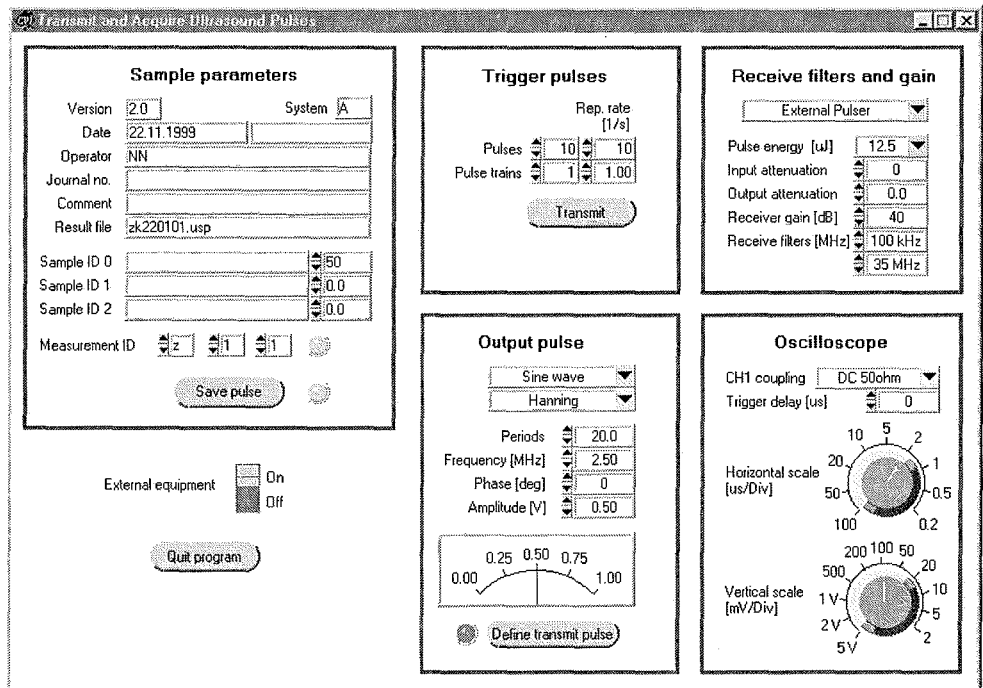


Figure 4.10. Acquisition of RF traces backscattered from the contrast agent. Graphical user interface used to control transmit pulses and the acquisition of RF traces.

Table 4.4. Measurement parameters and results stored from backscattered measurement.

Measurement parameters	Date and time of measurement Sample and operator identifiers Sample volumes
Trigger data	Number of trigger pulses and pulse repetition rate
Transmit pulse data	Pulse envelope, length, frequency, phase and amplitude
Receiver settings	Gain and attenuation, high- and lowpass filter settings
Oscilloscope	Coupling mode, trigger delay, horizontal and vertical scale Sample rate, trace length, memory segmentation
Received traces	Stored as 8-bit data points

of the oscilloscope memory. The portion of the received echoes to sample is selected by setting the trigger delay and the segment length. The sample rate is determined by the length of the memory segment. Possible settings are listed in Table 4.3. Most measurements are done using 50 or 100 μs trace length, giving sample rates of 50 or 25 Msa/s.

When a sequence of pulses is finished, the contents of the oscilloscope memory is transferred to the computer for processing and permanent storage.

The digitizer and the function generator run on separate clocks, not synchronized with each other. This is a limitation when testing techniques based on comparing two or more pulses, such as pulse inversion or Doppler methods.

The acquired RF pulses and measurement parameters are stored on the

computer disk in a binary format. The parameters stored are listed in Table 4.4.

Chapter 5

Estimation of Shell Material Properties

In the theory chapters, Chapter 2 and Chapter 3, it was postulated that a shell enclosing the bubble will alter its acoustic properties. The aim of this chapter is to investigate the effect of the shell for oscillations in the linear range. The measurement technique in Chapter 4.1 is applied to characterize a contrast agent consisting of polymer-shelled air bubbles. The theoretical models of Chapter 2 are compared with the experimental results, and are used to estimate values for the visco-elastic shell parameters, values that are not known *a priori*. It is further shown how the results can be used to calculate the stiffness of the whole microbubble, the bulk modulus. This links it to results reported in a previous, phenomenological study [56, 61]. A version of the methods described here have also been applied to characterize the ultrasound contrast agent *Sonazoid* from Nycomed [157].

The study described in this chapter has been accepted for publication in the *Journal of the Acoustical Society of America* in 2000 [62].

5.1 Composition of the Microbubbles

The substance investigated in this study was prepared by Nycomed (Nycomed Amersham, Oslo, Norway) as an experimental contrast agent for medical ultrasound imaging. The substance consists of air bubbles enclosed in a thin polymer shell. Bubble diameters are between 1 and 10 μm . Preparation and characterization of the microbubbles are described by Bjerknes et al. [10]. Figure 5.1 illustrates the composition of these polymeric microbubbles.

From the production process [10], it is estimated that the ratio between polymeric shell material and total microbubble volume is constant, with 15%

of the microbubble volume in the shell. This gives a constant ratio between shell thickness and microbubble radius, where the shell thickness is 5% of the microbubble radius.

The theoretical model describes the shell as a viscoelastic material with constant shear modulus G_S and viscosity η_S . The shear modulus and viscosity of a polymeric material are in general frequency dependent. The aim of this study was to characterize the contrast agent in the frequency range most commonly used in diagnostic medical imaging, from 1 to 8 MHz. It is assumed that G_S and η_S are constant within this range.

The shell material is not easily made in bulk quantities that allow conventional measurements of elastic properties. Instead, G_S and η_S are estimated from measurements of ultrasound absorption through a contrast agent suspension.

5.2 Theory

The theoretical modeling of the polymeric microbubbles is based on the model for a shell encapsulated gas bubble described in Chapter 2 and Chapter 3.

Several different models for the liquid and for the shell were presented in Chapter 3. The experimental measurements were done at small oscillation amplitudes, where the oscillation is linear. In the limit of small oscillation amplitudes, the different liquid and shell models of Chapter 3 yield identical results.

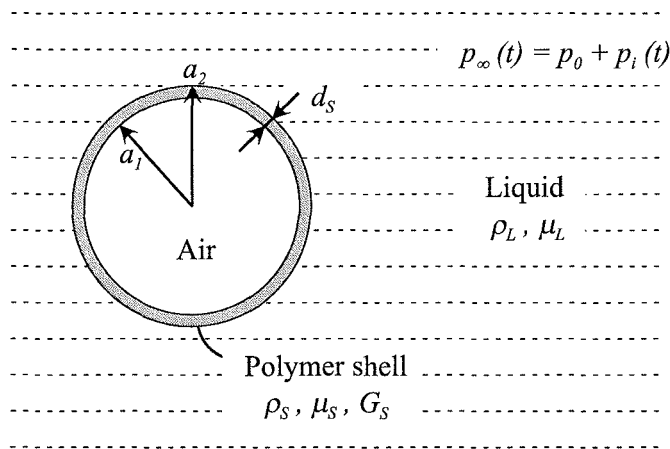


Figure 5.1. Drawing of the polymer-encapsulated air-filled microbubble.

5.2.1 Church's Model for *Albunex*: Comparison with the Models of Chapter 3

In 1995, Church presented a model for the oscillation of *Albunex* [22]. For bubbles in a thin shell, Church's model is equivalent to one of the models presented in Chapter 3, as will be shown in this section.

Church described air bubbles enclosed in a solid, incompressible, viscoelastic shell, described by a shear modulus G_S and a shear viscosity η_S . The liquid surrounding the bubbles is modeled as incompressible and Newtonian, with shear viscosity η_L . It is further assumed that the shell reduces surface tensions at the shell-liquid and shell-gas interfaces, so that surface tension can be neglected.

Under these assumptions, a nonlinear equation of motion for the bubble surface is

$$\begin{aligned} & \rho_L \left[\ddot{a}_2 a_2 + \frac{3}{2} \dot{a}_2^2 \right] + \rho_S \left[\ddot{a}_2 a_2 \left(\frac{a_2}{a_1} - 1 \right) + \dot{a}_2^2 \left(2 \frac{a_2}{a_1} - \frac{1}{2} \left(\frac{a_2}{a_1} \right)^4 - \frac{3}{2} \right) \right] \\ & = p_{ge} \left(\frac{a_{1e}}{a_1} \right)^{3\kappa} - p_\infty(t) - 4\eta_L \frac{\dot{a}_2}{a_2} - 4\eta_S \frac{V_S}{a_2^3} \frac{\dot{a}_1}{a_1} - 4G_S \frac{V_S}{a_2^3} \left(1 - \frac{a_{1e}}{a_1} \right), \quad (5.1) \end{aligned}$$

where $a_1(t)$ and $a_2(t)$ are the inner and outer shell radii, ρ_S and ρ_L are the densities of the shell material and of the surrounding liquid, p_{ge} is the equilibrium pressure in the gas inside the bubble, a_{1e} and a_{2e} are the inner and outer shell radii at equilibrium, $p_\infty(t)$ is the pressure in the liquid far from the bubble, κ is the polytropic exponent of the gas, $V_S = a_2^3 - a_1^3$, and dots denote differentiation with respect to time.

Equation (5.1) is Church's Equation (12). This has been rearranged to identify the different terms better, using the conservation of mass relation for an incompressible shell; $\dot{a}_1 a_1^2 = \dot{a}_2 a_2^2$.

Equation (5.1) is the basis for the theoretical description of the polymeric microbubbles investigated in this paper, using shell thickness, viscosity, and shear modulus different from those of *Albunex*. According to this description, the thickness d_S of the shell varies as the bubble oscillates, so that the shell volume is constant. The shell is thin compared to bubble radius, and use of this, $d_S(t) \ll a_2$, allows simplification of (5.1).

The left side of (5.1) represents inertia: Terms multiplied with ρ_S represent inertia of the shell, terms multiplied by ρ_L represent inertia of the liquid, and ρ_S and ρ_L are of the same order of magnitude. The inertia terms are expanded in the small parameter d_S/a_2 , keeping terms to the first order. This simplifies

the left side of (5.1) to

$$\rho_L \left[\ddot{a}_2 a_2 \left(1 + \frac{\rho_S d_S}{\rho_L a_2} \right) + \frac{3}{2} \dot{a}_2^2 \right]. \quad (5.2)$$

Hence, the shell contributes to the inertia of the oscillating bubble through a term of order d_S/a_2 , which can be neglected.

The right side of (5.1) represents restoring stiffness and damping viscous forces. The first three terms are known from the Rayleigh-Plesset equation for unshelled bubbles. The last two terms represent viscous and elastic forces due to motion and tension in the shell. The shell is thin, and terms of order d_S/a_2 are neglected. This reduces the last two terms in (5.1) to

$$4\eta_S \frac{V_S \dot{a}_1}{a_2^3 a_1} \approx 12\eta_S \frac{a_{1e}^2 d_{Se} \dot{a}_1}{a_2^3 a_1}, \quad (5.3a)$$

$$4G_S \frac{V_S}{a_2^3} \left(1 - \frac{a_{1e}}{a_1} \right) \approx 12G_S \frac{a_{1e}^2 d_{Se}}{a_2^3} \left(1 - \frac{a_{1e}}{a_1} \right), \quad (5.3b)$$

where d_{Se} is the shell thickness at rest. The shell viscosity and elasticity terms contain the relative shell thickness d_{Se}/a_2 multiplied with viscous and elastic shell properties η_S and G_S . The resulting terms may become large compared to other pressure terms. Hence, while the shell contribution to inertia is small and neglected, the contributions from the shell to stiffness and viscosity depend on G_S and η_S , and must be considered.

The result of these simplifications is a version of (5.1), suitable when the encapsulating shell is thin compared to the bubble diameter

$$\begin{aligned} \rho_L \left(\ddot{a}_2 a_2 + \frac{3}{2} \dot{a}_2^2 \right) &= p_{ge} \left(\frac{a_{1e}}{a_1} \right)^{3\kappa} - p_\infty(t) - 4\eta_L \frac{\dot{a}_2}{a_2} \\ &\quad - 12\eta_S \frac{a_{1e}^2 d_{Se} \dot{a}_1}{a_2^3 a_1} - 12G_S \frac{a_{1e}^2 d_{Se}}{a_2^3} \left(1 - \frac{a_{1e}}{a_1} \right). \end{aligned} \quad (5.4)$$

Equation (5.4) contains both inner radius a_1 and outer radius a_2 of the shell. It is reduced to an equation in outer radius $a = a_2(t)$ alone by setting

$$\frac{a_{1e}}{a_1} \approx \frac{a_{2e}}{a_2} \left(1 + \left(\frac{d_{Se}}{a_{2e}} - \frac{d_S}{a_2} \right) \right) \approx \frac{a_{2e}}{a_2} = \frac{a_e}{a}. \quad (5.5)$$

At equilibrium, the pressure in the gas inside the bubble is assumed to be equal to the hydrostatic pressure in the surrounding liquid, $p_{ge} = p_0$. This means that there is no tension in the shell at equilibrium. The pressure p_∞ far

from the bubble is the sum of the atmospheric pressure p_0 and the incoming acoustic pressure $p_i(t)$.

All these assumptions lead to the following reduced equation of motion, containing outer shell radius $a(t)$ as the only variable

$$\rho_L \left(\ddot{a}a + \frac{3}{2} \dot{a}^2 \right) = p_0 \left(\left(\frac{a_e}{a} \right)^{3\kappa} - 1 \right) - p_i(t) - 4\eta_L \frac{\dot{a}}{a} - 12\eta_S \frac{d_{Se} a_e^2}{a^3} \frac{\dot{a}}{a} - 12G_S \frac{d_{Se} a_e^2}{a^3} \left(1 - \frac{a_e}{a} \right). \quad (5.6)$$

This nonlinear equation is identical to the result obtained in Chapter 3, if the Rayleigh-Plesset equation (3.36) is used to model the liquid, and (3.151) gives the pressure at the bubble wall. The result above corresponds to using the “linear material - nonlinear geometry” model (3.145a) to describe the shell. This is a consequence of Church using the linear material parameters G_S and η_S to describe the shell, while nonlinear terms are caused by the nonlinear geometry of the oscillating bubble.

5.2.2 Linearization

The parameters G_S and η_S are estimated from acoustic measurements at low pressure amplitudes. Here, the oscillation is linear and (5.6) is solved analytically.

The bubble radius $a(t)$ is written

$$a(t) = a_e \left(1 + x(t) \right), \quad |x(t)| \ll 1. \quad (5.7)$$

Equation (5.6) is expanded in the radial displacement $x(t)$, keeping terms to the first order in x . This gives a simple linear equation for the forces acting on the surface of the bubble

$$ma_e \ddot{x} + Ra_e \dot{x} + sa_e x = -4\pi a_e^2 p_i(t), \quad (5.8)$$

with coefficients

$$m = 4\pi \rho_L a_e^3, \quad (5.9a)$$

$$s = 4\pi a_e \left(3\kappa p_0 + 12G_S \frac{d_{Se}}{a_e} \right), \quad (5.9b)$$

$$R = 4\pi a_e \left(4\eta_L + 12\eta_S \frac{d_{Se}}{a_e} \right). \quad (5.9c)$$

This is the same equation of motion as was found from a linear derivation in Chapter 2, see (2.31) and the modifications by the shell in Chapter 2.4.

Equation (5.8) is best handled in the frequency domain. Fourier-transformation yields

$$(\omega_0^2 - \omega^2 + i\omega\omega_0\delta)\hat{x}(\omega) = -\frac{1}{\rho_L a_e^2} \hat{p}_i(\omega), \quad (5.10)$$

with coefficients

$$\omega_0^2 = \frac{s}{m} = \frac{1}{\rho_L a_e^2} \left(3\kappa p_0 + 12G_S \frac{d_{S_e}}{a_e} \right), \quad (5.11a)$$

$$\delta = \frac{R}{\omega_0 m} = \delta_L + \delta_S, \quad (5.11b)$$

$$\delta_L = \frac{4\eta_L}{\omega_0 \rho_L a_e^2}, \quad (5.11c)$$

$$\delta_S = \frac{12\eta_S \frac{d_{S_e}}{a_e}}{\omega_0 \rho_L a_e^2}. \quad (5.11d)$$

The linear resonance frequency f_0 of the shell-encapsulated bubble is

$$f_0 = \frac{\omega_0}{2\pi} = \frac{1}{2\pi a_e} \sqrt{\frac{1}{\rho_L} \left(3\kappa p_0 + 12G_S \frac{d_{S_e}}{a_e} \right)}. \quad (5.12)$$

Compared to the free bubble, the shell increases resonance frequency through the shear modulus G_S , by increasing the stiffness of the bubble. Without a shell, when $d_{S_e} = 0$; and under adiabatic conditions, when $\kappa = \gamma$; the expression (5.12) reduces to the well-known Minnaert resonance frequency [113] for gas bubbles.

From (5.10) the radial oscillation $\hat{x}(\omega)$ as function of acoustic pressure $\hat{p}(\omega)$ is found

$$\hat{x}(\omega) = \frac{1}{\Omega^2 - 1 - i\Omega\delta} \frac{\hat{p}_i(\omega)}{\rho_L \omega_0^2 a_e^2}, \quad \Omega = \frac{\omega}{\omega_0}. \quad (5.13)$$

5.2.3 Acoustic Attenuation and Scatter

The increased attenuation caused by adding contrast agent to a liquid is given by the extinction cross section σ_e defined in Chapter 2. The expression for σ_e is found from (5.13) and (2.57) to

$$\sigma_e(a, \omega) = 4\pi a_e^2 \frac{c\delta}{a_e \omega_0} \frac{\Omega^2}{(1 - \Omega^2)^2 + \Omega^2 \delta^2} \quad \Omega = \frac{\omega}{\omega_0}. \quad (5.14)$$

At the low bubble concentrations studied here, the oscillations of the bubbles do not interact. The power absorbed by a bubble suspension is the sum of the power absorbed by the individual bubbles. This gives acoustic attenuation $\alpha(\omega)$ per unit distance in decibels, from (2.63)

$$\alpha(\omega) = 10(\lg e) \int_0^\infty \sigma_e(a, \omega) n(a) da \quad [dB], \quad (5.15)$$

where $n(a)da$ is the number of bubbles per unit volume with radius in $(a, a + da)$.

The scattering cross section $\sigma_s(a_e, \omega)$ is given by (2.43) as

$$\sigma_S(a_e, \omega) = 4\pi a_e^2 \frac{\Omega^4}{(\Omega^2 - 1)^2 + \Omega^2 \delta^2}. \quad (5.16)$$

5.2.4 Thermal and Acoustic Damping

The damping constants δ and the polytropic exponent κ for an oscillating gas bubble were derived in Chapter 2. The results are summarized as

$$\kappa = \operatorname{Re} \left(\frac{1}{\Phi(a_e, \omega)} \right), \quad (5.17a)$$

$$\delta_{th} = \frac{1}{\omega \omega_0} \frac{3p_0}{\rho_L a_e^2} \operatorname{Im} \left(\frac{1}{\Phi(a_e, \omega)} \right), \quad (5.17b)$$

$$\delta_c = \frac{\omega}{\omega_0} \frac{\omega a_e}{c}, \quad (5.17c)$$

$$\delta_{tot} = \delta_L + \delta_S + \delta_c + \delta_{th}. \quad (5.17d)$$

Thermal and acoustic damping were not part of the derivation of the equations of motion, (5.6) and (5.10). These extra damping terms can be added to the linearized expressions for extinction and scattering cross sections, (5.14) and (5.16), by replacing δ from (5.11d) with δ_{tot} from (5.17d).

5.3 Results

5.3.1 Size Distribution

Size distributions were measured using a *Coulter Multisizer* (Coulter Electronics, Luton, UK). The effect of varying bubble size was investigated by removing the larger bubbles by a flotation technique. Contrast agent was injected into a glass tube and left at rest for a specified time. The flotation speed of gas bubbles increases with diameter. By extracting bubbles from the bottom of the

tube after varying times, samples of varying size distribution were obtained. Samples were harvested after 30, 60, 120 and 180 minutes flotation time. The resulting size distributions, measured with the *Coulter Multisizer*, are plotted in Figure 5.2, showing how the procedure produced samples of successively smaller size.

5.3.2 Acoustic Attenuation Spectra

Acoustic attenuation was measured using the method described in Chapter 4.1. The attenuation spectra were measured using two broadband and unfocused transducers, one with center frequency 3.5 MHz and 13 mm aperture diameter, the other with 5.0 MHz center frequency and 10 mm aperture (*Panametrics Videoscan V-382-SU and V-326-SU*).

The sample cell was filled with 55 ml *Isoton II* (Coulter Electronics Ltd.), and samples of contrast agent were diluted in this. Sensitivity and signal-to-noise ratio were optimized by varying the dilution, depending on the size distribution of the sample investigated. Best results were obtained for dilutions

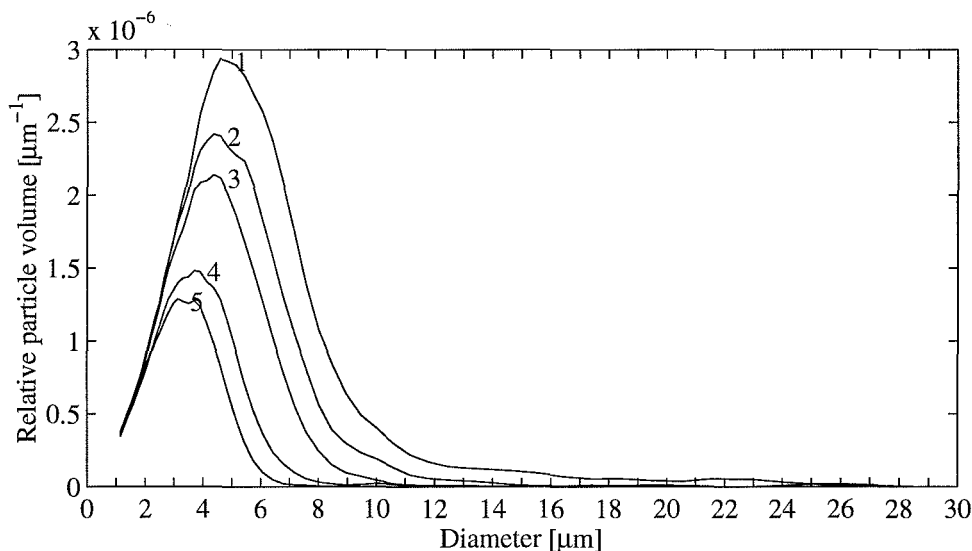


Figure 5.2. Size distribution of microbubble samples, plotted as relative volume of bubbles per μm . (1) is the original distribution, (2) to (5) are samples extracted from the bottom of a glass tube after flotation: (2) is after 30 minutes, (3) after 60 minutes, (4) after 120 minutes and (5) after 180 minutes flotation time.

giving acoustic attenuation around 3 dB/cm. This resulted in dilution factors between 1:2500 and 1:250, depending on the sample. Acoustic attenuation was verified to vary linearly with bubble concentration, and all results were scaled to a standardized dilution of 1:1000.

Acoustic attenuation spectra were measured on the samples shown in Figure 5.2. The results are plotted in Figure 5.3. The attenuation spectra are normalized to standardized dilution 1:1000. These results show how the overall attenuation level is reduced, the resonance frequency increased and the spectrum broadened as the larger bubbles are removed. In the region covered by both transducers, from 2.5 to 5.0 MHz, the curves from the different transducers overlap.

5.3.3 Estimation of Shell Parameters

The visco-elastic parameters G_S and η_S of the shell were estimated by comparing theoretically calculated acoustic attenuation spectra with the measured spectra plotted in Figure 5.3.

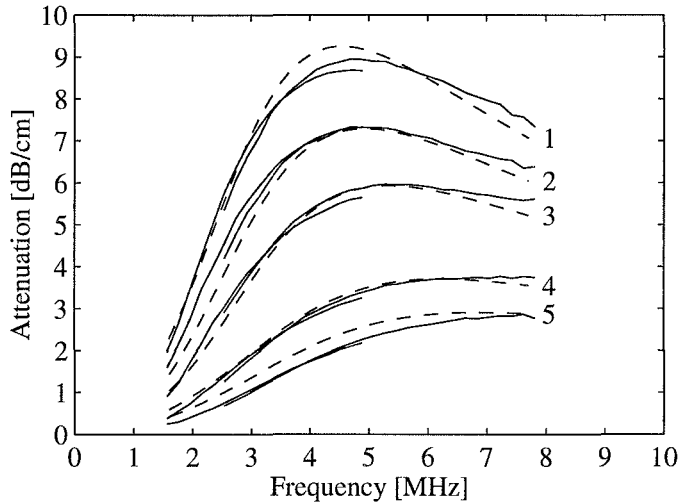


Figure 5.3. Acoustic attenuation spectra measured on the samples displayed in Figure 5.2. Solid lines are measured attenuation. Dashed lines show acoustic attenuation spectra calculated from size distributions, using the described theory. The viscoelastic properties G_S and η_S were adapted to the best fit between measured and calculated attenuation spectra. This result is for batch (a), see Table 5.1.

The theoretical spectra were calculated from the linearized model described in Chapter 5.2, using the measured size distributions shown in Figure 5.2. Acoustic attenuation $\alpha(\omega)$ in decibels was calculated from (5.14) and (5.15), using the total damping constant from (5.17d). The integral in (5.15) was replaced by a sum over the 64 logarithmically spaced *Coulter Multisizer* channels, spanning diameters from 1 to 30 μm ,

$$\alpha(\omega) = 10(\lg e) \sum_{k=1}^{64} \sigma_e(a_k, \omega) n_k \quad [dB]. \quad (5.18)$$

Here, a_k is the geometric mean radius of *Coulter Multisizer* channel k and n_k is the number of bubbles per unit volume counted in channel k .

The equation of motion, (5.6), contains the visco-elastic shell parameters G_S and η_S only as products of the parameters and the relative shell thickness, $G_S d_{S_e}/a_e$ and $\eta_S d_{S_e}/a_e$. The shell thickness was estimated to 5% of the bubble radius, as described in Chapter 5.1, giving

$$\frac{d_{S_e}}{a_e} = 0.05 = \text{constant}. \quad (5.19)$$

The exact value of the ratio d_{S_e}/a_e is not critical for the modeling, it enters into the calculations as a simple scaling of G_S and η_S . It is assumed that all microbubbles are equal, that is, have the same shell material properties G_S and η_S and relative thickness d_{S_e}/a_e .

The values of G_S and η_S were estimated by adjusting their values to minimize summed square difference between the measured and calculated spectra. The parameter values were then varied around these first estimates, and measured and calculated spectra were compared by visual inspection and by calculating the residual. The values of G_S and η_S were adjusted until the fit between measured and calculated spectra was judged unacceptable. This corresponded to a doubling of the summed square error between measured and calculated spectra, and was selected as limits for the confidence intervals of G_S and η_S .

This procedure was repeated for three different production batches of the polymeric microbubbles. Results for the individual batches are given in Table 5.1. The differences between the three batches are close to the uncertainty estimates for each batch. The differences are judged as significant, and may be caused by variations in production parameters between the batches.

The theoretically calculated attenuation spectra for one of the batches is plotted in the same graph as the measured spectra, Figure 5.3. The theoretical spectra for the four larger samples, (1) to (4), fit very well to the measured spectra. The attenuation calculated for the smallest sample (5) is higher

Table 5.1. Values for parameters estimated for the three different batches of polymer-encapsulated air bubbles, (a), (b) and (c). Shell thickness d_S was estimated from production process parameters and electron microscopy [10] to 5% of bubble radius for all samples. The viscoelastic shell parameters G_S and η_S and the microbubble bulk modulus K_p were estimated from acoustic measurements.

Batch	Shear modulus	Shear viscosity	Bulk modulus
	G_S [MPa]	η_S [Ns/m ²]	K_p [MPa]
(a)	10.6 ± 1.0	0.39 ± 0.04	2.2 ± 0.3
(b)	11.6 ± 1.2	0.48 ± 0.05	2.4 ± 0.3
(c)	12.9 ± 0.9	0.49 ± 0.03	2.7 ± 0.2

than the measured value. Microscopic images and comparisons of polymer and microbubble volume [10] indicate that the samples contain a very small fraction of small fragments of solid polymer material. These fragments will show up as small particles on the *Coulter Multisizer*, but have minimal effect on the attenuation. This may explain the reduced attenuation of the smallest size-fraction.

5.4 Some Calculations Based on the Results

5.4.1 Damping Constants

The total damping constant δ_{tot} is the sum of several damping terms, see (5.17d). The contributions from each of these terms are plotted in Figure 5.4 and Figure 5.5, for bubble diameters 4 μm and 8 μm . The value of δ_S is calculated from the value of η_S estimated from the measurements. The curves show that shell viscosity is the dominating damping mechanism for frequencies below 10 MHz.

Contributions from acoustic and thermal damping were not included in the derivation of the equation of motion (5.6). The curves in Figs. 5.4 and 5.5 indicate that these are not very important at frequencies below about 10 MHz. Acoustic damping starts to play a role only for frequencies above about 10 MHz for bubbles with diameter below 8 μm .

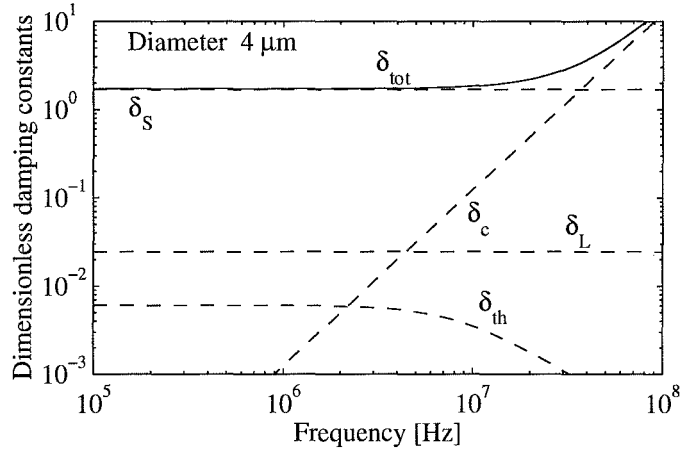


Figure 5.4. Dimensionless damping constants for a polymeric microbubble with diameter $4 \mu\text{m}$. Contributions from liquid viscosity δ_L , shell viscosity δ_S , acoustic radiation δ_c , thermal conduction in the gas δ_{th} , and the total damping $\delta_{tot} = \delta_L + \delta_S + \delta_c + \delta_{th}$. The shell viscosity is $\eta_S = 0.48 \text{ Ns/m}^2$.

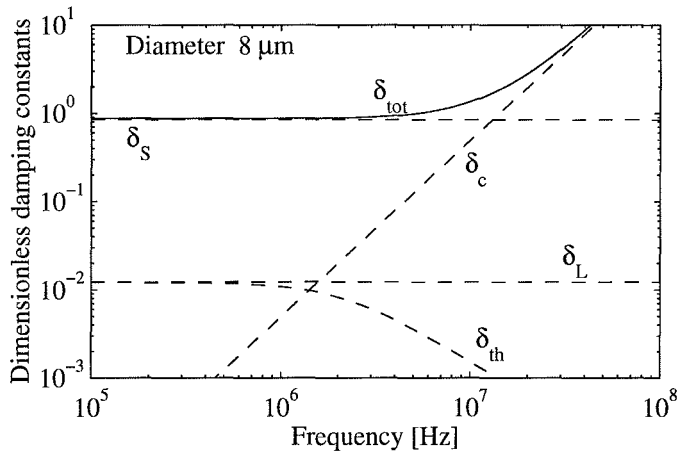


Figure 5.5. Dimensionless damping constants for a polymeric microbubble with diameter $8 \mu\text{m}$. Contributions from liquid viscosity δ_L , shell viscosity δ_S , acoustic radiation δ_c , thermal conduction in the gas δ_{th} , and the total damping $\delta_{tot} = \delta_L + \delta_S + \delta_c + \delta_{th}$. The shell viscosity is $\eta_S = 0.48 \text{ Ns/m}^2$.

5.4.2 Microbubble Stiffness

The bulk modulus K_p expresses the stiffness of the whole microbubble, composed of gas-filled interior and surrounding shell. It is informative to compare this microbubble stiffness with the bulk moduli of known materials. Bulk modulus K_p and bulk viscosity η_p are defined from the relation

$$\Delta p = -K_p \frac{\Delta V}{V_e} - \eta_p \frac{d}{dt} \left(\frac{\Delta V}{V_e} \right), \quad (5.20)$$

where Δp is the applied pressure, ΔV is the change in volume and V_e is the equilibrium volume. For the polymeric microbubbles, expressions for K_p and η_p are found from (5.8) to

$$K_p = \kappa p_0 + 4G_S \frac{dS_e}{a_e}, \quad (5.21a)$$

$$\eta_p = 4\eta_S \frac{dS_e}{a_e}. \quad (5.21b)$$

The bulk modulus for a polytropic gas is $K_g = \kappa p_0$. Compared to the free gas bubble, the bulk modulus of the shell-encapsulated bubbles increases due to the shear modulus of the shell. Bulk moduli for the polymeric microbubbles are estimated by inserting the value for G_S into (5.21a). This results in values for K_p of around 2.5 MPa, see Table 5.1. K_p and η_p are independent of the microbubble diameter when the ratio between shell thickness and microbubble diameter is constant. The value of K_p estimated for the polymeric microbubbles is compared with other materials in Table 5.2. According to these results, the polymeric microbubbles are approximately 20 times stiffer than free gas bubbles. The stiffness of the microbubbles is mainly determined by the shell, not by the air inside. The polymeric microbubbles are, however, 1000 times more compressible than water.

When the bubbles are described by their bulk modulus K_p , the resonance frequency f_0 from (5.12) can be expressed in a simple form analogous to the result by Minnaert [113]

$$f_0 = \frac{1}{2\pi a_e} \sqrt{\frac{3K_p}{\rho_L}}. \quad (5.22)$$

5.4.3 Resonance Frequency and Scattering Cross Section

Increased stiffness from shell elasticity causes the resonance frequency to increase. Increased damping from shell viscosity broadens the resonance peak

Table 5.2. Microbubble stiffness. Bulk modulus of the investigated polymer-shelled bubbles compared with other substances. Data from Kinsler et al. [73].

Substance	Bulk modulus K [MPa]
Air (isothermal)	0.10
Air (adiabatic)	0.14
Polymer-shelled air bubbles	2.5
Water (37°C)	2250
Steel	170000

and increases sound absorption. The resonance frequency calculated from (5.12) is compared with results for free gas bubbles, results are plotted in Figure 5.6. The resonance frequency for the polymeric microbubbles was found to be approximately 4 times higher than what is expected for air bubbles of the same diameter.

The scattering cross section is calculated from (5.16). Figure 5.7 shows

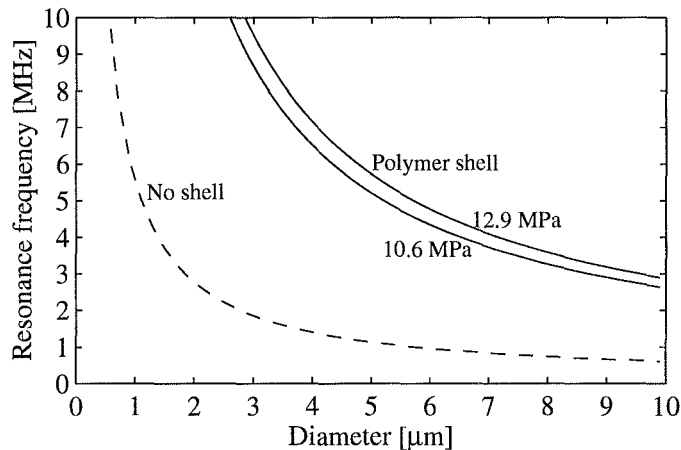


Figure 5.6. Calculated resonance frequency as function of bubble diameter. The solid line shows the values found for the bubbles encapsulated in a polymeric shell, while the dashed line shows values calculated for free air bubbles. The two curves for the polymeric microbubbles correspond to the parameter values $G_S=10.6$ MPa and $G_S=12.9$ MPa, see Table 5.1.

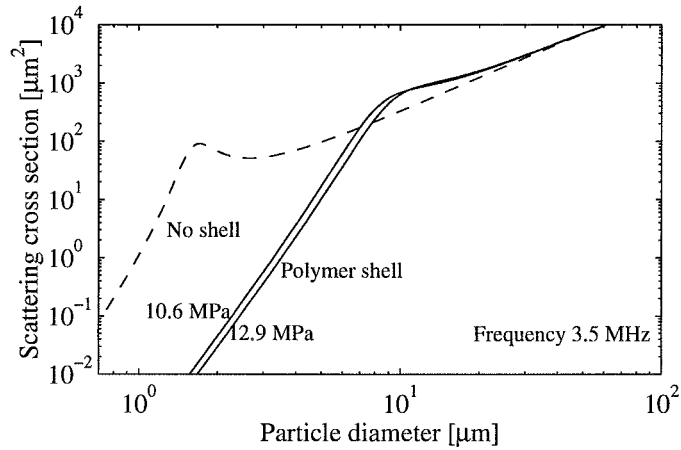


Figure 5.7. Scattering cross section for polymeric microbubbles (solid lines) and for free air bubbles (dashed line). The frequency is 3.5 MHz. The two curves for the polymeric microbubbles correspond to the parameter combinations $G_S=10.6$ MPa, $\eta_S=0.39$ Ns/m² and $G_S=12.9$ MPa, $\eta_S=0.49$ Ns/m².

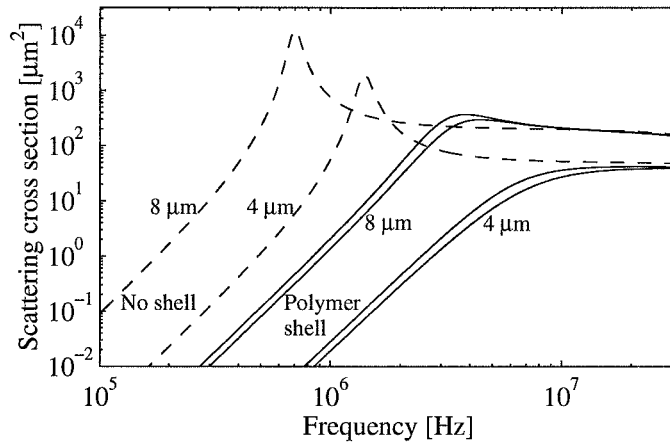


Figure 5.8. Scattering cross section as function of frequency for polymeric microbubbles (solid lines) and for free air bubbles (dashed line). Diameters are 4 μm and 8 μm . The two curves for the polymeric microbubbles correspond to the parameter combinations $G_S=10.6$ MPa, $\eta_S=0.39$ Ns/m² and $G_S=12.9$ MPa, $\eta_S=0.49$ Ns/m².

dependence on diameter, at frequency 3.5 MHz, while Figure 5.8 shows dependence on frequency for bubbles with diameters of 4 μm and 8 μm . Scattering cross sections of air bubbles without shells are plotted in the same diagrams for comparison. Figure 5.7 corresponds to Figure 8 in Church's article [22]. Figures 5.7 and 5.8 show how the resonance frequency increases and the resonance peak broadens and almost disappears, due to the viscoelastic polymeric shell.

5.5 Discussion

5.5.1 Shell Thickness

A critical assumption for the estimation of the viscoelastic shell parameters is that the ratio between shell thickness and bubble radius is constant. The basis for this assumption is the production process for the microbubbles [10]: A droplet with a constant fraction of dissolved polymeric material is converted to one air-filled, polymer-shelled microbubble, with proportionality between initial droplet size and resulting microbubble size. The good agreement between experimental and theoretical attenuation spectra supports this assumption.

The model was tested by assuming a constant shell thickness instead of constant ratio between shell thickness and radius. This gave poor agreement between measurements and calculations for any combination of G_S and η_S , supporting the assumption that shell thickness varies with bubble diameter.

Another critical assumption is that all bubbles of the same size are equal. The shell thickness is uniquely determined by the microbubble diameter, and the values of the viscoelastic material parameters of the shell are equal for all bubbles. Particle characterization methods [10] have not shown variations in shell thickness between bubbles of the same size. This supports the assumption. If there are variations in shell thickness or viscoelastic parameters, this would typically cause over-estimation of the shell viscosity η_S . The resulting broadening of the resonance peak could be interpreted as being caused by an increased damping of the oscillating bubble.

The shear modulus estimated for the shell material is low compared to the shear moduli of known solids. This can be explained if the polymeric shell material forms a loose, porous structure, instead of a compact material. Such a material would have a low shear modulus and a high shear viscosity, which agrees with the estimated values for G_S and η_S .

5.6 Summary

A model has been developed describing oscillations of gas bubbles encapsulated in a thin polymer shell. The model depends on viscoelastic parameters of the shell material that are not known *a priori*. A linearized version of the model was used to estimate the shell material properties shear modulus and shear viscosity from acoustic attenuation spectra. Good agreement between experimental and theoretical results was found. The results show that the polymer shell increases microbubble stiffness 20 times compared to a free gas bubble.

Chapter 6

A Comparison Between Three Different Contrast Agents

Chapter 5 presented a method to estimate the viscous and elastic material parameters of the shell material, based on acoustic measurements. For the polymeric microbubbles investigated, the measured resonance frequency was around 4 times higher than predicted by the theory for free gas-bubbles. This shift in resonance frequency was explained by the influence of the shell. The shell makes the bubble stiffer, and shifts the resonance frequency upwards.

The effect of the shell was quantified by modeling it as an incompressible, visco-elastic solid, described by a shear modulus G_S and shear viscosity η_S . Values for G_S and η_S were estimated from the experimental results, and it was concluded that the polymer shell increases the stiffness of the bubbles by about 20 times. The dynamics of these microbubbles were dominated by the properties of the encapsulating polymer shell.

6.1 Properties of *Albunex*, Polymeric Microbubbles and *Sonazoid*

The aim of this chapter is to apply the methods introduced in Chapter 5 to compare three different contrast agents. The basic composition of the three investigated agents is similar, they all consist of gas bubbles encapsulated in a shell. But the shell material is quite different for the three agents, and there are also differences in the size distributions and the microbubble volume concentrations.

The three agents that are compared are:

Albunex (Also called *Infuson*). *Albunex* consists of air bubbles encapsulated

in a thin shell of denatured human serum albumin (HSA) [19]. The *Albunex* sample investigated here was an experimental batch produced by Nycomed. Its parameters, especially the size distribution, may deviate from the parameters of the product today on the market under the name *Albunex*.

The results for *Albunex* are from a study in 1992, they have been published previously [29]. The raw data of this study are still available. The results were recalculated using the theoretical model in Chapter 2 and included for comparison with the other agents. Models for the relation between size and efficiency of *Albunex* have been published earlier [57, 158].

Polymer shelled microbubbles This is the agent that was studied in detail in Chapter 5. It is an experimental contrast agent prepared by Nycomed, consisting of air bubbles encapsulated in a polymer shell.

Sonazoid (Formerly called *NC100100*) This contrast agent was developed by Nycomed and is now in clinical trials. The agent consists of bubbles containing perfluorocarbon gas enclosed in a thin surfactant membrane. Results from acoustic characterization of this agent were presented at the 1998 joint ICA/ASA conference [59] and at the 1998 IEEE Ultrasonic Symposium [60].

6.1.1 Size Distributions

The size distributions of the three microbubble types were measured using a *Coulter Multisizer*. The results are plotted in Figure 6.1. The curves are normalized so that the not fractionated samples have equal volume of bubbles.

The *Albunex* samples were split into size fractions by filtering through *Nucleopore* filters of diameter 10 μm , 8 μm , 5 μm and 3 μm , as described in Reference [29]. The size distributions of these filtered samples are plotted with dashed lines in the figure.

The polymeric microbubbles are described in Chapter 5. This agent was fractionated by letting the microbubbles float in a glass tube, and harvesting from the bottom of the tube after predefined times. The size distributions of these fractions are plotted with dashed lines in the diagram.

The *Sonazoid* sample was not fractionated.

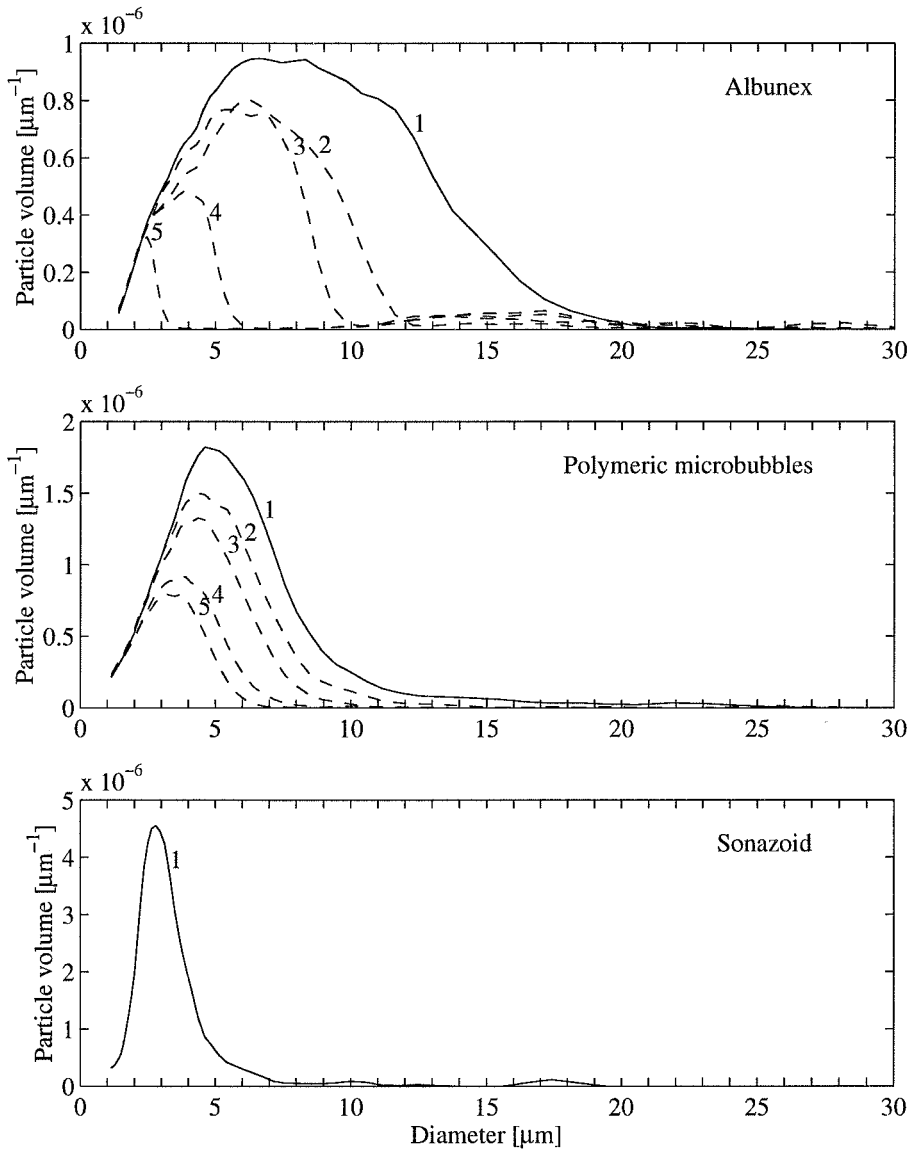


Figure 6.1. Size distributions of three different contrast agents. Upper diagram: *Albunex* microbubbles. (1) is the original sample, (2) to (5) are samples filtered through *Nucleopore* filters. Middle diagram: Polymeric microbubbles, from Chapter 5. (1) is the original distribution, (2) to (5) are fractionated samples obtained by flotation. Lower diagram: *Sonazoid*. The curves are normalized to equal volume of bubbles in the not fractionated samples (solid lines).

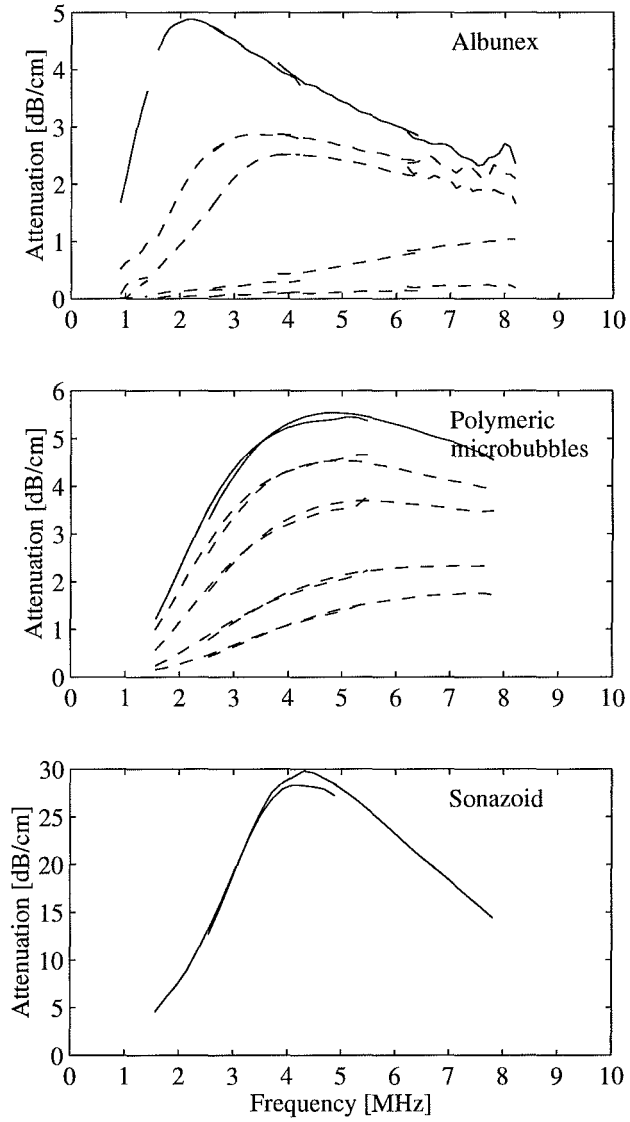


Figure 6.2. Acoustic attenuation spectra measured on the three contrast agents whose size distributions are plotted in Figure 6.1. The measurements are normalized to equal volume of bubbles in the not fractionated samples (solid lines).

6.1.2 Acoustic Attenuation Spectra

Acoustic attenuation spectra were measured to compare the acoustic properties of the different contrast agents. The polymeric microbubbles and *Sonazoid* were measured using the system for attenuation measurements described in Chapter 4. *Albunex* was measured using an older system based on the same measurement method, but with five transducers instead of two. The measurement system and method used on *Albunex* is described by de Jong et al. [29].

The results of the acoustic attenuation measurements are plotted in Figure 6.2. These are large differences between the three different contrast agents.

Albunex gives a resonance peak at a lower frequency than the others. For the unfiltered *Albunex* sample, the peak is at 2.2 MHz. As the larger *Albunex* microbubbles are removed by filtering, the resonance peak shifts towards higher frequencies. Marsh et al. [106, 107] have done the same attenuation measurements on *Albunex* produced by Mallinckrodt (St. Louis, USA), reporting similar results.

The polymeric microbubbles have a peak in attenuation at 4.8 MHz. This is at a higher frequency than for *Albunex*, and the resonance peak is much broader. This can partly be explained by the size distributions, as the polymeric microbubbles are smaller than the *Albunex* microbubbles. As the larger bubbles are removed by flotation, the resonance moves towards higher frequencies, and the peak broadens even more.

The attenuation from *Sonazoid* is higher than from the other substances. At equal volume concentration of bubbles, the *Sonazoid* gives about 5 times higher attenuation than *Albunex* and the polymeric microbubbles. *Sonazoid* also gives a narrower resonance peak than the other substances do. This can be explained by the narrower size distribution of *Sonazoid*. *Sonazoid* has a resonance peak around 4.2 MHz, lower than for the polymeric microbubbles. The *Sonazoid* bubbles are smaller than the polymeric microbubbles. Based on size alone, *Sonazoid* should show a higher resonance frequency than the polymeric microbubbles. An explanation to this apparent discrepancy is sought in differences in shell thickness and material properties.

Visual comparison between the size distributions and attenuation spectra in Figure 6.1 and Figure 6.2 gives the following impression:

The *Sonazoid* sample has maximum attenuation around the same frequency as the *Albunex* sample No. (3), which has about twice as large diameter. The resonance peak of *Sonazoid* is sharper than for the *Albunex* sample. This indicates that the *Sonazoid* bubbles are softer and have higher Q-values than the *Albunex* bubbles.

Compare the size distribution of the *Sonazoid* sample with sample No. (4)

Table 6.1. Comparison between three ultrasound contrast agents with different shell materials. Visco-elastic parameters estimated for the shell material and for the whole microbubble.

	Thickness d_S [nm]	Shell properties	
		Shear modulus G_S [MPa]	Shear viscosity η_S [Ns/m ²]
<i>Albunex</i>	15	120 ±20	2.2 ±0.8
Polymer shell	$50 \times \frac{a}{\mu m}$ ¹	11.5 ±2	0.4 ±0.1
<i>Sonazoid</i>	4.0	50 ±3	0.8 ±0.1

¹ The thickness of the polymer shell is proportional to the microbubble radius, equal to 5% of the radius. This is expressed as $(50 \times a/\mu m)$ nm, where a is the microbubble radius.

of the polymeric microbubbles. The polymer sample has slightly larger diameter. While the *Sonazoid* sample has a sharp resonance peak, the polymer sample shows a very broad spectrum with hardly any maximum within the observed frequency range. This indicates that the polymeric microbubbles behave like harder oscillators with lower Q-values than the *Sonazoid*-bubbles.

6.2 Estimates for Shell Material Properties

The visco-elastic parameters of the shell material for *Albunex* and *Sonazoid* were estimated by fitting measured and calculated attenuation spectra, using the method developed for the polymeric microbubbles in Chapter 5. The shell thickness for the substances was estimated from electron microscopic images and from measurements of shell material mass. These results were provided by Nycomed. The estimated shell parameters for the three substances are listed in Table 6.1.

6.2.1 Albunex

The results of previously published measurements on *Albunex* [29] were recalculated using the theoretical model from Chapter 2. The results are plotted in Figure 6.3.

The spectra for *Albunex* were fitted by assuming a shell thickness that was constant, that is, independent of the microbubble diameter. This assumption results in a much better agreement between measured and calculated atten-

uation spectra than modeling the shell thickness as proportional with the microbubble diameter. This is in accordance with what was expected from the composition of the *Albunex* microbubble: The shell is formed by a coagulation of HSA protein molecules around the air bubble. It is reasonable to assume that the thickness of this molecule layer does not depend on the size of the bubble, although this is not known exactly.

The fit between measured and calculated spectra is not as good for *Albunex* as it is for the polymeric microbubbles studied in Chapter 5. This is reflected in large uncertainties for the estimated shell parameter values. One reason for this may be that the *Albunex* microbubbles are rather unstable, and require very careful handling not to be damaged prior to or during the measurement. It is suspected that the handling procedure, including filtering, stirring and transportation between acoustic and size measurement systems, might have destroyed a small amount of *Albunex* microbubbles, and that this has caused the acoustic and size measurements to be done on slightly different microbubble samples. However, it may also be that the theoretical model does

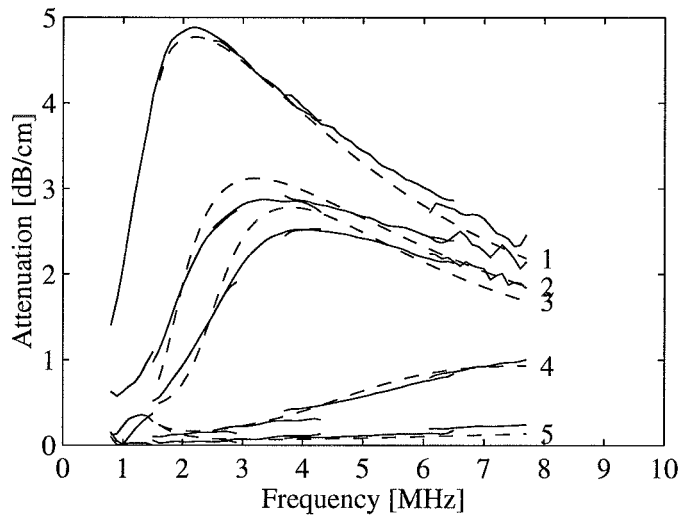


Figure 6.3. Measured and calculated acoustic attenuation spectra for *Albunex*. The solid lines are the measured attenuation spectra from Figure 6.2. (1) is for unfiltered *Albunex*, (2) to (5) are *Albunex* filtered through *Nucleopore* filters of varying pore diameters. The dashed lines show spectra calculated from the size distributions in Figure 6.1, using the shell properties for *Albunex* listed in Table 6.1. The curves are normalized to standardized bubble volume fraction $\phi = 10^{-5}$.

not work so well for the *Albunex* microbubbles as it does for the polymeric microbubbles.

6.2.2 *Sonazoid*

The measured and calculated acoustic attenuation spectra for *Sonazoid* are plotted in Figure 6.4.

The calculated spectrum was fitted by assuming a shell thickness that was constant, that is, independent of the microbubble diameter. The calculations gave equally good fits between measured and calculated spectra either the shell thickness was modeled as constant or as proportional to the bubble diameter. This is probably because the size distribution of *Sonazoid* is so narrow that it does not contain much information about how properties vary with diameter. No fractionation was done on the *Sonazoid* sample.

The assumption of constant shell thickness was selected based the composition of *Sonazoid*. The microbubble shell is composed of a monolayer of molecules, and it is likely that the shell thickness does not depend on the microbubble diameter.

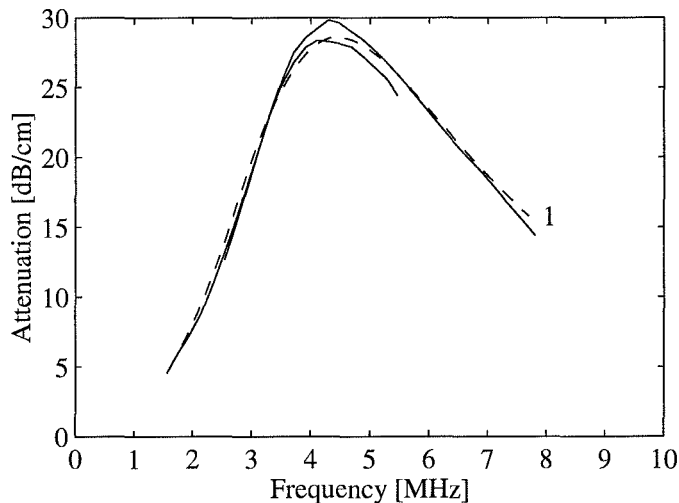


Figure 6.4. Measured and calculated acoustic attenuation spectra for *Sonazoid*. The solid line is the measured attenuation spectrum from Figure 6.2. The dashed line shows the spectrum calculated from the size distribution in Figure 6.1, using the shell properties for *Sonazoid* listed in Table 6.1. The curves are normalized to standardized bubble volume fraction $\phi = 10^{-5}$.

The fit between measured and calculated spectra for the investigated *Sonazoid* sample is excellent. However, only one fraction with a rather narrow size distribution was investigated. A good fit between measured and calculated results is easier to obtain for such a narrow size distribution than for several samples with different sizes.

6.3 Sensitivity to Hydrostatic Pressure

It is critical that the contrast agent bubbles can withstand the hydrostatic pressures in the heart ventricles and in the arterial system. The pressure stability of the agents was investigated by measuring acoustic attenuation spectra before, during and after exposure to 120 mmHg static pressure, using the system for pressure measurements described in Chapter 4.

The agents were diluted in *Isoton II*, and acoustic attenuation spectra were measured. The measurement sequence is described in Chapter 4, it is summarized as follows: First, 3 spectra are measured at 10 seconds intervals. The pressure valve is then opened, and either 3 or 9 spectra are measured while the sample is under pressure, also at 10 seconds intervals. The pressure is then released, and the last 3 spectra are measured. The pressure was 120 mmHg in all the measurements reported here.

6.3.1 Polymeric Microbubbles

The results of pressure measurements on polymeric microbubbles are plotted in Figure 6.5.

Before the pressure is applied, the attenuation spectrum has a resonance peak around 4.5 MHz, and there is no significant difference between the three spectra measured. When the pressure valve is opened and 120 mmHg pressure is applied, the resonance peak shifts downwards to 3.9 MHz. The attenuation decreases slightly with time during the 90 seconds the pressure is applied. After the pressure is released, the spectra goes back to the shape it had before pressure was applied, but the attenuation is slightly reduced, by about 3%.

The difference between the spectra measured before and after pressure is significant, but is probably not of any practical importance. It is most likely caused by a destruction of a small amount of bubbles by the hydrostatic pressure. It may also be caused by bubbles floating away from the sound path during the time of measurement. However, given the very slow rising speed of these microbubbles, flotation is not likely to have caused the reduced attenuation.

The resonance peak shifts down during the exposure to pressure. From the

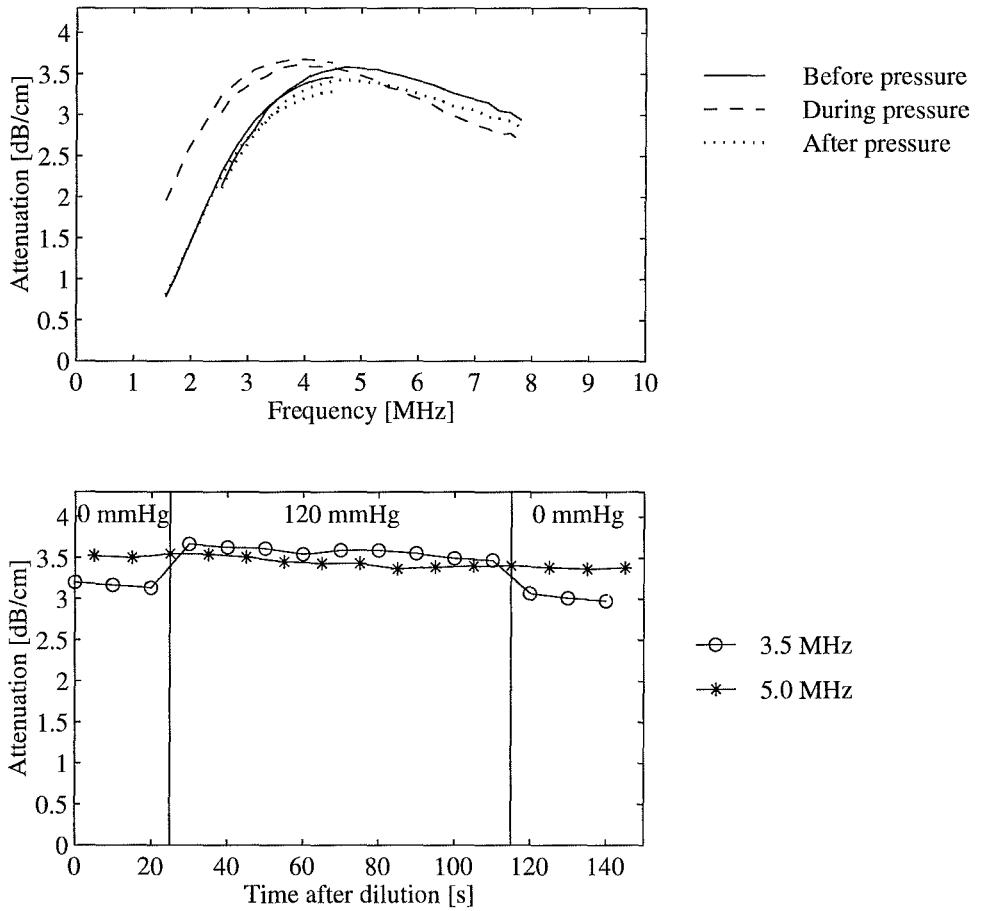


Figure 6.5. Pressure stability of the polymeric microbubbles. The upper diagram shows acoustic attenuation spectra measured before, during and after exposure to 120 mmHg static over-pressure. The two lines in the spectra correspond to measurements with two different transducers. The bottom diagram shows the attenuation values at the center frequencies of the transducers, plotted as function of time. The pressure was applied at *time* = 25 seconds and released at *time* = 115 seconds. The resonance is shifted towards lower frequencies during exposure to pressure. The effect of the pressure is reversible.

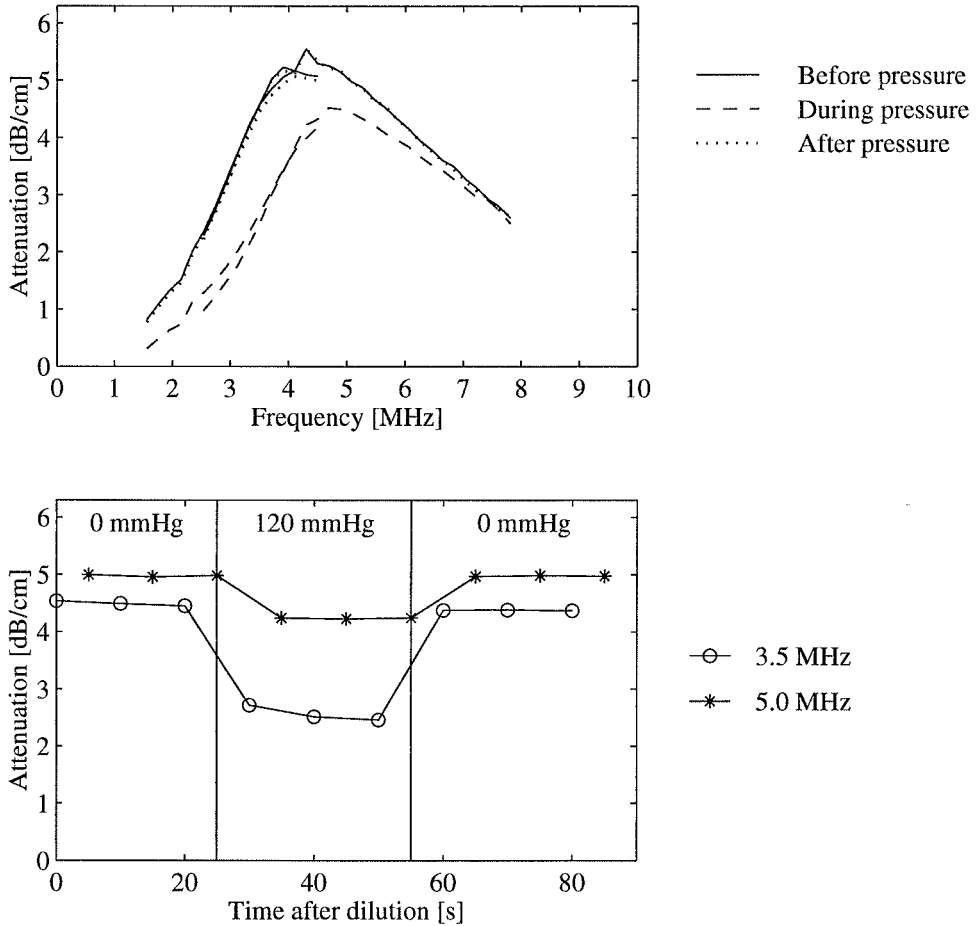


Figure 6.6. Pressure stability of *Sonazoid*. The upper diagram shows acoustic attenuation spectra measured before, during and after exposure to 120 mmHg static over-pressure. The two lines in the spectra correspond to measurements with two different transducers. The bottom diagram shows the attenuation values at the center frequencies of the transducers, plotted as function of time. The pressure was applied at *time* = 25 seconds and released at *time* = 55 seconds. The resonance is shifted towards higher frequencies during exposure to pressure. The effect of the pressure is reversible.

theoretical models for linear resonance frequency in Chapter 2, the resonance frequency is expected to increase if the bubble diameter is decreased and the bubble stiffened, e.g. by an increased external pressure. For this substance, the opposite effect is observed. From Chapter 5, it was concluded that the polymeric microbubbles were much stiffer than air bubbles, and that the behavior of these bubbles was dominated by the shell, not by the air inside them. The downshift in resonance frequency during hydrostatic pressure can be explained by the shell being curled and made more flexible during hydrostatic pressure.

6.3.2 *Sonazoid*

The results of pressure measurements on *Sonazoid* are plotted in Figure 6.6.

Before the pressure is applied, the attenuation spectrum has a resonance peak around 4.0 MHz. There is no significant difference between the three spectra measured. When the pressure is applied, the resonance peak shifts upwards to 4.7 MHz. The attenuation decreases slightly with time during the 30 seconds the pressure is applied. After the pressure is released, the spectra goes back to the value it had before pressure was applied. The difference between the spectra measured before and after pressure is not significant

Sonazoid gives an increased resonance frequency when it is exposed to hydrostatic over-pressure. This is as expected from the theoretical models in Chapter 2, if the pressure causes the bubbles to shrink and stiffen.

6.4 Velocity Dispersion

Gas bubbles are known to introduce velocity dispersion. Observation of the oscilloscope screen during measurements have showed only very small time shifts in the received pulses when the contrast agents were added, much smaller than half a wavelength of the acoustic pulse.

Changes in phase velocity after introduction of contrast agent are calculated from the pulses used to calculate acoustic attenuation spectra. The attenuation measurement system described in Chapter 4 allow detection of small changes in relative velocity, changes that are not easily seen by observing the pulses on the oscilloscope.

6.4.1 Calculation of Phase Velocity

The phase velocity is calculated from the phase of the pulses received after traversing twice through the sample cell with the contrast agent.

The voltage $V(t)$ received at the transducer is described as

$$V(t) = \sum_n v_n e^{i(\omega_n t - k_n z - \theta_n)}, \quad (6.1)$$

where v_n is the amplitude of frequency component n , ω_n is the angular frequency, t is the time after the pulse was emitted, k_n is the acoustic wavenumber, and z is the distance through the contrast agent suspension. θ_n is a phase constant that incorporates the effect of transmission, reflection from the back wall, and of the phase of the transfer function of the transducer. The phase $\phi(\omega)$ of the received voltage is, from (6.1)

$$\phi(\omega) = -k(\omega)z - \theta(\omega), \quad (6.2)$$

where the wavenumber k_n for frequency component n is rewritten as $k(\omega)$. The wavenumber relates to the phase velocity $c(\omega)$ as

$$k(\omega) = \frac{\omega}{c(\omega)}, \quad (6.3)$$

where $c(\omega)$ is the frequency dependent phase velocity in the contrast agent suspension.

The phase velocity in the contrast agent suspension is calculated by comparing the phase of two pulses: One that has traveled through the contrast agent suspension and one reference pulse that has traveled through a liquid of known velocity. The phase difference between the two pulses is

$$\Delta\phi = \phi - \phi_0 = z(k_0 - k) = \omega z \left(\frac{1}{c_0} - \frac{1}{c} \right), \quad (6.4)$$

where ϕ is the phase of the pulse, and ϕ_0 is the phase of the reference pulse. k and k_0 are the wavenumbers in the contrast agent suspension and in the reference liquid. This allows the phase velocity in the contrast agent suspension $c(\omega)$ to be calculated from the phase difference by

$$\frac{1}{c(\omega)} = \frac{1}{c_0} - \frac{\phi_m - \phi_0}{\omega z}. \quad (6.5)$$

6.4.2 Measured Dispersion

The velocity dispersion curves were calculated for two of the substances, the polymeric microbubbles and *Sonazoid*. The raw data pulses for *Albunex* were no longer available for such calculations.

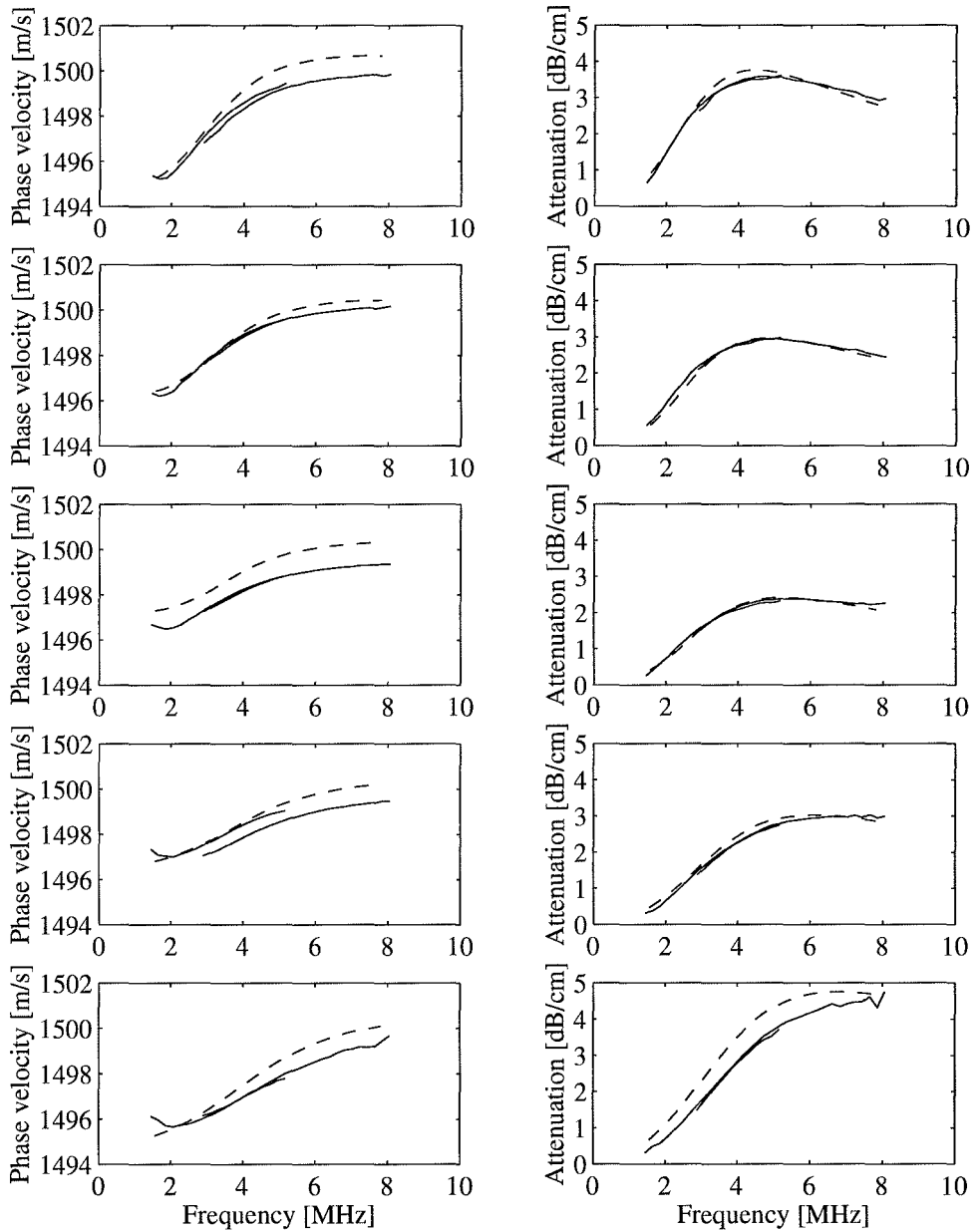


Figure 6.7. Phase velocity and attenuation measured on the polymeric microbubbles. The solid lines show measured velocity and attenuation. The dashed lines show theoretical curves calculated from the measured size distributions, using the model for a shell-encapsulated bubble and parameters from Table 6.1.

Dispersion curves for the polymeric microbubbles are plotted in Figure 6.7. Dispersion curves for *Sonazoid* are plotted in Figure 6.8. The attenuation spectra for the samples are plotted in the same figures. These curves are not normalized to equal concentration, as the dispersion does not show a simple linear variation with bubble concentration.

The curves were calculated using the parameters

$$\begin{array}{ll} \text{Distance through contrast agent} & z = 63 \text{ mm} \\ \text{Speed of sound in } \textit{Isoton II} & c_0 = 1500 \text{ m/s} \end{array} \quad (6.6)$$

The results in Figure 6.7 and Figure 6.8 show that the variations in phase velocity introduced by the contrast agents at realistic concentrations is less than 1%. “Realistic concentrations” means concentrations that increase the attenuation by a few dB/cm.

The phase velocity and attenuation as function of frequency were calculated from equation (2.109i) in Chapter 2. The size distributions $n(a)$ used in the calculations were measured by the *Coulter Multisizer*, see Figure 6.1.

The theoretical dispersion and attenuation curves for the polymeric microbubbles and for *Sonazoid* are plotted in the same figures as the measured values, Figure 6.7 and Figure 6.8. The solid lines show measured results, the dashed lines show results calculated from the size distributions. The shell properties used to calculate the dispersion and attenuation curves are listed in Table 6.1. The agreement between measured and calculated results is good.

The calculated dispersion curve for *Sonazoid* is compared with the theoretical curve for air bubbles without a shell in Figure 6.9. The shell encapsulating

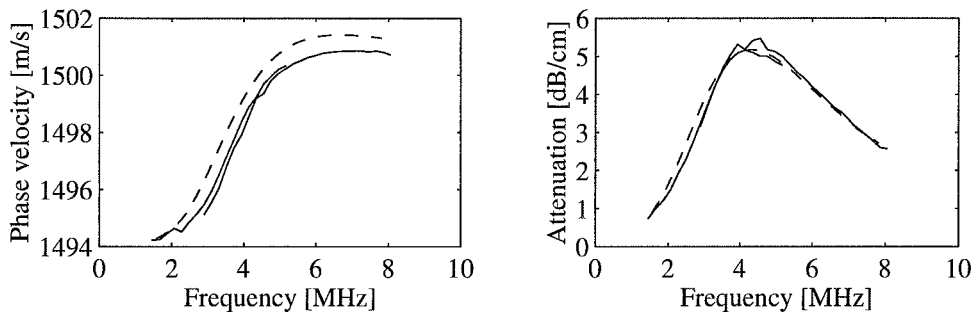


Figure 6.8. Phase velocity and attenuation measured on *Sonazoid*. The solid lines show measured velocity and attenuation. The dashed lines show theoretical curves calculated from the measured size distributions, using the model for a shell-encapsulated bubble and parameters from Table 6.1.

the *Sonazoid* bubble reduces both velocity dispersion and attenuation considerably compared to free air bubbles.

6.5 Theoretical Calculations Based on the Results

The results in this chapter have showed that there are differences between the three contrast agents, and that these differences must be explained by differences in the thickness and mechanical properties of the shell. Table 6.1 lists the properties of the different shell materials estimated from the acoustic attenuation measurements. The theory in Chapter 2 gives models for how various linear acoustic properties of the bubbles can be calculated from these shell parameters. The following sections gives the results of some of these calculations, with emphasis on how the different shell parameters give different results for the three agents, and how they compare with the theory for free air bubbles.

6.5.1 Resonance Frequency and Bulk Modulus

The bulk modulus K_p and the resonance frequency f_0 are calculated from the equations (5.21a) and (5.22) in Chapter 5, using the shell property estimates in Table 6.1. The results, as function of bubble diameter, are plotted in Figure 6.10 and Figure 6.11. The theoretical result for an air bubble is plotted in the same diagram for comparison.

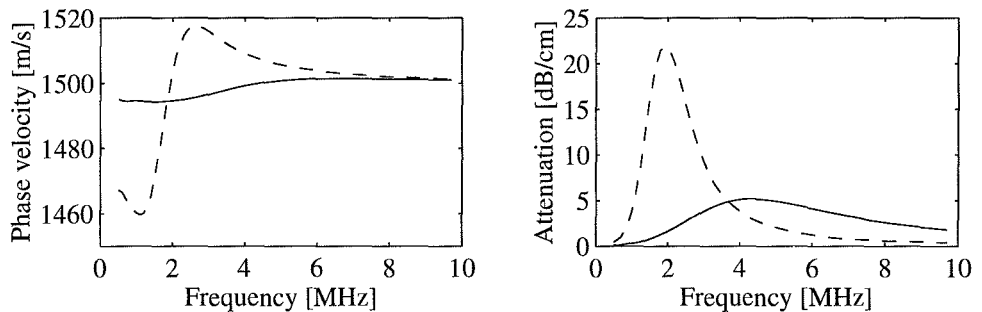


Figure 6.9. Dispersion and attenuation curves calculated for *Sonazoid* compared with air bubbles of the same size. The solid lines are the curves from Figure 6.8, calculated for *Sonazoid* using the estimated shell material properties in Table 6.1. The dashed lines are results calculated for air bubbles of the same size distribution.

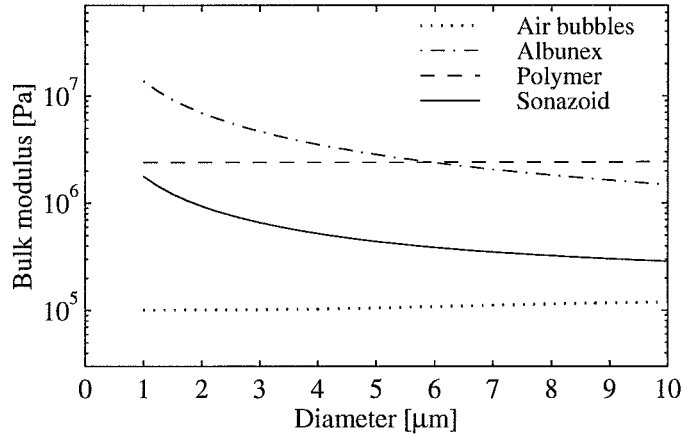


Figure 6.10. Calculated bulk modulus as function of diameter for the three different contrast agents. The theoretical result for a free air bubble is included for comparison.

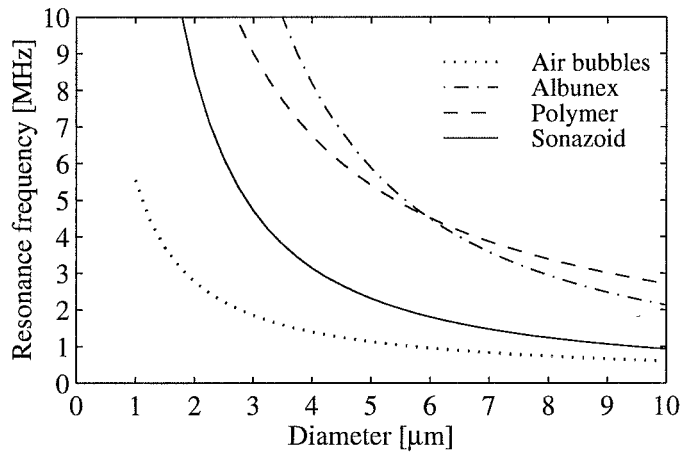


Figure 6.11. Resonance frequency as function of diameter for the three different contrast agents. The theoretical result for a free air bubble is included for comparison.

The main conclusion from the curves in Figure 6.11 is that all the investigated contrast agents have higher resonance frequency than free air bubbles of the same size. The reason for this is found in Figure 6.10: The shell encapsulated contrast agent bubbles are stiffer than the free air bubbles, quantified by their higher bulk modulus.

The dependence of diameter is different between the three bubble types. This is caused by the differences in shell thickness: The polymeric microbubbles have a shell that is assumed proportional to the bubble diameter, while the shell thickness of *Albunex* and *Sonazoid* is assumed constant.

According to the results, the polymeric microbubbles and *Albunex* have around four times higher resonance frequency than air-bubbles of the same size. The resonance frequency of *Sonazoid* is around twice that of air bubbles.

The curves in Figure 6.10 and Figure 6.11 are calculated for driving acoustic frequency equal to 3.5 MHz. The bulk modulus shows a weak dependence on frequency, through the variation in the polytropic exponent κ of the gas. In the diameter and frequency range investigated here, the oscillation is close to isothermal, corresponding to $\kappa \approx 1.0$ independent of the type of gas. The dependence on κ is seen in the curve for the free air bubble, which would have been constant for a constant value of κ .

6.5.2 Scattering Cross Section

The scattering cross section for the different bubble types are calculated using the described theoretical model and parameters. The scattering cross section is plotted as function of diameter in Figure 6.12 and as function of frequency in Figure 6.13. These curves show how the resonance peak is broadened and shifted towards higher diameters and frequencies for the shell encapsulated bubbles. The broadening is explained by the increased damping caused by the viscosity in the shell material.

6.5.3 Damping Constants

The dimensionless damping constants for the three different substances were calculated from the estimated shell parameter values. The results for 3 μm diameter bubbles are plotted in Figure 6.14, and the results for 5 μm diameter bubbles are plotted in Figure 6.15. Results for air bubbles of equal diameter are included for comparison. According to these results, the shell viscosity is the dominating damping mechanisms for all bubbles and diameters for frequencies below 10 MHz. The polymeric microbubbles are more damped than *Albunex* and *Sonazoid*.

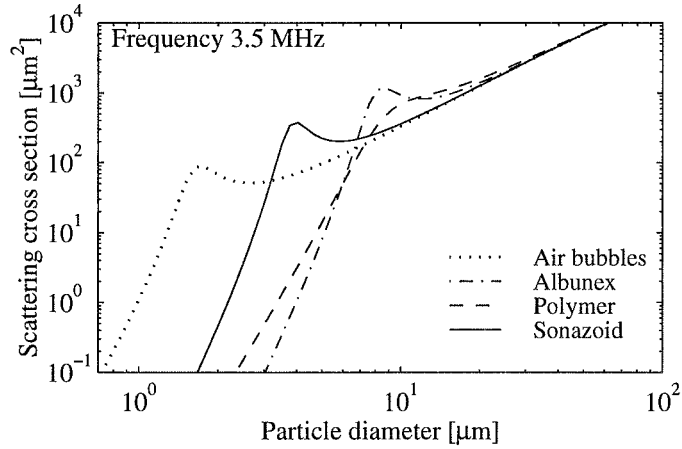


Figure 6.12. Scattering cross section as function of diameter for the three different contrast agents. The theoretical result for a free air bubble is included for comparison.

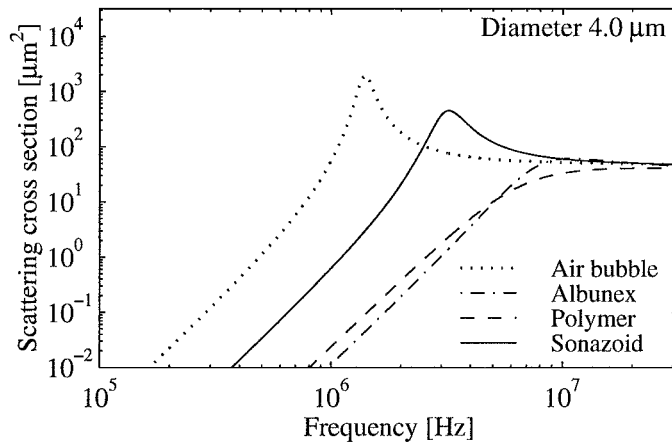


Figure 6.13. Scattering cross section as function of frequency for the three different contrast agents. The theoretical result for a free air bubble is included for comparison.

Note that the presence of a shell changes the values of the other damping constants; δ_{th} , δ_L and δ_c change when the bubble is enclosed in a shell. This is a consequence of the definition of the damping constant δ as depending on the resonance frequency ω_0 . The change in ω_0 due to the shell causes the other damping constants to change when a shell is present.

6.6 Summary: Comparison between the Agents

The main result of this chapter, is that there are differences between the three contrast agents *Albunex*, polymeric microbubbles, and *Sonazoid* that cannot be explained by the bubble size alone.

The acoustic attenuation spectra for all three agents show an increased resonance frequency compared to what is predicted for gas bubbles. This increase in resonance frequency is different for the three agents, and is used to estimate the shell stiffness of the agents. It is concluded that the stiffness of all three agents is mainly determined by the encapsulating shell, not by the gas inside the bubbles. The three agents are different, with the polymeric microbubbles and *Albunex* being the stiffest, and *Sonazoid* being considerably more flexible. A typical *Sonazoid* bubble still has a bulk modulus of around 600 kPa, which is about 6 times the stiffness of a free gas bubble.

The main conclusion from the pressure stability measurements is that the polymeric microbubbles and *Sonazoid* are stable when exposed to hydrostatic pressures found in the cardiac system. Exposed to 120 mmHg pressure, a measurable change in acoustic properties is seen. This change is reversible. When the pressure is released, the initial behavior is retained. The change in acoustic properties during pressure is too small to affect the performance of the products in an ultrasound investigation. When exposed to hydrostatic pressure, *Sonazoid* shows an upshift in resonance frequency, as expected from theory. The response polymeric microbubbles gives a downshift in resonance frequency, which is not so readily explained. It is postulated that this downshift is caused by the shell becoming more flexible, e.g. curled, when the bubbles are exposed to static pressure.

The dispersion measurements show that the introduction of contrast agent bubbles changes the speed of sound in the liquid by less than 1%, for relevant concentrations of microbubbles. The experimental results fit well to the theoretical dispersion curves calculated for shell-encapsulated bubbles. It is concluded that the dispersion introduced by the bubbles is measurable, but the change in sound velocity is too small to cause any distortion of the images.

The estimated shell material parameters are combined with the theory to calculate several acoustic properties of the bubbles. These calculations give

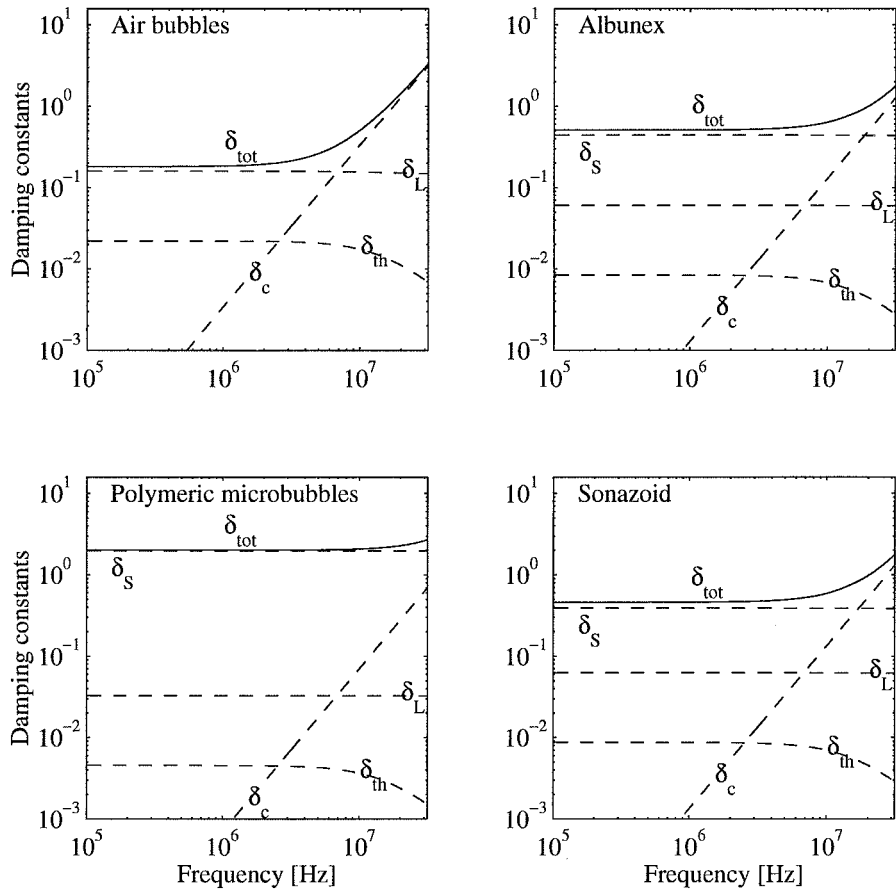


Figure 6.14. Damping constants for the three different contrast agents. The curves are calculated for a $3 \mu\text{m}$ diameter bubble, based on the estimated shell parameter values. Results for a free air bubble are included for comparison. δ_{th} is damping from thermal conduction in the gas, δ_s is from shell viscosity, δ_L is from viscosity in the liquid, δ_c from acoustic radiation and δ_{tot} is the total damping constant.

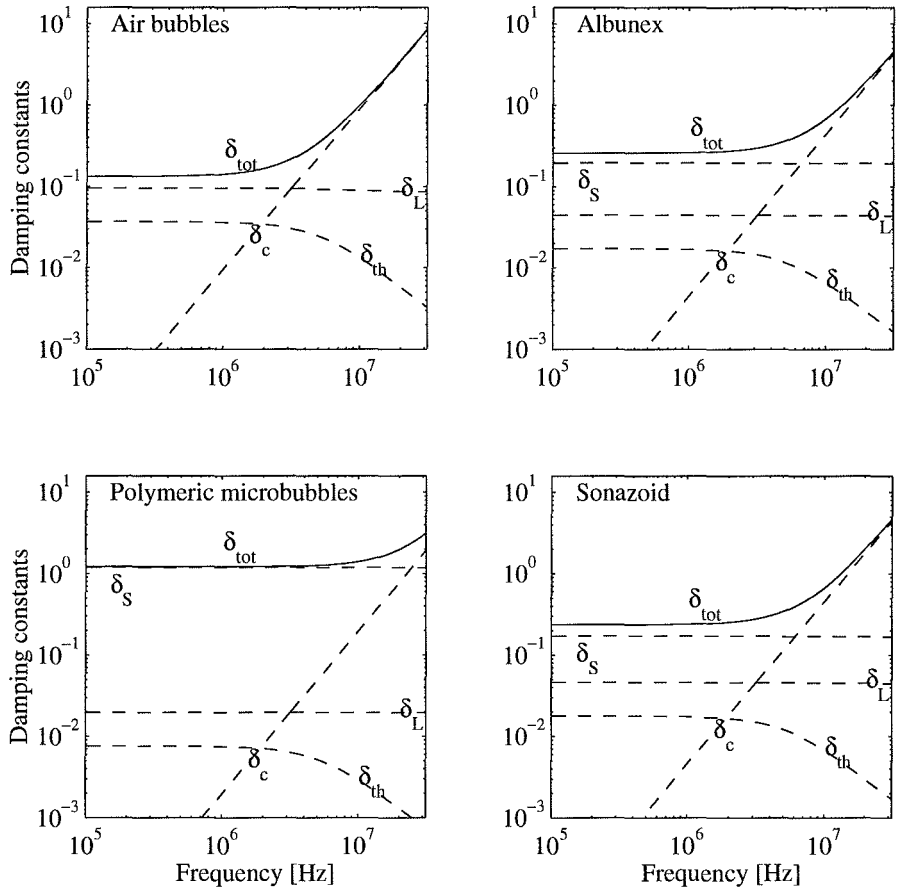


Figure 6.15. Damping constants for the three different contrast agents. The curves are calculated for a $5 \mu\text{m}$ diameter bubble, based on the estimated shell parameter values. Results for a free air bubble are included for comparison. δ_{th} is damping from thermal conduction in the gas, δ_S is from shell viscosity, δ_L is from viscosity in the liquid, δ_c from acoustic radiation and δ_{tot} is the total damping constant.

as results an increased resonance frequency compared to free bubbles of the same size. The curves for scattering cross section are shifted towards higher frequencies and larger diameters compared to the curves for free bubbles. The dimensionless damping constants for all three substances are dominated by the viscosity in the shell. The damping is increased compared to the damping of the free bubble.

Chapter 7

Scatter at Higher Harmonics

The oscillation of gas bubbles is known to be highly nonlinear for moderate driving pressure amplitudes [88]. “Moderate amplitude” means amplitude between 100 and 500 kPa, amplitudes that occur frequently in diagnostic ultrasound imaging. The nonlinear oscillations cause the bubbles to radiate sound at harmonics of the driving acoustic pressure pulse.

This chapter presents results of a study that measured experimentally the scatter at higher harmonics from *Sonazoid*. The experiments were done using the system for backscatter measurements described in Chapter 4.2. The echoes received at the higher harmonics of the transmit frequency were compared with simulations using the theory in Chapter 3.

A shortened version of this chapter was published at the *1999 IEEE Ultrasonics Symposium* [58].

7.1 Experimental Setup

The experimental setup is described in Chapter 4.2. Separate transducers were used for transmit and receive, to obtain the bandwidth needed to receive the higher harmonics of the transmit pulse. The experimental configuration is illustrated in Figure 7.1. See also Figure 4.9 on page 113 for details.

Shaped ultrasound pulses are generated by the programmable function generator (*Wavetek 395*), amplified by 50dB in the power amplifier (*ENI 2100L*) and transferred to the transmitting transducer. The transmitting transducer had center frequency 1 MHz, a large aperture diameter of 38 mm and was strongly focused. The focal length was 50 mm, giving an F-number of 1.3 (*Panametrics Videoscan V392-SU*). Parameters of the transducers used for transmit and receive are listed in Table 7.1.

The transmitting transducer insonified a sample of *Sonazoid* diluted in

Table 7.1. Parameters of the transducers used to measure harmonic scatter.

			Transducers	
			Transmit	Receive
Center frequency	f	MHz	1.0	5.0
Aperture diameter	D	mm	38	10
Focal length	F	mm	50	∞
Panametrics part No.			V392-SU	V326-SU

Isoton II. The contrast agent suspension was contained in a sample cell with thin Mylar film acting as acoustic windows. The transducers and the sample cell with contrast agent was submerged in degassed tap water, acting as transmission medium for the sound pulses.

Scattered sound pulses were received by an unfocused, broadband, 5 MHz

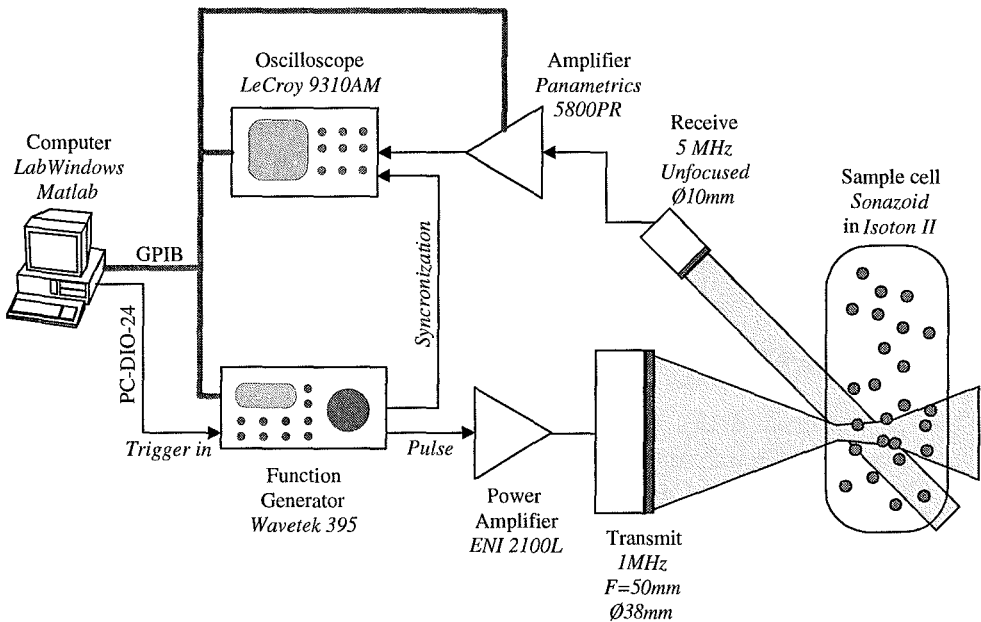


Figure 7.1. Measurement setup for detecting harmonics. The large focused 1 MHz transducer is used for transmit ultrasound pulses. The smaller, unfocused 5 MHz transducer is used to receive scattered echoes from the contrast agent.

Table 7.2. Parameters of the transmit pulses used to measure harmonic scatter.

Frequency	f_i	MHz	1.0
Sample rate	f_s	Msa/s	100
No. of cycles	N_c		20
Voltage amplitudes			
From function generator	V_i	mV	20, 50, 100, 200 and 500
From power amplifier	V_{out}	V	3, 8, 15, 30 and 80
Pulse envelope	$w_M[n]$		Hanning window
Pulse repetition rate	f_{pr}	1/s	10
No. of pulses	N_p		5
Pressure amplitudes			
Measured maxima	P_{max}	kPa	34, 85, 170, 340 and 850
Estimated averages	P_{mean}	kPa	17, 43, 85, 170 and 430

transducer placed at an angle to the transmitting transducer (*Panametrics Videoscan V326-SU*), see Table 7.1. The receiving transducer was aimed at the focal region of the transmitting transducer, as illustrated in Figure 7.1. The received signals were amplified in the receiver section of the *Panametrics 5800PR* ultrasound pulser/receiver and transmitted to the digital oscilloscope (*LeCroy 9310AM*) for digitizing.

The function generator and the digital oscilloscope were connected to the PC-type computer (*Dell Pentium II*) over a GPIB interface. The transmit pulses were programmed and oscilloscope traces were sampled by the computer using the programs described in Chapter 4.2.

7.1.1 Transmit Pulses

The transmit pulses were 20 cycles long sine wave bursts enclosed in a Hanning window, defined in the computer and generated by the *Wavetek* arbitrary function generator. The driving pulse voltage $v(t)$ is expressed as

$$v(t_n) = V_i w_M[n] \sin(2\pi f_i n / f_s), \quad (7.1)$$

where V_i is the voltage amplitude, $w_M[n]$ is a Hanning window of length $M = N_c * f_s / f_i$ [126], N_c is the number of cycles in the pulse, f_s is the sample rate and f_i is the driving frequency. Values of these parameters are

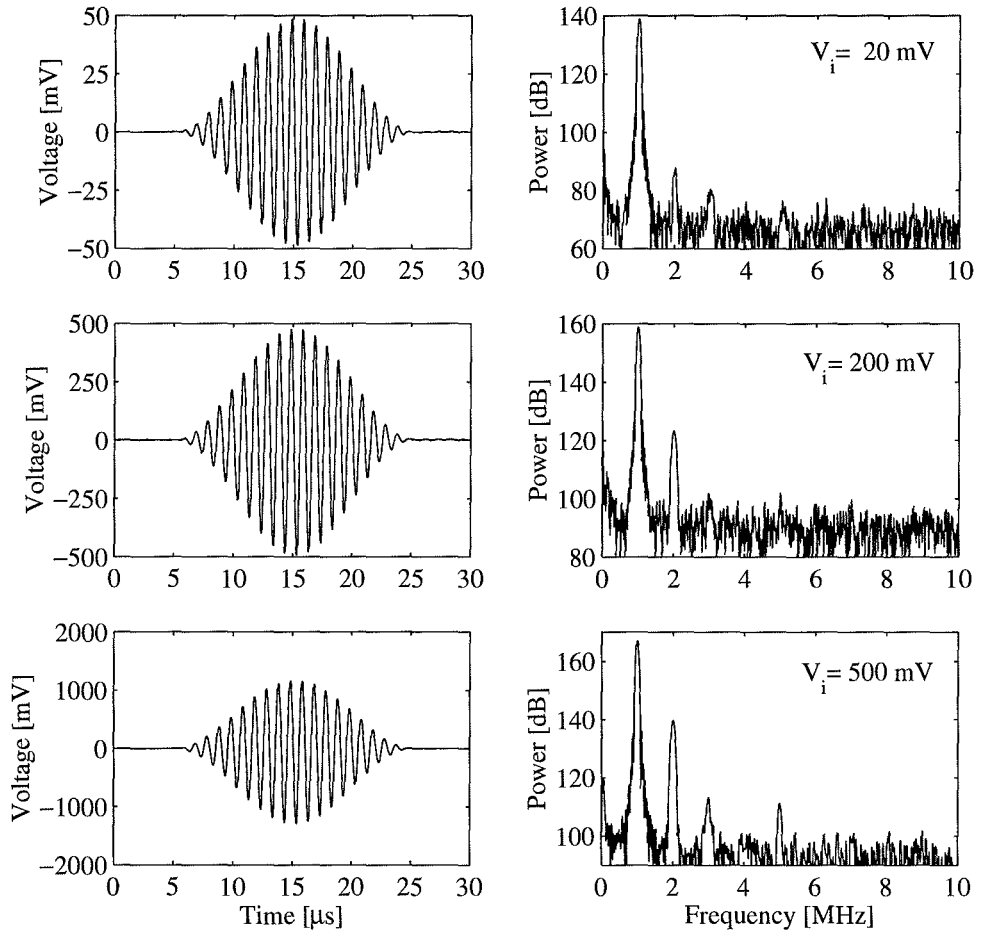


Figure 7.2. Transmitted pulses measured with a *GEC Marconi* membrane hydrophone in focus of the transmitting transducer. The output voltage amplitude from the *Wavetek 395* function generator was set to $V_i = 20, 200$ and 500 mV. The pulses were specified as 20 cycles long sine-wave bursts enclosed in a Hanning-envelope. The center frequency was 1 MHz. The measured spectra are characterized by a narrow main peak at the transmit frequency, low side lobe levels and some 2nd and 3rd harmonics for the higher driving voltages.

listed in Table 7.2. The long pulses were used to obtain a good separation between the harmonics in the received spectra, while the Hanning envelope gave good suppression of the side lobes.

Varying transmit amplitudes were tested by adjusting the voltage from the Wavetek function generator. The open circuit voltage amplitude V_i was varied from 20 mV to 500 mV in 5 steps, see Table 7.2.

The output impedance of the function generator and the input impedance of the *ENI 2100L* RF power amplifier were both 50Ω . The pulses from the function generator were amplified by 50 dB in the power amplifier. The resulting voltages from the power amplifier are listed in Table 7.2.

The transmit pulses and their power spectra were measured with a calibrated hydrophone (*Y-33-7611*, 1 mm bilaminar membrane hydrophone, GEC-Marconi, Chelmsford, UK). The results, measured where the pressure was maximum, are plotted in Figure 7.2. The spectra are characterized by a narrow peak at the transmit frequency, low sidelobe levels outside the main peak, and smaller peaks at the 2nd and 3rd harmonics of the transmit frequency. The peaks at the harmonics increase more strongly than the main peak as the drive voltage increases. The harmonic peaks in the transmit spectra are assumed to be caused by nonlinear propagation through the water. The peak at the third harmonic can also be caused by nonlinearities in the power amplifier.

7.1.2 Receiver Characteristics

An estimate for the frequency response of the receiving transducer was found by measuring its transmit characteristics.

The receiving transducer was excited by short pulses from the *Panametrics 5800PR* pulser/receiver, set at the lowest pulse energy, $12.5 \mu\text{J}$. The transmitted pulse was measured with the *GEC Marconi* membrane hydrophone. The measured pulse and its power spectrum are plotted in Figure 7.3. This spectrum was used as an estimate for the frequency response of the receiving transducer.

7.2 Results

7.2.1 Received Spectra

The suspension was kept in motion during the measurement, causing the echoes to be uncorrelated between different transmit pulses. The echoes from stationary targets are correlated between pulses, and this was used to identify the part of the received traces coming from the contrast agent microbubbles.

The spectral power density in the received traces was estimated by Welch's method [168]. This algorithm is available in *Matlab* as the function *psd* [109]. The sampled traces were subdivided into overlapping segments, and each segment enclosed in a Hanning window. The spectral power density was estimated as the average of the spectral power densities of these segments, calculated from the FFT of each segment. The sample and calculation parameters are listed in Table 7.3. The resulting power spectra were averaged over 5 successive pulses fired at pulse repetition rate 10 pulses/s. These measurements were repeated twice for each driving voltage.

The resulting received spectral power densities are plotted in Figure 7.4. The left column of diagrams show the received spectra for different transmit amplitudes. The middle column of diagrams show the same spectra after compensating for the estimated frequency response of the receiving transducer.

The lowest driving amplitude gives a low peak at the 2nd harmonic, in addition to the peak at the driving frequency 1 MHz. As the driving amplitude increases, peaks at higher harmonics emerge. The power at the harmonics increases more strongly than the level at the driving frequency. For the highest driving pressure amplitude, estimated to about 430 kPa, the microbubbles were destroyed by the acoustic pulses. The received spectra lost its harmonic

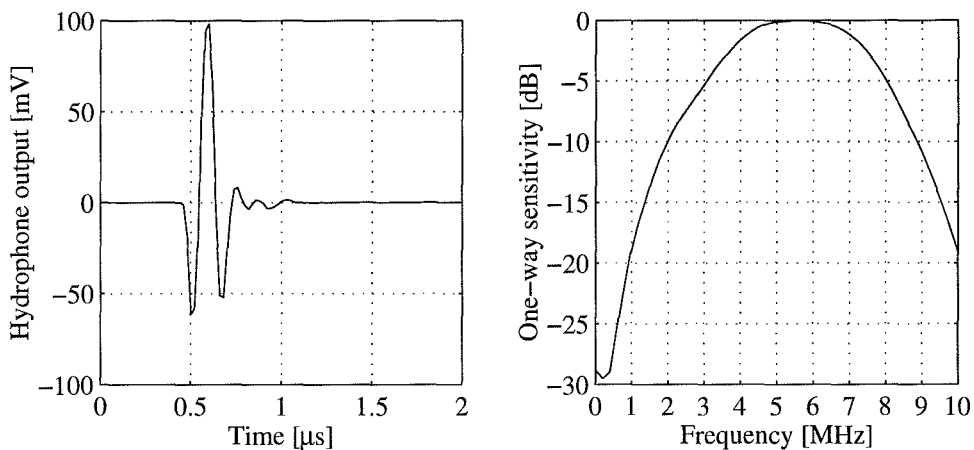


Figure 7.3. Pulses measured with the membrane hydrophone when using the 5 MHz receiving transducer as transmitter. The transducer was excited by short pulses from the Panametrics 5800PR pulser/receiver. The spectrum was used as estimate for the relative receiving sensitivity of the transducer, and used to correct measured spectra for receiver characteristics.

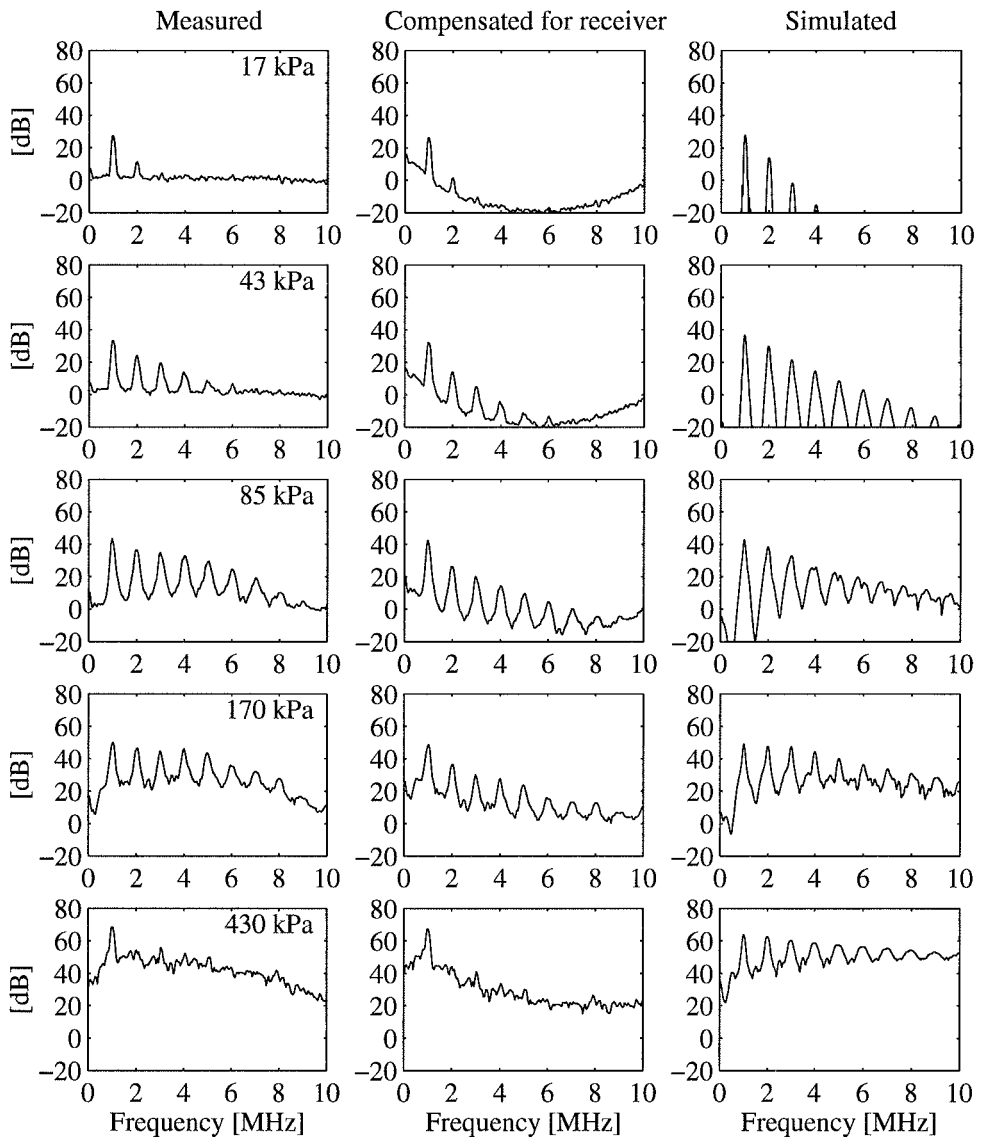


Figure 7.4. Received spectra after transmitting 20 cycles pulses at frequency 1 MHz. Transmit amplitudes were varied from approximately 17 to 430 kPa. The left panels show spectra received by the 5 MHz transducer. The center panels show the same spectra after compensating for the estimated frequency response of the receiver. The right panels show simulated responses for the same pulses, calculated from a visco-elastic shell model.

Table 7.3. Sampling parameters and data used to calculate spectral power density by Welch's method.

Sample parameters	
Sample rate	50 Msa/s
Total sampled length	2500 points $\hat{=}$ 50 μ s
Echoes from contrast agent	2048 points $\hat{=}$ 40 μ s
Distance sampled	30 mm
Spectral power estimator	
Length of FFTs	1024 points $\hat{=}$ 20 μ s
Overlap between FFTs	512 points
Envelope around FFTs	Hanning window
Number of FFTs per trace	3
Frequency resolution	0.05 MHz

structure, and the backscattered power level decreased as the contrast agent bubbles were exposed to several ultrasound pulses.

7.2.2 Simulated Spectra

The size distribution of the *Sonazoid* contrast agent was measured with a *Coulter Multisizer* and used as input for simulating the spectra. The size distribution is plotted in Figure 7.5.

The theoretical spectra were calculated from the Rayleigh-Plesset model with radiation damping added, described by (3.89) on page 76. The effect of the shell was included using the exponential shell model described in Chapter 3.4.2 ((3.145d) on page 89). The shell material parameters for *Sonazoid* were estimated from acoustic attenuation spectra, as described in Chapter 6 (Table 6.1 on page 140). The shell material properties used in the simulations were

$$G_S = 50 \text{ MPa}, \quad \eta_S = 0.8 \text{ Ns/m}^2, \quad d_S = 4.0 \text{ nm}. \quad (7.2)$$

The simulated spectra were calculated as incoherent sums of the power spectra from the single bubbles, using the measured size distribution.

The simulations should be done for pressure amplitudes equal to the actual pressures in the overlap region between the two transducers. The transmitted pressure pulses were measured where the amplitude was maximum. The pressure in an ultrasound beam varies both along and perpendicular to the

acoustic axis. For the circular, focussed transducer used in this experiment, this variation can be modeled quite straightforward [2]. A simulation of the scattered signals should include this variation, by using a weighted sum over the pressure levels in the region studied. This weighted sum over pressure levels has not been calculated, partly because of the computational complexity and partly because the overlap region from which signals were received is not exactly known.

Instead, the simulations were done for average pressure levels roughly estimated to half of the maximum pressures measured. The resulting pressure amplitude values used in the simulations are listed in Table 7.2. This estimates for average pressure amplitude was varied, and the results did not change critically because of this.

The results of these theoretical simulations are plotted in the right column of diagrams in Figure 7.4.

The measured and simulated spectra show the same tendency in the development of the harmonics. The actual pressure driving the bubbles is not accurately known, reducing the accuracy of the comparison. For the highest amplitude, 430 kPa, the bubbles were destroyed by the ultrasound pulses, and the measured results cannot be compared with the simulations.

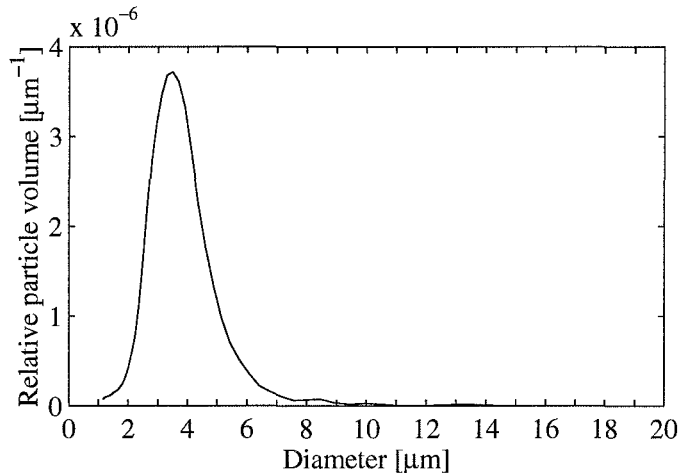


Figure 7.5. Size distribution of the *Sonazoid* sample used to measure scatter at higher harmonics.

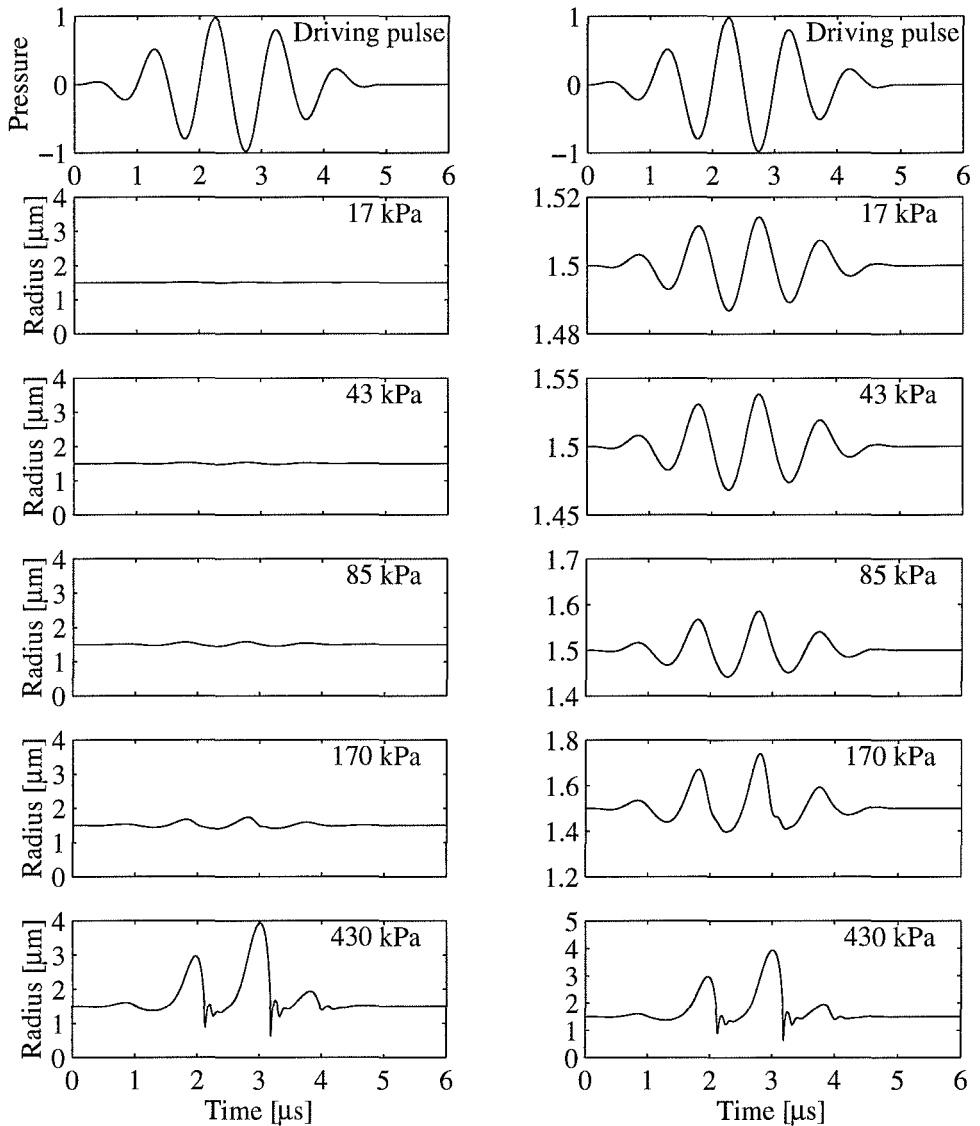


Figure 7.6. Simulated radial oscillation of a *Sonazoid* bubble with diameter $3 \mu\text{m}$. Transmit pulses: 5 cycles at frequency 1 MHz, amplitudes from 17 to 430 kPa. The upper panels show the driving ultrasound pulses, normalized to unit amplitude. The left column of graphs show the radial oscillation plotted with equal y-axis scale, to allow comparison with the equilibrium bubble radius. The right column shows the same results plotted with varying y-axis scale, to illustrate the shape of the oscillations.

7.3 Simulated Bubble Radius and Bubble Destruction

The simulated radial oscillation patterns for the different driving amplitudes are plotted in Figure 7.6. The plotted traces are for *Sonazoid* microbubbles with diameter $3\ \mu\text{m}$. To make the figures easier to interpret, the radial oscillation is plotted for 5 cycle pulses instead of the 20 cycle pulses used to calculate the spectra.

Figure 7.6 shows that for driving pressure amplitudes below about 200 kPa, the radial oscillation amplitude is small compared to the bubble radius. When the driving pressure amplitude increases from 170 kPa to 430 kPa, the radial oscillation increases dramatically. For 430 kPa, the maximum radius of the bubble is almost 3 times its equilibrium radius.

The radial oscillation patterns in Figure 7.6 show a linear and symmetric bubble oscillation for the lower driving amplitudes. As the amplitude increases, the oscillation pattern starts to deviate from this symmetric response, and the response looks more nonlinear.

These simulated radial oscillation traces can be compared with the spectra of the traces scattered from the *Sonazoid* bubbles. The spectra contained increasingly more harmonics as the driving pressure increased, corresponding to an increasingly more nonlinear response from the microbubbles. For the highest driving amplitude, the bubbles were destroyed by the acoustic pulses.

The scattered sound pressure contains more harmonics than the radial bubble oscillation. This is explained by the radiated pressure being roughly proportional to the bubble surface acceleration. In the frequency domain, this corresponds to multiplying the radial oscillation spectra by ω^2 to obtain the spectra of the radiated sound. This causes the radiated pressure to show a more nonlinear response, with higher harmonic levels, than the radial bubble oscillation.

For 430 kPa driving pressure, the radial oscillation amplitude becomes larger than the equilibrium bubble radius. Experimentally, it was observed that the bubbles were rapidly destroyed at this pressure amplitude. Quantitative models for instability of oscillating bubbles were studied by Plesset in 1954 [134], more elaborate models are given by Hsieh and Plesset [65] and by Eller and Crum [38]. These studies consider the growth of shape oscillations in free bubbles, describing the bubble oscillations with spherical harmonics. Reviews of this approach to bubble stability is given by Plesset and Prosperetti [136] and in the book by Leighton [93]. The models, especially those by Hsieh and Plesset and by Eller and Crum, end up with rather elaborate criteria for the stability of oscillating bubbles.

These models for surface stability were formulated for free air or vapor bubbles, and need modifications to be valid for the shell encapsulated bubbles studied here. This has not been done.

A very simple criterion for the stability of bubbles was given by Plesset and Mitchell in 1956 [135, 93], who studied the stability of free vapor bubbles in water. Plesset and Mitchell's stability criteria are formulated by the ratio between the maximum and the minimum bubble radius as

$$\frac{a_{max}}{a_{min}} \begin{cases} < 5 & \text{Bubble is stable.} \\ > 10 & \text{Bubble is unstable.} \end{cases} \quad (7.3)$$

Figure 7.7 shows the ratio between maximum and minimum bubble radius from the simulated bubble oscillations. The ratio between a_{max} and a_{min} is plotted as function of the driving acoustic pressure amplitude. The Plesset-Mitchell stability criteria are indicated for comparison. It must be warned that these criteria were derived for vapor bubbles, and cannot be expected to be directly valid for the encapsulated, gas filled *Sonazoid* microbubbles studied.

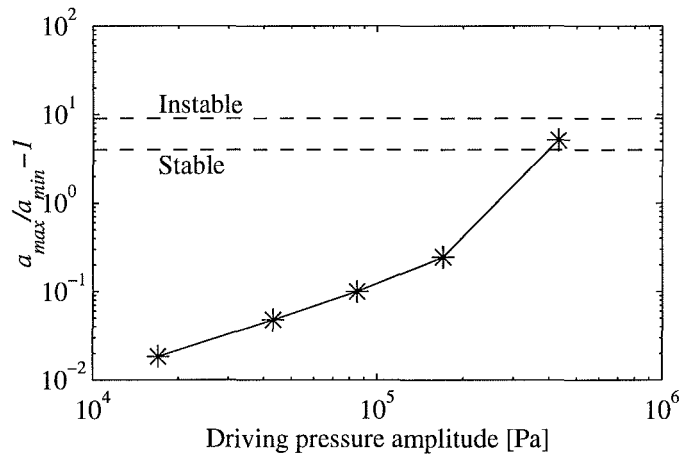


Figure 7.7. Simulated ratio between maximum a_{max} and minimum a_{min} bubble radius during the oscillations, plotted as function of the driving pulse amplitude. The values for a_{min} and a_{max} are taken from Figure 7.6. The Plesset-Mitchell [135] stability criteria for vapor bubbles are indicated for comparison. Experimentally, the bubbles were observed to be destroyed by the sound pulses for the highest driving amplitude, corresponding to the last point on this graph.

7.4 Discussion

The experimental results in this chapter have verified that the scatter of sound from *Sonazoid* is nonlinear at pressure amplitudes used in diagnostic medical imaging.

The comparison between measured and simulated spectra show the same tendency in the development of the harmonics. The comparison is rather rough, mainly because of uncertainties in the actual transmit pressure levels. An exact quantitative conclusion cannot be drawn from the comparison. But the similarity between measured and simulated spectra, and the tendency with increasing drive level, is good enough to have confidence that the model describes the main features of the bubble oscillation.

The simulations were repeated using the theoretical model for a bubble without shell, by setting the shell thickness in (7.2) to $d_{se} = 0$. These simulations predicted much higher harmonics than what was measured, giving a very poor agreement between the measured and simulated spectra.

Bubble destruction from exposure to the acoustic pulses was observed for the highest driving pressure only. The simulated bubble radial oscillation gave as result that the maximum bubble radius was approximately three times the equilibrium radius for this driving amplitude. This corresponds well with the observed destruction: Bubbles are destroyed when the oscillation amplitude becomes large compared to the equilibrium radius.

There seems to be a threshold effect in the maximum radius. When the driving pressure passes from 170 kPa to 430 kPa, a dramatic increase in maximum bubble radius is observed. This can be compared with the particle stiffness, the bulk modulus. This was estimated in Chapter 6 to about 700 kPa for a *Sonazoid* bubble of diameter 3 μm . Since the bubble stiffness is nonlinear, the bulk modulus is not constant: It decreases as the bubble is expanded. For driving frequencies below resonance, the bubble oscillation is mainly determined by the bubble stiffness. When the negative pressure amplitude approaches or exceeds the bubble bulk modulus, the stiffness force that limits bubble expansion is small, and the bubble can be expanded to a very large radius. Under these conditions, the bubble expansion is limited only by the inertia of the displaced liquid and by the duration of the negative pressure cycle.

7.5 Conclusion

Form these experiments, it is concluded that the nonlinear scatter from *Sonazoid* can be predicted using the model for a shell-encapsulated bubble. Mod-

eling the *Sonazoid* microbubble as gas bubbles without a shell gives strong deviations from the experimentally observed spectra.

This study is a preliminary experiment giving promising results regarding the validity of the theoretical understanding of the nonlinear scatter from *Sonazoid*. More studies are needed to test the model more completely. Better calibration of the pressure field from the transmitting transducer is needed, as is better calibration of the receiver. Different transmit frequencies should also be tested.

Chapter 8

Simulations of Nonlinear Bubble Response

8.1 Implementation of Nonlinear Bubble Models

The models described in Chapter 3 have been implemented using the numerical software package *Matlab* (The Math Works Inc., Natick, Mass., USA). The implementation is done as a set of functions in *Matlab*. Graphical user interfaces have been written, to allow quick and intuitive user operation.

The *Matlab* functions calculate the bubble response to a driving ultrasound pulse, using one of the liquid models in Chapter 3 together with a model for the shell.

The input pulse driving the bubble is defined by the user. It is either a “synthetic pulse” specified by a set of pulse parameters, or it is a measured pulse loaded from a file. The user also specifies parameters of the bubble: radius and thickness, elasticity, and viscosity of the shell. A list of the input parameters is found in Table 8.1. The graphical user interface used to operate the program and an example of calculated results are displayed in Figure 8.1.

The response is calculated by simulating the ordinary differential equation corresponding to the selected liquid model, with the boundary condition at the bubble surface given by the shell model, see Chapter 3. The response is simulated in time domain: bubble radius as function of time, and radiated acoustic pressure at distance 1 m from the bubble center. For comparison, the bubble response can also be calculated from the linearized model in Chapter 2.

The bubble dynamics is modeled by a second order ordinary differential equation. This equation is solved numerically using an embedded Runge-Kutta algorithm of order 4 and 5 [70], using the coefficients by Dormand and Prince [35]. This algorithm is available a standard function in *Matlab* [108],

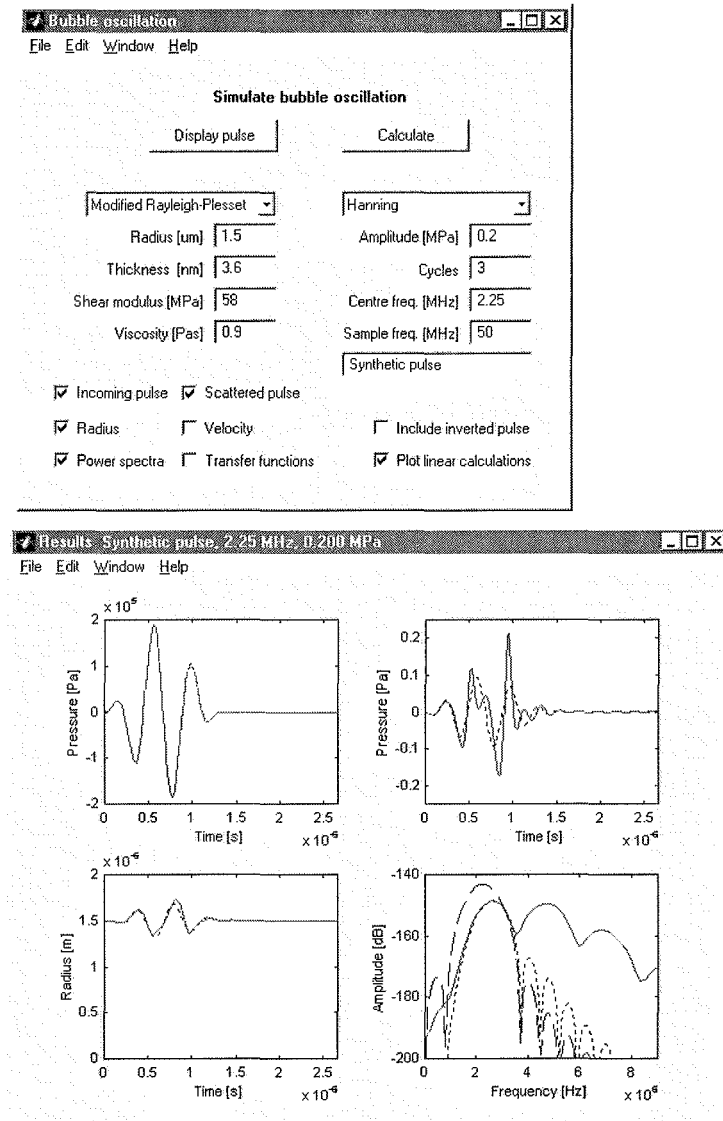


Figure 8.1. Graphical user interface windows used to simulate bubble response. The upper window is the user interface used to run the program. The lower window is an example of a *Bubblesim* calculation. The graphs show the the driving ultrasound pulse (upper left), the simulated scattered pulse (upper right), the bubble radius (lower left) and the spectra of incoming and scattered pulse (lower right). Results of a linearized model are plotted with dotted lines for comparison.

Table 8.1. Simulation of bubble bubble response to a driving ultrasound pulse. Input parameters specified by the user.

Bubble parameters	Bubble radius [μm] Shell thickness [nm] Shell shear modulus [MPa] Shell shear viscosity [Ns/m^2]
Driving sound pulse	
Measured	Load from file. Specify file name
Synthetic	Frequency [MHz] Amplitude [MPa] Length [cycles] Envelope (Rectangular, Hanning, cosine-tapered rectangular etc.)
Theoretical model	Rayleigh-Plesset Modified Rayleigh-Plesset Trilling Keller-Miksis
Results to plot	Driving pulse $p_i(t)$ Scattered pulse at distance 1 m $p_s(t)$ Bubble radius $a(t)$ Bubble wall velocity $\dot{a}(t)$ Power spectra $P_i(f), P_s(f)$ Linear transfer functions $H_x(f), H_p(f)$ Inverted pulses Linear model calculations

called *ODE45*. The implementation of this algorithm is described in detail by Champine and Reichelt [150].

For some combinations of bubble radius and driving pulse parameters, the resulting differential equation can become *stiff*, making the numerical solution more difficult. Stiff means that there are large variations in the time scales involved. Stiffness mainly occurs at low driving frequency and large driving pressure amplitude. Here, the bubble radius changes slowly during the expan-

sion phase, but can go through very rapid changes in radius and velocity in the compressional phase. For these stiff conditions, a multistep ODE solver of variable order can be more suited than the Runge-Kutta algorithm described above [71]. The stiff ODE solver of order 1 to 5 available as *Matlab* function *ODE15s* [108, 150] has proven to be more reliable and stable for solving some of these more extreme situations.

8.1.1 Simulation Parameters

The rest of this chapter describes results of bubble simulations using the program *Bubblesim*. The equations and parameters used in these simulations are taken from Chapter 3. They are summarized here as

Equation of motion: Rayleigh-Plesset with radiation damping (Equation (3.89) on page 76)

$$a\ddot{a} + \frac{3}{2}\dot{a}^2 - \frac{p_L - p_0 - p_i}{\rho} - \frac{a}{\rho c}\dot{p}_L = 0. \quad (8.1a)$$

Boundary condition: Pressure p_L at the bubble wall, using the exponential shell model (Equations (3.145d) on page 89 and (3.151) on page 92)

$$p_L = -4\eta_L \frac{\dot{a}}{a} + 12 \frac{d_{Se}}{a_e} \left(G_S x_0 (1 - e^{-x/x_0}) + \eta_s e^{-x/x_1} \dot{x} \right) + p_0 \left(\frac{a_e}{a} \right)^{3\kappa}, \quad (8.1b)$$

$$x = \frac{a - a_e}{a_e}, \quad \dot{x} = \frac{\dot{a}}{a_e}, \quad x_0 = \frac{1}{8}, \quad x_1 = \frac{1}{4}.$$

Shell parameters, estimated in Chapter 6 (Table 6.1 on page 140)

$$d_{Se} = 4.0 \text{ nm}, \quad G_S = 50 \text{ MPa}, \quad \eta_S = 0.8 \text{ Ns/m}^2. \quad (8.1c)$$

8.2 Pulse Inversion

Pulse Inversion Imaging is a promising technique for contrast agent imaging. The technique consists of transmitting two pulses with inverted polarity into the tissue. The nonlinear response is singled out by looking at differences in the echoes from the two pulses. Since the bubble responds more nonlinearly than the tissue, this should enhance the bubble echoes compared to the tissue echoes. The processing is normally done by summing the received signals, but using the Doppler demodulated signal has also been suggested [156].

Bubbles are known to respond nonlinearly to a driving ultrasound pulse, the response being asymmetric in compression and expansion. It is therefore no surprise that a bubble responds differently to pulses with inverted polarity.

Experimental observations of the response of single contrast agent bubbles to inverted ultrasound pulses was reported by Morgan et al. in 1997 [116, 115]. They observed that the scattered pulses were not inverted, but looked more like phase-shifted copies of each other. They also reported differences in frequency content in the responses of the inverted pulses.

In Chapter 3, it was shown that in a linear system, the response of two inverted pulses are inverted copies of one another: Let $L\{x\}$ be a linear operator describing the system. The response to an inverted input signal is

$$L\{x(t)\} = y(t), \quad L\{-x(t)\} = -L\{x(t)\} = -y(t). \quad (8.2)$$

The inverted input causes an inverted response, and the sum of the responses vanishes

$$L\{x(t)\} + L\{-x(t)\} = y(t) - y(t) = 0, \quad (8.3)$$

This is not true for a nonlinear system. The nonlinear system is described by the operator $N\{x\}$, giving

$$N\{-x(t)\} \neq -N\{x(t)\}, \quad N\{x(t)\} + N\{-x(t)\} \neq 0, \quad (8.4)$$

For the nonlinear system, the sum of the responses to inverted signals does not vanish.

The aim of this section is to simulate the response to inverted pulses, showing how some of the reported results can be understood from the bubble dynamics, based on the theoretical models from Chapter 3. The pulse amplitude is varied to investigate the transition from a linear to a nonlinear response as the amplitude increases.

The contrast agent microbubbles are modeled as gas bubbles encapsulated in a thin shell. The dynamics of the liquid is described by the Rayleigh-Plesset equation, modified to include radiation damping, as described in Chapter 3. The shell is modeled as viscoelastic, using the material parameters estimated for *Sonazoid* in Chapter 6. The exponential shell model is used. This results in the theoretical model for *Sonazoid* summarized in the equations (8.1a), (8.1b) and (8.1c). All simulations are done on a $1.5 \mu\text{m}$ radius ($3.0 \mu\text{m}$ diameter) *Sonazoid* microbubble. The simulation parameters are listed in Table 8.2.

Morgan et al. [115] refer to calculations using the Gilmore equation, without a shell encapsulating the gas. Results from this model ought to agree qualitatively with the shell-encapsulated model used here. But the shell model predicts a stiffer and more damped microbubble, which may cause differences in amplitude and frequency scaling.

Table 8.2. Parameters used to simulate response to inverted pulses. For definitions, see Chapter 3.

Bubble	Radius	1.5 μm
Shell	Thickness	4.0 nm
	Shear modulus	50 MPa
	Shear viscosity	0.8 Ns/m ²
Driving pulse	Frequency	2.25 and 6.0 MHz
	Amplitude	10 to 500 kPa
	Length	3 cycles
	Envelope	Hanning window
Liquid model	Rayleigh-Plesset with radiation damping (Chapter 3, (3.89) on page 76)	
Shell model	Exponential (Chapter 3, (3.145d) on page 89)	
Calculated results	Scattered sound pulse	
	Scattered sound spectrum	
	Bubble radius	

8.2.1 Results of Simulations

Driving pulses with center frequency 2.25 MHz and 6.0 MHz were tested. The pressure amplitudes were varied from 10 to 500 kPa. See Table 8.2 for details. The driving pulses are plotted in Figure 8.2.

Simulated responses from the bubble are plotted in Figures 8.3 to 8.11. The first of the driving pulses is denoted “positive”, the second, being equal to the first with inverted polarity, is denoted “negative”. This choice of names is arbitrary.

Time Responses

Figure 8.3 shows simulated scattered pressure for driving pulse frequency 2.25 MHz. The amplitude is scaled with the amplitude of the driving pulse.

The two first columns in Figure 8.3 show the responses to the individual driving pulses. For the lowest amplitudes, the responses look like inverted copies of each other. As the driving pressure increases, the responses start to

deviate this. For the highest driving amplitudes, the responses look more like phase-shifted versions of one another. This is as reported experimentally by Morgan et al. [115]. The simulations also show that the response amplitudes increases more than linearly with the driving pulse amplitude.

The third column of pulses in Figure 8.3 display the sums of the two individual responses. For the lower amplitudes, the sum of the two responses is much weaker than the response from each pulse, demonstrating that the response in this range is dominantly linear. As the pressure amplitude passes 100 kPa, the summed responses become comparable to the responses of the individual pulses. The bubble response is highly nonlinear at these higher amplitudes.

Cross-Correlations

Figure 8.4 shows the cross-correlation of the responses to the positive and negative pulses, from Figure 8.3.

For the lowest driving amplitudes, the cross-correlation has a negative peak reaching -1 at zero time lag, $t = 0$. This corresponds to the two pulses being dominantly inverted copies of one another. Two lower positive peaks are found at time shifts corresponding to half a period time shift, $t = \pm\frac{1}{2}T = \pm 0.22 \mu\text{s}$.

When the driving pressure amplitudes increases above 100 kPa, the negative peak at $t = 0$ decreases and eventually vanishes. As the driving amplitude increases, the positive peak at time lag $t = -\frac{1}{2}T$ becomes the dominating peak in the cross correlation plots.

This change in the cross-correlation peak illustrates the transformation in response as the driving pressure increases: The responses change from inverted versions to time shifted versions of one another, the dominating peak in the cross-correlation plot moves from a negative peak at $t = 0$ to a positive peak at $t = -\frac{1}{2}T$.

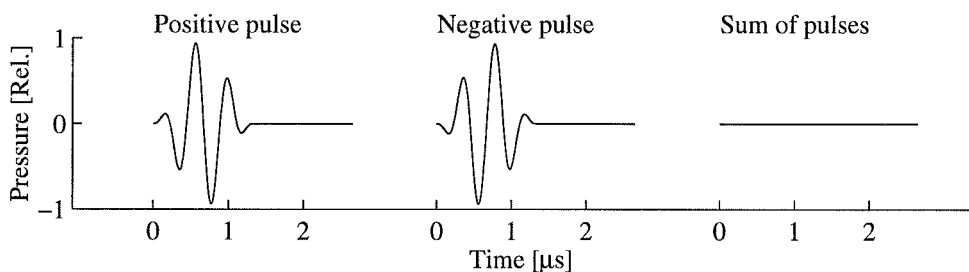


Figure 8.2. Driving inverted pulses. Frequency 2.25 MHz.

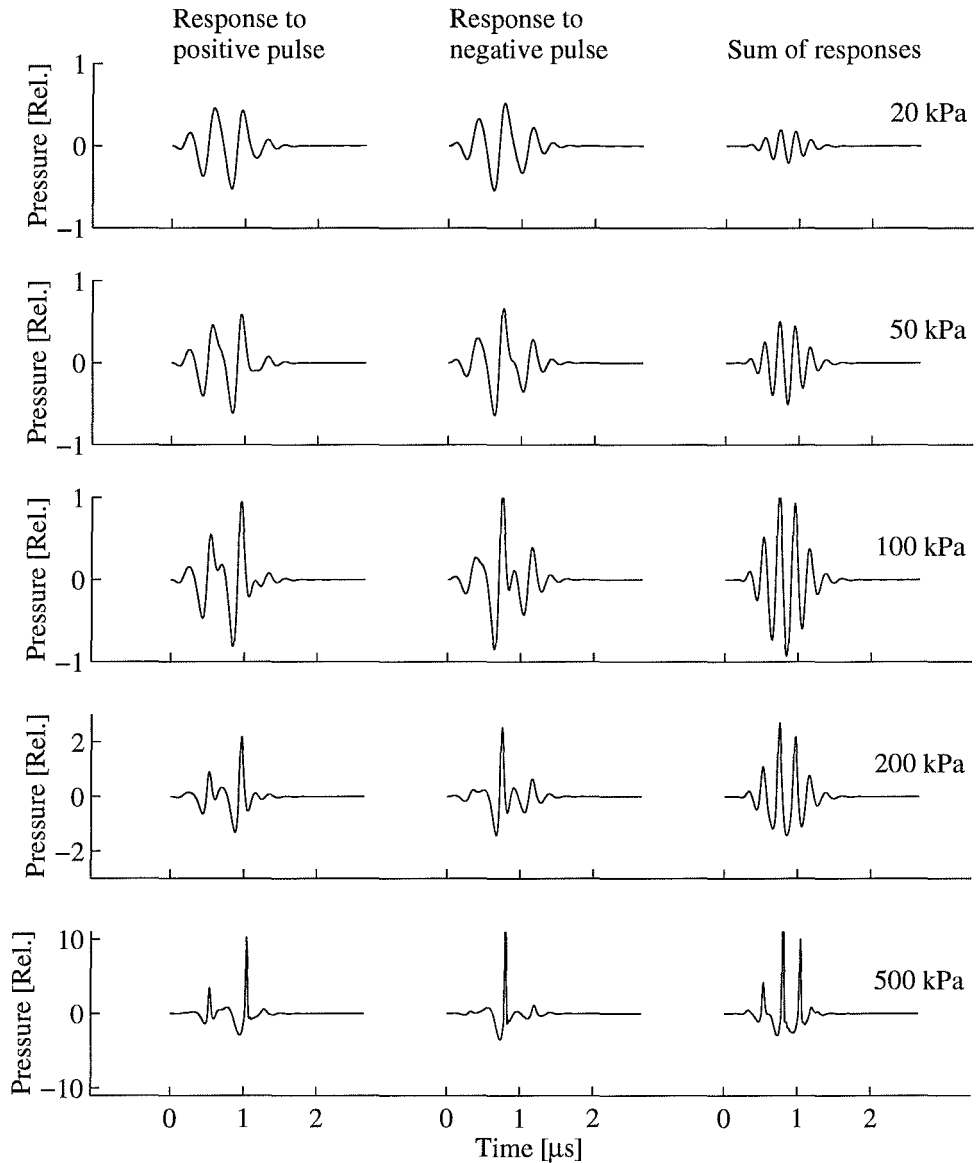


Figure 8.3. Response to inverted pulses for various driving amplitudes. Frequency 2.25 MHz. Responses to the positive pulse (left), to the negative pulse (middle) and the sum of the responses (right). The amplitudes are normalized to the driving pulse amplitude.

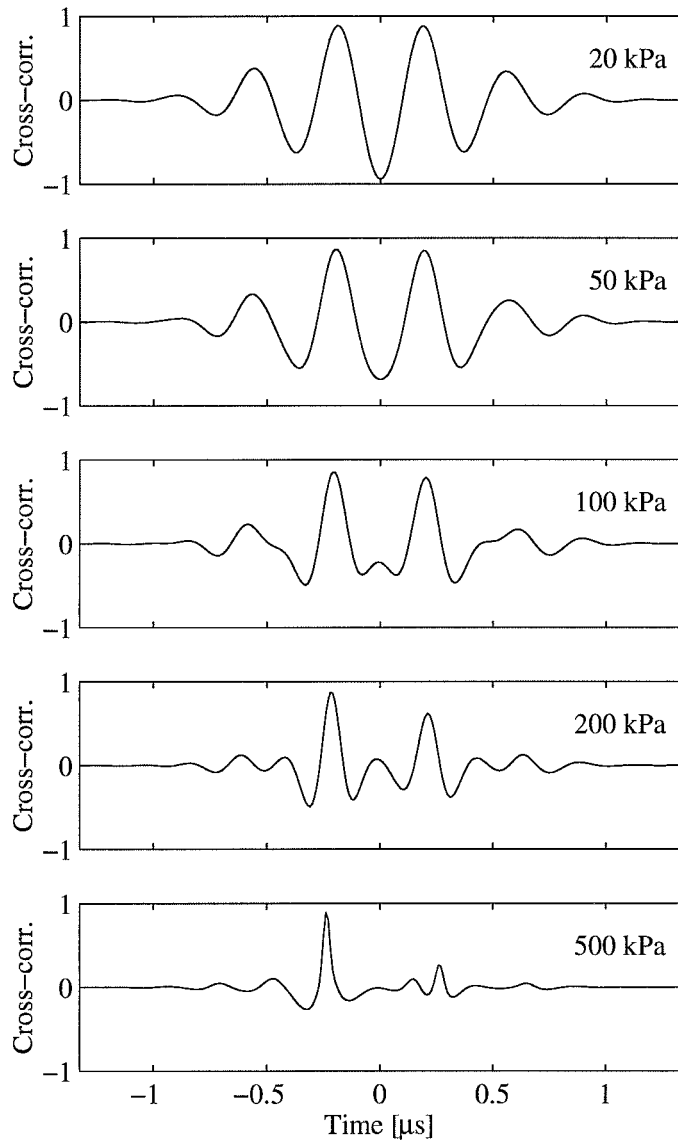


Figure 8.4. Cross-correlations of the responses in Figure 8.3. Frequency 2.25 MHz.

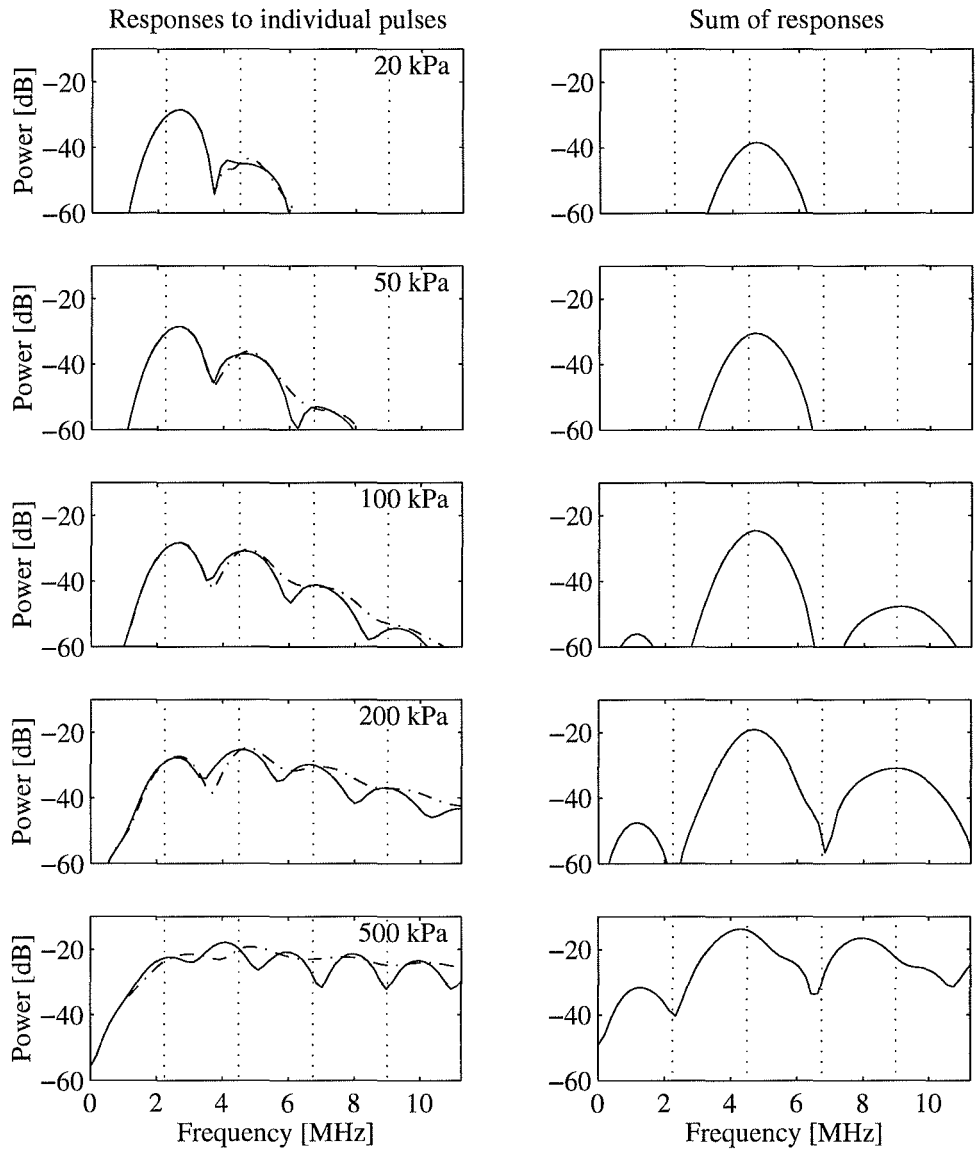


Figure 8.5. Spectra of the responses in Figure 8.3. Frequency 2.25 MHz. The left column of graphs is the response to the individual pulses, positive pulse (solid line) and negative pulse (dashed line). The right column is the spectra of the summed responses. The driving frequency and its harmonics are marked with dotted lines in the plots.

Spectra

Power spectra of the pulses in Figure 8.3 are plotted in Figure 8.5. The left column of graphs shows the power spectra of the responses, the right column shows the spectra of the summed responses.

At the lowest driving amplitudes, the spectra of the individual responses has a peak around the transmit frequency. As the driving pressure amplitude increases, peaks appears at the harmonics of the transmit frequency. For the highest driving amplitudes, the harmonic peaks overlap, and the spectra become smeared out.

The spectra of the individual pulses are very similar for the lowest drive levels. This agrees with the impression from Figure 8.3 that these responses are close to linear. As the drive level increases above 100 kPa, differences start to occur in the response spectra. The spectra from positive and inverted pulses are very similar around the driving frequency, but deviate outside this main lobe.

The right column in Figure 8.5 shows the spectra of the summed responses from Figure 8.3. The sum spectra have their main peak at the second harmonic of the transmit frequency. The driving frequency is completely suppressed.

As the drive level increases, the height of this second harmonic peak increases rapidly. It reaches approximately the same level as the peaks of the individual pulses for a driving pressure amplitude of 100 kPa. This corresponds to the results from the summed responses in Figure 8.5.

These spectra show how the pulse inversion and summation technique suppresses the driving frequency and enhances the second harmonic. More general, the pulse inversion technique suppresses the odd harmonics and enhances the even harmonics.

An interesting change occurs at the highest driving amplitude, 500 kPa. At this amplitude, the suppression of the odd harmonics is not so strong, and there is some energy around the driving frequency. This is interesting, as the weak nonlinearities from propagation through tissue tend to suppress the driving frequency completely. Hence, signals received around the driving frequency after pulse inversion and summation may further enhance echoes from bubbles above echoes from tissue.

Radius

Figure 8.6 displays the simulated bubble radius as function of time, for the various driving amplitudes. The left column of plots is the bubble response to the positive pulse, the middle column is the response to the negative pulse. The right column shows the two radial responses together.

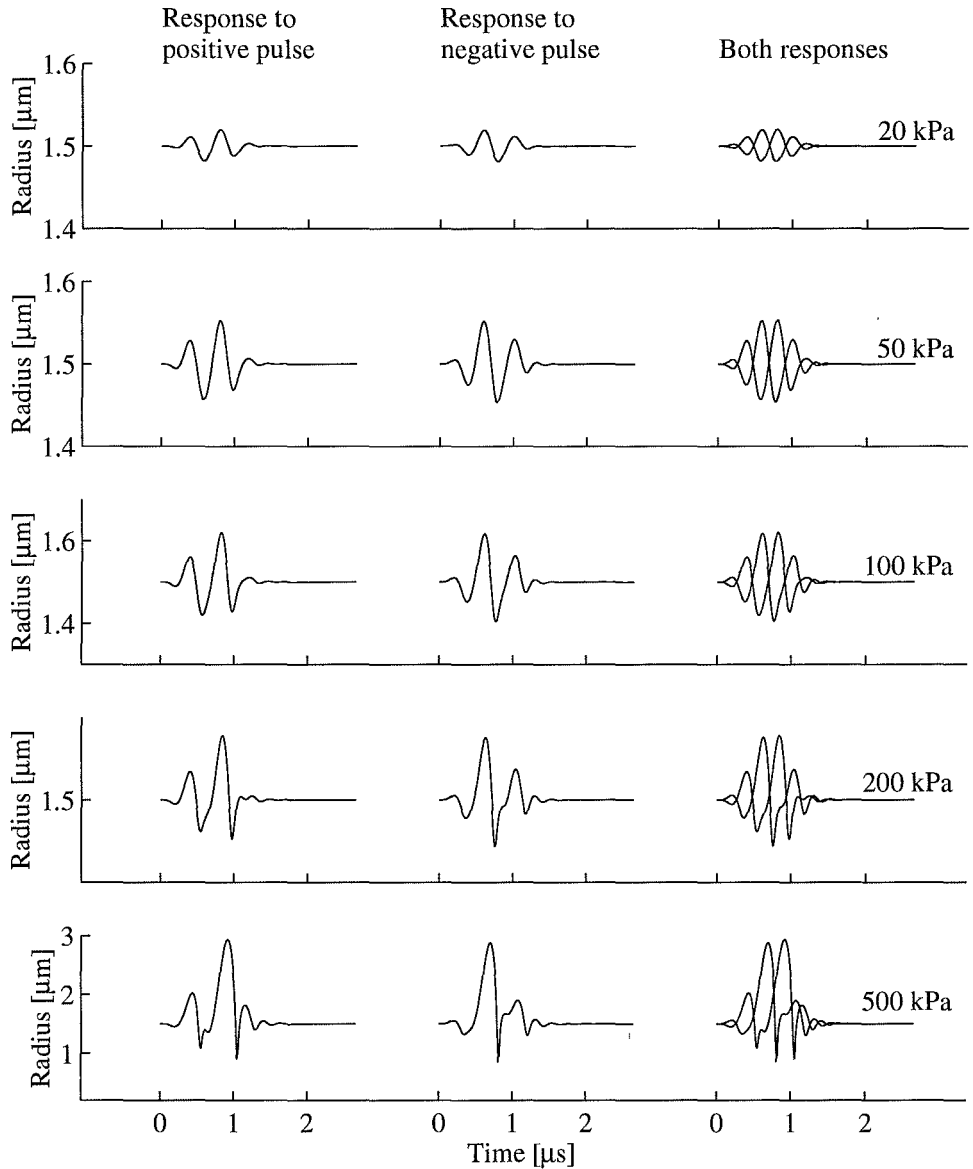


Figure 8.6. Simulated bubble radius for the responses displayed in Figure 8.3. Response to the positive pulse (left column) to the negative pulse (middle column), and both responses together (right column) The y-axis scale differs between the plots.

For the lowest driving amplitudes, the bubble radius oscillates gently around its equilibrium value. The radial oscillation amplitude is here much smaller than the equilibrium radius. As the driving amplitude increases, the radial oscillation amplitude becomes comparable to the equilibrium radius, and the asymmetric nature of the oscillation becomes clear. The bubble is easier to expand than to compress. For the highest amplitude, the radial oscillations look more like phase-shifted than inverted versions of one another. At the highest amplitude, the oscillation pattern is mainly determined by the negative half cycles of the driving pressure pulses.

Frequency Dependence

The results in Figure 8.3 to Figure 8.6 were calculated for driving frequency 2.25 MHz. The same calculations for driving frequency 6.0 MHz are plotted in Figure 8.8 to Figure 8.11. The driving pulses are plotted in Figure 8.2.

The frequency 6.0 MHz is rather high for medical ultrasound imaging. This frequency was selected to illustrate the response for a driving frequency above resonance frequency of the bubble.

The frequency 2.25 MHz is below resonance for the bubble, while 6.0 MHz is above resonance. The tendencies in the 6.0 MHz graphs are similar to those in the 2.25 MHz graphs, but there are differences. The bubble response is less nonlinear at 6.0 MHz. This can be seen by noting that the summed response and the level of the second harmonic is much lower for 6.0 MHz than for 2.25 MHz driving frequency. The transition in the response from inverted to phase-shifted versions is not seen for 6.0 MHz driving frequency.

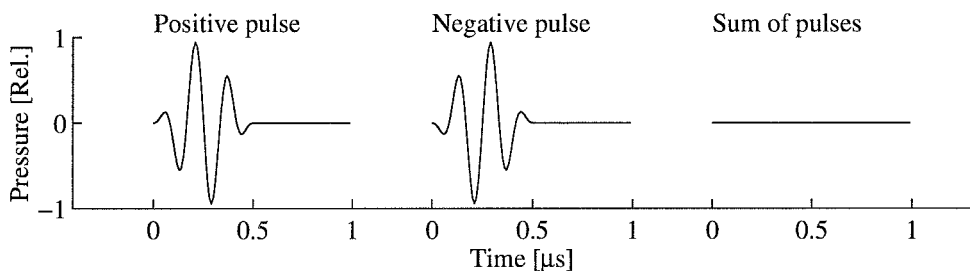


Figure 8.7. Driving inverted pulses. Frequency 6.0 MHz.

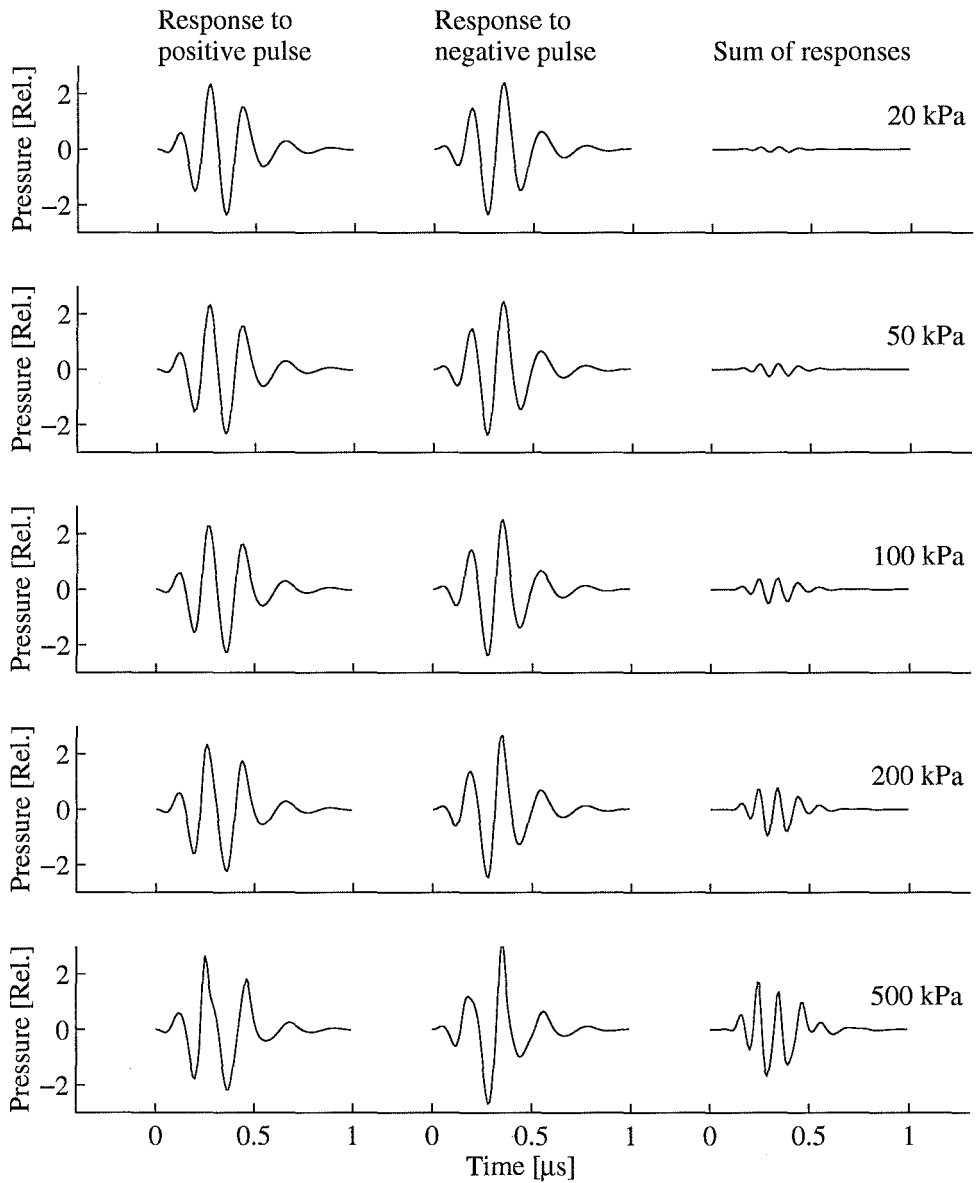


Figure 8.8. Response to inverted pulses for various driving amplitudes. Frequency 6.0 MHz. Responses to the positive pulse (left), to the negative pulse (middle) and the sum of the responses (right). The amplitudes are normalized to the driving pulse amplitude.

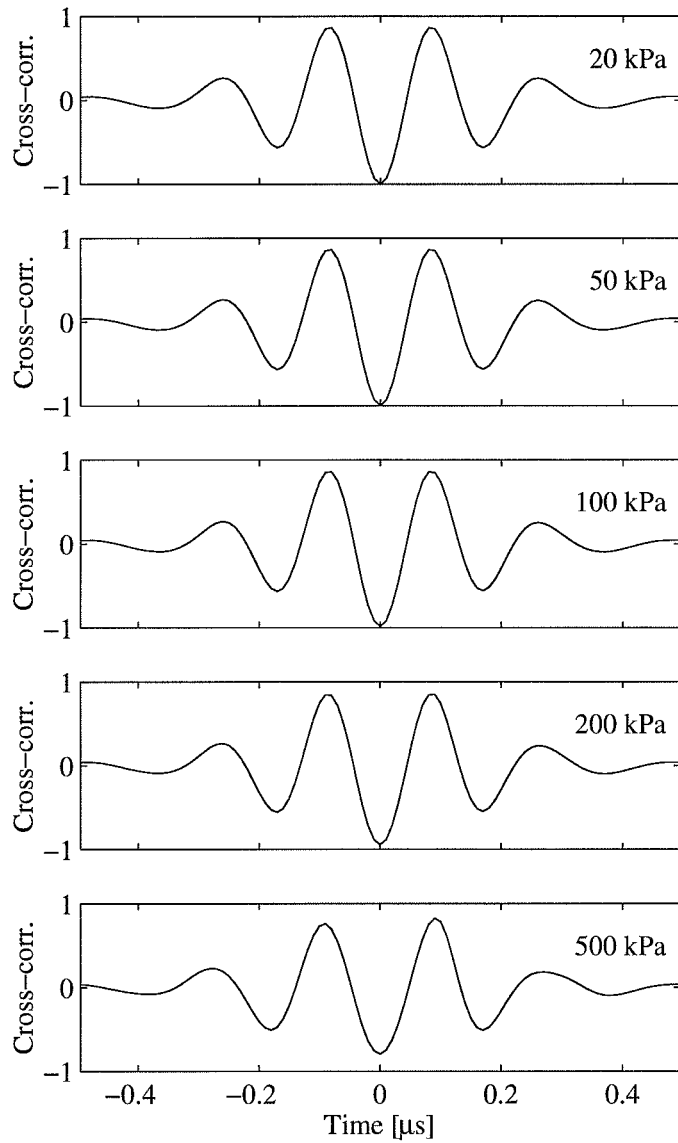


Figure 8.9. Cross-correlations of the responses in Figure 8.8. Frequency 6.0 MHz.

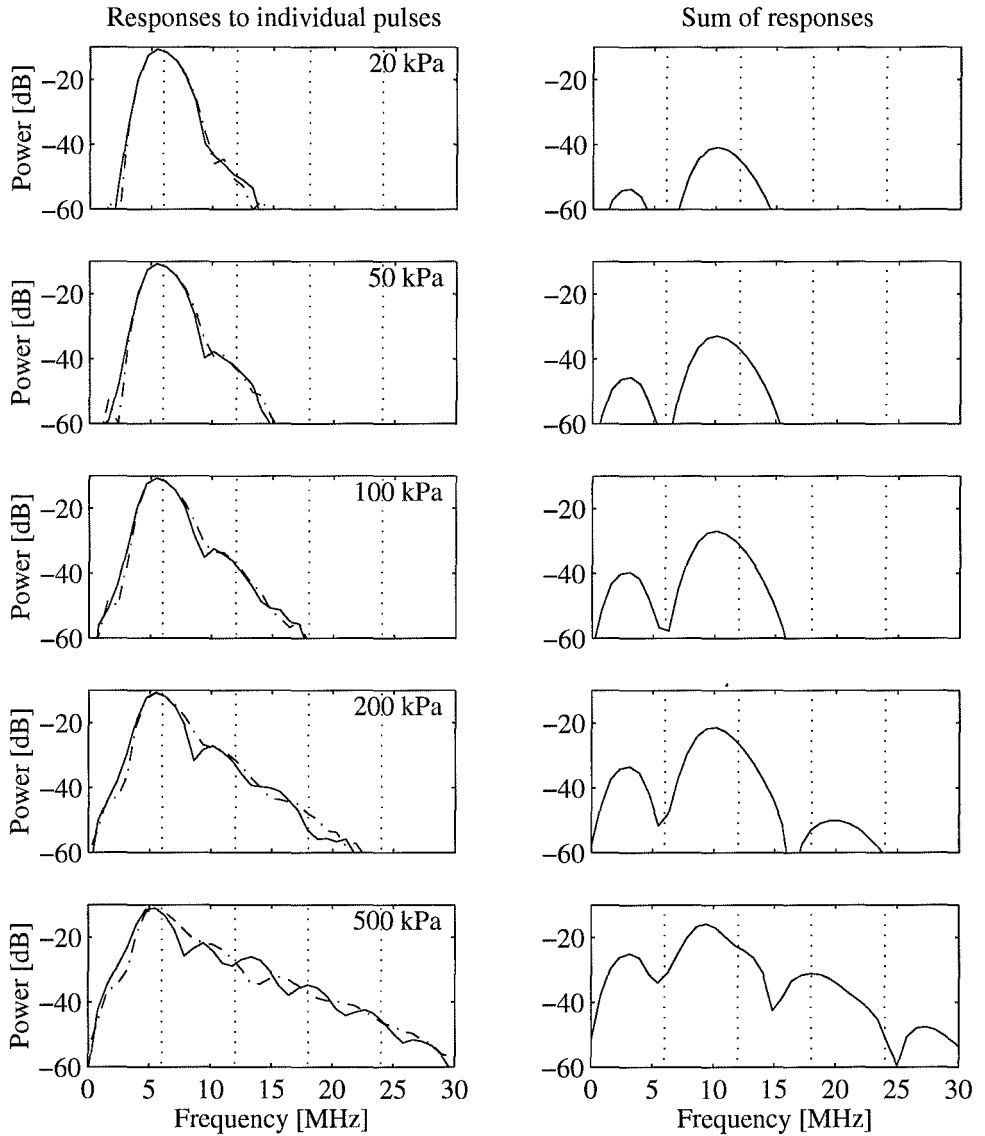


Figure 8.10. Spectra of the responses in Figure 8.8. Frequency 6.0 MHz. The left column of graphs is the response to the individual pulses, positive pulse (solid line) and negative pulse (dashed line). The right column is the spectra of the summed responses. The driving frequency and its harmonics are marked with dotted lines in the plots.

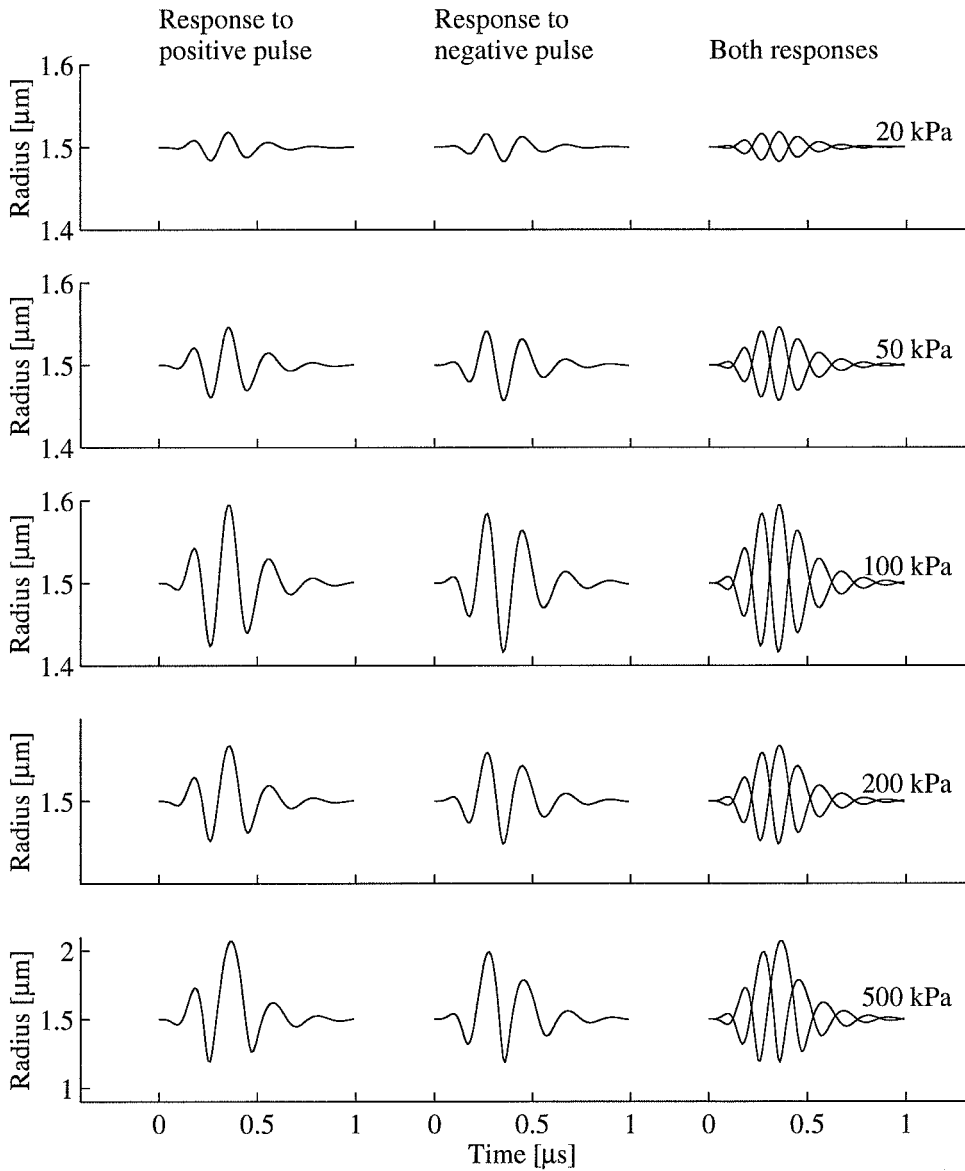


Figure 8.11. Simulated bubble radius for the responses displayed in Figure 8.8. Response to the positive pulse (left column) to the negative pulse (middle column), and both responses together (right column). The y-axis scale differs between the plots.

Physical Interpretation of the Phase-Shift

At low frequencies, below resonance, the radial amplitude is in phase with the driving pressure. The bubble oscillation follows the driving acoustic pressure. When the pressure amplitude is high, the rarefying pressure phase expands the microbubble to a large volume. During the compressional phase, the bubble contracts, driven by the external pressure and by the inertia of the surrounding liquid. The bubble wall reaches a high velocity before stopping against the internal pressure in the bubble and the tension in the shell. The acceleration associated with this stopping and reversion of the bubble wall is much higher than the acceleration when the velocity reverses in the expanded phase. This causes the positive pressure peak radiated in the compressional phase to be higher than the negative pressure radiated in the expansion phase. When the radial expansion is large, the radiated sound is dominated by positive pressure peaks emitted about half a period after the rarefactional half cycles of the driving pressure pulse.

Hence, for high amplitude, low frequency pulses, the signals radiated from the bubbles are mainly due to the negative pressure half cycles of the driving pressure pulses. For frequencies above resonance, the radial oscillation is out of phase with the driving pressure, and the effect is not as evident.

8.2.2 Summary and Comments

For driving frequency below resonance, the bubble model predicts responses to inverted pulses that look more like phase-shifted versions than like inverted versions of one another. The phenomenon requires the driving amplitude to be above a certain value, about 100 kPa. This is not a high pressure amplitude in diagnostic ultrasound imaging.

The nonlinear response is stronger for low driving frequencies. The driving frequency should be below the resonance frequency of the microbubble, which for *Sonazoid* is around 4 MHz.

The power spectra of the sound scattered from the positive and negative pulses are slightly different. For detection purposes, this frequency difference has strong advantages over earlier reports of frequency shift from contrast agents [114, 64], because the pulse-inversion technique gives a reference for the shift. However, nonlinear frequency shifts are also introduced by nonlinear sound propagation through tissue [8]. This propagation effect is enhanced if the tissue contains contrast agent bubbles.

8.3 Subharmonic Oscillations

Under certain conditions, bubbles driven by an acoustic field can go into *subharmonic oscillations*. These are oscillations on integer fractions of the driving frequency f_i . The most well known subharmonic is at $\frac{1}{2}f_i$, but subharmonics at $\frac{1}{3}f_i$, $\frac{1}{4}f_i$ etc. are also reported. Related to subharmonics are ultraharmonics, which are the harmonics of the subharmonics: $\frac{3}{2}f_i$, $\frac{5}{2}f_i$, $\frac{2}{3}f_i$ etc.

Sub- and ultraharmonics require a strongly nonlinear response from the bubble. The occurrence of an order $\frac{1}{2}$ subharmonic, a period doubling, can be viewed as the first step in a development towards a chaotic response [94]. The transition in bubble response from a harmonic distortion via a subharmonic to a chaotic response was measured experimentally by Lauterborn and Cramer in 1981 [89]. Parlitz et al. in 1990 [131] applied chaos theory to describe this transition, modeling the bubble with a modified Keller-Miksis equation. Chaos theory will not be applied in this thesis.

Subharmonic oscillations of order $\frac{1}{2}$ were measured by Esche in 1952 [42]. Subharmonic oscillation requires the driving amplitude to exceed a certain threshold. This was measured in 1968 by Neppiras [121], and derived theoretically by Eller and Flynn in 1969 [39]. This threshold effect is not present in other nonlinear effects: The level at the higher harmonics increase gradually, although stronger than linearly, with increasing driving pressure amplitude. Eller and Flynn reported the subharmonic response to be strongly frequency dependent, requiring the driving frequency to be around twice the resonance of the bubble for order $\frac{1}{2}$ subharmonics.

Prosperetti gave an analytical treatment of subharmonics in two articles from 1974 and 1975 [138, 139]. He found the subharmonic oscillation mode to depend strongly on the initial conditions when the bubble is driven into excitations by an acoustic pulse. Computer simulations of oscillating bubbles were published in 1976 by Lauterborn [88]. He showed harmonics, sub- and ultraharmonics, and a strong frequency dependence. Lotsberg et al. [104] reported in 1996 the observation of subharmonic oscillations in the contrast agent *Infuson* (*Infuson* is the same as *Albunex*). Shi et al. [153] in 1999 reported results of measurements of subharmonics *in vitro* and *in vivo* on two different microbubble contrast agents. In 1999, Shankar modified Prosperetti's analytical treatment to include a bubble encapsulated in a shell [152].

8.3.1 Simulations of Subharmonic Response

This chapter presents results of simulations of subharmonic oscillations on *Sonazoid*, using the nonlinear bubble models from Chapter 3. The model used is summarized in the equations (8.1a), (8.1b) and (8.1c) in Chapter 8.1. The

Table 8.3. Parameters used to simulate subharmonic response. For definitions, see Chapter 3.

Bubble	Radii	1.0 to 3.0 μm
Shell	Thickness	4.0 nm
	Shear modulus	50 MPa
	Shear viscosity	0.8 Ns/m ²
Driving pulse	Frequency	2.0 to 8.0 MHz
	Amplitude	20 to 1000 kPa
	Length	10 cycles or CW
	Envelopes	Hanning and cosine-tapered rectangular window
Liquid model	Rayleigh-Plesset with radiation damping (Chapter 3, (3.89) on page 76)	
Shell model	Exponential (Chapter 3, (3.145d) on page 89)	
Results calculated	Bubble radius	
	Power spectrum of the scattered sound	

simulation parameters are listed in Table 8.3.

The difference between these simulations and previous simulation studies, is the shell encapsulating the bubble. This shell has a strong influence on the stiffness and viscosity of the oscillating bubble, as shown in Chapters 5 and 6.

The simulation studies in this chapter concentrate on how the level of the order $\frac{1}{2}$ subharmonic depends on parameters of the bubble and the driving acoustic field: Bubble radius, sound frequency and pressure amplitude.

A precursor to this study was done in collaboration with Terje Orskaug [128], who was then a student at NTNU.

CW Response

The CW-response was simulated numerically by driving the bubble with 30 cycles long sine wave pulses. To reduce transients, the first and last $\frac{1}{10}$ of the pulses were tapered by a half-cycle cosine function. The CW response was taken as the response of 12 cycles, cycle 15 to cycle 26, of the totally

Table 8.4. List of figures showing results of simulations of subharmonic response.

Figure	Bubble diameter [μm]	Driving frequency [MHz]	Pulse length [cycles]	Pulse envelope
8.12, page 195	2.0	2.0	CW	
8.13, page 196	3.0	4.0	CW	
8.14, page 197	4.0	4.0	CW	
8.15, page 198	6.0	3.0	CW	
8.19, page 206	2.0	2.0	10	Hanning
8.20, page 207	3.0	4.0	10	Hanning
8.21, page 208	4.0	4.0	10	Hanning
8.22, page 209	6.0	3.0	10	Hanning
8.23, page 210	2.0	2.0	10	Cos-tapered rectangular
8.24, page 211	3.0	4.0	10	Cos-tapered rectangular
8.25, page 212	4.0	4.0	10	Cos-tapered rectangular
8.26, page 213	6.0	3.0	10	Cos-tapered rectangular

Driving pressure amplitudes: 20, 100, 500 and 1000 kPa.

30 cycles calculated. The start, after cycle 15, was chosen to ensure that the initial transients were damped out. The number of cycles included, 12, was chosen to include possible subharmonic responses of order $\frac{1}{2}$, $\frac{1}{3}$ and $\frac{1}{4}$. These subharmonics are periodic with 2, 3 and 4 times the period of the driving pulse. The 12 cycles of the driving pulse contain all these periods.

CW responses are not the most relevant for diagnostic ultrasound imaging. Ultrasound imaging uses short, broadband pulses, and transients are always important. The conversion from CW to a pulse response is not given for a nonlinear system. But the CW responses give valuable information about where and when a subharmonic response is likely to occur, and it gives an impression of the strength of the subharmonic response.

A selection of CW responses are displayed in the figures on the following pages, illustrating the subharmonic oscillation phenomenon and the transition to a subharmonic response as the driving amplitude increases. The parameter combinations used in these plots are listed in Table 8.4.

Figure 8.12 shows the response of a $2\ \mu\text{m}$ diameter bubble driven at 2 MHz. No subharmonic response can be seen in this response. As the driving pressure amplitude increases from 20 kPa to 1 MPa, the harmonic distortion increases gradually. In the spectra, this is manifested by the harmonics increasing as the driving amplitude increases. No frequency components are found below the driving frequency or between the harmonics.

Figure 8.13 shows the response of the $3\ \mu\text{m}$ diameter bubble driven at 4 MHz. For the lower driving amplitudes, up to 500 kPa, this bubble shows the same tendency as the smaller bubble: Increasing harmonic distortion, but no sub- or ultraharmonics. Driven by the highest pressure, 1 MPa, the radial oscillation includes a mode at twice the period of the driving sound. This causes a peak at half the driving frequency in the spectra. Peaks also emerge at the odd harmonics of this, at $\frac{3}{2}$, $\frac{5}{2}$ etc. of the driving frequency. This is an example of development of sub- and ultraharmonics.

This effect is stronger for the $4\ \mu\text{m}$ diameter bubble driven at 4 MHz, Figure 8.14. This larger bubble's radial oscillation enters into the subharmonic mode for a lower driving amplitude, 500 kPa. At the highest driving pressure, the radial oscillation is dominated by the oscillation at the double period.

The oscillation of the largest bubble, diameter $6\ \mu\text{m}$ driven at 3 MHz is plotted in Figure 8.15. This bubble diameter is around the maximum allowed by the capillaries in our body. For driving amplitude 500 kPa, the radial oscillation of this bubble is dominated by the $\frac{1}{2}$ order subharmonic. At the highest driving amplitude, 1 MPa, the oscillation of this bubble loses its periodicity, and the response looks more chaotic. In the spectrum, the harmonic peaks are replaced by a noisy looking response.

This transition from harmonic distortion via subharmonics to a chaotic response agrees qualitatively with the experimental results of Lauterborn and Cramer [89] and with the simulations of Parlitz et al. [131] (see e.g. Figure 15 in Reference [131]).

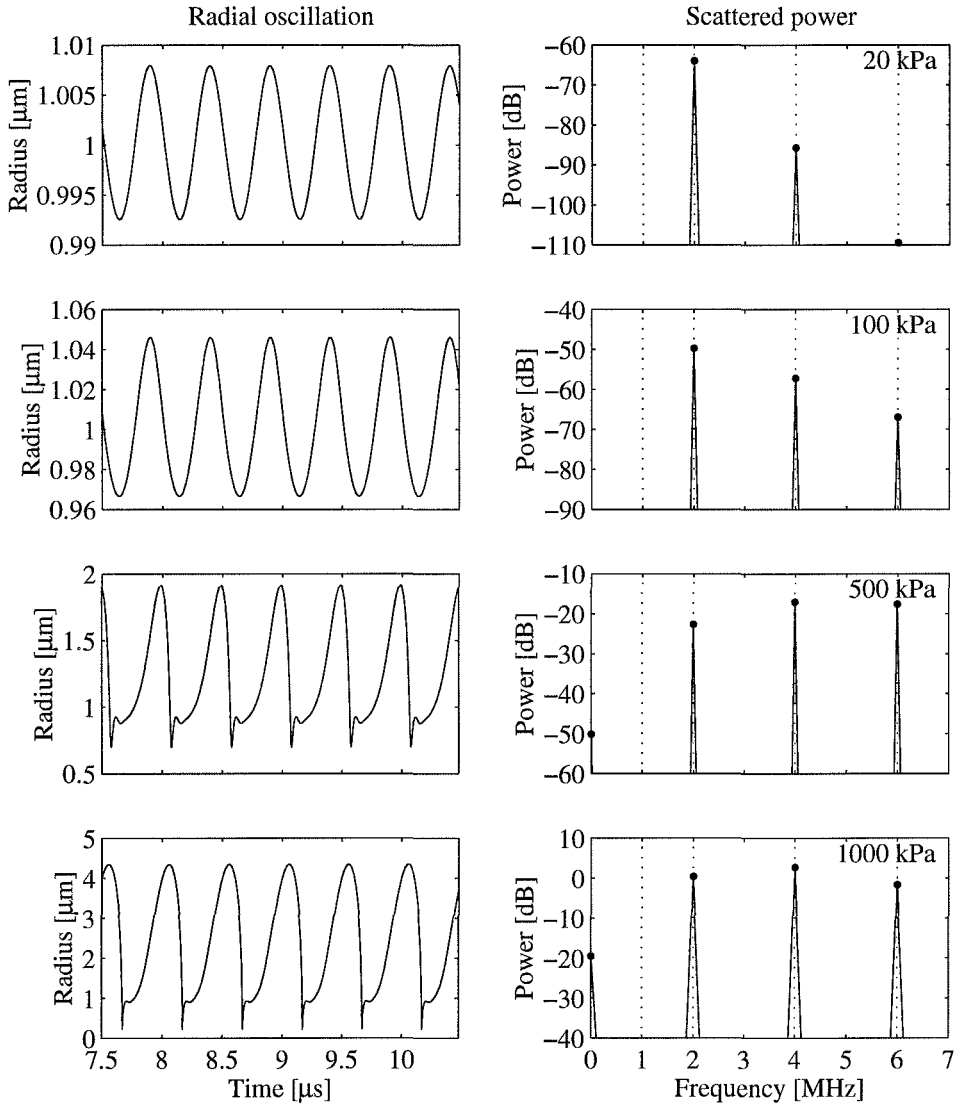


Figure 8.12. Simulated bubble radius (left), and scattered power (right). Driven by CW at frequency 2.0 MHz. Bubble diameter 2.0 μm .

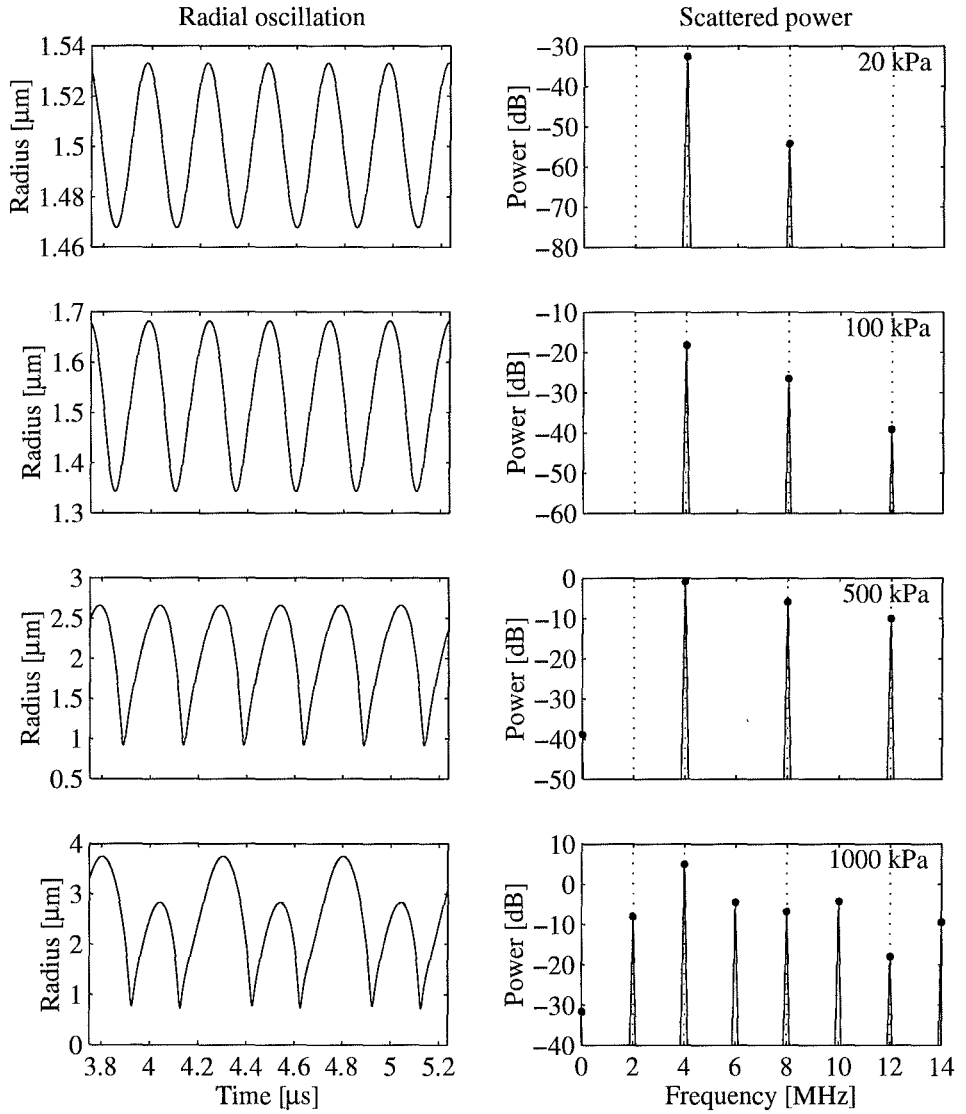


Figure 8.13. Simulated bubble radius (left), and scattered power (right). Driven by CW at frequency 4.0 MHz. Bubble diameter $3.0 \mu\text{m}$.

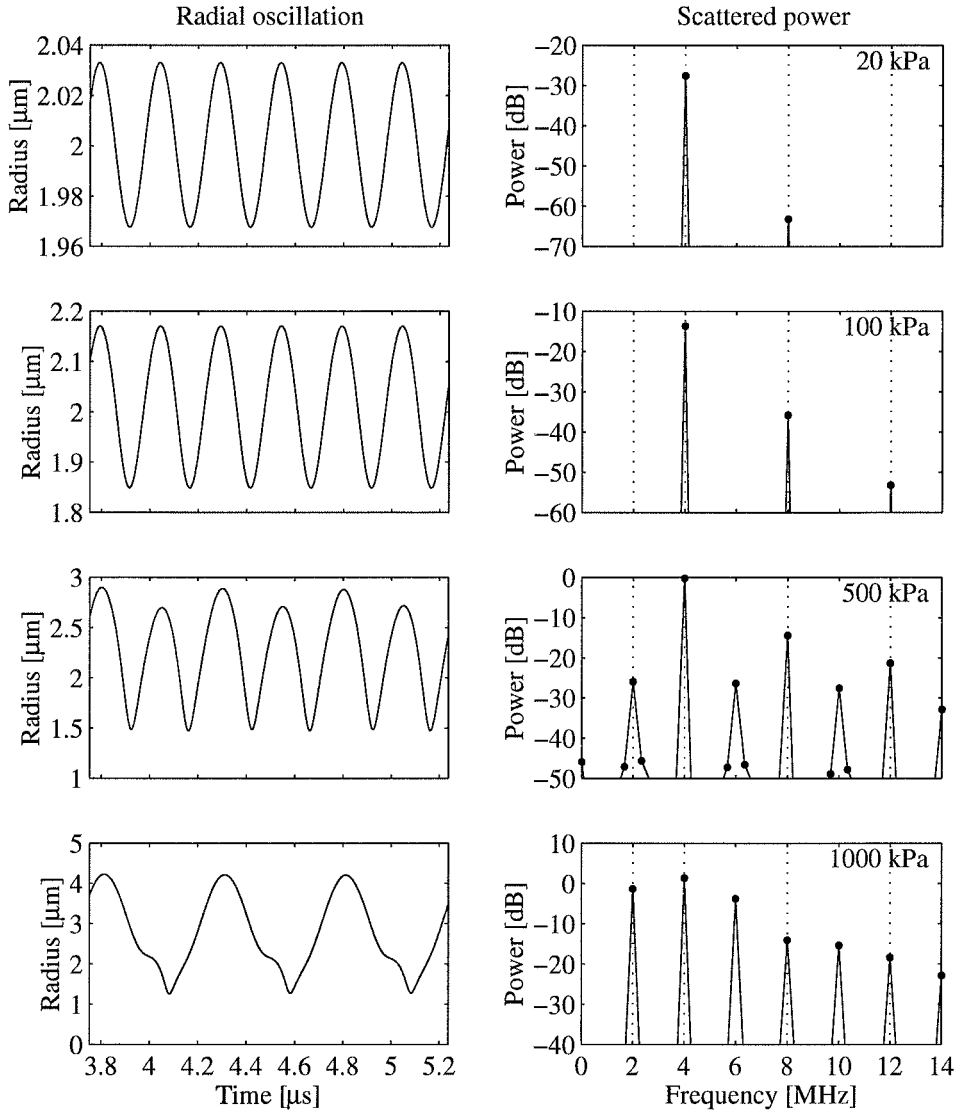


Figure 8.14. Simulated bubble radius (left), and scattered power (right). Driven by CW at frequency 4.0 MHz. Bubble diameter 4.0 μm .

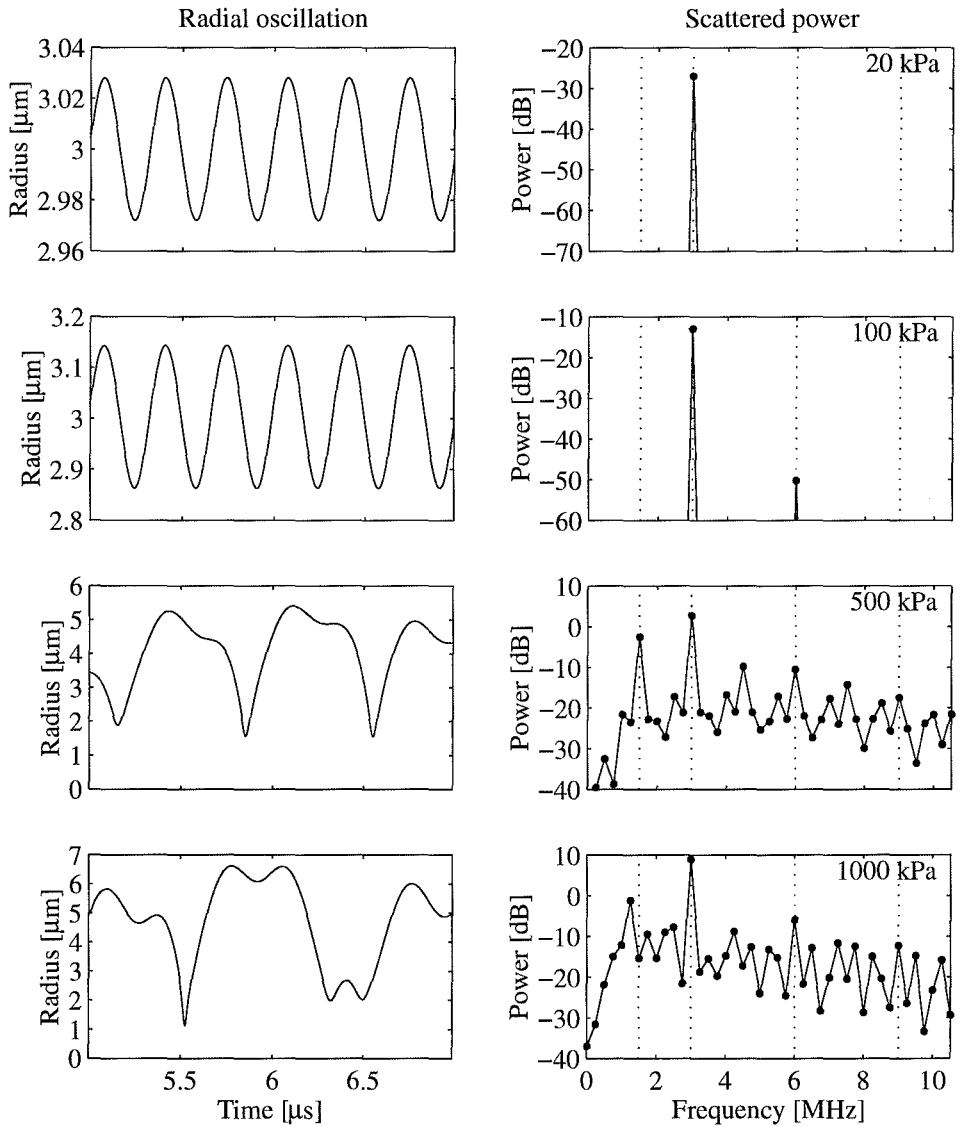


Figure 8.15. Simulated bubble radius (left), and scattered power (right). Driven by CW at frequency 3.0 MHz. Bubble diameter 6.0 μm .

Table 8.5. Simulation of subharmonics. Summary of results for subharmonic of order $\frac{1}{2}$.

Bubble diameter [μm]	Resonance frequency [MHz]	Frequency limits [MHz]	
		500 kPa	1000 kPa
≤ 2.5		No subharmonic	No subharmonic
3	4.7	No subharmonic	≥ 4
4	3.1	3.5 to 6	2 to 7.5
5	2.3	2 to 5	≤ 5.5
6	1.8	≤ 4	≤ 4.5

Strength of the Scattered Subharmonic

The level of the order $\frac{1}{2}$ subharmonic was calculated from the simulated CW responses. The results are plotted as function of driving frequency in Figure 8.16 for driving pressure 500 kPa and in Figure 8.17 for driving pressure 1000 kPa.

The responses at the lower driving pressure, 500 kPa, displays a smooth variation with frequency. The subharmonic response is present in a limited frequency band. The conclusions are summarized in Table 8.5.

The responses at the highest driving pressure, 1000 kPa, displays a not so smooth variation with frequency, see also the chaotic response at the highest driving amplitude in Figure 8.15. Especially the largest bubble, 6 μm diameter, shows an irregular frequency dependence at the lowest frequencies. Inspection of the time traces for this bubble revealed an irregular, chaotic looking oscillation pattern, and small changes in driving frequency could cause large variations in the oscillation pattern. This agrees with the simulations of Parlitz et al. [131].

The subharmonic response for 1 MPa driving pressure is present in a wider frequency band than for 500 kPa. The main conclusions are summarized in Table 8.5.

8.3.2 Comments and Relation to Earlier Results

The results of these simulations give tendencies for the dependence on driving amplitude, frequency and bubble diameter. These tendencies are compared with the analytical calculations available in the literature. The simulations presented here differ from earlier results by the simulations being done for a

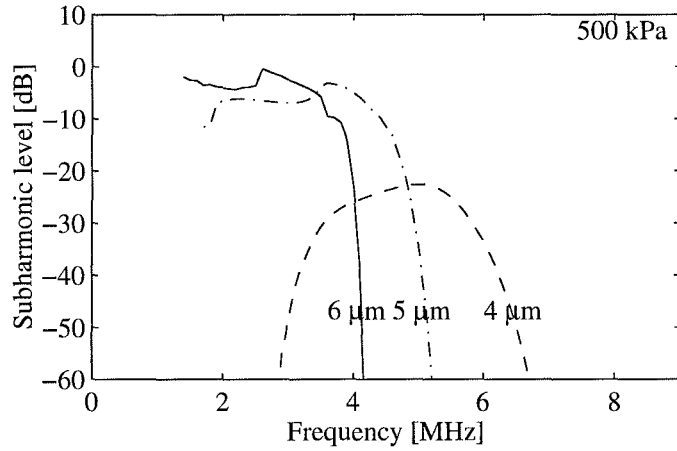


Figure 8.16. Level of the order $\frac{1}{2}$ subharmonic as function of driving frequency. Driving pressure amplitude 500 kPa. Bubble diameters 4, 5 and 6 μm .

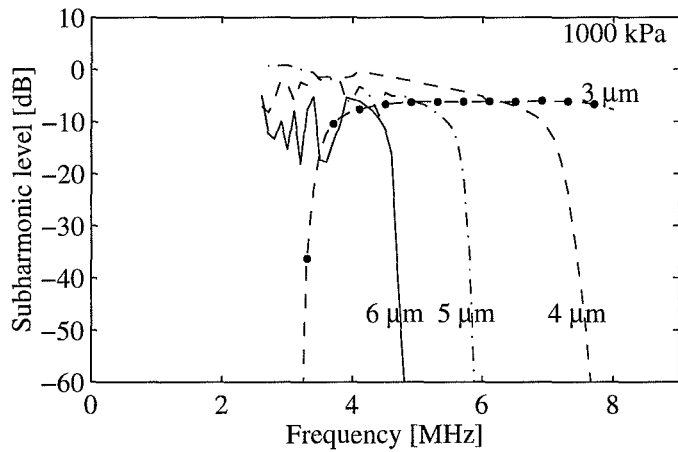


Figure 8.17. Level of the order $\frac{1}{2}$ subharmonic as function of driving frequency. Driving pressure amplitude 1000 kPa. Bubble diameters 3, 4, 5 and 6 μm .

shell-encapsulated bubble, with shell properties as estimated for Nycomed's *Sonazoid* contrast agent. The comparable results in the literature are for free air bubbles. The shell-encapsulated *Sonazoid* bubble is stiffer, causing a higher resonance frequency, and has a higher damping, or lower Q-value, than the free air-bubble.

Threshold

The simulations predict that the subharmonic oscillation has a threshold. A subharmonic mode is present only above a certain driving pressure amplitude. This is seen in Figure 8.13 to Figure 8.15, where the subharmonic oscillation suddenly appears at a certain driving pressure. Contrary to this, the harmonics increase gradually with driving amplitude.

The minimum pressure amplitude required to get a subharmonic oscillation for any *Sonazoid* bubble or frequency was 500 kPa.

A threshold effect is reported for bubbles without shell [121, 39, 138], but the simulated threshold for *Sonazoid* is higher than reported values for free bubbles.

Neppiras [121] measured sound scattered at the subharmonic frequency for driving pressure above 40 kPa. The bubbles studied by Neppiras were larger, and the frequencies were in the kilohertz-range. These large bubbles are less damped than the μm -sized bubbles studied here, and are therefore expected to give a lower threshold. The theoretical results of Eller and Flynn [39] show that the threshold for the subharmonic mode increases and the frequency band widens when the damping of the bubble increases. Prosperetti [138] calculated subharmonic responses for pressure amplitudes around 50 kPa, also for free bubbles.

The free air bubbles in the referred studies have stiffness, measured as bulk modulus, of 100 to 140 kPa. The bulk modulus of *Sonazoid* was estimated in Chapter 6 to between 400 and 900 kPa, decreasing with increasing diameter, see Figure 6.10 on page 151. In addition, the *Sonazoid* bubbles are more damped than the free bubbles, as shown in Figure 6.14 on page 155 and Figure 6.15 on page 156.

This higher stiffness and increased damping of *Sonazoid*, caused by the shell, can explain why the simulated thresholds for subharmonic oscillations of *Sonazoid* are higher than the values reported in the literature for free air bubbles.

Frequency Dependence

The plots of subharmonic strength against frequency, Figure 8.16 and Figure 8.17, show a strong frequency dependence. The subharmonic response is present in a limited frequency band for each bubble. This band moves towards lower frequencies as the bubble diameter increases, which is consistent with the decrease in resonance frequency as the diameter increases.

This observation is compared with the resonance frequency for *Sonazoid*, estimated from the experiments in Chapter 6 (Figure 6.11 on page 151). The estimated resonance frequencies are listed in Table 8.5, for comparison. According to the simulations, a subharmonic response is achieved for driving frequencies f_i between f_0 and $2f_0$, where f_0 is the resonance frequency of the bubble.

Eller and Flynn [39] found analytically that the subharmonic mode requires a driving frequency around twice the resonance frequency of the bubble to be excited. For heavily damped bubbles, the threshold level increases and the frequency band widens compared to undamped bubbles. Prosperetti [138] extended the calculations of Eller and Flynn, showing that in some frequency ranges, two stable oscillation modes can exist, one with and one without a subharmonic. Which one of these modes is excited depends on the initial conditions. Prosperetti found that a subharmonic mode may exist for frequencies up to about $f_i = 2f_0$.

Diameter Dependence

A subharmonic mode could not be achieved for bubble diameters smaller than $3 \mu\text{m}$. For the lowest amplitude giving a subharmonic, 500 kPa, the subharmonic level of the $4 \mu\text{m}$ diameter bubble is much weaker than the response of the larger bubbles, with diameter $5 \mu\text{m}$ and $6 \mu\text{m}$. For the highest driving amplitude, 1000 kPa, the maximum subharmonic level is independent of the diameter. The main difference between the bubble sizes, is in which frequency band the subharmonic mode is achieved.

These simulations differ from previous results for the free bubbles by the relation between bubble size and frequency. The *Sonazoid* bubbles are around 4 to 9 times stiffer than the free bubbles of equal size, giving a resonance frequency that is 2 to 3 times higher. This means that the *Sonazoid* bubbles should give a response comparable to free bubbles of 2 to 3 times smaller diameter. The damping of *Sonazoid* is larger than for the free bubble, giving a wider frequency dependence.

The observation that the larger bubbles are more easily driven into subharmonic oscillation can be explained by the larger bubbles being less damped

than the smaller ones. The larger bubbles have higher Q-values than the smaller bubbles, and the ability to single out and oscillate around its resonance frequency is greater for the larger bubbles.

The shell gets more important the smaller the bubbles are. The contribution from the shell to the microbubble bulk modulus increases as the bubble diameter decreases. This causes the smaller bubbles to require higher driving pressure amplitudes to reach the subharmonic mode than the larger bubbles do.

8.3.3 Pulse Responses

The CW responses in the previous section were chosen to avoid transients. But transients are important in diagnostic ultrasound imaging. This section will show results of the same simulations for pulses of finite length.

The pulse responses were simulated for driving pulses defined as 10 cycles long sine wave bursts, enclosed either in a Hanning or in a cosine-tapered rectangular envelope. The *cosine-tapered rectangular envelope* $w_c[n]$ is defined as a rectangular envelope with the first and last $\frac{1}{10}$ tapered by a half cycle cosine function. This is mathematically described as

$$w_c[n] = \begin{cases} \frac{1}{2}(1 - \cos \pi \frac{n}{N_e}) & 0 \leq n < N_e \\ 1 & N_e \leq n \leq N - N_e \\ \frac{1}{2}(1 - \cos \pi \frac{N-n}{N_e}) & N - N_e < n < N \\ 0 & n < 0 \text{ or } n \geq N, \end{cases} \quad (8.5)$$

where $N=10$ is the number of cycles in the driving pulse and $N_e = N/10$ defines the first and last parts of the envelope being tapered by a cosine function. The shape and power spectra of these two driving pulses are plotted in Figure 8.18.

The *cosine-tapered rectangular envelope* was selected to have a pulse that is flat over a large portion of its extent, but has a smoother start and end than a rectangular envelope. The cosine-tapered pulse has less transients and lower sidebands than the rectangular pulse, and it is easier to obtain experimentally. The Hanning envelope is an example of a smoother pulse shape, with low sidebands in the power spectrum. The low sidelobe level makes it easier to separate a nonlinear response from sideband leakage. The Hanning pulses do not contain a portion of oscillations with constant amplitude.

A selection of pulse responses are displayed in the figures on the following pages. The parameter combinations used in the plots are listed in Table 8.4 on page 193.

Hanning Envelope

The results for the 2 μm diameter bubble excited by a Hanning pulse, Figure 8.19, shows the same tendency as the CW response for the same bubble, Figure 8.12 on page 195. The harmonic distortion increases as the driving amplitude increases, but no subharmonic is seen.

The 3 μm diameter bubble, Figure 8.20, shows the same tendency. No subharmonic is found. This is in contrast to the CW response for this diameter-frequency combination at 1 MPa driving pressure, Figure 8.13 on page 196.

The response of the 4 μm and 6 μm bubbles driven at 1 MPa, Figure 8.21 and Figure 8.22, show an interesting effect. The first half of these responses display strong harmonic distortion, but no subharmonic. About halfway in the pulses, the oscillation changes abruptly to being dominated by an oscillation at twice the driving period, and this mode lasts for the rest of the pulse duration. This gives sub- and ultraharmonic peaks in the response spectra.

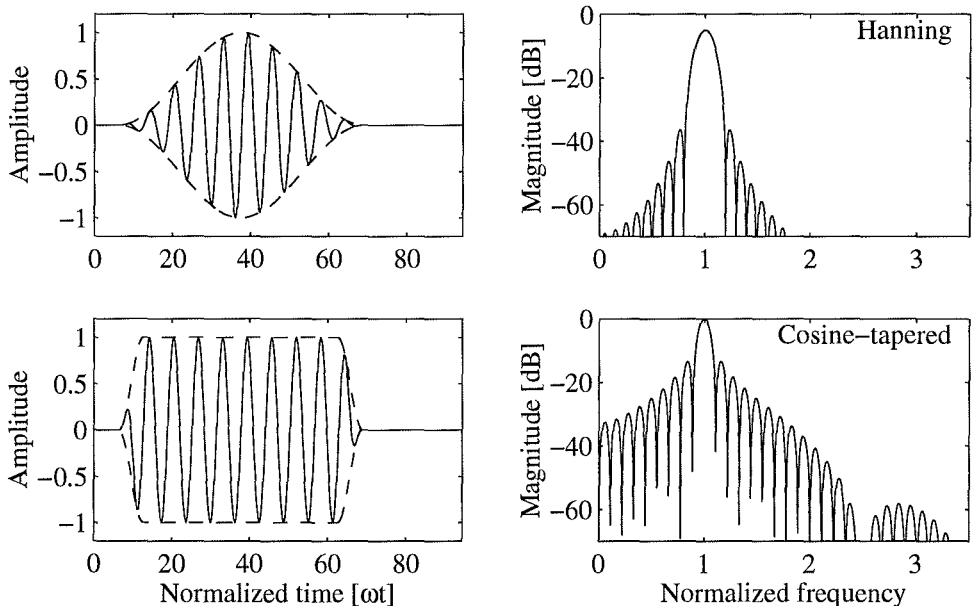


Figure 8.18. Driving pulses for simulating subharmonic response: Pulse shapes (left) and power spectra (right). The pulses are defined as 10 cycles enclosed in either a Hanning envelope (upper diagram) or a cosine tapered rectangular envelope (lower diagram).

Cosine-Tapered Rectangular Envelope

Figure 8.23 shows the responses of the 2 μm and bubbles driven by cosine-tapered rectangular envelope pulses. These responses show the same effect as for the Hanning envelope, increasing harmonic distortion with increasing drive pressure, but no subharmonic.

The responses plotted in Figure 8.24 and Figure 8.25, for the 3 μm and 4 μm diameter bubbles, are basically equal to the CW response. A subharmonic is seen for pressure amplitudes 500 kPa and 1000 kPa. This subharmonic oscillation pattern starts immediately. This is in contrast to the responses to the Hanning-pulse, Figure 8.20 and Figure 8.21. The Hanning pulse gave a subharmonic only for the 4 μm bubble driven at 1000 kPa, where a transition from harmonic distortion to subharmonic response occurred halfway in the pulse duration.

The response of the 6 μm bubble is plotted in Figure 8.26. The 500 kPa driving amplitude shows a subharmonic oscillation pattern that starts about halfway into the pulse. For the highest driving amplitude, 1 MPa, the response starts with a rather irregular oscillation pattern, mainly at half the driving frequency. About halfway into the pulse, this pattern switches to a more regular, but strongly asymmetric oscillation pattern, at half the driving frequency. In the spectrum, the subharmonic peak is seen to be at a frequency lower than $\frac{1}{2}$ the driving frequency, and the harmonic and ultraharmonic peaks are smeared out to a chaotic, noisy looking pattern.

8.3.4 Difference between Pulse and CW Responses

The pulse and CW responses simulated in this chapter show that a subharmonic mode is not always obtained as a response to a pulse, even if the CW response predicts the presence of a subharmonic. The subharmonic pattern needs time to develop.

The simulated pulse responses show an important phenomenon not present in the CW cases. In some situations, the oscillation pattern switches abruptly halfway in the pulse, changing the oscillation pattern from a harmonic distortion to a subharmonic oscillation. This time-dependent change cannot be found by studying CW responses. The phenomenon agrees with the analytical results of Prosperetti [138, 139], who showed that under some conditions, different stable oscillation patterns may exist depending on the initial conditions, and that the oscillation mode may jump from one pattern to the other. Which oscillation mode is obtained in a specific situation, depends on the initial conditions. This switch in oscillation mode was found for the largest driving amplitudes in Figures 8.21, 8.22 and 8.26.

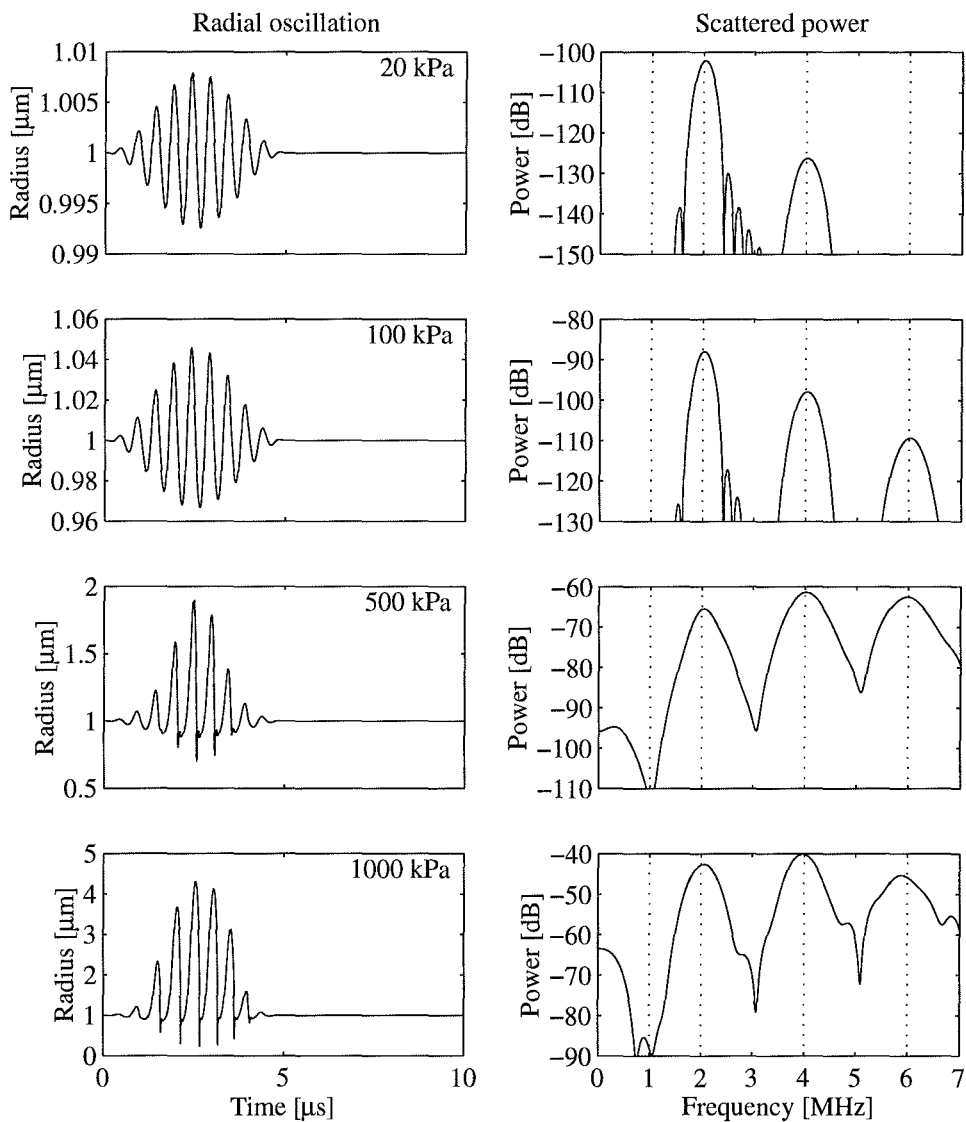


Figure 8.19. Simulated bubble radius (left), and scattered power (right). Driving Pulse: 10 cycles in a Hanning envelope, frequency 2.0 MHz. Bubble diameter 2.0 μm .

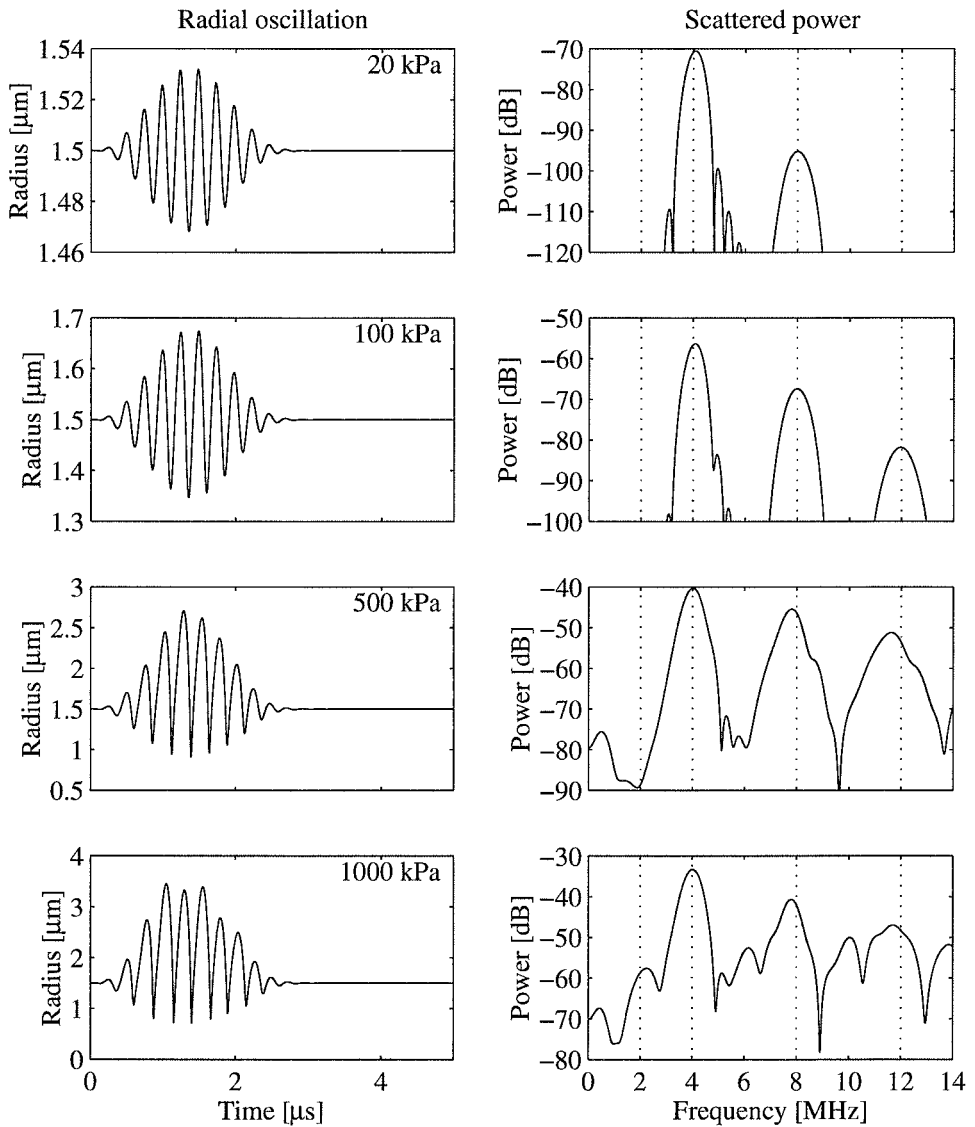


Figure 8.20. Simulated bubble radius (left), and scattered power (right). Driving Pulse: 10 cycles in a Hanning envelope, frequency 4.0 MHz. Bubble diameter 3.0 μm .

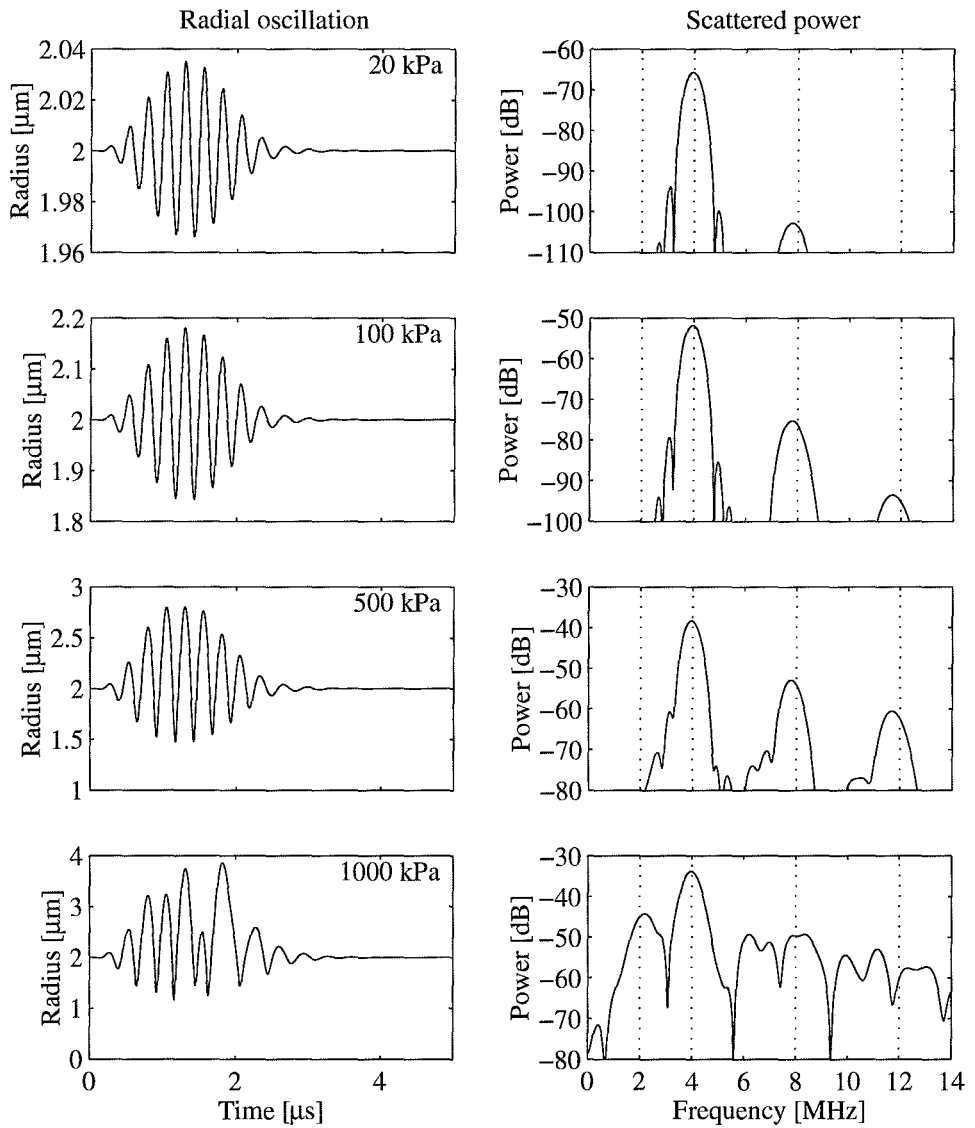


Figure 8.21. Simulated bubble radius (left), and scattered power (right). Driving Pulse: 10 cycles in a Hanning envelope, frequency 4.0 MHz. Bubble diameter 4.0 μm .

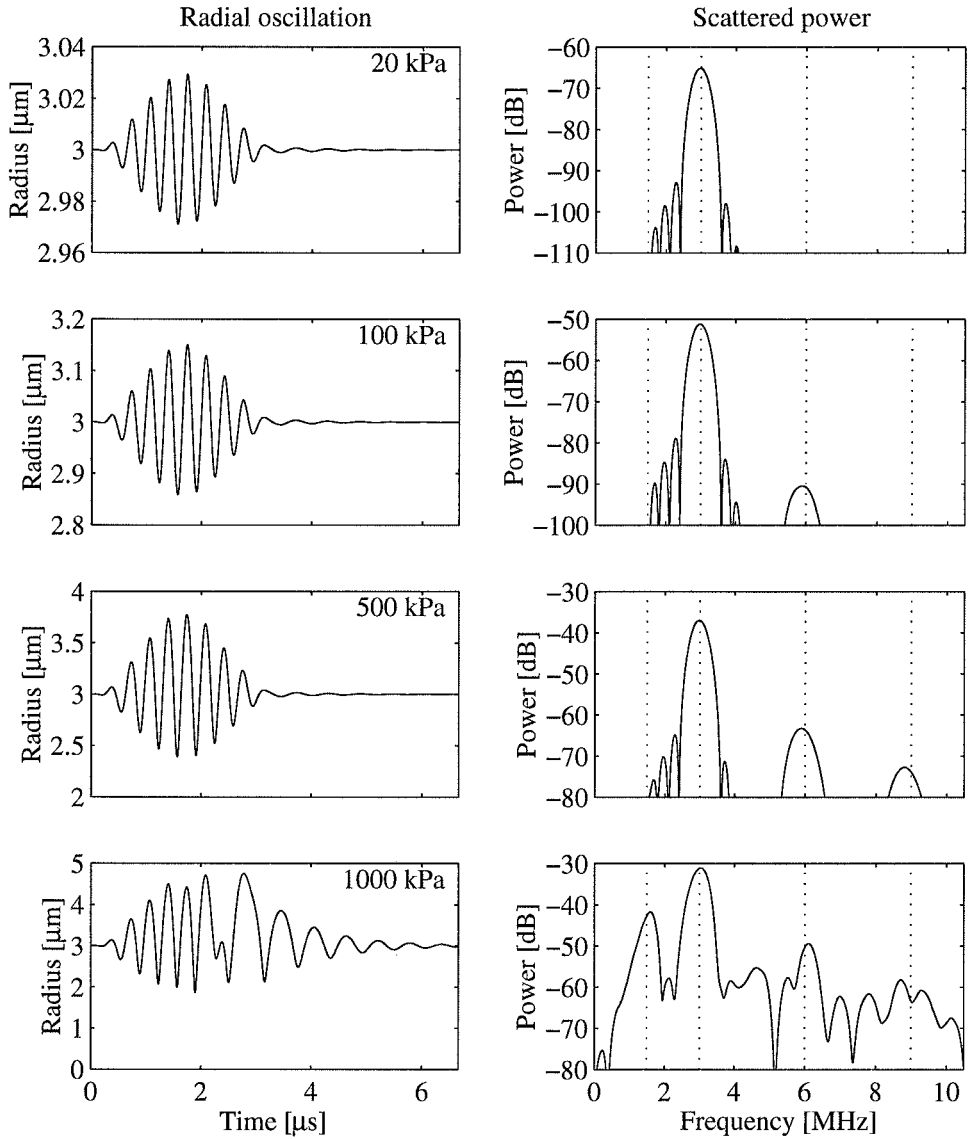


Figure 8.22. Simulated bubble radius (left), and scattered power (right). Driving Pulse: 10 cycles in a Hanning envelope, frequency 3.0 MHz. Bubble diameter 6.0 μm .

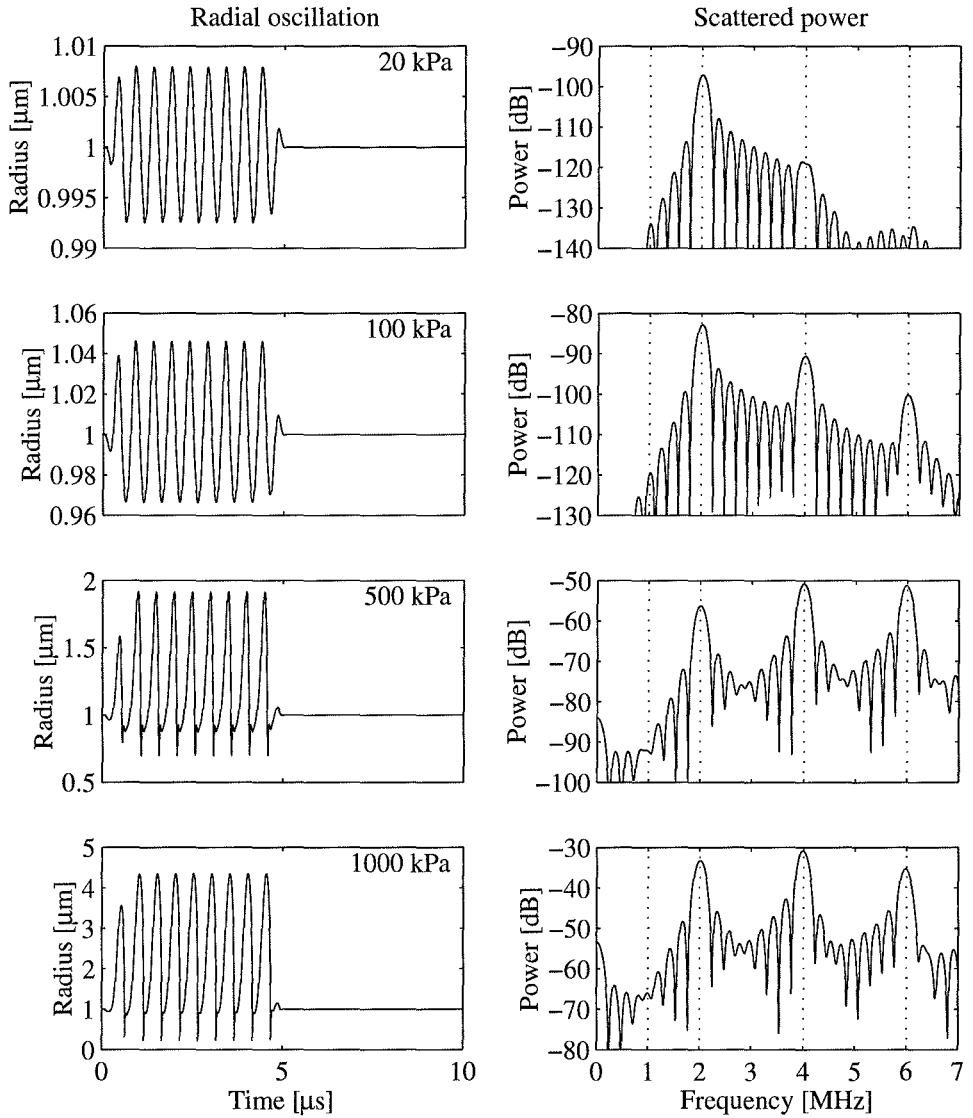


Figure 8.23. Simulated bubble radius (left), and scattered power (right). Driving Pulse: 10 cycles in a cosine-tapered rectangular envelope, frequency 2.0 MHz. Bubble diameter 2.0 μm .

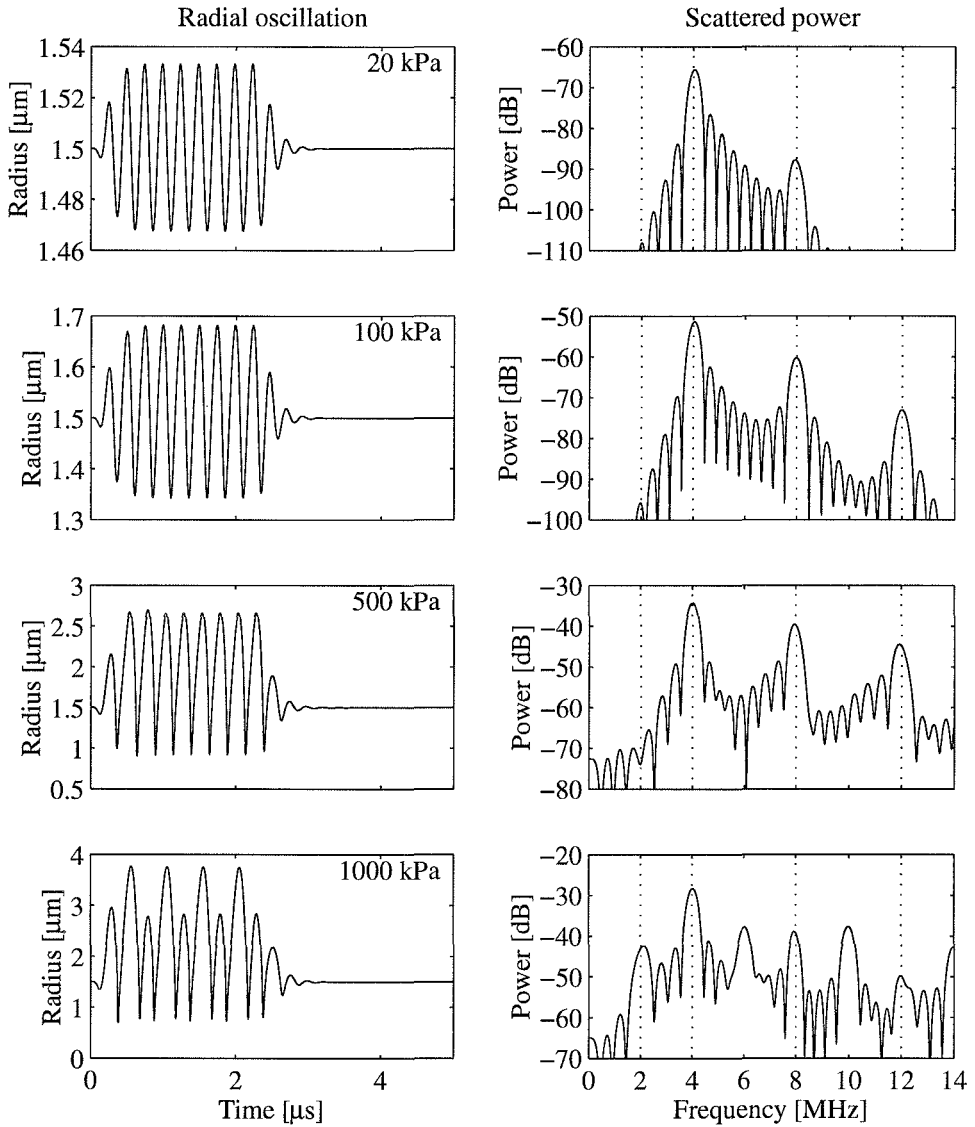


Figure 8.24. Simulated bubble radius (left), and scattered power (right). Driving Pulse: 10 cycles in a cosine-tapered rectangular envelope, frequency 4.0 MHz. Bubble diameter 3.0 μm .

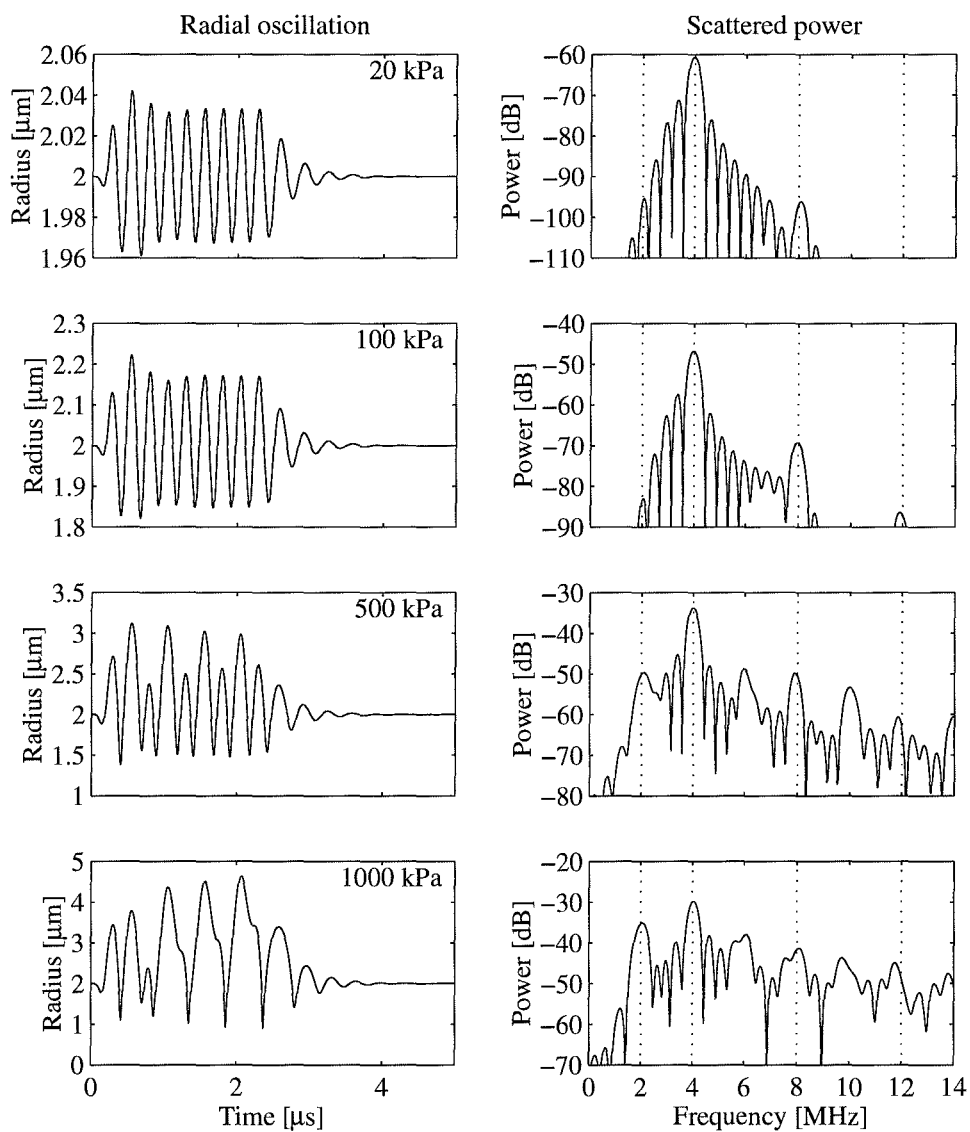


Figure 8.25. Simulated bubble radius (left), and scattered power (right). Driving Pulse: 10 cycles in a cosine-tapered rectangular envelope, frequency 4.0 MHz. Bubble diameter 4.0 μm .

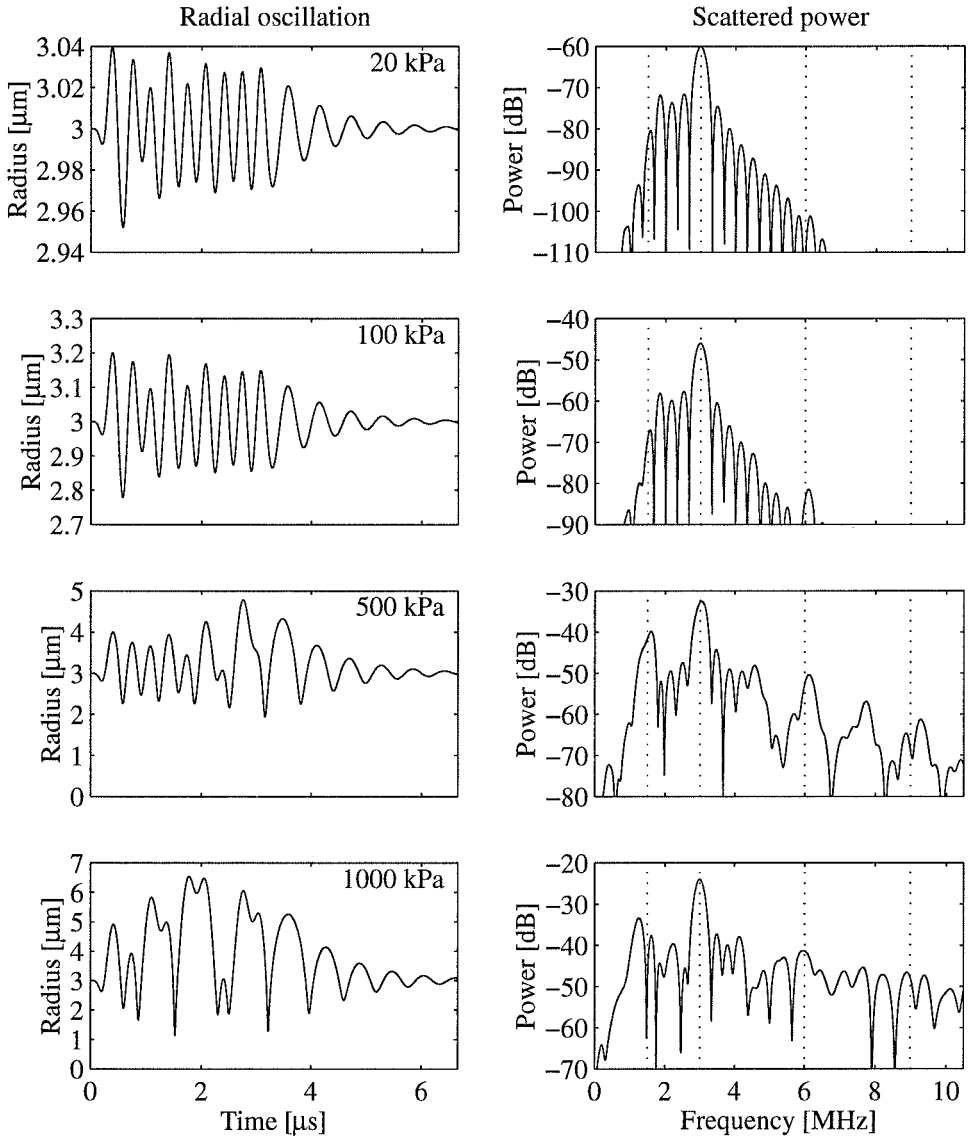


Figure 8.26. Simulated bubble radius (left), and scattered power (right). Driving Pulse: 10 cycles in a cosine-tapered rectangular envelope, frequency 3.0 MHz. Bubble diameter 6.0 μm .

Chapter 9

Summary and Conclusions

The main topic of this thesis is the acoustic properties of gas bubbles encapsulated in a shell.

Three contrast agents for medical ultrasound imaging have been investigated experimentally, all consisting of gas bubbles encapsulated in a shell. It was found that the shell increases the stiffness and viscosity of the bubbles, increasing the resonance frequency and the damping of the oscillating microbubble.

To characterize the agents, two different experimental acoustic measurement systems were developed and built. One system measures the acoustic attenuation as function of frequency, the other system records the scattered sound from a contrast agent sample exposed to specified sound pulses.

Based on the theory and the experimental results, a numerical simulation program was developed. The program models the response of a contrast agent bubble to a driving ultrasound pulse. Simulations using this program were used to investigate and hopefully improve the understanding of the mechanisms behind various nonlinear ultrasound imaging techniques.

Extensive theoretical background chapters have been included. The material in the theory chapters has been collected from many sources, both textbooks and journals. This has been put together to give the necessary background for the measurement systems, the shell properties estimation and the nonlinear simulation programs. The theory chapters concentrate on effects of encapsulating the gas bubble in a shell. There exist publications about the behavior of shelled bubbles, and textbooks of mechanical engineering contain models for the behavior of spherical shells. But a collection of this material with application to and consequences for ultrasound contrast agents is not found elsewhere.

Experimental Equipment and Software Resulting from this Work

The thesis has resulted in three products that will hopefully prove useful in the future characterization of ultrasound contrast agents

- A system to measure acoustic attenuation spectra, with the option of adding a hydrostatic pressure. This system is combined with software that can combine the measured spectra and size distributions read from a *Coulter Multisizer*, and estimate the microbubble stiffness.
- A system that can transmit specified ultrasound pulses into a sample of contrast agent and record the scattered signals on digital format.
- A simulation program that models the bubble response to a specified driving ultrasound pulse.

All these systems have been constructed to be easy and user-friendly to operate. The experimental measurement systems are now routinely in use at Nycomed.

Suggestions for Future Work

Much work remains before the characterization and understanding of contrast agents for medical ultrasound imaging is complete.

This thesis has concentrated entirely on the *in vitro* behavior of the agents. The extension of these methods to clinical use of the agents remains.

The experimental characterization methods all study a large number of bubbles. The possibility of studying single bubbles, visualizing the radial oscillation with a camera, will provide much extra information about the agents. Such experiments are now becoming available, and will certainly provide new insight about the behavior of the agents. When studying single bubbles, however, it is always the question how representative that single bubble is, and if the experimental technique changes its properties. I therefore believe that single bubble experiments and measurements on bubble clouds are both needed for contrast agent characterization.

More sophisticated theoretical models for the oscillating liquid are available from the literature. The simulations have shown that in some extreme cases, the bubble wall velocity can approach the speed of sound in the liquid. For these cases, the Gilmore model would be more suited than the simpler models used in this thesis. The Gilmore model could be combined with the shell models from this thesis.

This thesis has concentrated on the characterization, understanding and modeling on the bubbles. A next step would be to use the experimental

methods and the simulation programs to improve ultrasound contrast imaging, either by creating improved contrast agents or by creating measurement techniques that can extract more information from the agents.

References

- [1] A. L. Anderson and L. D. Hampton. Acoustics of gas-bearing sediments: 1. Background. *J. Acoust. Soc. Am.*, 67:1865–1889, 1980.
- [2] B. A. Angelsen. *Waves, Signals and Signal Processing in Medical Ultrasonics*, volume I, chapter 6. [3].
- [3] B. A. Angelsen. *Waves, Signals and Signal Processing in Medical Ultrasonics*. Dept. of Physiology and Biomedical Engineering, Norwegian University of Science and Technology, Trondheim, Norway, 1996.
- [4] B. A. Angelsen, L. Hoff, and T. F. Johansen. Simulation of gas bubble scattering for large Mach-numbers. In *1999 IEEE Ultrasonics Symposium Proceedings*. [67].
- [5] M. Averkiou, D. Roundhill, and J. Powers. A new imaging technique based on the nonlinear properties of tissues. In *1997 IEEE Ultrasonics Symposium Proceedings*, pages 1561–1566. [145].
- [6] G. H. Aylward and T. J. Findlay. *SI Chemical data*, chapter 5 and 27. [7].
- [7] G. H. Aylward and T. J. Findlay. *SI Chemical data*. Jacaranda Wiley Ltd., Milton, Australia, 3rd edition, 1998.
- [8] A. C. Baker. Personal communication.
- [9] R. T. Beyer. The parameter B/A. In M. F. Hamilton and D. T. Blackstock, editors, *Nonlinear Acoustics*, chapter 2, pages 25–39. [53].
- [10] K. Bjercknes, P. Sontum, G. Smistad, and I. Agerkvist. Preparation of polymeric microbubbles: Formulation studies and product characterisation. *Int. J. Pharm.*, 158:129–136, 1997.
- [11] F. A. Boyle and N. P. Chotiros. Nonlinear acoustic scattering from a gassy popoelastc seabed. *J. Acoust. Soc. Am.*, 103:1328–1336, 1998.
- [12] R. E. Caflisch, M. J. Miksis, G. C. Papanicolaou, and L. Ting. Effective equations for wave propagation in bubbly liquids. *J. Fluid. Mech.*, 153:259–273, 1985.
- [13] P. H. Chang, K. K. Shung, S.-J. Wu, and H. B. Levene. Second harmonic imaging and harmonic Doppler measurements with Alburnex. *IEEE Trans. Ultrason., Ferroelectr., Freq. Contr.*, 42:1020–1027, 1995.

- [14] J. Chapelon, V. Newhouse, D. Catignol, and P. Shankar. Bubble detection and sizing with a double frequency doppler system. *Ultrasonics*, 26:148–154, 1988.
- [15] J. Chapelon, P. Shankar, and V. Newhouse. Ultrasonic measurement of bubble cloud size profiles. *J. Acoust. Soc. Am.*, 78:196–201, 1985.
- [16] X. Chen and A. Prosperetti. Thermal processes in the oscillation of gas bubbles in tubes. *J. Acoust. Soc. Am.*, 104:1389–1398, 1998.
- [17] C. Chin and P. Burns. Experimental verification of ensemble model for scattering by microbubbles population in a contrast agent. In *1998 IEEE Ultrasonics Symposium Proceedings*, pages 1827–1830. [146].
- [18] C. Chin and P. Burns. Predicting acoustic response of a microbubble population for contrast imaging. In *1997 IEEE Ultrasonics Symposium Proceedings*, pages 1557–1560. [145].
- [19] C. Christiansen, H. Kryvi, P. C. Sontum, and T. Skotland. Physical and biochemical characterization of AlburnexTM, a new ultrasound contrast agent consisting of air-filled albumin microspheres suspended in a solution of human albumin. *Biotechnol. Appl. Biochem.*, 19:307–320, 1994.
- [20] T. Christopher. Finite amplitude distortion-based inhomogenous pulse echo ultrasonic imaging. *IEEE Trans. Ultrason., Ferroelectr., Freq. Contr.*, 44:125–139, 1997.
- [21] T. Christopher. Experimental investigation of finite amplitude distortion-based, second harmonic pulse echo ultrasonic imaging. *IEEE Trans. Ultrason., Ferroelectr., Freq. Contr.*, 45:158–162, 1998.
- [22] C. C. Church. The effects of an elastic solid surface layer on the radial pulsations of gas bubbles. *J. Acoust. Soc. Am.*, 97:1510–1521, 1995.
- [23] K. Commander and A. Prosperetti. Linear pressure waves in bubbly liquids: Comparison between theory and experiment. *J. Acoust. Soc. Am.*, 85:732–746, 1989.
- [24] L. A. Crum. The polytropic exponent of gas contained within air bubbles pulsating in a liquid. *J. Acoust. Soc. Am.*, 73:116–120, 1983.
- [25] P. A. Dayton, K. E. Morgan, A. L. Klibanov, G. H. Brandenburger, and K. W. Ferrara. Optical and acoustical observations of the effect of ultrasound on contrast agents. *IEEE Trans. Ultrason., Ferroelectr., Freq. Contr.*, 46:220–232, 1999.
- [26] N. de Jong and R. Cornet. Higher harmonics of vibrating gas-filled microspheres. Part one: simulations. *Ultrasonics*, 32:447–453, 1994.
- [27] N. de Jong and R. Cornet. Higher harmonics of vibrating gas-filled microspheres. Part two: measurements. *Ultrasonics*, 32:455–459, 1994.
- [28] N. de Jong and L. Hoff. Ultrasound scattering properties of Alburnex microspheres. *Ultrasonics*, 31:175–181, 1993.

- [29] N. de Jong, L. Hoff, T. Skotland, and N. Bom. Absorption and scatter of encapsulated gas filled microspheres: theoretical considerations and some measurements. *Ultrasonics*, 30:95–103, 1992.
- [30] A. Despopoulos and S. Silbernagl. *Color Atlas of Physiology*, page 60. [33].
- [31] A. Despopoulos and S. Silbernagl. *Color Atlas of Physiology*, pages 78–79. [33].
- [32] A. Despopoulos and S. Silbernagl. *Color Atlas of Physiology*, pages 160–161. [33].
- [33] A. Despopoulos and S. Silbernagl. *Color Atlas of Physiology*. Georg Thieme Verlag, Stuttgart, Germany, 2nd edition, 1984.
- [34] C. Devin. Survey of thermal, radiation and viscous damping of pulsating air bubbles in water. *J. Acoust. Soc. Am.*, 31:1654–1667, 1959.
- [35] J. Dormand and P. Prince. A family of embedded Runge-Kutta formulae. *J. Comp. Appl. Math.*, 6:19–26, 1980.
- [36] F. A. Duck, A. C. Baker, and H. C. Starrit, editors. *Ultrasound in Medicine*. Medical Science Series. Institute of Physics Publishing, Bristol, UK, 1998.
- [37] A. I. Eller. Damping constants of pulsating bubbles. *J. Acoust. Soc. Am.*, 47:1469–1470, 1970.
- [38] A. I. Eller and L. A. Crum. Instability of the motion of a pulsating bubble in a sound field. *J. Acoust. Soc. Am.*, 47:762–767, 1970.
- [39] A. I. Eller and H. G. Flynn. Generation of subharmonics of order one-half by bubbles in a sound field. *J. Acoust. Soc. Am.*, 46:722–727, 1969.
- [40] D. Epstein and J. B. Keller. Expansion and contraction of planar, cylindrical and spherical underwater gas bubbles. *J. Acoust. Soc. Am.*, 52:975–980, 1971.
- [41] P. Epstein and M. Plesset. On the stability of gas bubbles in liquid-gas solutions. *J. Chem. Phys.*, 18:1505–1509, 1950.
- [42] R. Esche. Untersuchung der Schwingungskavitation in Flüssigkeiten. *Acustica*, 2:AB208–AB218, 1952.
- [43] M. Fatemi and J. F. Greenleaf. Ultrasound-stimulated vibro-acoustic spectrography. *Science*, 280:82–85, 1998.
- [44] M. Fatemi and J. F. Greenleaf. Application of radiation force in noncontact measurement of the elastic parameters. *Ultrasonic Imaging*, 21:147–154, 1999.
- [45] H. G. Flynn. Cavitation dynamics. I. A mathematical formulation. *J. Acoust. Soc. Am.*, 57:1379–1396, 1975.
- [46] H. G. Flynn. Cavitation dynamics. II. Free pulsations and models for cavitation bubbles. *J. Acoust. Soc. Am.*, 58:1160–1170, 1975.
- [47] F. Fox and K. Herzfeld. Gas bubbles with organic skin as cavitation nuclei. *J. Acoust. Soc. Am.*, 26:984–989, 1954.

- [48] P. Frinking and N. de Jong. Acoustic modelling of shell-encapsulated gas bubbles. *Ultrasound Med. Biol.*, 24:523–533, 1998.
- [49] P. Frinking, N. de Jong, and E. I. Cespedes. Scattering properties of encapsulated gas bubbles at high ultrasound pressure. *J. Acoust. Soc. Am.*, 105:1989–1996, 1999.
- [50] F. Gilmore. The growth and collapse of a spherical bubble in a viscous compressible liquid. *Calif. Inst. of Tech. Hydrodyn. Lab Rep. 26-4*, 1952.
- [51] R. Gramiak and P. Shah. Echocardiography of the aortic root. *Invest. Radiol.*, 3:356–366, 1968.
- [52] M. F. Hamilton and D. T. Blackstock. Model equations. In *Nonlinear Acoustics*, chapter 3, pages 1–62. [53].
- [53] M. F. Hamilton and D. T. Blackstock, editors. *Nonlinear Acoustics*. Academic Press, San Diego, USA, 1998.
- [54] C. Herring. Theory of the pulsations of the gas bubble produced by an underwater explosion. *OSRD Report No. 236*, 1941.
- [55] S. Hilgenfeldt, D. Lohse, and M. Zomack. Heat deposition in microbubble ultrasound contrast agents. In *Ultrasonics International '99 joint with 1999 World Congress on Ultrasonics*, Copenhagen, Denmark, 1999.
- [56] L. Hoff. Acoustic properties of ultrasonic contrast agents. *Ultrasonics*, 34:591–593, 1996.
- [57] L. Hoff and C. Christiansen. Consideration about the contribution to acoustic backscatter from Albunex microspheres with different sizes. *J. Ultrasound. Med.*, 13:181–182, 1994.
- [58] L. Hoff and T. F. Johansen. Nonlinear scatter from Sonazoid. Theory and experiments. In *1999 IEEE Ultrasonics Symposium Proceedings*. [67].
- [59] L. Hoff and P. C. Sontum. Acoustic characterisation of Nycomed's NC100100 contrast agent. In *Proceedings of the 16th International Congress on Acoustics and the 135th Meeting of the Acoustical Society of America*, pages 1835–1836. [78].
- [60] L. Hoff and P. C. Sontum. Acoustic characterisation of Nycomed's NC100100 contrast agent. In *1998 IEEE Ultrasonics Symposium Proceedings*, pages 1799–1802. [146].
- [61] L. Hoff, P. C. Sontum, and B. Hoff. Acoustic properties of shell-encapsulated, gas-filled ultrasound contrast agents. In *1996 IEEE Ultrasonics Symposium Proceedings*, pages 1441–1444. [98].
- [62] L. Hoff, P. C. Sontum, and J. M. Hovem. Oscillations of polymeric microbubbles: Effect of the encapsulating shell. *J. Acoust. Soc. Am.*, 2000. Accepted.
- [63] J. Hogg. Neutropil kinetics and lung injury. *Physiol. Rev.*, 67:1249–1295, 1987.

- [64] S. Holm, M. Myhrum, and L. Hoff. Modelling of the ultrasound return from Alburnex microspheres. *Ultrasonics*, 32:123–130, 1994.
- [65] D. Hsieh and M. S. Plesset. Theory of rectified diffusion of mass into gas bubbles. *J. Acoust. Soc. Am.*, 33:206–215, 1961.
- [66] E. Y. Hwang, J. B. Fowlkes, and P. L. Carson. Variables controlling contrast generation in a urinary bladder model. *J. Acoust. Soc. Am.*, 103, 1998.
- [67] *1999 IEEE Ultrasonics Symposium Proceedings*, IEEE, New York, USA, To be published in 2000.
- [68] J. B. Keller and I. I. Kolodner. Damping of underwater explosion bubble oscillations. *J. Acoust. Soc. Am.*, 27:1152–1161, 1956.
- [69] J. B. Keller and M. Miksis. Bubble oscillations of large amplitude. *J. Acoust. Soc. Am.*, 68:628–633, 1980.
- [70] D. Kincaid and W. Cheney. *Numerical Analysis*, chapter 8.3, pages 581–588. [72].
- [71] D. Kincaid and W. Cheney. *Numerical Analysis*, chapter 8.12, pages 655–661. [72].
- [72] D. Kincaid and W. Cheney. *Numerical Analysis*. Brooks/Cole Publishing Company, Pacific Grove, California, USA, 2nd edition, 1996.
- [73] L. E. Kinsler, A. B. Frey, A. B. Coppens, and J. V. Sanders. *Fundamentals of Acoustics*, chapter A10, pages 460–463. [74].
- [74] L. E. Kinsler, A. B. Frey, A. B. Coppens, and J. V. Sanders. *Fundamentals of Acoustics*. John Wiley & Sons, Inc., New York, USA, 3rd edition, 1982.
- [75] J. Kirkwood and H. Bethe. The pressure wave produced by an underwater explosion. *OSRD Report No. 588*, 1942.
- [76] O. D. Kripfgans, J. B. Fowlkes, and P. L. Carson. Characterization of ultrasound contrast agents by short pulse excitation. In *Proceedings of the 16th International Congress on Acoustics and the 135th Meeting of the Acoustical Society of America*, pages 2187–2188. [78].
- [77] S. Krishnan and M. O’Donnel. Suppression of propagating second harmonic in non-linear imaging. In *1997 IEEE Ultrasonics Symposium Proceedings*, pages 1567–1570. [145].
- [78] P. K. Kuhl and L. A. Crum, editors. *Proceedings of the 16th International Congress on Acoustics and the 135th Meeting of the Acoustical Society of America*, Seattle, USA, 1998.
- [79] W. M. Lai, D. Rubin, and E. Krempl. *Introduction to Continuum Mechanics*, chapter 3.7, pages 97–99. [81].
- [80] W. M. Lai, D. Rubin, and E. Krempl. *Introduction to Continuum Mechanics*, chapter 5.21, pages 291–292. [81].

- [81] W. M. Lai, D. Rubin, and E. Kreml. *Introduction to Continuum Mechanics*. Pergamon Press, Oxford, UK, 3rd edition, 1993.
- [82] L. D. Landau and E. M. Lifshitz. *Fluid Mechanics*, chapter I, §1-10, pages 1–26. [85].
- [83] L. D. Landau and E. M. Lifshitz. *Fluid Mechanics*, chapter VIII, §64, pages 251–255. [85].
- [84] L. D. Landau and E. M. Lifshitz. *Fluid Mechanics*, chapter II, §15, pages 44–49. [85].
- [85] L. D. Landau and E. M. Lifshitz. *Fluid Mechanics*, volume 6 of *Course of Theoretical Physics*. Butterworth-Heinemann, Oxford, UK, 2nd edition, 1987.
- [86] G. M. Lanza, R. L. Trousil, K. D. Wallace, J. H. Rose, C. S. Hall, S. M. J., J. G. Miller, P. R. Eisenberg, P. J. Gaffney, and S. A. Wickline. In vitro characterization of a novel, tissue-targeted ultrasonic contrast system with acoustic microscopy. *J. Acoust. Soc. Am.*, 104:3665–3672, 1998.
- [87] G. M. Lanza, K. D. Wallace, M. J. Scott, W. Cacheris, D. Abendschein, D. Christy, A. Sharkey, J. G. Miller, P. Gaffney, and S. A. Wickline. A novel site-targeted ultrasonic contrast agent with broad biomedical application. *Circulation*, 94:3334–33340, 1996.
- [88] W. Lauterborn. Numerical investigation of nonlinear oscillations of gas-bubbles in liquids. *J. Acoust. Soc. Am.*, 59:283–293, 1976.
- [89] W. Lauterborn and E. Cramer. Subharmonic route to chaos observed in acoustics. *Phys. Rev. Letters*, 47:1445–1448, 1981.
- [90] T. G. Leighton. *The Acoustic Bubble*, chapter 3.4, pages 172–190. [96].
- [91] T. G. Leighton. *The Acoustic Bubble*, chapter 3.8.2 and 4.1.2, pages 261–263 and 298–301. [96].
- [92] T. G. Leighton. *The Acoustic Bubble*, chapter 4.2, pages 301–311. [96].
- [93] T. G. Leighton. *The Acoustic Bubble*, chapter 4.3.3, pages 335–338. [96].
- [94] T. G. Leighton. *The Acoustic Bubble*, chapter 4.4.7 (c), pages 421–424. [96].
- [95] T. G. Leighton. An introduction to acoustic cavitation. In F. A. Duck, A. C. Baker, and H. C. Starrit, editors, *Ultrasound in Medicine*, chapter 11, pages 199–224. [36].
- [96] T. G. Leighton. *The Acoustic Bubble*. Academic Press Ltd., London, UK, 1st edition, 1994.
- [97] T. G. Leighton, D. Ramble, and A. Phelps. The detection of tethered and rising bubbles using multiple acoustic techniques. *J. Acoust. Soc. Am.*, 101:2626–2635, 1997.
- [98] M. Levy, S. Schneider, and B. McAvoy, editors. *1996 IEEE Ultrasonics Symposium Proceedings*, IEEE, New York, USA, 1997.

- [99] P.-C. Li. Pulse compression for finite amplitude distortion based harmonic imaging using coded waveforms. *Ultrasonic Imaging*, 21:1–16, 1999.
- [100] D. R. Lide, editor. *CRC Handbook of Chemistry and Physics*, chapter 6, page 8. [103].
- [101] D. R. Lide, editor. *CRC Handbook of Chemistry and Physics*, chapter 6, page 12. [103].
- [102] D. R. Lide, editor. *CRC Handbook of Chemistry and Physics*, chapter 6, page 151. [103].
- [103] D. R. Lide, editor. *CRC Handbook of Chemistry and Physics*. CRC Press, Boca Raton, Florida, USA, 71th edition, 1990.
- [104] O. Lotsberg, J. M. Hovem, and B. Aksum. Experimental observations of sub-harmonic oscillation in Infuson bubbles. *J. Acoust. Soc. Am.*, 99:1366–1369, 1996.
- [105] N. Lu, A. Prosperetti, and S. Yoon. Underwater noise emissions from bubble clouds. *IEEE J. Ocean. Eng.*, 15:275–285, 1990.
- [106] J. Marsh, C. Hall, M. Hughes, J. Mobley, J. Miller, and G. Brandenburger. Broadband trough-transmission signal loss measurements of Albunex suspensions at concentrations approaching in vivo doses. *J. Acoust. Soc. Am.*, 101:1155–1161, 1997.
- [107] J. Marsh, M. Hughes, C. Hall, S. Lewis, R. Trousil, G. Brandenburger, H. Levene, and J. Miller. Frequency and concentration dependence of the backscatter coefficient of the ultrasound contrast agent Albunex. *J. Acoust. Soc. Am.*, 104:1654–1666, 1998.
- [108] The MathWorks Inc., Natick, MA, USA. *MATLAB Function Reference. Volume 1: Language. Version 5*, Revised for Matlab 5.2, 1998.
- [109] The MathWorks Inc., Natick, MA, USA. *Signal Processing Toolbox for use with MATLAB. User's Guide. Version 4*, Second printing, revised for Matlab 5.2, 1998.
- [110] H. Medwin. Counting bubbles acoustically: a review. *Ultrasonics*, 15:7–13, 1977.
- [111] D. Miller. Ultrasonic detection of resonant cavitation bubbles in a flow tube by their second harmonic emissions. *Ultrasonics*, 22:217–224, 1981.
- [112] D. L. Miller. Frequency relationships for ultrasonic activation of free microbubbles, encapsulated microbubbles and gas-filled micropores. *J. Acoust. Soc. Am.*, 104:2498–2505, 1998.
- [113] M. Minnaert. On musical air-bubbles and the sounds of running water. *Philos. Mag.*, 16:235–248, 1933.

- [114] M. J. Monaghan, J. Metcalfe, S. Odunlami, A. Waaler, and D. Jewitt. Digital radiofrequency echocardiography in the detection of myocardial contrast following intravenous administration of Albunex. *European Heart Journal*, 14:1200–1209, 1993.
- [115] K. Morgan, M. Averkiou, and K. Ferrara. The effect of the phase of transmission on contrast agent echoes. *IEEE Trans. Ultrason., Ferroelectr., Freq. Contr.*, 45:872–875, 1998.
- [116] K. Morgan, P. Dayton, D. Kruse, A. Klibanov, G. Brandenburger, and K. Ferrara. Effect of imaging parameters on the echoes from ultrasonic contrast agents. In *1997 IEEE Ultrasonics Symposium Proceedings*, pages 1593–1596. [145].
- [117] P. Morse and K. Ingard. *Theoretical Acoustics*, chapter 8.2, pages 418–441. [120].
- [118] P. Morse and K. Ingard. *Theoretical Acoustics*, chapter 7.1, pages 306–332. [120].
- [119] P. Morse and K. Ingard. *Theoretical Acoustics*, chapter 14.4, pages 863–873. [120].
- [120] P. Morse and K. Ingard. *Theoretical Acoustics*. Princeton University Press, New Jersey, USA, First Princeton University Press edition, 1986.
- [121] E. Neppiras. Subharmonic and other low-frequency emission from bubbles in sound-irradiated liquids. *J. Acoust. Soc. Am.*, 46:587–601, 1968.
- [122] E. Neppiras and B. Noltingk. Cavitation produced by ultrasonics: Theoretical considerations for the onset of cavitation. *Proc. Phys. Soc.*, B64:1032–1038, 1951.
- [123] V. Newhouse and P. Shankar. Bubble size measurements using the nonlinear mixing of two frequencies. *J. Acoust. Soc. Am.*, 75:1473–1477, 1984.
- [124] R. Nishi. The scattering and absorption of sound waves by a gas bubble in a viscous liquid. *Acustica*, 33:65–74, 1975.
- [125] B. Noltingk and E. Neppiras. Cavitation produced by ultrasonics. *Proc. Phys. Soc.*, B63:674–685, 1950.
- [126] A. V. Oppenheim and R. W. Schaefer. *Discrete-Time Signal Processing*, chapter 7.2, pages 465–478. [127].
- [127] A. V. Oppenheim and R. W. Schaefer. *Discrete-Time Signal Processing*. Prentice Hall, Upper Saddle River, New Jersey, USA, second edition, 1999.
- [128] T. Orskaug. Subharmonisk spredning fra NC100100. Student project report. Norwegian University of Science and Technology, Dept. of Telecommunications, Trondheim, Norway, 1999.
- [129] J. Österman and C. Nordling. *Physics Handbook*, chapter F-1.5, pages 35–39. Studentlitteratur, Lund, Sweden, 4th edition, 1987.

- [130] L. A. Ostrovsky, A. M. Sutin, I. A. Sustova, A. I. Matveyev, and A. I. Popatov. Nonlinear, low-frequency sound generation in a bubble layer: Theory and laboratory experiment. *J. Acoust. Soc. Am.*, 104:722–726, 1998.
- [131] U. Parlitz, V. Englisch, C. Scheffczyk, and W. Lauterborn. Bifurcation structure of bubble oscillators. *J. Acoust. Soc. Am.*, 88:1061–1077, 1990.
- [132] D. Phillips, X. Chen, R. Baggs, D. Rubens, M. Violante, and K. J. Parker. Acoustic backscatter properties of the particle/bubble ultrasound contrast agent. *Ultrasonics*, 36:883–892, 1998.
- [133] M. S. Plesset. The dynamics of cavitation bubbles. *J. Appl. Mech.*, 16:277–282, 1949.
- [134] M. S. Plesset. On the stability of fluid flows with spherical symmetry. *J. Appl. Phys.*, 25:96–98, 1954.
- [135] M. S. Plesset and T. Mitchell. On the stability of the spherical shape of a vapor cavity in a liquid. *Quart. Appl. Math.*, 13, 1956.
- [136] M. S. Plesset and A. Prosperetti. Bubble dynamics and cavitation. *Ann. Rev. Fluid. Mech.*, 9:145–185, 1977.
- [137] H. Poritsky. The collapse or growth of a spherical cavity in a viscous fluid. In *Proceedings of the First U.S. National Congress on Applied Mechanics*, pages 813–821, New York, USA, 1952.
- [138] A. Prosperetti. Nonlinear oscillations of gas bubbles in liquids: Steady-state solutions. *J. Acoust. Soc. Am.*, 56:878–885, 1974.
- [139] A. Prosperetti. Nonlinear oscillations of gas bubbles in liquids: Transient solutions and the connection between subharmonic signal and cavitation. *J. Acoust. Soc. Am.*, 57:810–821, 1975.
- [140] A. Prosperetti. Thermal effects and damping mechanisms in the forced radial oscillations of gas bubbles in liquids. *J. Acoust. Soc. Am.*, 61:17–27, 1977.
- [141] A. Prosperetti. Bubble phenomena in sound fields: part one. *Ultrasonics*, 22:69–77, 1984.
- [142] A. Prosperetti. Bubble phenomena in sound fields: part two. *Ultrasonics*, 22:115–124, 1984.
- [143] Rayleigh, Lord. On the pressure developed in a liquid during the collapse of a spherical cavity. *Philos. Mag.*, 34:94–98, 1917.
- [144] Rayleigh, Lord. *The Theory of Sound*, volume II, chapter XV, §296, pages 149–154. Dover Publications, New York, USA, 2nd edition, 1945.
- [145] S. Schneider, M. Levy, and B. McAvoy, editors. *1997 IEEE Ultrasonics Symposium Proceedings*, IEEE, New York, USA, 1998.
- [146] S. Schneider, M. Levy, and B. McAvoy, editors. *1998 IEEE Ultrasonics Symposium Proceedings*, IEEE, New York, USA, 1999.

- [147] L. Segel and G. Handelman. *Mathematics Applied to Continuum Mechanics*, chapter 3.1, pages 78–88. [149].
- [148] L. Segel and G. Handelman. *Mathematics Applied to Continuum Mechanics*, chapter 4.2-4.3, pages 159–173. [149].
- [149] L. Segel and G. Handelman. *Mathematics Applied to Continuum Mechanics*. Dover Publications, Inc., New York, USA, Dover edition, 1987.
- [150] L. Shampine and M. Reichelt. The MATLAB ODE suite. *SIAM Journal on Scientific Computing*, 18:1–22, 1997.
- [151] P. Shankar and J. Chapelon. Fluid pressure measurement using bubbles insonified by two frequencies. *Ultrasonics*, 24:333–336, 1986.
- [152] P. Shankar, P. Krishna, and V. Newhouse. Subharmonic backscattering from ultrasound contrast agents. *J. Acoust. Soc. Am.*, 106:2104–2110, 1999.
- [153] W. T. Shi, F. Forsberg, A. L. Hall, R. Y. Chiao, J.-B. Liu, S. Miller, K. E. Thomenius, M. A. Wheatley, and B. Goldberg. Subharmonic imaging with microbubble contrast agents: Initial results. *Ultrasonic Imaging*, 21:79–84, 1999.
- [154] E. Silberman. Sound velocity and attenuation in bubbly mixtures measured in standing wave tubes. *J. Acoust. Soc. Am.*, 29:925–933, 1957.
- [155] D. H. Simpson and P. N. Burns. Perfusion imaging with pulse inversion Doppler and microbubble contrast agents: In vivo studies of the myocardium. In *1998 IEEE Ultrasonics Symposium Proceedings*, pages 1783–1786. [146].
- [156] D. H. Simpson, C. T. Chin, and P. N. Burns. Pulse inversion Doppler: A new method for detecting nonlinear echoes from microbubble contrast agents. *IEEE Trans. Ultrason., Ferroelectr., Freq. Contr.*, 46:372–382, 1999.
- [157] P. C. Sontum, J. Østensen, K. Dyrstad, and L. Hoff. Acoustic properties of NC100100 and their relationship with the microbubble size distribution. *Invest. Radiol.*, 34:268–275, 1999.
- [158] P. C. Sontum, P. Walday, K. Dyrstad, L. Hoff, S. Frigstad, and C. Christiansen. Effect of microsphere size distribution on the ultrasonographic contrast efficacy of air-filled albumin microspheres in the left ventricle of dog hearts. *Invest. Radiol.*, 32:627–635, 1997.
- [159] M. Strasberg. The pulsation frequency of nonspherical gas bubble in liquids. *J. Acoust. Soc. Am.*, 25:536–537, 1953.
- [160] M. Strasberg. Gas bubbles as sources of sound in liquids. *J. Acoust. Soc. Am.*, 28:20–26, 1956.
- [161] R. Thurasingham. Sound speed in bubbly water at megahertz frequencies. *Ultrasonics*, 36:767–773, 1998.
- [162] L. Trilling. The collapse and rebound of a gas bubble. *J. Appl. Phys.*, 23:14–17, 1952.

- [163] D. Tucker and V. Welsby. Ultrasonic monitoring of decompression. *The Lancet*, I:1253, 1968.
- [164] V. Uhlendorf. Physics of ultrasound contrast imaging: Scattering in the linear range. *IEEE Trans. Ultrason., Ferroelectr., Freq. Contr.*, 41:70–79, 1994.
- [165] V. Uhlendorf, T. Fritzsche, and S. J. Ultraschallverfahren und Schaltungen zu deren Durchföhrung. *European patent EP 0 357 167 A1*, 1988.
- [166] M. Vacher and G. Gimenez. Nonlinear behaviour of microbubbles: Application to their ultrasonic detection. *Acustica*, 54:274–283, 1984.
- [167] P. Waterman and R. Truell. Multiple scattering of waves. *J. Math. Phys.*, 2:512–537, 1961.
- [168] P. Welch. The use of Fast Fourier Transform for the estimation of power spectra: A method based on time averaging over short, modified periodograms. *IEEE Trans. Audio Electroacoust.*, AU-15:70–73, 1967.
- [169] T. Wittingham. The purpose and techniques of acoustic output measurement. In F. A. Duck, A. C. Baker, and H. C. Starrit, editors, *Ultrasound in Medicine*, chapter 7, pages 129–148. [36].
- [170] Z. Ye. On sound scattering and attenuation of Alunex bubbles. *J. Acoust. Soc. Am.*, 100:2011–2028, 1996.

